Geochemistry of Mars and implications for organic carbon preservation — observations from rover data and terrestrial analogs

Thesis by

Hemani Kalucha

In Partial Fulfillment of the Requirements for the Degree of

Doctor of Philosophy

CALIFORNIA INSTITUTE OF TECHNOLOGY

Pasadena, California

2026

(Defended May 19, 2025)

Hemani Kalucha
ORCID: 0009-0002-5953-3250

ACKNOWLEDGEMENTS

Thank you to my advisor, Woody Fischer, for giving me the chance to work on a space mission as I had always dreamed of doing and for suggesting I do a PhD. I never would have dared to do it otherwise. I would like to thank the rest of my thesis committee – John Grotzinger, George Rossman, Miquela Ingalls, and Michael Brown, for their support and for being infectious teachers who exposed me to the wonders of geology. In addition, I thank Paul Asimow, Mike Lamb, Ben Johnson, and Alex Sessions for their valuable help and input in my research. And Paul Asimow again for taking us on a once in a lifetime Pahoehoe trip. There is a long list of staff, post-docs, and grad students without whom my research could not have been completed and I will try to list them completely now: Madison Douglas, Yutian Ke, Hanna Leapaldt, Ellen Olsen, Chi Ma, Nathan Dalleska, Hannah Dion-Kirschner, Emily Geyman, Justin Nghiem, Fenfang Wu, Michael Takasa, Mark Garcia, and Martin Hohmann. I appreciate you for taking the time to help me. This department would be gloomier without Jen Schechet and Julie Lee. Thank you for your warmth.

This thesis would not exist without the most valuable player, the Perseverance Rover. It was a joy to be part of this mission and participate in the data acquisition and analysis firsthand. I feel privileged to have worked with some of the most famous names in Mars science already, as a part of the 400 scientist strong rover team. Specifically, I want to thank Adrian Broz for being the best collaborator, scientist, and mentor all in one. I cannot imagine this experience without him. Next, I thank Nina Lanza for being a true mentor and I'm proud to say, friend, to me through this whole journey. Another person I must thank for being my partner in crime on this mission is Denise Buckner. Last but not least, thank you to Katie Stack for her time and mission wisdom.

My grad school experience was completely shaped by the privilege of living in California. I am so grateful I got to spend my 20s in these mountains and amongst the redwoods and the sequoias. Most of all, I got through the hard times and laughed through the good times because of my dear friends, old and new, you know who you are. Thank you for taking care of me. Caltech's greatest gift to me was introducing me to James Mullahoo.

Of course, all of this would be impossible without my parents. They are to thank for everything else in my life.

I hope my grandma is looking down at me proudly for this.

ABSTRACT

Curiosity and Perseverance rovers have been exploring ancient river and lake deposits in Gale Crater and Jezero Crater, Mars since 2012 and 2021, respectively. Understanding the geochemistry of these environments at small scales is key to assembling a thorough picture of the habitability of Mars through time. In Chapter 2, I proposed that the formation of certain sulfate minerals in Gale Crater is the result of pyrite oxidation as opposed to evaporation of lake water. This has significant implications for the ancient environment of Gale Crater since these deposits do not represent eras of the ancient lake drying out but rather extended continuity and stability of the aqueous system, which shows greater promise for habitability. Chapters 3-5 studied terrestrial analog sites for geochemical and textural characteristics of rock packages in Jezero crater in order to assess their biosignature preservation potential in the form of organic carbon. In the hyper arid river deposits of the Amargosa River in Death Valley, California, organic carbon persisted in fluvial deposits at low abundance despite oxidizing conditions and saturated sediments, and suggested that ancient river deposits on Mars may retain traces of organics in fine-grained deposits if they are present during deposition. Comparing concretions found in the lake deposits of Jezero Crater to terrestrial concretions of similar mineralogy and formation mechanism, all three sites of terrestrial concretions contained significant concentrations of organic carbon (up to ~2 wt.%), which suggested that concretions at Jezero Crater reflect local sites of enhanced biosignature preservation potential. In the hypersaline sulfate and carbonate rich deposits of lakes in British Columbia, Canada, organic carbon is correlated with abundance of salt minerals specifically. The samples with the highest organic C content (up to ~23 wt. %) also have high salt content (up to ~75 wt. %). This designates hypersaline lakes as key preservers of organic carbon and salts as the highest priority mineral target for finding organic carbon on Mars. In summary, this PhD demonstrates that detailed analysis of the mineral deposits on Mars at the centimeter to micrometer scale reveal early Mars to be a highly habitable planet.

PUBLISHED CONTENT AND CONTRIBUTIONS

Chapter 3 is published as: Kalucha, H., Douglas, M. M., Lamb, M. P., Ke, Y., & Fischer, W. W. (2024). Low but persistent organic carbon content of hyperarid river deposits and implications for ancient Mars. *Journal of Geophysical Research: Planets*, *129*(5), e2023JE008182. DOI: 10.1029/2023JE008182

- H. Kalucha and W. W. Fischer conceived the study. H. Kalucha performed all the data analysis and wrote the manuscript with help from all authors.

Chapter 4 is published as: Kalucha, H., Broz, A., Randazzo, N., Aramendia, J., Madariaga, J. M., Garczynski, B., ... & Wiens, R. C. (2024). Probable concretions observed in the Shenandoah Formation of Jezero Crater, Mars and comparison with terrestrial analogs. *Journal of Geophysical Research: Planets*, *129*(8), e2023JE008138. DOI: 10. 1029/2023JE008138

- H. Kalucha and A. Broz conceived the study. H. Kalucha performed all the data analysis and wrote the manuscript with help from all authors. The SuperCam instrument was originally proposed by R. Wiens and S. Maurice.

TABLE OF CONTENTS

LIST OF ILLUSTRATIONS AND TABLES

Chapter 1

INTRODUCTION

The question of whether Mars once supported life seems insurmountable at first but is too fundamental to not attempt to answer. There is an additional complexity of whether traces of life were even preserved if life in fact existed on Mars. The answers lie in the geological record of Mars. We can begin to chip away at this problem by following both a top down approach and a bottom up approach in tandem. The top down approach consists of examining traces that life on Earth in Mars-like environments (known as terrestrial analogs) leaves behind in the rock record of Earth and searching for those features in the rock record of Mars. We call these traces *biosignatures*. A robust definition of biosignature is "any phenomenon for which biological processes are a known possible explanation and whose potential abiotic causes have been reasonably explored and ruled out" [Gillen et al., 2023]. The bottom up approach relies on our understanding of what life on Earth needs to survive and searching for evidence of those environmental conditions on Mars, one again as inferred from the rock record. If these approaches were to converge in a singular deposit, it would be a strong case for evidence of past life on Mars. However, the exploration tools currently available to use are orbital satellites and rovers on the surface. These missions are instrument limited and cannot conclusively identify ancient life. This makes Mars Sample Return [McCubbin et al., 2025], a mission designed to bring back sample cores from Jezero Crater on Mars back to Earth, critical to answering the question of life on Mars.

Biosignatures range from physical features to chemical signals to biotic molecules at the scale of centimeters to microns. Examples of physical features are stromatolites (ancient microbial dome structures), fossils, and microbially precipitated mineral textures (like framboidal pyrite) [Malaterre et al., 2023]. Chemical signals can include trace metal enrichments associated with organics in rock layers, stable isotope anomalies, carbon and sulfur isotope fractionation, and mineral assemblages in redox disequilibrium [Malaterre et al., 2023]. Biotic molecules such as DNA, amino acids, peptides, lipids, and pigments are the most common but can extend to anything with sufficient molecular complexity that requires life to make it [Malaterre et al., 2023]. Often, these molecules are products of reactions that would be kinetically inhibited in the environment. Of course, it is imperative to distinguish any potential biosignature from false positives, examples of which are extensively discussed in McMahon and Cosmidis (2023). The ladder of life detection has determined a hierarchy to the above biosignatures in terms of increasing strength of evidence for life [Neveu et al., 2018].

Examples of environmental conditions conducive to life are known as habitability markers. The habitability of an environment is defined by availability of liquid water, organic and inorganic building blocks, energy sources, and gradients in redox, temperature, pH, and energy disequilibria [Neveu et al., 2018]. In terrestrial settings, this may look like a lake with redox gradients over its depth or streams of different compositions mixing together or hot springs and hydrothermal vents emitting various gases [Hays et al., 2017].

On the other hand, environments that best preserve signs of life are sometimes at odds with environments most conducive to supporting life. Biosignatures tend to be preserved in quiescent conditions and rocks that were not subject to high temperature and pressure as this tends to overwrite any delicate features [Hays et al., 2017]. Organic matter burial is highest in oxygen poor, shallow, reducing conditions with high sedimentation rates [Burdige, 2007]. These sides must be balanced for us to be able to find signs of life in the rock record.

The last 20 years of rover exploration on Mars has revealed incredible similarities between the red planet and ours. Mars is and was sedimentologically active [McLennan et al., 2018]. Ancient Mars had lakes [Michalski et al., 2022], rivers [Dickson et al., 2021], deltas [Toffoli et al., 2021], wind blown dunes [Vaz et al., 2023], and glaciers [Galofre et al., 2022]. Present day Mars is actively carved by frost and ice sublimation, mass wasting and landslides, and dust devils and dunes [Murdoch et al., 2022; Diniega et al., 2021]. Furthermore, surface and subsurface water has produced weathered deposits all over the planet's surface [Ye and Michalski, 2022]. There is an abundance and diversity of clay minerals present globally [Du et al., 2023]. Significant sulfate, carbonate, and chloride deposits have been found across Mars [Bridges et al., 2019; Kite and Conway, 2024; Das et al., 2025]. Last but not least, several oxidants have been detected on the surface and many forms of iron oxide are ubiquitous in the deposits [Lasne et al., 2016]. All of this is evidence of a physically and chemically active planet, which is critical for life.

1.1 Very Brief Geologic History of Mars

From Ehlmann et al. (2011): Mars history is divided into four major eras: Pre-Noachian (4.5-4.1 Ga), Noachian (4.1-3.7 Ga), Hesperian (3.7-3 Ga), and Amazonian (3 Ga to Present). The magnetic field of the planet was active until ~3.7 Ga [Mittleholz et al., 2020]. Large impacts occurred into the Noachian. Major volcanism continued until the Hesperian and perhaps became episodic in the Amazonian. The Noachian is dominated by Fe, Mg smectite clay deposits. In the late Noachian, there is a transition to Al rich clays and in the mid Hesperian, a transition to hydrated silica. The salt deposits are largely carbonates in the Late Noachian but transition to being sulfate dominated by the end of the Hesperian.

1.2 Landing Sites Referenced in this Thesis

Gale crater is a ~155 km wide ~3.8 Ga complex crater just south of the equator [Cabrol et al., 1999; Edgett and Malin, 2000]. Gale has a layered mound at the center named Aeolis Mons, or informally, Mount Sharp. After 10 years of exploring Mount Sharp, Curiosity Rover found that its layers reveal a transition of Mars climate from warm and wet in the late Noachian to dry through the Hesperian and into the early Amazonian [Vasavada, 2022]. Gale crater is an endorheic basin: many valley networks empty into Gale crater but there are no outlet channels [Ehlmann and Buz, 2015]. Thus, surface runoff created the initial rock packages in the crater. After surface runoff dried up, Gale Crater likely continued to have significant water activity through a regional groundwater system into the early Amazonian [Roseborough et al., 2021].

Jezero crater is ~45 km wide, ~3.8 Ga crater on the northwestern edge of the Isidis impact basin on Mars [Werner, 2008; Fassett and Head, 2008; Mustard et al., 2007]. Since the Isidis impact basin is one of the oldest and biggest impact craters on Mars, studying the region in and around Jezero crater provides an opportunity understand the composition and weathering of some of the earliest crust on

Mars [Horgan et al., 2020; Ehlmann et al., 2009; Mustard et al., 2009; Goudge et al., 2015]. Jezero crater has two inlet channels and one outlet channel [Horgan et al., 2020]. Delta and river systems exist on top of the crater floor where each of the inlet channels feed into the crater and created a lake that probably lasted from the Late Noachian to Early Hesperian [Ehlmann et al., 2008; Fassett & Head, 2005; Goudge et al., 2015, 2017, 2018; Mangold et al., 2021; Schon et al., 2012; Farley et al., 2022, Stack et al., 2024; Paige et al., 2024; [Mangold et al., 2021; Stack et al., 2024; Ives et al., 2023; Gwizd et al., 2024]. Unlike Gale Crater, Jezero Crater was likely not subject to significant groundwater inflow [Horvath and Andrews-Hanna, 2024].

1.3 Missions Referenced in the Thesis

From Grotzinger et al. (2012): Curiosity Rover has been exploring Gale Crater since 2012. It is equipped with engineering cameras, science cameras, a drill, a dust removal tool, a robotic arm, environmental sensors, and six science instruments. MastCam is a color panoramic camera pair mounted 6.5 feet high. It has a resolution of 150 microns per pixel at 2 meters and 7.4 cm per pixel at 1 kilometer. MAHLI (Mars Hend Lens Imager) is a close up imager on the end of the robotic arm with a resolution as high as 13.9 microns per pixel. The elemental composition of the rocks is measured by APXS (Alpha Particle X-ray Spectrometer) and ChemCam, a spatially resolved laser induced breakdown spectrometer. The minerals in the rocks are detected by CheMin, and x-ray diffraction instrument. Organic and inorganic compounds are detected by SAM (Sample Analysis at Mars), a gas chromatography mass spectrometer and tunable laser spectrometer. It can also measure carbon, sulfur, and oxygen isotopes. RAD (Radiation assessment detector) measures high energy particles on the Martian surface. DAN (Dynamic Albedo of Neutrons) is neutron generator designed to detect subsurface water and ice.

From Farley et al. (2020): Perseverance Rover has been exploring Jezero Crater since 2021. It is equipped with engineering cameras, science cameras, a drill, a sampling system, a dust removal tool, an abrading tool, a robotic arm, environmental sensors, and five science instruments. MastCam-Z is exactly like the MastCam instrument on Curiosity rover except higher resolution at long distances. SuperCam is like the ChemCam instrument except that it is additionally equipped with a visible-infrared spectrometer and a long-distance Raman spectrometer. SHERLOC (Scanning Habitable Environments with Raman and Luminescence for Organics and Chemicals) can detect spatially resolved inorganic and organic compounds on the surface of Mars with a Raman and fluorescence spectrometer. The laser has a 100 micron spot size and the two cameras that have a 10.1 micron and 15.9 micron per pixel resolution. PIXL (Planetary Instrument for X-ray Lithochemistry) is a spatially resolved x-ray fluorescence spectrometer with a 120 micron spot size and a 50 micron per pixel camera resolution. MOXIE (Mars Oxygen ISRU Experiment) was designed to produce oxygen from the Martian atmosphere in preparation for sending humans to Mars. RIMFAX (Radar Image for Mars' Subsurface Experiment) is a ground penetrating radar designed to detect shallow subsurface geologic structure.

1.4 Broad Scale Surface Processes

As rovers have explored Mars through the decades, evidence for three widespread and significant weathering processes has emerged. Rocks and soils from the landing sites of Viking 1 (Chryse Planitia), Sojourner (Ares Vallis), and the Mars Exploration Rovers (Gusev crater and Meridiani Planum) shared the following characteristics: secondary sulfate and iron oxide rich soils, Fe,Mg

sulfate cemented sandstones, the detection of ferric sulfate minerals such as jarosite, and an aluminum deficient assemblage of secondary minerals [Hurowitz and McLennan, 2007 and references therein]. This assemblage was explained by low water-to-rock ratio, low-pH sulfur acid weathering conditions during the late Noachian to Hesperian eras (~3.85 to 3 billion years ago).

In addition to the continued detection of sporadic jarosite at Curiosity's landing site (Gale crater), many other sulfate minerals (gypsum, bassanite, anhydrite, starkeyite, kieserite, and akageneite) were detected ubiquitously in the stratigraphy as well as in enriched intervals corresponding to the Glen Torridon region, Vera Rubin Ridge, and the Mg-sulfate bearing unit [Vaniman et al., 2024 and references therein]. Textural and sedimentological observations of the sulfate suggest saline groundwater as a source for the calcium sulfates, acidic groundwater for the jarosite, and brine weathering for the magnesium sulfate deposits [Vaniman et al., 2024; Rapin et al., 2019; Bristow et al., 2021]. Gale crater therefore reveals the importance of brine weathering as a surface process on Mars. Perseverance's landing site, Jezero crater, hosts a fan in the sedimentary basin interbedded with lacustrine deposits. The lacustrine unit, Hogwallow Flats, consists of sediments enriched in Fe-Mg sulfates (20-30 wt.%) [Broz et al., 2024 and references therein]. Based on textural and chemical analyses, there is evidence of both sulfate deposition in a hypersaline environment and acid weathering. Thus, the two returned samples from this unit [McCubbin et al., 2025] have been impacted by both processes.

Most recently, Gale and Jezero craters have revealed evidence of wet-dry cycling in sediments. Textural analyses of the basal Mg-sulfate bearing unit reveal sulfate bearing polygonal ridges with Y-junctions, a crack morphology exclusive to sediments that have experienced wet-dry cycling [Rapin et al., 2023; Stein et al., 2018]. The Bright Angel unit within Neretva Vallis, the inlet channel of Jezero crater, is rich in aluminosilicate clay minerals and iron oxides and has a subangular blocky structure [Hurowitz et al., 2025; Broz et al., 2025]. On Earth, these features are most commonly found in paleosols (ancient soils) that have experienced wet-dry cycling [Broz et al., 2025]. Organics were detected in Bright Angel by the Raman spectrometer on the rover, SHERLOC [Hurowitz et al., 2025]. Therefore, the returned sample from this unit [McCubbin et al., 2025] will have organics subjected to wet-dry cycling.

1.5 Goals of the Thesis

Rovers in multiple landing sites across Mars have allowed us to determine that there are certain common broad scale surface processes that have chemically altered Martian sediments. To learn about the astrobiological potential of these sediments, we have to zoom in to the scale of centimeters to microns. In this thesis, by zooming into particular deposits, we see intriguing mineral assemblages and sedimentological features that suggest a chemically diverse and active planet. When we compare these deposits to terrestrial analogs, we find that Mars is full of habitable environments that are also set up for preservation of life.

References

Bridges, J. C., Hicks, L. J., & Treiman, A. H. (2019). Carbonates on Mars. In *Volatiles in the Martian crust* (pp. 89-118). Elsevier.

Bristow, T. F., Grotzinger, J. P., Rampe, E. B., Cuadros, J., Chipera, S. J., Downs, G. W., ... & Vasavada, A. R. (2021). Brine-driven destruction of clay minerals in Gale crater, Mars. *Science*, *373*(6551), 198-204.

Broz, A. P., Horgan, B., Kalucha, H., Johnson, J. R., Royer, C., Dehouck, E., ... & Wiens, R. C. (2024). Diagenetic History and Biosignature Preservation Potential of Fine-Grained Rocks at Hogwallow Flats, Jezero Crater, Mars. *Journal of Geophysical Research: Planets*, *129*(11), e2024JE008520.

Broz, A. P., Kalucha, H., Benison, K., Horgan, B., Klidaras, A., Manelski, H., … & Bell, J. (2025, March). Green Reduction Spots in Red Beds of the Bright Angel Formation, Jezero Crater, Mars and implication for biosignature preservation potential. In *56th Lunar and Planetary Science Conference* (p. 1706).

Burdige, D. J. (2007). Preservation of organic matter in marine sediments: controls, mechanisms, and an imbalance in sediment organic carbon budgets?. *Chemical Reviews*, *107*(2), 467-485.

Cabrol, N. A., Grin, E. A., Newsom, H. E., Landheim, R., & McKay, C. P. (1999). Hydrogeologic evolution of Gale crater and its relevance to the exobiological exploration of Mars. *Icarus*, *139*(2), 235-245.

Das, E., Glotch, T. D., Edwards, C. S., Ye, C., Milliken, R. E., Rogers, A. D., ... & Norberg, K. (2025). Remote determination of Martian chloride salt abundances. *Journal of Geophysical Research: Planets*, *130*(3), e2024JE008541.

De Toffoli, B., Plesa, A. C., Hauber, E., & Breuer, D. (2021). Delta deposits on Mars: A global perspective. *Geophysical Research Letters*, *48*(17), e2021GL094271.

Dickson, J. L., Lamb, M. P., Williams, R. M. E., Hayden, A. T., & Fischer, W. W. (2021). The global distribution of depositional rivers on early Mars. *Geology*, *49*(5), 504-509.

Diniega, S., Bramson, A. M., Buratti, B., Buhler, P., Burr, D. M., Chojnacki, M., ... & Widmer, J. M. (2021). Modern Mars' geomorphological activity, driven by wind, frost, and gravity. *Geomorphology*, *380*, 107627.

Du, P., Yuan, P., Liu, J., & Ye, B. (2023). Clay minerals on Mars: An up-to-date review with future perspectives. *Earth-Science Reviews*, *243*, 104491.

Ehlmann, B. L., & Buz, J. (2015). Mineralogy and fluvial history of the watersheds of Gale, Knobel, and Sharp craters: A regional context for the Mars Science Laboratory Curiosity's exploration. *Geophysical Research Letters*, *42*(2), 264-273.

Ehlmann, B. L., Mustard, J. F., Fassett, C. I., Schon, S. C., Head III, J. W., Des Marais, D. J., ... & Murchie, S. L. (2008). Clay minerals in delta deposits and organic preservation potential on Mars. *Nature Geoscience*, *1*(6), 355-358.

Ehlmann, B. L., Mustard, J. F., Murchie, S. L., Bibring, J. P., Meunier, A., Fraeman, A. A., & Langevin, Y. (2011). Subsurface water and clay mineral formation during the early history of Mars. *Nature*, *479*(7371), 53-60.

Ehlmann, B. L., Mustard, J. F., Swayze, G. A., Clark, R. N., Bishop, J. L., Poulet, F., ... & Murchie, S. L. (2009). Identification of hydrated silicate minerals on Mars using MRO-CRISM: Geologic context near Nili Fossae and implications for aqueous alteration. *Journal of Geophysical Research: Planets*, *114*(E2).

Farley, K. A., Stack, K. M., Shuster, D. L., Horgan, B. H. N., Hurowitz, J. A., Tarnas, J. D., ... & Zorzano, M. P. (2022). Aqueously altered igneous rocks sampled on the floor of Jezero crater, Mars. *Science*, *377*(6614), eabo2196.

Farley, K. A., Williford, K. H., Stack, K. M., Bhartia, R., Chen, A., de la Torre, M., ... & Wiens, R. C. (2020). Mars 2020 mission overview. *Space Science Reviews*, *216*, 1-41.

Fassett, C. I., & Head III, J. W. (2005). Fluvial sedimentary deposits on Mars: Ancient deltas in a crater lake in the Nili Fossae region. *Geophysical Research Letters*, *32*(14).

Fassett, C. I., & Head III, J. W. (2008). Valley network-fed, open-basin lakes on Mars: Distribution and implications for Noachian surface and subsurface hydrology. *Icarus*, *198*(1), 37-56.

Gillen, C., Jeancolas, C., McMahon, S., & Vickers, P. (2023). The call for a new definition of biosignature. *Astrobiology*, *23*(11), 1228-1237.

Goudge, T. A., Milliken, R. E., Head, J. W., Mustard, J. F., & Fassett, C. I. (2017). Sedimentological evidence for a deltaic origin of the western fan deposit in Jezero crater, Mars and implications for future exploration. *Earth and Planetary Science Letters*, *458*, 357-365.

Goudge, T. A., Mohrig, D., Cardenas, B. T., Hughes, C. M., & Fassett, C. I. (2018). Stratigraphy and paleohydrology of delta channel deposits, Jezero crater, Mars. *Icarus*, *301*, 58-75.

Goudge, T. A., Mustard, J. F., Head, J. W., Fassett, C. I., & Wiseman, S. M. (2015). Assessing the mineralogy of the watershed and fan deposits of the Jezero crater paleolake system, Mars. *Journal of Geophysical Research: Planets*, *120*(4), 775-808.

Grau Galofre, A., Whipple, K. X., Christensen, P. R., & Conway, S. J. (2022). Valley networks and the record of glaciation on ancient Mars. *Geophysical Research Letters*, *49*(14), e2022GL097974.

Grotzinger, J. P., Crisp, J., Vasavada, A. R., Anderson, R. C., Baker, C. J., Barry, R., ... & Wiens, R. C. (2012). Mars science laboratory mission and science investigation. *Space Science Reviews*, *170*, 5-56.

Gwizd, S., Stack, K. M., Ives, L., Gupta, S., Randazzo, N., Lamb, M., ... & Bell, J. (2024, March). Depositional History of the Upper Sequence of the Western Fan: Evidence for Late-Stage Fluvial and Potential Igneous Activity, Jezero Crater, Mars. In *55th Lunar and Planetary Science Conference (LPSC)*. Lunar and Planetary Institute.

Hays, L. E., Graham, H. V., Des Marais, D. J., Hausrath, E. M., Horgan, B., McCollom, T. M., ... & Lynch, K. L. (2017). Biosignature preservation and detection in Mars analog environments. *Astrobiology*, *17*(4), 363-400.

Horgan, B. H., Anderson, R. B., Dromart, G., Amador, E. S., & Rice, M. S. (2020). The mineral diversity of Jezero crater: Evidence for possible lacustrine carbonates on Mars. *Icarus*, *339*, 113526.

Horvath, D. G., & Andrews-Hanna, J. C. (2024). The hydrology of the Jezero crater paleolake: Implications for the climate and limnology of the lake system from hydrological modeling. *Earth and Planetary Science Letters*, *635*, 118690.

Hurowitz, J. A., & McLennan, S. M. (2007). A∼ 3.5 Ga record of water-limited, acidic weathering conditions on Mars. *Earth and Planetary Science Letters*, *260*(3-4), 432-443.

Hurowitz, J. A., Tice, M. M., Allwood, A. C., Cable, M. L., Hand, K. P., Murphy, A. E., ... & Wolf, Z. U. (2025, March). THE DETECTION OF A POTENTIAL BIOSIGNATURE BY THE PERSEVERANCE ROVER ON MARS. In *56th Lunar and Planetary Science Conference* (p. 2581).

Ives, L., Stack, K., Gupta, S., Grotzinger, J. P., Lamb, M. P., Barnes, R., ... & Hamran, S. E. (2023, December). Reassessing the sedimentary depositional origin of the Jezero crater western fan's

curvilinear unit: reconciling orbital and rover observations. In *AGU Fall Meeting Abstracts* (Vol. 2023, pp. P43A-04).

Kite, E. S., & Conway, S. (2024). Geological evidence for multiple climate transitions on Early Mars. *Nature Geoscience*, *17*(1), 10-19.

Lasne, J., Noblet, A., Szopa, C., Navarro-González, R., Cabane, M., Poch, O., ... & Coll, P. (2016). Oxidants at the surface of Mars: a review in light of recent exploration results. *Astrobiology*, *16*(12), 977-996.

Malaterre, C., Ten Kate, I. L., Baqué, M., Debaille, V., Grenfell, J. L., Javaux, E. J., ... & Postberg, F. (2023). Is there such a thing as a biosignature?. *Astrobiology*, *23*(11), 1213-1227.

Malin, M. C., & Edgett, K. S. (2000). Sedimentary rocks of early Mars. *Science*, *290*(5498), 1927-1937.

Mangold, N., Gupta, S., Gasnault, O., Dromart, G., Tarnas, J. D., Sholes, S. F., ... & Williford, K. H. (2021). Perseverance rover reveals an ancient delta-lake system and flood deposits at Jezero crater, Mars. *Science*, *374*(6568), 711-717.

Mangold, N., Gupta, S., Gasnault, O., Dromart, G., Tarnas, J. D., Sholes, S. F., ... & Williford, K. H. (2021). Perseverance rover reveals an ancient delta-lake system and flood deposits at Jezero crater, Mars. *Science*, *374*(6568), 711-717.

McCubbin, F. M., Farley, K. A., Harrington, A. D., Hutzler, A., & Smith, C. L. (2025). Mars Sample Return: From collection to curation of samples from a habitable world. *Proceedings of the National Academy of Sciences*, *122*(2), e2404253121.

McLennan, S. M., Grotzinger, J. P., Hurowitz, J. A., & Tosca, N. J. (2019). The sedimentary cycle on early Mars. *Annual Review of Earth and Planetary Sciences*, *47*(1), 91-118.

McMahon, S., & Cosmidis, J. (2022). False biosignatures on Mars: anticipating ambiguity. *Journal of the Geological Society*, *179*(2), jgs2021-050.

Michalski, J. R., Goudge, T. A., Crowe, S. A., Cuadros, J., Mustard, J. F., & Johnson, S. S. (2022). Geological diversity and microbiological potential of lakes on Mars. *Nature Astronomy*, *6*(10), 1133-1141.

Mineralogy of the Nili Fossae region with OMEGA/Mars Express data: 1. Ancient impact melt in the Isidis Basin and implications for the transition from the Noachian to Hesperian. *Journal of Geophysical Research: Planets*, *112*(E8).

Mittelholz, A., Johnson, C. L., Feinberg, J. M., Langlais, B., & Phillips, R. J. (2020). Timing of the martian dynamo: New constraints for a core field 4.5 and 3.7 Ga ago. *Science Advances*, *6*(18), eaba0513.

Murdoch, N., Stott, A. E., Gillier, M., Hueso, R., Lemmon, M., Martinez, G., ... & Mimoun, D. (2022). The sound of a Martian dust devil. *Nature Communications*, *13*(1), 7505.

Mustard, J. F., Ehlmann, B. L., Murchie, S. L., Poulet, F., Mangold, N., Head, J. W., ... & Roach, L. H. (2009). Composition, morphology, and stratigraphy of Noachian crust around the Isidis basin. *Journal of Geophysical Research: Planets*, *114*(E2).

Mustard, J. F., Poulet, F., Head, J. W., Mangold, N., Bibring, J. P., Pelkey, S. M., ... & Neukum, G. (2007). Mineralogy of the Nili Fossae region with OMEGA/Mars Express data: 1. Ancient impact melt in the Isidis Basin and implications for the transition from the Noachian to Hesperian. *Journal of Geophysical Research: Planets*, *112*(E8).

Neveu, M., Hays, L. E., Voytek, M. A., New, M. H., & Schulte, M. D. (2018). The ladder of life detection. *Astrobiology*, *18*(11), 1375-1402.

Paige, D. A., Hamran, S. E., Amundsen, H. E., Berger, T., Russell, P., Kakaria, R., ... & Horgan, B. H. (2024). Ground penetrating radar observations of the contact between the western delta and the crater floor of Jezero crater, Mars. *Science Advances*, *10*(4), eadi8339.

Rapin, W., Dromart, G., Clark, B. C., Schieber, J., Kite, E. S., Kah, L. C., ... & Lanza, N. L. (2023). Sustained wet–dry cycling on early Mars. *Nature*, *620*(7973), 299-302.

Rapin, W., Ehlmann, B. L., Dromart, G., Schieber, J., Thomas, N. H., Fischer, W. W., ... & Vasavada, A. R. (2019). An interval of high salinity in ancient Gale crater lake on Mars. *Nature Geoscience*, *12*(11), 889-895.

Roseborough, V., Horvath, D. G., & Palucis, M. C. (2021). Was Gale crater (Mars) connected to a regionally extensive groundwater system?. *Geophysical Research Letters*, *48*(6), e2020GL092107.

Schon, S. C., Head, J. W., & Fassett, C. I. (2012). An overfilled lacustrine system and progradational delta in Jezero crater, Mars: Implications for Noachian climate. *Planetary and Space Science*, *67*(1), 28-45.

Stack, K. M., Ives, L. R., Gupta, S., Lamb, M. P., Tebolt, M., Caravaca, G., ... & Wiens, R. C. (2024). Sedimentology and Stratigraphy of the Shenandoah Formation, Western Fan, Jezero Crater, Mars. *Journal of Geophysical Research: Planets*, *129*(2), e2023JE008187.

Stein, N., Grotzinger, J. P., Schieber, J., Mangold, N., Hallet, B., Newsom, H., ... & Dehouck, E. (2018). Desiccation cracks provide evidence of lake drying on Mars, Sutton Island member, Murray formation, Gale Crater. *Geology*, *46*(6), 515-518.

Vaniman, D., Chipera, S., Rampe, E., Bristow, T., Blake, D., Meusburger, J., ... & Fraeman, A. (2024). Gypsum on Mars: A Detailed View at Gale Crater. *Minerals*, *14*(8), 815.

Vasavada, A. R. (2022). Mission overview and scientific contributions from the Mars Science Laboratory Curiosity rover after eight years of surface operations. *Space Science Reviews*, *218*(3), 14.

Vaz, D. A., Silvestro, S., Chojnacki, M., & Silva, D. C. (2023). Constraining the mechanisms of aeolian bedform formation on Mars through a global morphometric survey. *Earth and Planetary Science Letters*, *614*, 118196.

Werner, S. C. (2008). The early Martian evolution—Constraints from basin formation ages. *Icarus*, *195*(1), 45-60.

Ye, B., & Michalski, J. R. (2022). Chemical weathering over hundreds of millions of years of greenhouse conditions on Mars. *Communications Earth & Environment*, *3*(1), 266.

Chapter 2

DIAGENETIC, NON-EVAPORATIVE ORIGIN FOR SULFATE SALTS AT GALE CRATER

Hemani Kalucha[1], Eliza Carter[1], John P. Grotzinger[1], Joel A. Hurowitz[2], and Woodward W. Fischer[1]

[1] California Institute of Technology

[2] Stony Brook University

2.1 Abstract

Sulfate salts are deposited most commonly as evaporites on Earth, however, this is not their only origin. Pyrite oxidation during subsurface weathering is another common process on Earth that also produces a suite of sulfate salts—including the acidic phases jarosite and alunite—in sedimentary deposits. On Mars, the occurrence of sedimentary (non-vein-forming) sulfate salts has typically been interpreted as the result of an environmental evaporitic process. While these processes certainly occurred on Mars, we observed several specific occurrences of sulfate salts and their pseudomorphs in the sedimentary strata preserved in Gale Crater that are likely non evaporitic. These occurrences are not associated with bedded precipitates that might indicate a primary origin, nor are they associated with diagnostic sedimentary structures, including desiccation cracks, breccias, and tepee structures, that might indicate an early diagenetic origin. The sporadicity of these crystals implies a localized post-depositional process, which we propose to be oxidation of sulfide-bearing minerals like pyrite and pyrrhotite. If post-depositional pyrite and pyrrhotite oxidation took place in Gale Crater strata as it does perennially in terrestrial examples, it would have generated a significant amount of acidity that could dissolve a large proportion of surface carbonates in contact with the same fluids**.**

2.2 Plain Language Summary

Curiosity Rover has found light-toned, prismatic crystals scattered in the bedrock in scarce locations along its traverse in Gale Crater. Previously, these crystals have been interpreted as gypsum ($CaSO_4$) evaporites, which are sedimentary deposits that form over time in a highly evaporative climate. Based on sedimentological and geochemical arguments, we instead propose that the the formation of these crystals is driven by pyrite (FeS_2) oxidation. When pyrite is exposed to oxygen and water, the redox reaction produces acidity along with a variety of sulfate minerals and oxides. Curiosity has detected the reactants and products of this reaction multiple times in its traverse as well as co-located in the bedrock of the sulfate crystals. Pyrite oxidation is especially effective at dissolving carbonate minerals in the process and very little sulfide is needed to dissolve a large amount of carbonate, which has the potential to explain the lack of surface carbonates in association with specific sulfate occurrences in Gale Crater.

2.3 Introduction

Orbital detections revealed widespread distribution of sulfate-bearing minerals on Mars (Carter et al., 2013). Sulfate minerals were also found in sedimentary layers at Meridiani Planum based on findings from the Mars Exploration Rovers (MER) (Mclennan et al., 2005). At Gale Crater, CheMin (Chemistry and Mineralogy instrument) analyses of drill samples show pervasive anhydrite, bassanite, and gypsum throughout Curiosity's traverse; these samples were typically aimed at bedrock targets, but included vein and nodules occasionally. The occurrences of polyphase sulfates in Gale strata were correlated with magnetite and haematite (Vaniman et al., 2018). In addition, calcium sulfate veins and nodules were

prevalent as infill of light-toned fractures in the rock post sedimentation and partial cementation (Nachon et al. 2014) and magnesium sulfate-rich nodules were well documented throughout the Murray formation (Sun et al., 2020).

In addition to bedrock and diagenetic features, an enrichment of calcium sulfate was found in a third setting at Gale: scattered crystal pseudomorphs in sedimentary bedrock (Figure 2.1; Rapin et al., 2019). The crystals appear as slender laths in the Mojave rock face (Figure 2.2A) of the Pahrump Hills member, as sporadic aggregates in the Sibasa rock face (Figure 2.2C) of the Vera Rubin Ridge, and swallowtail twin molds (Figure 2.2D) in the Jura member. These lenticular crystals were previously characterized as evaporites (Kah et al., 2018). However, these phases did not display evidence of compaction, did not appear to comprise a majority of the bedrock, and were not associated with sedimentary indicators of an evaporative environment (desiccation cracks, early diagenetic or evaporite withdrawal breccias, or tepee structures). In addition, these crystals were located in an interval with a complex mineral assemblage composed of both authigenic clays and sparse occurrences of jarosite in the same bedrock (Hurowitz et al., 2017; Fraeman et al., 2020).

An evaporite interpretation of these sulfate crystals may have been previously favored for the following reasons. More than 95% by volume of Phanerozoic and Neoproterozoic evaporites on Earth are dominated by gypsum and anhydrite (hydrous and anhydrous calcium sulfate salts, respectively) and halite (Warren, 2010). Sulfate-rich evaporites tend to form in carbonate-poor and calcium-rich neutral waters, which can be sourced from a mix of hydrothermal, marine, lacustrine, basinal, and meteoric waters (Warren, 2010; Spencer, 2000). Given the lack of carbonate detections at Gale Crater and the hydrology of the basin (Horvath and Andrews-Hanna, 2021), this process is reasonable to invoke. Evaporite deposits help constrain the local water budget and signify the emergence of at least regionally arid climate (net evaporation), which places constraints on the habitability of a region (Hardie, 1991). The stratigraphy of Mt. Sharp in Gale Crater suggests a large-scale transition from a wetter, lacustrine climate to a drier climate (Milliken et al., 2010), which allows the interpretation of evaporites at a much smaller, local scale to fit in.

However, sulfate salts are also commonly produced on Earth through a non-evaporitic pathways in sedimentary rocks: oxidation of sedimentary sulfide-bearing species such as pyrite, pyrrhotite, and hydrogen sulfide. In certain settings, this reaction produces large, intergrown cm-scale gypsum crystals within the mud/silt/sand matrix concentrated stratigraphically along zones of preferential permeability that can be exploited by oxidizing groundwater (Bain, 1990). The sulfates in this setting (Bain, 1990) were notably co-located with iron oxide along joints, sand layers, and root trace fossils and cemented with iron oxides and hydroxides. The iron oxides were derived from the oxidation of pyrite. The pyrite was present in prodelta muds, which initially sheltered it from oxidation (Bain, 1990). It is important to note here that the initial deposition of pyrite occurred syndepositonally with the muddy sediment in circumneutral pH waters. However, the later oxidation of pyrite occurred in oxidizing, calcium-rich ground waters and the redox reactions associated with pyrite oxidation temporarily lowered the pH of the local environment. This specific example of

sulfide oxidation demonstrates the time separation between deposition and diagenesis that can occur as well as the the local nature of this reaction. In addition, pyrite oxidation occurred abiotically and produced crystals of the same morphology and size as those found in Gale Crater.

Postdepositional pyrite oxidation producing iron oxide, jarosite, and gypsum was also observed in the subsurface lowland swamps of the Skernjå delta, Denmark. The resulting acidic sulfate solution produced a pH decrease down to 2 that was highly localized: it was strictly limited to the 2 km wide surficial presence of pyrite and a depth of only 1 m in the subsurface, due to limits on O_2 transport and penetration (Postma, 1983). This post-depositional emplacement of sulfate salts is not limited to unlithified sedimentary deposits but has also been commonly observed in ancient fine-grained sedimentary rocks undergoing incipient oxidative weathering via oxygenated subsurface fluids (Slotznick et al. 2022). The petrogenesis of sulfate salts tied to pyrite oxidation (and other sulfide-bearing phases) develops with a secular change in the redox states and processes operating in a sedimentary basin; such a transition is common throughout Earth history wherein sedimentary basins accumulating sediment are often anaerobic and accumulate pyrite either diagenetically or depositionally prior to the rise of atmospheric dioxygen (Johnson et al. 2014; Fischer et al. 2016), and are then tectonically uplifted and subject to oxidizing, meteoritic fluids. We considered whether or not Mars might have hosted a similar mechanism of sulfate salt petrogenesis by examining specific sulfate occurrences within the sedimentary strata exposed today in Gale Crater.

Given that evidence of the chemical ingredients needed to form non-evaporative sulfate salts (water, pyrite and pyrrhotite, and evidence of high potential oxidants) have been observed in sedimentary strata at Gale (Grotzinger et al., 2015; Fraeman et al., 2020; Wong et al., 2022; Lanza et al., 2016; Vaniman et al., 2014), the chemical reaction products (jarosite, gypsum, iron (hydr)oxides) are co-located in these instances at Gale, and the efficacy of this process at a variety of scales (at least on Earth), we set out to quantify how frequently and abundantly these crystals occurred and evaluate potential mechanisms of formation.

2.3.1 Geologic Setting

Curiosity rover, over 3000 sols, has explored more than 300 m of clay-bearing stratigraphy developed over a long-lived fluvio-lacustrine environment (Grotzinger et al., 2015). Gale Crater (3.8-3.6 billion years old) is interpreted to host a river that gave way downdip to a delta that emptied water and sediment into a standing lake. Crater infilling with layers of sediment from wet and dry periods followed by erosion created the central peak (Mount Sharp) as it is seen today (Grotzinger et al., 2015). The targets considered in this paper are part of the Murray formation, the basal units exposed north of Mount Sharp (Figure 2.1). The Murray formation is largely composed of finely laminated mudstone and interbedded sandstone layers, reflecting the interfingering of lacustrine mud and fluvio-deltaic sand deposits that range from proximal to distal lacustrine settings (Stack et al., 2018). In addition, the Sutton Island member contains rare horizons with desiccation cracks, suggesting episodic

intervals of wetting and drying at this lake margin (Stein et al., 2018). Where best developed, such as at the Old Soaker outcrop (Stein et al., 2018), these features indicative of sub-aerial exposure have no associated enrichments of any kind of salts. The overlying Blunts Point member contains an extensive network of cross-cutting calcium sulfate veins in the finely laminated mudstone, and the upper Pettegrove Point and Jura members contain abundant haematite mineralization; more generally, the upper Murray formation displays textural and geochemical evidence of complex and pervasive post-depositional alteration and mineralization (Fraeman et al., 2016; Sun et al., 2019, and references therein).

2.4 Materials and Methods

The goal of our analysis was to constrain the timing (deposition versus diagenesis) of crystal pseudomorph mineralization, size and spacing of crystals, as well as stratigraphic presence or absence. We used MAHLI (Mars Hand Lens Imager) images obtained by Curiosity Rover (Grotzinger et al. 2012, Edgett et al. 2012), to analyze sulfate crystals present in the bedrock from Sol 0 to 2405. MAHLI is a magnifying hand lens with a wide field of view (31.1x23.3 degrees) and active in visible wavelengths (395-670 nm), which made it suitable to detect the presence or absence of crystals in the bedrock. We selected type 'C' or lossless images from the MAHLI RDR (reduced data records). A total of 3296 images of bedrock on 485 different Sols made up the dataset; the subset of MAHLI images that contained identifiable sulfate crystals were mapped, with the results shown in Figure 2.1 with respect to elevation.

To quantify the crystal abundance in the outcrop exposures, we projected a 4 cm diameter circle on to what was the visibly densest section of crystals in the image. The circle was then divided into 75 equal-area sections. The percent abundance was calculated as the fraction of sections with visible crystals out of the total. In certain cases, the enclosing circle was slightly larger than the actual size of the image; the total number of sections was then reduced to only those covering the image.

MAHLI images also enabled the quantification of the size of crystals in each image as well as the distance to the nearest neighbor. The crystals were traced such that the end points of the polygon lengths and widths could be mapped in the spatial coordinates of the image. The size of the crystal was defined as the Euclidean distance between the longer of the two end points. The nearest neighbor was found by calculating the Euclidean distances from the center of each crystal to all other centers and selecting the absolute minimum distance in this array. The size and distance were converted from pixel grid units to micrometers by an image spacing constant parameter provided in the metadata, which assumed a constant spatial resolution across the analytical domain. Due to the minimal amount of change in relief in a close-up image of bedrock, constant spatial resolution held valid. Crystals with a diameter less than 3 pixels were excluded since they could not be accurately distinguished from sand-sized sedimentary particles.

2.5 Results

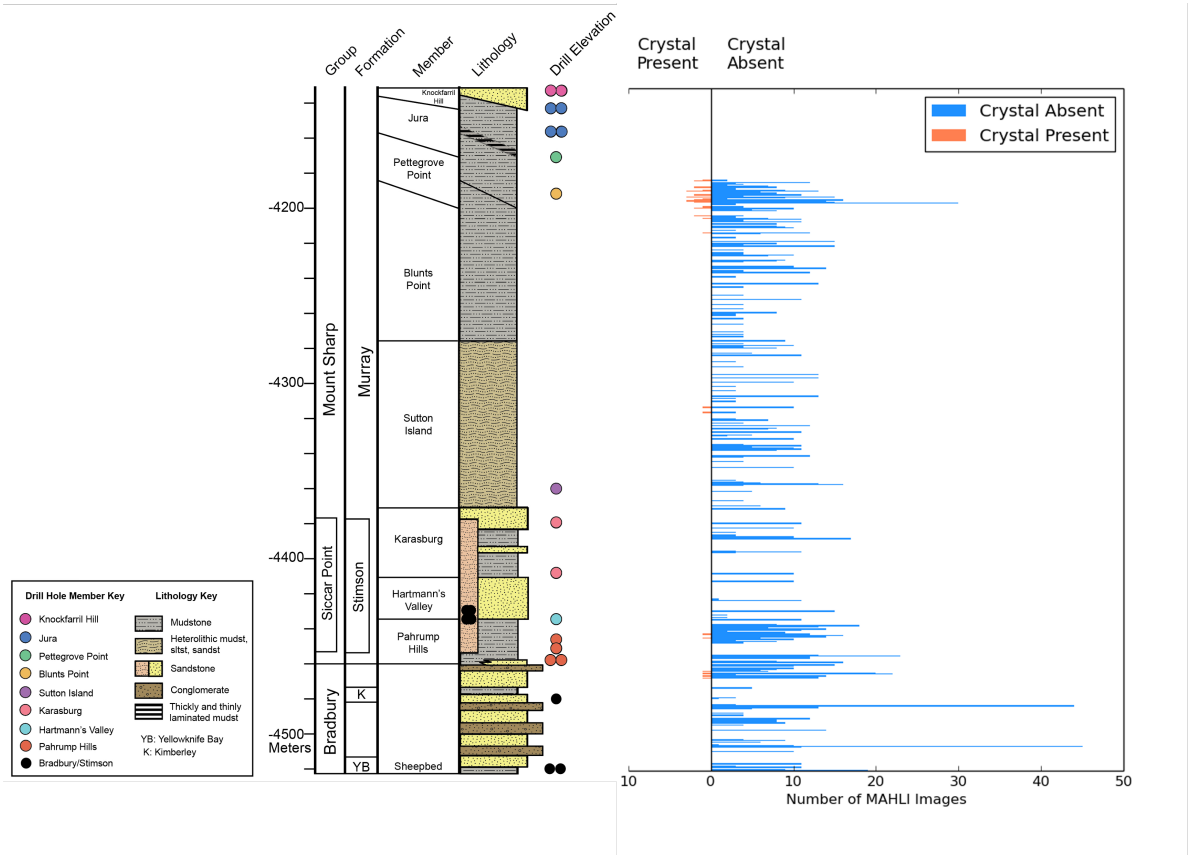

Figure. 2.1. Occurrences of sulfate crystals in stratigraphy. Left: summary of the stratigraphic record at Gale, showing the major sedimentary units as of Sol 3000. Right: all MAHLI images as of Sol 2450, classified in which sulfate crystals are present (number of images with crystals represented by the length of the orange bar) or absent (number of images with no crystals represented by the length of the blue bar) in the bedrock.

Figure 2.2 presents four different representative images of the development of putative sulfate salt crystals and/or crystal molds along the traverse. The chemical and mineralogical data from bedrock containing crystals is no different from adjacent bedrock without crystals (Rampe et al., 2017; Kah et al., 2018; Fraeman et al., 2020); we therefore agree with the previous interpretation that the crystals are pseudomorphs (Kah et al., 2018); we will hereafter refer to the pseudomorphs as crystal molds. The crystal molds were consistently lighter toned than the surrounding bedrock, and tend to grow poikilotopically. On the surface, they appeared to have a long, thin prismatic cross section with potentially pyramidal ends. The images resolved swallowtail twinning (Figure 2.2B,D) in the molds as well. There was also no discernible spatial congregation or preferred orientation of the crystal molds, as previously noted by Kah et al. (2018). Furthermore, the crystal molds did not appear rotated by compaction or deformed in any way by the sediment matrix. In the Jura member (Figure

2.2D), the crystal molds appeared to cross cut the primary lamination, and the sediment is not deformed, suggesting they formed after compaction of the fine-grained sediment. The molds match the morphology of flat, prismatic, elongated, white gypsum crystals most closely. Iron and magnesium salts, though common on Mars, are two orders of magnitude more soluble than gypsum (Jambor et al., 2000), and are therefore less likely to form in a subsurface, non-evaporative setting. Despite a lack of definitive mineralogical data, the above sedimentological and geochemical arguments strongly suggest that the crystal molds were once gypsum and formed during diagenesis instead of deposition. This precludes the crystal molds from being an evaporite deposit, which is a primary texture that occurs during deposition (Schreiber and Tabakh, 2000).

While conspicuous examples exist in certain exposures, the overall occurrence of crystal morphologies along Curiosity's traverse through Gale stratigraphy is remarkably rare (Figure 2.1). Out of a total of 3296 MAHLI bedrock images, only 50 images contained these sulfate crystal molds. Even in the case of up to 45 images taken of different bedrock areas on the same Sol, the molds are notably absent. Data show that they occurred in clusters, around -4450 (bottom most bed of Pahrump Hills), -4300 (upper layers of Sutton Island), and -4150 (Jura member) meters in elevation. When sorted by facies, the crystal molds were most proportionately observed in mudstone (90%), followed by sandstone, and lastly siltstone. The sporadicity of the crystal mold occurrences on a formation magnitude scale requires a localized and heterogeneous post-depositional process, which aligns with the mechanism proposed in Bain (1990) closely. In addition, the strong association of the crystals with mudstones points to initial deposition of sulfur in mudstone, such as detrital pyrite and other sulfide bearing minerals.

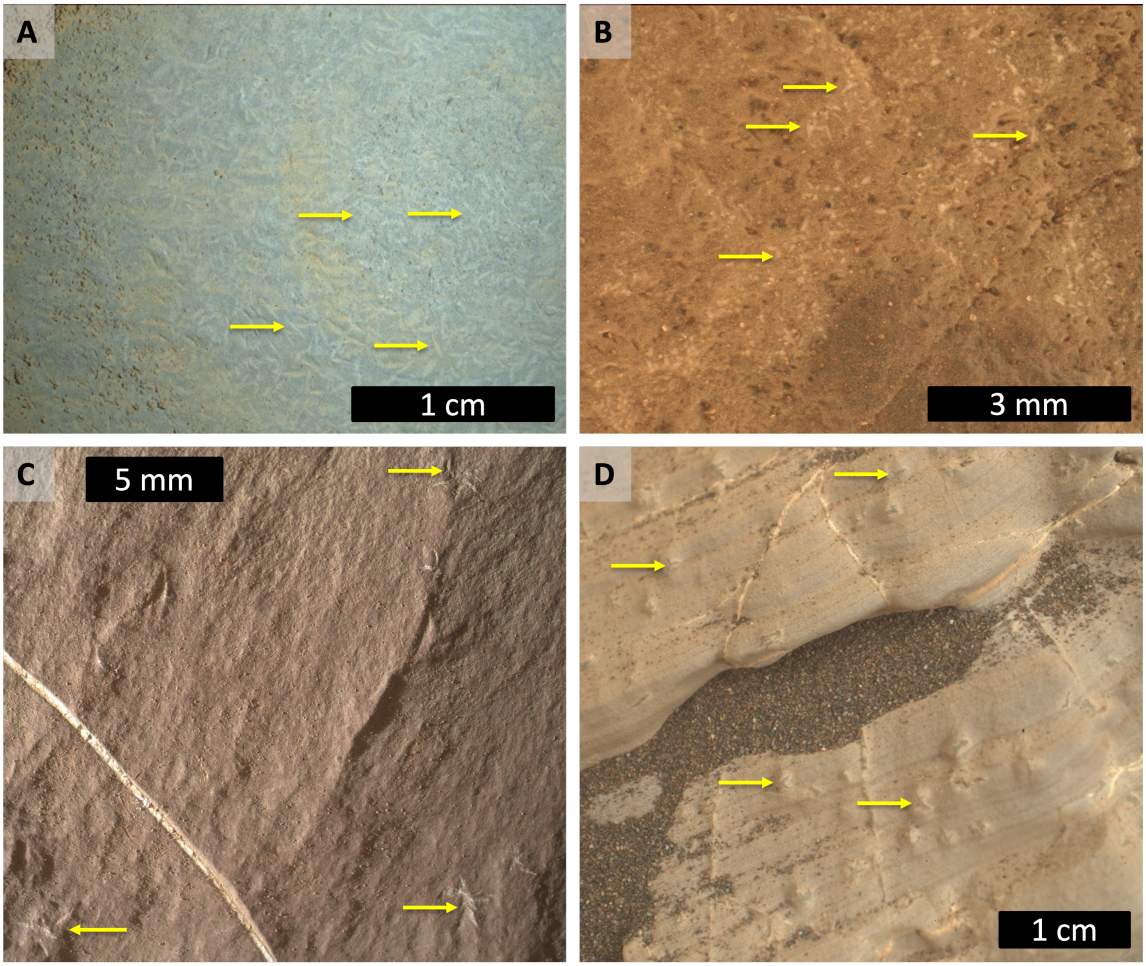

Figure. 2.2. Representative MAHLI images showing the morphologies of sulfate crystals in the bedrock. (A) crystal laths in 0809MH0004460030300907C00 (B) swallow-tail twins and aggregates in 1679MH0006490010603546C00 (C) aggregates in 1863MH0001760010702122C00 (D) swallow-tail molds in 1925MH0002910010703316C00.

On a outcrop magnitude scale, that is, within the bedrock itself, a numerical analysis of four MAHLI images with the highest density of crystal molds demonstrated the relationship between crystal size and crystal spacing. The size distributions of crystal molds varied somewhat across the exposures (Fig. 2.3). The lengths of the crystal molds ranged from 50 to 2000 micrometers, which is approximately the same range as reported in Figure 8a of Kah et al. (2018); they analyzed targets Pelona (sol 805), Mojave (sol 809), and Mojave2 (sol 880). However, we found a mean length of 655 micrometers over 50 images, which is shorter than the mean of the set of three images reported in Kah et al. (2018) (1200-1400 micrometers). This difference probably reflects the much larger size of our current data, and/or differences in crystal identification and measurement methodologies as we report 435 crystals in the image taken on Sol 809, whereas they report 658 crystals for the same image.

All four crystal size distributions followed log normal distributions, as observed by Kah et al. (2018). The nearest neighbor distributions of the same 4 MAHLI images (Figure 2.3B) were more symmetrically distributed than the right-skewed size distributions. Most importantly, the mean of these distributions was always greater than the mean of the corresponding size distribution by a ratio of 1.05, 1.58, 1.97, and 2.20, respectively. Thus, the crystals were spaced from another by at least an average crystal length in each case, but more frequently by approximately two crystal lengths.

Furthermore, in each image analyzed, the abundance of crystals in the spherical segment area analyzed was limited to a very small fraction of the rock. 76% of the images that contained crystals yielded an abundance of less than 3%. Only two images exceeded a crystal abundance of 20%. This numerical analysis demonstrates that the crystals do not make up a majority of the bedrock and therefore cannot be formed through evaporation. An evaporitic deposit would have interlocking crystals filling the entire bredrock instead of such low density of crystal occurrences (Schreiber and Tabakh, 2000). For this reason, these crystal mold occurrences are also dissimilar to reworked gypsum crystals in clastic deposits (Benison et al., 2007) as they are not abundant enough to be classified as such.

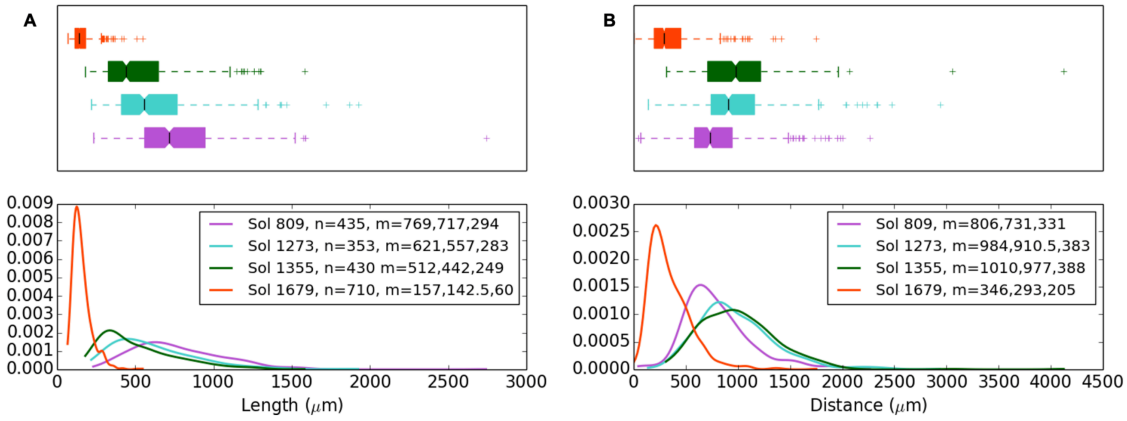

Figure. 2.3. Quantification of crystal size and spacing. (A) size distribution of crystals in four most densely populated MAHLI images. n refers to number of crystals, the numbers after m refer to mean, median, standard deviation, respectively. (B) nearest neighbor distribution of crystals in the same four images with mean, median, and standard deviation. The distributions show consistency amongst sample images of crystals.

When considering the bulk mineralogy of the bedrock hosting these crystal molds, pyrite oxidation offers a more complete explanation. Curiosity has consistently sampled disequilibrium mineral assemblages in the Murray Formation; for example, the Sebina Drill hole sample contained Ca-sulfate, hematite, primary igneous minerals, clay minerals, and jarosite (Bristow et al., 2018). In addition, Chemin and SAM detected Fe-smectites, siderite, Fe/Mg sulfate, oxidized organics, and chloride in several of the drill holes from the Glen Torridon Region, suggesting a complex set of redox processes in this unit (McAdam et al.,

2022); this disequilibrium is consistent with a temporal lag between the deposition of detrital or authigenic sulfides in a reducing environment, and its subsequent oxidation due to secular environmental change. In particular, the Mohave 2 sample (which specifically has crystal molds on the surface) contained jarosite dated to 2.57 Ga (Martin et al., 2018), which demonstrated that these sulfates are significantly younger than the age of the sedimentary rocks in which they occur and had to be formed through a post-depositional process. The timing of emplacement of these crystals also post-dates compaction of the bedrock. It is useful to therefore explore other interpretations that might better explain the origin of these deposits, considering post-depositional processes. Evaporitive processes and reworking of sulfate crystals cannot explain the presence of jarosite co-located in the bedrock.

2.6 Discussion

Terrestrial examples of redox reactions with sulfides are common. Jarosite, gypsum, and other metal sulfate deposits interbedded with mudstones (the dominant lithology associated with the crystal molds in Gale Crater) are found in the Smoking Hills formation of the Canadian Arctic. These minerals were deposited in sediments bathed in euxinic bottom water and early porewater conditions and underwent sedimentary inversion and then oxidation upon exposure to meteoric fluids (Grasby et al., 2022). Secondary gypsum precipitates are associated with primary pyrite mineral particles in the non-evaporitic Chattanooga Shale (Bates and Strahl, 1957). Iron oxyhydroxides appear at the weathering front of oxidizing fluids reaching buried pyrite in Shale Hills, Pennsylvania (Gu et al., 2020). The Rio Tinto river is a present-day site of pyrite and other sulfide-bearing mineral oxidation that produces assemblages of jarosite and iron oxides (Mavris et al., 2018). These examples produce deposits that look similar to the crystal moulds in the bedrock images of Gale Crater, and match the end mineralogy found in the bedrock of the crystal moulds. It is therefore likely that they are also analogs of the chemistry and fluid movement that could have occurred at Gale Crater,

The formation of the sulfate crystals is plausibly explained by the series of overall reactions highlighted in Bain (1990). To start, pyrite and other iron-bearing sulfides (like pyrrhotite) in detrital basaltic sediments or produced authigenically (Franz et al., 2018; McAdam et al., 2022) are exposed to dioxygen in a wet environment such as the lake in Gale Crater post-lithification.

$$\boldsymbol{FeS_2 + \frac{7}{2}O_2 + H_2O \rightarrow Fe^{2+} + 2SO_4{}^{2-} + 2H^+} \qquad (\mathbf{1})$$

Equation 1 shows an idealized version of the chemistry, however, it is recognized that this chemistry is part of an oxidative cascade that yields additional solids that include ferric sulfate salts like jarosite and iron oxides hematite, and magnetite; each of these phases are commonly recognized and often abundant in the Murray formation (Hurowitz et al., 2017; Rampe et al., 2017). In water-limiting cases, for example after the lake waters have receded into the subsurface, ground water containing divalent ions (e.g. Ca^{2+}, Mg^{2+}) or existing

carbonate deposits as suggested by the petrology of ALH84001 (Mittlefehldt, 1994) can react with sulfate derived from sulfide oxidation,

$$SO_4^{2-} + Ca^{2+} + H_2O \rightarrow CaSO_4.xH_2O \qquad (2)$$

to produce polyphase sulfate salts such as bassanite, anhydrite, and gypsum depending on temperature, salinity, and water activity of the fluid (Van Driessche et al., 2017; Reigl et al., 2022). These Ca-sulfate phases have been detected in various proportions across the Murray formation as well, especially in the same location as magnetite and hematite (Vaniman et al., 2018). While CheMin (with a detection limit of 1%) was not able to unambiguously detect pyrite and pyrrhotite, this is rather unsurprising: even pyrite rich black shales on Earth only contain ~1-2% pyrite (Slotznick et al., 2022). The SAM instrument indirectly detects reduced sulfur bearing phases at much higher sensitivity, and indicated reduced sulfur phases in samples from the Glen Torridon region in the Kilmarie (mudstone) and Edinburgh (sandstone) drill holes, as well as in the Jura Member: Rock Hall and Highfield (mudstone with sandstone lenses) drill holes (Wong et al. 2022). The SAM analyses of mudstone samples in the Sheepbed member contained large inorganic sulfide fractions compared to the quantity of organic sulfide detected (Table S4, Eigenbrode et al., 2018). It therefore seems plausible, if not highly likely, that Gale sediments contain highly reactive S-bearing phases that can do a significant amount of post-depositional chemical work in the presence of oxidants. Overall, the transformation from iron sulfides and disulfides to sulfate salts occurs with a time lag.

Sulfide oxidation reactions can be buffered by co-occurring carbonates like siderite, which was detected in a total of three Murray formation drill samples (Kilmarie, Glen Etive 1, and Glen Etive 2) with a bulk abundance up to 1.8% (Thorpe et al. 2022). The acidity (protons) generated by sulfur oxidation (e.g. equation (1)) promotes the rapid dissolution of even less soluble carbonate salts like siderite:

$$FeCO_3 + 2H^+ \rightarrow Fe^{2+} + CO_2 + H_2O \qquad (3)$$

Bicarbonate is eventually released as carbon dioxide, and because the midpoint potentials are similar to those required for pyrite oxidation the iron is oxidized further to ultimately form hematite, magnetite, and other iron oxide phases. On Earth, pyrite oxidation is the cause of substantial carbonate dissolution during incipient weathering of mudrocks (e.g. Slotznick et al. 2022). If the carbonates on Mars used to align in composition with the carbonates in ALH84001, in that they consisted of Ca, Mg, and Fe cations, the iron was likely partitioned into iron oxides or jarosite and the lower solubility of calcium sulfate likely produced gypsum over any magnesium sulfate salt. Any magnesium released from carbonate dissolution would accumulate in solution since most of the phases that it would precipitate in are highly soluble (e.g., Mg-sulfate, Mg-carbonate).The veins in Gale Crater are pure calcium sulfate (Nachon et al., 2014). Both of these occurrences of calcium sulfate suggest a previous calcium-rich source, which we suggest is calcium bearing carbonate that used to be more prevalent on the surface of Mars. The lack of evidence of carbonate dissolution in this bedrock remains a

puzzling aspect of these deposits. Space previously occupied by carbonates may have been filled with a cement of a different composition, eroded as a point of weakness in the bedrock, or removed by chemical weathering following uplift and exposure. The bedrock exposures at Gale Crater are not continuous laterally or vertically and have been subject to billions of years of chemical and physical weathering such that earlier diagesis is likely overprinted.

The rate of abiotic pyrite oxidation was found to be between $\mathbf{10^{-8}}$ and $\mathbf{10^{-9}}$mol/m^2/s and is dependent on surface area as well as concentration and supply of oxidants (Johnson et al., 2014; Williamson et al., 1994); pyrrhotite oxidation is typically 20-100 times faster—all else kept equal—due to its structure (Belzile et al. 2004). While abiotic oxidation of pyrite and pyrrhotite is facile, microbes are capable of accelerating the reaction by approximately an order of magnitude (Percak-Dennett et al., 2017); the large interval of time between the deposition of the sedimentary rocks at Gale and the 2.56 Ga jarosite provide more than enough time for sulfur oxidation to occur abiotically. Carbonates and sulfides are typically oxidatively removed three orders of magnitude faster than silicates (Bufe et al. 2021). As a record of how effective this reaction is, Hercod et al. (1998) studied clay covered limestone bedrock to ascertain the effect of pyrite oxidation on the limestone independent of rainfall. They found that ~9 times more limestone was removed than pyrite on a molar basis. Of the total mass of bedrock dissolved by weathering, pyrite oxidation constituted 11%, and sulfuric acid released accounts for nearly half of all carbonates dissolved. The weathering front left behind iron oxides, hydroxides, and weathered calcite. For alkaline waters (pH 10-12), carbonate is able to complex with iron and thereby sustains the oxidation process, where it would otherwise decelerate with the development of lower pH fluids and less reactive iron oxhydroxide rims around the pyrite grains (Huminicki and Rimstidt, 2009; Caldeira et al. 2010). The efficacy of this reaction can potentially explain the lack of surface carbonates in these areas of Gale Crater.

Strata preserved in Gale Crater appeared to have reacted with a suite of different fluids from depositional to post-depositional alteration and weathering with an overall secular change in the oxidation state of the fluids: from anoxic conditions during deposition to produce phases like siderite and ferrous clays (Fraeman et al., 2020) to conditions with high potential oxidants available for reactions (Lanza et al,. 2016; Mitra and Catalano 2019) during late diagenesis and nascent weathering. In particular, oxyhalogen species are highly effective as sulfide oxidants and have been detected in Gale Crater in abundance (Mitra et al., 2023). Detrital and/or authigenic pyrite and pyrrhotite phases variably appear in these rocks, and these phases should be considered highly reactive to the latter fluids given their redox properties. Pyrite oxidation has previously been offered as one potential explanation of the high abundance of acidic sulfate salts like jarosite observed at Meridiani Planum by Zolotov and Shock (2005) and high abundance of sulfates on Mars in general (Chevrier and Mathe, 2007).

According to Schwenzer et al. (2016)'s modelling, even if there was three times the amount of pyrite compared to siderite in a starting assemblage, the carbonate buffer would not be exhausted and prevents the fluid from becoming acidic; thus, the pH of Gale Crater would

not be significantly disturbed by this process and the effects of pyrite oxidation would remain as local as the clustering of these crystal molds. It is critical to note that pyrite oxidation explains the occurrence of these sulfate crystals without contradicting the rest of Gale's circumneutral depositional waters as inferenced from the clay mineral phases present in these deposits.

Sulfide-bearing mineral phases are common in Mars' crust. They are present in every Martian meteorite in abundances up to 0.7 wt % (Tarnas et al., 2021); the Gusev Crater Adirondack basalt target contained ~3 wt% S (as SO_3) (Gellert et al., 2004). Sulfide and disulfide minerals are thought to be more prevalent on Mars due to its mafic crust, and the lower oxygen fugacity and high sulfur fugacity of the Martian mantle (Tarnas et al., 2021 and references therein). It is therefore reasonable to conclude that—unless dioxygen was common in the atmosphere of early Mars--detrital pyrite and pyrrhotite derived from erosion of the crater rim catchment would be present in Gale sediments. If post-depositional pyrite and pyrrhotite oxidation took place in Gale Crater strata as it does perennially in terrestrial examples, it would have generated a significant amount of acidity that could dissolve a large proportion of surface carbonates in contact with the same fluids. The occurrence of pyrite oxidation in this way implies a different ancient environment for Gale Crater, where these deposits do not represent eras of the ancient lake drying out but rather extended continuity and stability of the aqueous system, which shows greater promise for habitability.

References

Deng, A., & Stauffer, D. R. (2006), On improving 4-km mesoscale model simulations. *Journal of Applied Meteorology and Climatology*, *45*(3), 361–381. doi:10.1175/JAM2341.1

Bain, R. J. (1990), Diagenetic nonevaporative origin for gypsum. *Geology*, 18, 447–450.

Bates, T., Strahl, E. O. (1957), Mineralogy, petrography, and radioactivity of representative samples of Chattanooga Shale. *GSA Bulletin*, 68 (10): 1305–1314. doi: https://doi.org/10.1130/0016-7606(1957)68[1305:MPAROR]2.0.CO;2

Belzile, N., Chen, Y.-W., Cai, M.-F., & Li, Y. (2004), A review on pyrrhotite oxidation. *Journal of Geochemical Exploration*, 84(2), 65–76. https://doi.org/10.1016/j.gexplo.2004.03.003

Benison, K. C., Bowen, B. B., Oboh-Ikuenobe, F. E., Jagniecki, E. A., LaClair, D. A., Story, S. L., ... & Hong, B. Y. (2007). Sedimentology of acid saline lakes in southern Western Australia: newly described processes and products of an extreme environment. *Journal of Sedimentary Research*, *77*(5), 366-388.

Bufe, A., Hovius, N., Emberson, R., Rugenstein, J. K. C., Galy, A., Hassenruck-Gudipati, H. J., & Chang, J.-M. (2021), Co-variation of silicate, carbonate and sulfide weathering drives CO2 release with erosion. *Nature Geoscience*, 14(4), 211–216. https://doi.org/10.1038/s41561-021-00714-3

Caldeira, C. L., Ciminelli, V. S. T., & Osseo-Asare, K. (2010), The role of carbonate ions in pyrite oxidation in aqueous systems. *Geochimica et Cosmochimica Acta*, 74(6), 1777–1789. https://doi.org/10.1016/j.gca.2009.12.014

Carter, J., Poulet, F., Bibring, J.-P., Mangold, N., and Murchie, S. (2013), Hydrous minerals on Mars as seen by the CRISM and OMEGA imaging spectrometers: Updated global view, *Journal of Geophysical Research; Planets*, 118, 831– 858, doi: 10.1029/2012JE004145.

Chevrier, V., & Mathé, P. E. (2007), Mineralogy and evolution of the surface of Mars: A review. *Planetary and Space Science*, 55(3), 289–314. https://doi.org/10.1016/j.pss.2006.05.039

Edgett, K. S., Yingst, R. A., Ravine, M. A., Caplinger, M. A., Maki, J. N., Ghaemi, F. T., et al. (2012), Curiosity's Mars Hand Lens Imager (MAHLI) Investigation. *Space Science Reviews*, 170(1–4), 259–317. https://doi.org/10.1007/s11214-012-9910-4

Fischer, Woodward W., James Hemp, and Jena E. Johnson. (2016), Evolution of oxygenic photosynthesis. *Annual Review of Earth and Planetary Sciences* 44: 647-683.

Fraeman, A. A., Ehlmann, B. L., Arvidson, R. E., Edwards, C. S., Grotzinger, J. P., Milliken, R. E., et al. (2016), The stratigraphy and evolution of lower Mount Sharp from spectral, morphological, and thermophysical orbital data sets: Stratigraphy and Evolution of Mount Sharp. *Journal of Geophysical Research: Planets*, 121(9), 1713–1736. https://doi.org/10.1002/2016JE005095

Fraeman, A. A., Edgar, L. A., Rampe, E. B., Thompson, L. M., Frydenvang, J., Fedo, C. M., ... & Wong, G. M. (2020), Evidence for a diagenetic origin of Vera Rubin ridge, Gale crater, Mars: Summary and synthesis of Curiosity's exploration campaign. *Journal of Geophysical Research: Planets*, 125(12), e2020JE006527.

Gellert et al. (2004), Chemistry of Rocks and Soils in Gusev Crater from the Alpha Particle X-ray Spectrometer. *Science* 305, 829-832. DOI:10.1126/science.1099913

Grasby, S. E., Percival, J. B., Bilot, I., Ardakani, O. H., Smith, I. R., Galloway, J., et al. (2022), Extensive jarosite deposits formed through auto-combustion and weathering of pyritiferous mudstone, Smoking Hills (Ingniryuat), Northwest Territories, Canadian Arctic – A potential Mars analogue. *Chemical Geology*, 587, 120634. https://doi.org/10.1016/j.chemgeo.2021.120634

Grotzinger, J. P., Gupta, S., Malin, M. C., Rubin, D. M., Schieber, J., Siebach, K., et al. (2015), Deposition, exhumation, and paleoclimate of an ancient lake deposit, Gale crater, Mars. *Science*, 350(6257), aac7575–aac7575. https://doi.org/10.1126/science.aac7575

Grotzinger, John P., Crisp, J., Vasavada, A. R., Anderson, R. C., Baker, C. J., Barry, R., et al. (2012), Mars Science Laboratory Mission and Science Investigation. *Space Science Reviews*, 170(1–4), 5–56. https://doi.org/10.1007/s11214-012-9892-2

Gu et al. (2020), Deep abiotic weathering of pyrite. *Science* 370, eabb8092. DOI:10.1126/science.abb8092

Hardie, L. A. (1991). On the Significance of Evaporites. *Annual Review of Earth and Planetary Sciences*, 19, 131–168.

Hercod, D. J., Brady, P. V., & Gregory, R. T. (1998), Catchment-scale coupling between pyrite oxidation and calcite weathering. *Chemical Geology*, 151(1–4), 259–276. https://doi.org/10.1016/S0009-2541(98)00084-9

Horvath, D. G., & Andrews-Hanna, J. C. (2021). The hydrology and climate of Mars during the sedimentary infilling of Gale crater. *Earth and Planetary Science Letters*, *568*, 117032.

Huminicki, D. M., & Rimstidt, J. D. (2009). Iron oxyhydroxide coating of pyrite for acid mine drainage control. *Applied Geochemistry*, 24(9), 1626-1634.
Hurowitz, J. A., Grotzinger, J. P., Fischer, W. W., McLennan, S. M., Milliken, R. E., Stein, N., et al. (2017), Redox stratification of an ancient lake in Gale crater, Mars. *Science*, 356(6341), eaah6849. https://doi.org/10.1126/science.aah6849
Jambor, J. L., Nordstrom, D. K., & Alpers, C. N. (2000), Metal-sulfate Salts from Sulfide Mineral Oxidation. *Reviews in Mineralogy and Geochemistry*, 40(1), 303–350. https://doi.org/10.2138/rmg.2000.40.6
Johnson, Jena E., et al. (2014), O2 constraints from Paleoproterozoic detrital pyrite and uraninite. *GSA Bulletin* 126.5-6 (2014): 813-830.
Jakosky, B. M. (2021), Atmospheric loss to space and the history of water on Mars. Annual *Review of Earth and Planetary Sciences*, 49, 71-93.
Kah, L. C., Stack, K. M., Eigenbrode, J. L., Yingst, R. A., & Edgett, K. S. (2018). Syndepositional precipitation of calcium sulfate in Gale Crater, Mars. *Terra Nova*, 30(6), 431–439. https://doi.org/10.1111/ter.12359
Lanza, N. L., Wiens, R. C., Arvidson, R. E., Clark, B. C., Fischer, W. W., Gellert, R., et al. (2016), Oxidation of manganese in an ancient aquifer, Kimberley formation, Gale crater, Mars: Manganese Fracture Fills in Gale Crater. *Geophysical Research Letters*, 43(14), 7398–7407. https://doi.org/10.1002/2016GL069109
Martin, P. E., Farley, K. A., Baker, M. B., Malespin, C. A., Schwenzer, S. P., Cohen, B. A., … Navarro-González, R., (2017), A two-step K-Ar experiment on Mars: Dating the diagenetic formation of jarosite from Amazonian groundwaters. *Journal of Geophysical Research: Planets*, 122, 2803–2818. https://doi.org/ 10.1002/2017JE005445
Mavris, Javier Cuadros, José Miguel Nieto, Janice L. Bishop, Joseph R. Michalski (2018), Diverse mineral assemblages of acidic alteration in the Rio Tinto area (southwest Spain): Implications for Mars. *American Mineralogist* 103 (12): 1877–1890. doi: https://doi.org/10.2138/am-2018-6330
McAdam, A. C., Sutter, B., Archer, P. D., Franz, H. B., Wong, G. M., Lewis, J. M. T., et al. (2022), Evolved gas analyses of sedimentary rocks from the Glen Torridon clay-bearing unit, Gale crater, Mars: Results from the Mars Science Laboratory Sample Analysis at Mars instrument suite. *Journal of Geophysical Research: Planets*, 127, e2022JE007179. https://doi.org/10.1029/2022JE007179
McLennan, S. M., Bell, J. F., Calvin, W. M., Christensen, P. R., Clark, B. C., de Souza, P. A., et al. (2005), Provenance and diagenesis of the evaporite-bearing Burns formation, Meridiani Planum, Mars. *Earth and Planetary Science Letters*, 240(1), 95–121. https://doi.org/10.1016/j.epsl.2005.09.041
Milliken, R. E., Grotzinger, J. P., & Thomson, B. J. (2010). Paleoclimate of Mars as captured by the stratigraphic record in Gale Crater. *Geophysical Research Letters*, *37*(4).
Mittlefehldt, D. W. (1994), ALH84001, a cumulate orthopyroxenite member of the Martian meteorite clan. *Meteoritics*, 29(2), 214-221.
Mitra, K., & Catalano, J. G. (2019). Chlorate as a potential oxidant on Mars: Rates and products of dissolved Fe(II) oxidation. *Journal of Geophysical Research: Planets*, 124, 2893– 2916. https://doi.org/10.1029/2019JE006133
Nachon, M., Clegg, S. M., Mangold, N., Schröder, S., Kah, L. C., Dromart, G., et al. (2014), Calcium sulfate veins characterized by ChemCam/Curiosity at Gale crater, Mars:

Calcium Sulfate Veins at Gale Crater. *Journal of Geophysical Research: Planets*, 119(9), 1991–2016. https://doi.org/10.1002/2013JE004588

Ramirez, R. M., & Craddock, R. A. (2018), The geological and climatological case for a warmer and wetter early Mars. *Nature Geoscience*, 11(4), 230-237.

Rampe, E. B., Ming, D. W., Blake, D. F., Bristow, T. F., Chipera, S. J., Grotzinger, J. P., ... Achilles, C. N. (2017), Mineralogical trends in mudstone deposits from the Murray formation, Gale Crater, Mars. *Earth and Planetary Science Letters*, 471, 172–185.

Rapin, W., Ehlmann, B. L., Dromart, G., Schieber, J., Thomas, N. H., Fischer, W. W., et al. (2019), An interval of high salinity in ancient Gale crater lake on Mars. *Nature Geoscience*, 12(11), 889–895. https://doi.org/10.1038/s41561-019-0458-8

Percak-Dennett, E, He, S, Converse, B, et al. (2017), Microbial acceleration of aerobic pyrite oxidation at circumneutral pH. *Geobiology*. 15: 690– 703. https://doi.org/10.1111/gbi.12241

Reigl, S., Van Driessche, A. E., Mehringer, J., Koltzenburg, S., Kunz, W., & Kellermeier, M. (2022). Revisiting the roles of salinity, temperature and water activity in phase selection during calcium sulfate precipitation. CrystEngComm, 24(8), 1529-1536.

Stamenković V, Ward LM, Mischna M, Fischer WW (2018), O2 solubility in Martian near-surface environments and implications for aerobic life. *Nature Geoscience.* Dec;11(12):905-9.

POSTMA, D. (1983). Pyrite and siderite oxidation in swamp sediments. *Journal of Soil Science,* 34(1), 163-182.

Schreiber, B. C., & Tabakh, M. E. (2000). Deposition and early alteration of evaporites. *Sedimentology*, *47*, 215-238.

Schwenzer, S. P., Bridges, J. C., McAdam, A., Steer, E. D., Conrad, P. G., Kelley, S. P., ... & Sutter, B. (2016), Modeling of sulphide environments on Mars. *LPSC.*

Slotznick, Sarah P., et al. (2022), Reexamination of 2.5-Ga "whiff" of oxygen interval points to anoxic ocean before GOE. *Science Advances* 8.1: eabj7190

Spencer, R. J. (2000), Sulfate Minerals in Evaporite Deposits. *Reviews in Mineralogy and Geochemistry*, 40(1), 173–192. https://doi.org/10.2138/rmg.2000.40.3

Stack, K. M., Grotzinger, J. P., Lamb, M. P., Gupta, S., Rubin, D. M., Kah, L. C., et al. (2019), Evidence for plunging river plume deposits in the Pahrump Hills member of the Murray formation, Gale crater, Mars. *Sedimentology*, 66(5), 1768–1802. https://doi.org/10.1111/sed.12558

Stein, N., Grotzinger, J. P., Schieber, J., Mangold, N., Hallet, B., Newsom, H., et al. (2018), Desiccation cracks provide evidence of lake drying on Mars, Sutton Island member, Murray formation, Gale Crater. *Geology*, 46(6), 515–518. https://doi.org/10.1130/G40005.1

Sun, V. Z., Stack, K. M., Kah, L. C., Thompson, L., Fischer, W., Williams, A. J., et al. (2019), Late-stage diagenetic concretions in the Murray formation, Gale crater, Mars. *Icarus*, 321, 866–890. https://doi.org/10.1016/j.icarus.2018.12.030

Tarnas, J. D., Mustard, J. F., Sherwood Lollar, B., Stamenković, V., Cannon, K. M., Lorand, J.-P., et al. (2021), Earth-like Habitable Environments in the Subsurface of Mars. *Astrobiology*, 21(6), 741–756. https://doi.org/10.1089/ast.2020.2386

Thorpe, M. T., Bristow, T. F., Rampe, E. B., Tosca, N. J., Grotzinger, J. P., Bennett, K. A., et al. (2022), Mars Science Laboratory CheMin Data From the Glen Torridon Region

and the Significance of Lake-Groundwater Interactions in Interpreting Mineralogy and Sedimentary History. *Journal of Geophysical Research: Planets*, 127(11). https://doi.org/10.1029/2021JE007099

Torres, M. A., West, A. J., & Li, G. (2014), Sulphide oxidation and carbonate dissolution as a source of CO2 over geological timescales. *Nature*, 507(7492), 346–349. https://doi.org/10.1038/nature13030

Treiman, A. H., Bish, D. L., Vaniman, D. T., Chipera, S. J., Blake, D. F., Ming, D. W., et al. (2016), Mineralogy, provenance, and diagenesis of a potassic basaltic sandstone on Mars: CheMin X-ray diffraction of the Windjana sample (Kimberley area, Gale Crater). *Journal of Geophysical Research: Planets*, 121(1), 75–106. https://doi.org/10.1002/2015JE004932

Van Driessche, A. E., Stawski, T. M., Benning, L. G., & Kellermeier, M. (2017). Calcium sulfate precipitation throughout its phase diagram. *New Perspectives on Mineral Nucleation and Growth: From Solution Precursors to Solid Materials*, 227-256

Vaniman, D. T., Martínez, G. M., Rampe, E. B., Bristow, T. F., Blake, D. F., Yen, A. S., et al. (2018), Gypsum, bassanite, and anhydrite at Gale crater, Mars. *American Mineralogist*, 103(7), 1011–1020. https://doi.org/10.2138/am-2018-6346

Warren, J. K. (2010), Evaporites through time: Tectonic, climatic and eustatic controls in marine and nonmarine deposits. *Earth-Science Reviews*, 98(3–4), 217–268. https://doi.org/10.1016/j.earscirev.2009.11.004

Williamson, M.A., and Rimstidt, J.D., (1994), The kinetics and electrochemical rate-determining step of aqueous pyrite oxidation: *Geochimica et Cosmochimica Acta*, v. 58, p. 5443–5454, doi:10.1016/0016-7037(94)90241-0.

Wong, G. M., Franz, H. B., Clark, J. V., McAdam, A. C., Lewis, J. M. T., Millan, M., et al. (2022), Oxidized and Reduced Sulfur Observed by the Sample Analysis at Mars (SAM) Instrument Suite on the Curiosity Rover Within the Glen Torridon Region at Gale Crater, Mars. *Journal of Geophysical Research:* Planets, 127(9). https://doi.org/10.1029/2021JE007084

Zolotov, M. Y., & Shock, E. L. (2005), Formation of jarosite-bearing deposits through aqueous oxidation of pyrite at Meridiani Planum, Mars. *Geophysical Research Letters*, 32(21), L21203. https://doi.org/10.1029/2005GL02425

Chapter 3

LOW BUT PERSISTENT ORGANIC CARBON CONTENT OF HYPERARID RIVER DEPOSITS AND IMPLICATIONS FOR ANCIENT MARS

H. Kalucha[1], M.M. Douglas[1], M.P. Lamb[1], Y. Ke[1], and W.W. Fischer[1]

[1] California Institute of Technology

3.1 Abstract

Mars has many well-exposed fluvial ridges and fluvio-deltaic basins; in two of these locations, the Curiosity and Perseverance rovers are currently searching for signs of habitability. The distribution of organic carbon that might persist in ancient fluvial deposits present on Mars is not well understood. In this study, we set out to assess the preservation potential of organic carbon in a hyperarid fluvial environment with observations and analyses of the Amargosa River in Death Valley, California (United States). The lower reaches of the Amargosa River in Badwater Basin are nearly devoid of plants and contain low gradient, meandering channels, making them a valuable terrestrial analog for early martian fluvial systems. We analyzed sediment taken from fluvial deposits exposed in cutbanks of two bends of a meandering channel. We found total organic carbon abundances that were on average 0.15% up to a meter below the surface. X-ray diffraction and electron microscopy analyses revealed a suite of high redox potential mineral phases (including iron and manganese oxides) mixed with detrital and authigenic silicates, carbonate, and sulfate salts at or close to redox equilibrium with pore fluids in contact with the atmosphere. This finding highlighted that organic carbon can persist in fluvial deposits at low abundance despite oxidizing conditions and saturated sediments, and suggested that ancient fluvial deposits on Mars may retain traces of organics in fine-grained deposits were they present during deposition.

3.2 Plain Language Summary

The Curiosity and Perseverance rovers are currently searching for signs of past life on Mars in two ancient river deposits. Since carbon on the surface of Mars could originate from meteorites and chemical reactions in addition to potential Martian life forms, it is valuable to identify sedimentary environments that best preserve biospheric organic carbon. The distribution of organic carbon that might persist in ancient river deposits on Mars is not well understood, yet this understanding is crucial to detecting evidence for past life on Mars. In this study, we set out to determine the preservation potential of organic carbon in an arid, fluvial environment. The Amargosa River (Death Valley, California, United States) hosts a low gradient, single threaded river, running through a catchment with little of any vegetation, making it a valuable terrestrial analog for early Martian fluvial systems. We found that organic carbon can persist in fine-grained river sediments at low abundance despite oxidizing conditions in the subsurface. Our results suggested that fine-grained ancient river deposits on Mars are the most promising sampling targets for the Perseverance rover to detect traces of potential life on Mars.

3.3 Introduction

Mars has extensive sedimentary deposits which record a time when the planet was warmer and wetter (Grotzinger et al., 2015; Williford et al., 2018). It is clear that Mars was once a habitable planet. There is now an intense effort to understand whether or not the planet hosted life (or its precursor chemistry) (Arvidson and Catalano, 2018; Grotzinger et al., 2015; Rampe et al., 2020). Today, the Perseverance rover builds on this progress by searching for remnants of microbial life in the preservation of organic matter in the fine-

grained, fluvio-deltaic and lacustrine sediments at Jezero Crater (Williford et al., 2018). Understanding organic carbon preservation on Mars is therefore critical to fulfilling the science goals of the Perseverance mission.

So far, missions have landed in smaller Noachian (4.1 to 3.7 Ga) and early Hesperian (3.7 Ga onwards) alluvial and deltaic fan deposits in craters. However, there are many other fluvio-deltaic features exposed at the surface of Mars, often recognized by networks of ridges due to differential aeolian erosion that has occurred over billions of years since the rivers were active (Dickson et al. 2021). These ridges are located in large sedimentary basins undergoing inversion in which erosion of fluvial stratigraphy preferentially exposes channel body deposits (Cardenas et al., 2022). They provide a valuable archive of ancient Mars surface environments and processes and likely also contain sedimentary organic carbon. It is unclear what fraction of organic carbon phases initially present on Mars would be preserved in these environments and what depositional facies might be most likely to do so.

A range of physical, chemical, and potentially biological processes could be responsible for producing organic molecules on Mars. Meteorites deliver a range of organic carbon phases to the surface of Mars (Frantseva et al., 2018). In addition, several abiotic processes that produce organics on Earth may have occurred on early Mars such as cyano-sulfidic chemistry, serpentinization, sabatier reactions, and Miller-Urey spark discharge (Sasselov et al., 2020; Steele et al., 2022; McCollom et al., 2013). Most interestingly, life produces organics (measured on Earth in terms of primary productivity). When rivers were active on Mars, the carbon from these potential sources would have been subject to riverine transport, reaction, and burial/preservation. Organic molecules have been detected in mudstone and fluvial sandstone on Mars (Freissinet et al., 2015; Sutter et al., 2017; Eigenbrode et al., 2018; Szopa et al., 2020; Millan et al., 2022; House et al., 2022; Stern et al., 2022), but organic carbon abundances are uncertain.

Previous studies of terrestrial systems have determined that organic carbon preservation varies according to the sedimentary materials, depositional environment, and the lability of the carbon (Repasch et al., 2022; Liu et al., 2022). Organic carbon is better preserved at locations with rapid sedimentation or saturated pore waters because the molecules are exposed to oxygen for a shorter period of time (Hartnett et al., 1998). Mineral-bound organic carbon is able to persist for millennia compared to free organic carbon in oxygenated environments, especially with smaller grain sizes due to greater surface area (Hemingway et al., 2019; Ke et al., 2022; Stecko and Young, 2000; Bianchi et al., 2007). Redox availability and mineral catalysts have the opposite effect, accelerating microbial degradation of organic matter (Kleber et al., 2021). Lastly, refractory, polymerized carbon is much harder to degrade and is therefore preferentially preserved (Burdige et al., 2007). Earth serves as a valuable analog to understand how organic carbon is cycled with river sediment from transport to preservation (Galy et al., 2015; Resplandy et al., 2018; Gislason et al., 2006). Rivers transport significant amounts of inorganic carbon as particles and dissolved in the water column. Particulate organic carbon (POC) associated with sediment in active suspended fluvial transport on Earth typically contains 1-2 % OC with some

outliers up to 90% (Ke et al., 2022). Though OC content is typically higher in finer grained sediments, many other factors such as precipitation, tectonics, and temperature impact OC loading. OC associated with fluvial sediment can be buried in river deposits or bank sediment. The average organic content of bank sediment is much lower than POC content (on average ~0.8%) (Cao et al., 2017, Sutherland, 1998, Skorbilowicz and Skorbilowicz, 2008), and can be as low as 0.09% (Zhang et al., 2020). Bank sediment typically contains an OC rich soil/overbank layers established at the top of the floodplain. OC content is lower in the deposits that underlie those upper layers (Torres et al., 2020, Lininger et al., 2018, Douglas et al., 2022, Scheingross et al., 2022, Repasch et al., 2021).

Most studies on Earth measure the impact of perennial rivers with high biospheric OC turnover on the terrestrial carbon cycle over decades to millennia. Increasing mean annual precipitation and mean annual temperature creates high OC turnover, such that the measured biospheric OC is relatively younger in rivers in warmer and wetter climates (Eglinton et al., 2021). As a result, OC in rivers with geographically hot and humid climates has higher turnover than OC in rivers flowing in low temperature, low precipitation climates. There is a lack of measurements of TOC for arid riverine settings, but measurements from temperate and polar settings indicate that organic carbon is more persistent in colder terrestrial environments and might persist on Mars. Climate during the Mars river-forming era is debated as either warm and wet or cold and dry (Wordsworth et al., 2015; Scherf and Hammer 2020). Regardless of the climate, there is general agreement that Martian rivers did not have biotic input from plants and that the water on Mars has dried since then (Scheller et al. 2021). Thus, any OC observed by rovers today may have had to be preserved over millions or even billions of years in a cold and dry ancient river deposit. To understand the potential OC preservation in these environments, it is useful to study OC preservation on Earth in a dry, depositional fluvial environment generally devoid of vegetation.

In this study, we set out to assess the initial organic carbon preservation potential of a Martian fluvial environment by conducting measurements of a modern process analog environment: the Amargosa River in Death Valley, California, USA. The lower reaches of the Amargosa River in Badwater Basin are nearly devoid of plants and yet contain low gradient, meandering channels, making them a valuable terrestrial analog for early Martian fluvial systems. We analyzed the mineral assemblage of the floodplain sediment taken from cutbanks of two bends of a meandering channel and measured TOC content of these samples.

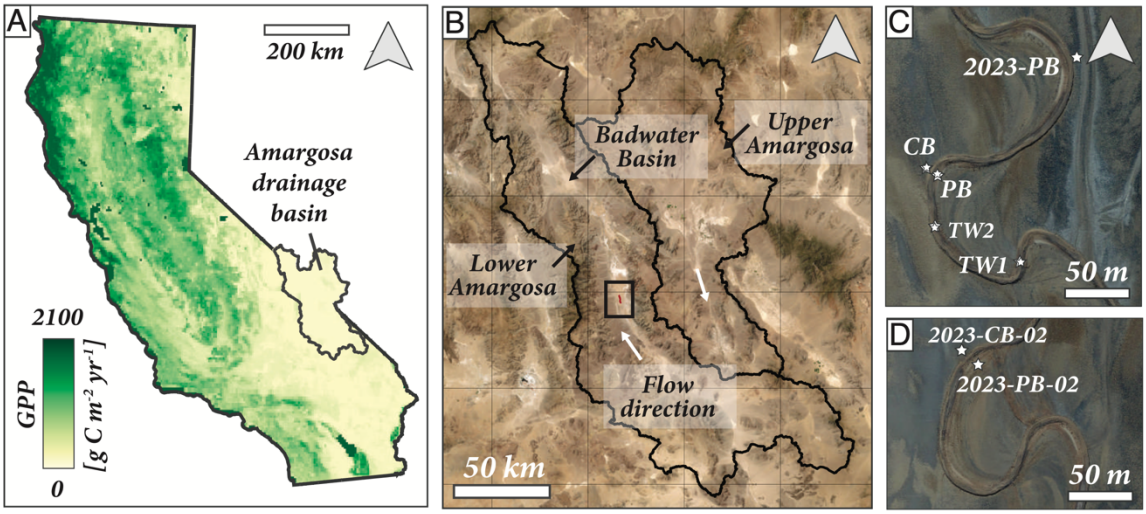

Figure 3.1. Map of study reach within the Amargosa River catchment in Death Valley. A) Location of the Amargosa River catchment in California, USA, shown with observations of gross primary productivity as observed by NASA MODIS (Moderate Resolution Imaging Spectrometer 0.05 degree latitude resolution) overlain; the standing vegetation and rates of primary production in the catchment are among the lowest known on the Earth surface. B) Outline of both parts of Amargosa River catchment with flow direction shown. Sampling Site (black rectangle) is in the sinuous, single-threaded, downstream section of the river with the channel terminating in Badwater Basin. C) Bend 1 sampling sites. 2023-PB was sampled in 2023. CB, PB, TW1, TW2 were sampled in 2019. D) Bend 2 sampling sites. 2023-CB-02 and 2023-PB-02 were sampled in 2023. CB = cutbank (the outer side of the channel subject to erosion due to bend curvature), PB = point bar (the inner side of the channel subject to deposition due to bend curvature), TW = thalweg (the deepest part of the channel).

3.3.1 Geologic Setting

The Amargosa River is a single-threaded, depositional alluvial river (Belcher et al. 2019). Our study reach of the Amargosa is situated in Death Valley, California, between the Panamint Range and the Black Mountains (Hooke, 1972). The study reach (36.112°, -116.815°, elevation of -81.5 m) is located in the Great Basin, which has been subject to tectonic extension since Miocene time, is subsiding at ~1 mm/year, and contains more than 3 km of valley fill (Ku et al., 1998; Li et al., 1996; Ielpi, 2019 and references therein). The Amargosa River in the study reach has a channel slope of 3.25x10-4 and bankfull depth of about 1 m (Douglas, 2023). It currently terminates in a distributary channel network that empties into Badwater Basin, the lowest elevation point in North America. The lower part of the Amargosa River is ephemeral and the channel bed is typically covered in salt crusted desiccation cracks between flow events.

The Amargosa drains a geologically varied catchment (Belcher et al. 2019; Anderson, 2005). The headwaters originate in the Pahute Mesa and Black and Timber Mountains, which consist of alternating thick platform-carbonate and clastic sequences from the late

Proterozoic and Paleozoic, Miocene aged andesitic and rhyolitic lava flows, and peralkaline tuffs (Minor et al., 1993). As the river flows southwards, it sources sediment from the Funeral Mountains, the Nopah Range, Kingston Range (including Amargosa Chaos basin) and the Spring Mountains, which are dominated by Paleozoic carbonate rocks and Proterzoic and lower Cambrian siliciclastics (Belcher et al., 2019). The siliciclastics consist of quartzite, mudstone, carbonate, chert, and interbedded shale (Topping, 1993). The Lower Amargosa receives input from alluvial fans of the Panamint and Black mountains before it terminates in Badwater Basin. The bedrock of both these mountain ranges consists of the same lower Cambrian siliciclastic rocks and Paleozoic carbonate rocks as in the upstream mountain ranges above in addition to Cenozoic volcanic rocks, and quaternary alluvium and valley fill (Belcher et al., 2019 and references therein). Due to the angle of faulting, the carbonates are the topographic highs of the mountains overlaid intermittently by the volcanic rocks: both of these are the likely source of the fine sediment being washed off the fans at the edge of the valley into the Amargosa River.

Importantly, the Amargosa river also sources sediment from playa deposits of various ages. Lake Tecopa continuously occupied the Great Basin from 9+/- 2 million years ago to as late as 150,000 years ago. A detailed study of Lake Tecopa mudstone mineralogy revealed that the sediment contains detrital quartz, plagioclase feldspar, potassium feldspar, magadiite, carbonates, halite, gypsum, and small amounts of amphiboles as well as sepiolite, montmorillonite, mica, illite, saponite, and mixed layer clays and chlorite. In addition, the authigenic minerals are calcite and dolomite, sepiolite, magadiite, potassium feldspar, montmorillonite, zeolites, and the saline minerals (Starkey and Blackmon, 1979). The Amargosa River (Upper Amargosa in Figure 3.1B) first flowed into Tecopa Basin from the north before 765 ka. After 200 ka, Lake Tecopa and the Amargosa River (Lower Amargosa in Figure 3.1B) drained into Lake Manly from the south (Reheis et al., 2020). During the Pleistocene, the Great Basin experienced alternating wet and dry intervals during the glacial and interglacial periods, respectively. The wet intervals are characterized by three separate lake high stands (26 ka, 18ka, and 12ka), creating episodes of alternating evaporitic and clastic sedimentation in the lake basin (Anderson and Wells, 2003). Many of the deposits in the study reach are therefore weathered materials that have been recemented with salts on the surface. A 185 m core extracted from Badwater Basin consists of halite dominated mud in the uppermost 7.7 meters (Ku et al., 1998; Li et al., 1996; Lowenstein et al., 1999).

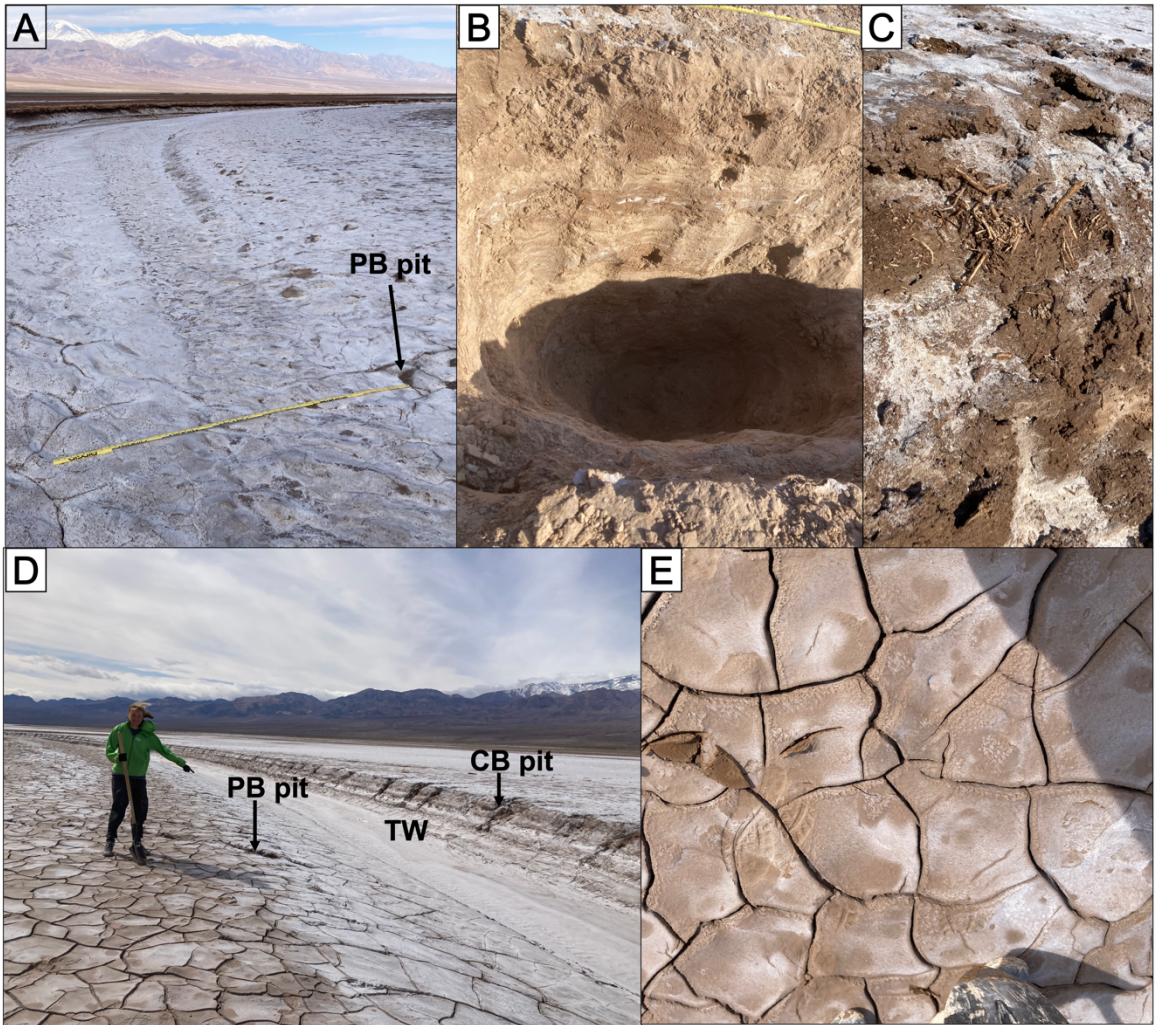

Figure 3.2. Amargosa River Field Site. A) Field site showing complete channel at Bend 1 where 2023-PB was dug with meter scale stick and point bar pit location; B) 1.35 m PB pit (Bend 1, 2023-PB); C) wood chips and salt crust at bankfull level; D) locations of PB, TW, CB pits in Bend 2 (where 2023-PB-02 and 2023-CB-02 was dug) in one cross section; E) close up of mud cracks in D.

Though the Amargosa River has previously been examined as a potential analog for single-threaded rivers on Mars (Ielpi and Lapôtre, 2020; Ielpi et al., 2020; Ielpi, 2018), these studies primarily relied on remote sensing and lacked geochemical measurements of the materials that make up the alluvial deposits. The Amargosa catchment near Badwater Basin has also been investigated by orbital spectrometers as a Mars analog with ground truth mineralogical measurements (Baldridge et al., 2003), which found majority quartz, anhydrite, calcite, halite, orthoclase, dolomite, and gypsum, and minor amounts of muscovite, anorthoclase, albite, and thenardite. Their x-ray diffractometer (XRD) spectra also showed trace zeolite, glauberite, proberite, iron sulfide, and illite.

The Amargosa River is an interesting analog to martian fluvial settings in that it is a single threaded, low gradient river, with the lowest primary productivity on Earth: The NPP (net primary productivity) of the area is up to 2.5x10-4 kgC m-2 yr-1, which is the lowest on the surface of the Earth except in some permafrost areas (Running and Zhao, 2021). For comparison, the delivery of carbon via dust infall to the martian surface is a maximum of 3x105 kg yr-1, asteroid impacts are is 1.21x105 kg yr-1, and comets are is 1.3x104 kg yr-1, adding up to a total of 4.34x105 kgC yr-1 (Frantseva et al. 2018). This translates to 3x10-9 kg C m-2 yr-1 on Mars. However, during the late heavy bombardment (~4 Ga), the estimated mass flux of micrometeoroids to Mars was elevated to 2.3x1018 kg over 200 million years (Court and Sephton, 2014), or 7.94x10-3 kgC m-2 yr-1 for that period. Death Valley is one of the driest places on Earth: mean annual precipitation was measured as 52.4 mm (Belcher et al., 2019). This climate strongly inhibits vegetation growth; of 257 surveyed channel bends of the Amargosa, 97.7% were unvegetated (Ielpi, 2019). Despite this climate, the Amargosa catchment experiences rare ephemeral flows that move sediment and define the river morphology (Douglas, 2023).

3.4 Materials and Methods

3.4.1 Field sampling

We sampled ~20 km south of Badwater Basin in the sinuous, downstream section of the Amargosa River in 2019 and 2023. We focused on two bends a kilometer apart on the active ephemeral channel (coordinates in Table S1). Both bends are highly sinuous and preserve the chronology of fluvial deposition clearly; neither bend hosted any plants. Between 2019 and 2023, the river experienced several episodes of severe flooding in September 10, 2022 and the winter of 2023.

At Bend 1 (Figure 3.1C), we dug a point bar pit (2023-PB) and two separate thalweg pits (TW1 and TW2). We also dug a cutbank pit (CB), a shallow thalweg pit (TW), and a point bar pit (PB), which formed a channel cross-section. We collected samples at different depths (Table S1, Figure 3.3) and recorded different grain sizes and depositional features that were present. At Bend 2 (Figure 1D), we dug point bar (2023-PB-02), shallow thalweg, and cutbank pits (2023-CB-02), forming a cross-section and again collected samples at many depths. Samples taken in 2023 are labeled with the collection year in Figure 3.1C,D. Samples taken in 2019 do not have a year label in Figure 3.1C,D. We measured grain size using a sand card and hand lens in the field to produce stratigraphic columns to contextualize the samples. Surface material was removed using a trowel, shovels and trenching tools. Samples were collected by ethanol-cleaned tools and then sealed in Whirlpak bags. In the lab, samples were gently disaggregated with a mortar and pestle, homogenized, and then dried in an oven for 48-96 hours at 50 °C prior to analytical measurements. We did not use a procedural blank to assess contamination during this procedure.

3.4.2 Elemental Analyzer (EA) and Isotope Ratio Mass Spectrometry (IRMS)

The EA-IRMS was used to detect the bulk %TOC (total organic carbon) and δ13C (stable carbon isotope ratio) of the 2019 samples. For 2019 samples, 0.1 g of each sample was decarbonated with 10 ml of 2 M HCl and stirred. The samples were then left non-agitated

overnight. After neutralization, the samples were dried in the oven at 70 °C for 48 hours. The TOC and δ13C measurements were made by a Costech Elemental Analyzer connected to a Delta V Plus Isotope Ratio Mass Spectrometer via a ConFlo IV Universal Interface, using 1 mg of sample for 2019 samples. The isotope ratios are reported in per mille, relative to Vienna Pee Dee Belemnite (VPDB), and calibrated using Urea (-27.8‰). Sample preparation for the 2023 samples followed the same procedure, though 1 g of sample was decarbonated with 30 ml of 1 M HCl. TOC content of the 2023 samples was measured using a Costech Elemental Analyzer on 5 mg of sample and calibrated using Acetanilide. For all analyses, the peak area of analytical blanks (tin capsules) was subtracted from the peak area of samples and standards before being converted to wt% TOC using results from the standards.

3.4.3 Scanning electron microscopy

To image sediment particles, determine their sizes and characteristics, and analyze their geochemistry, we used a scanning electron microscope (SEM) at the 1-1000 μm scale. The samples were mounted as monodisperse powders onto carbon tape, carbon coated, and imaged by a Zeiss 1550VP FESEM (field emission SEM), equipped with in-lens SE, below-lens SE, variable pressure SE, and BSE (back scanning electron) detectors. The elemental compositions of the samples were mapped using an Oxford X-Max SDD X-ray Energy Dispersive Spectrometer (EDS) system. The EHT (accelerating voltage) was set to 15 kV and the working distance was 7.9 mm. The X-ray detector is capable of detecting Be to U elements. By comparison with known standard materials, the elemental analysis has an accuracy of 5% and detection limit of ~0.5%.

3.4.4 X-ray diffractometer (XRD)

An XRD was used to detect the bulk crystalline minerals by measuring the diffraction angles in each sample, which correspond to characteristic crystal lattice spacings of key minerals via Bragg's Law. Only samples from 2019 were analyzed. Powdered samples were pressed into a brass holder to produce a randomly oriented specimen. The XRD analysis was conducted on a Panalytical X'Pert Pro, which has a Cu-Kalpha anode at 35 kV and 40 mA. The scans had a 2θ start position of 10.0° to an end position of 79.95° and a step size of 0.03°. The scan step time was 1 second. Identification of minerals was made using Highscore software. Fine-grained (<~100 μm) clay minerals do not produce clear diffraction patterns, so it is possible that the XRD underestimated the abundance of clay minerals in our samples.

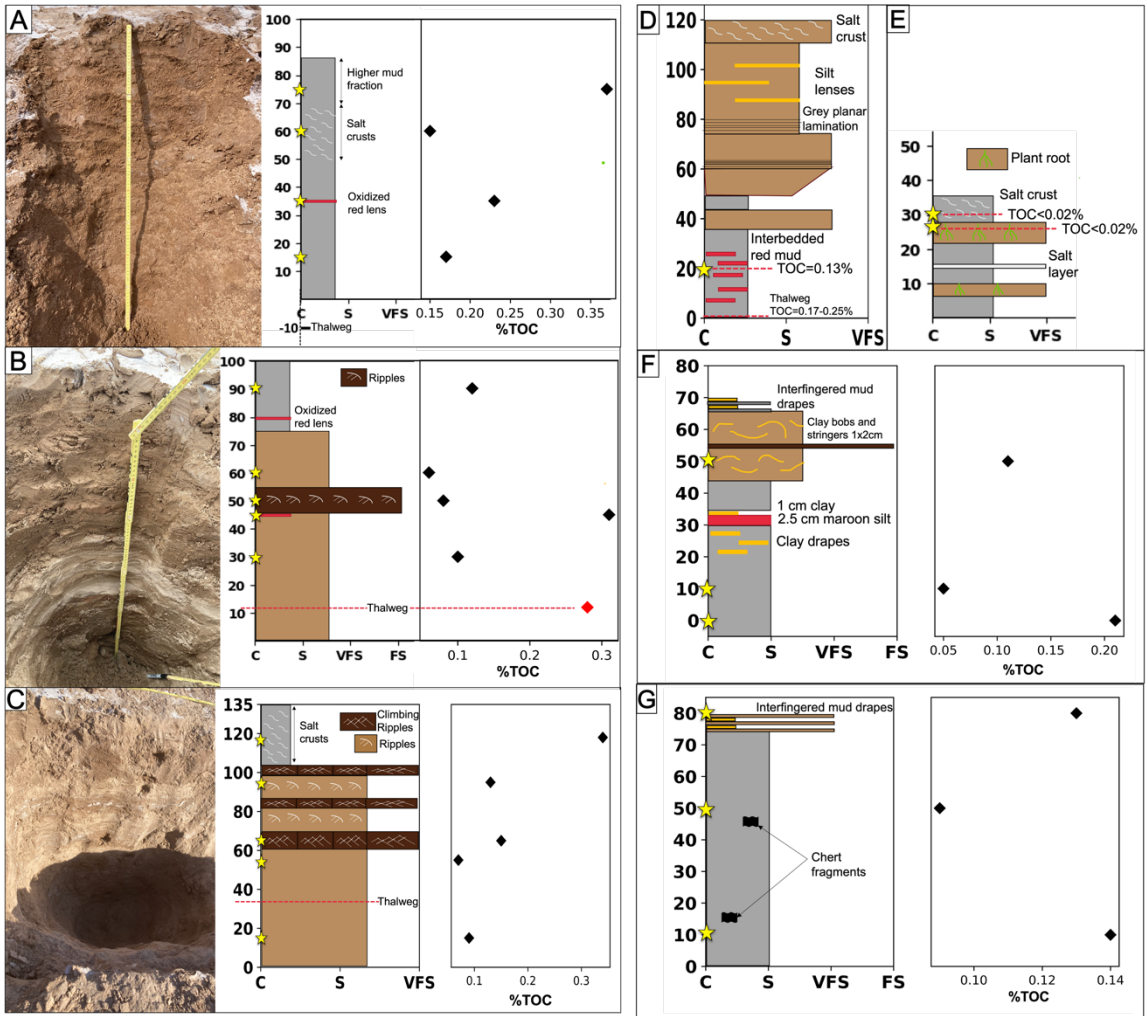

Figure 3.3. Stratigraphic Columns. A) Photograph, stratigraphic column of cutbank (2023-CB-02) in cm, %TOC (total organic carbon) vs height (cm). B) Photograph, stratigraphic column of opposing point bar pit (2023-PB-02) in cm, and %TOC (total organic carbon) vs height (cm). Both from Bend 2 on the map in Figure 3.1D and pictured in Figure 3.2D. C) Photograph, stratigraphic column, and %TOC (total organic carbon) vs height (cm) of point bar 2023-PB (Figure 3.1C, Bend 1). D) Stratigraphic column of cutbank CB in Figure 3.1C (Bend 1) with TOC values marked at sampling points. E) Stratigraphic column of point bar PB in Figure 3.1C (Bend 1) with TOC values marked at sampling points. F) Stratigraphic column of thalweg pit TW1 (Figure 3.1C, Bend 1) and %TOC (total organic carbon) vs height (cm). G) Stratigraphic column of thalweg pit TW2 (Figure 3.1C, Bend 1) and %TOC (total organic carbon) vs height (cm). Yellow stars are sample locations. C=clay, S=silt, VFS=very fine sand, FS=fine sand. In all cases, the top of the stratigraphic column corresponds to the top of the bank or the surface of the thalweg.

3.4.5 Grain Size

Because of the small particle sizes present in these sedimentary deposits, we measured grain diameter using laser diffraction with the Malvern Mastersizer 3000. We used

subsamples that were already decarbonated via the method above in Section 2.2. Organics were removed by suspending the sediment in 25 mL of 30% hydrogen peroxide at room temperature for 3 hours. The samples were then rinsed and put through the Mastersizer. To prevent flocculation or the breaking apart of clay particles, we used the propellor at 2000 rpm instead of using the sonicator. Measurements were repeated until the relative standard deviation was <5% for 3 consecutive measurements.

3.4.6 Attenuated reflectance (ATR)

To investigate clay minerals in our samples, the infrared spectrum of the samples was taken by a Nicolet Magna 860 FTIR (fourier transform infrared) with an ATR (attenuated reflectance) accessory in the sample compartment. ATR quantifies the changes to an internally reflected infrared beam that goes through a diamond crystal and protrudes ~1 μm deep into a bulk powdered solid sample. The unique vibrational bond energies of the molecules present produce a spectrum of absorptions. The spectra were divided by the background of the sample and ten spectra were collected per sample in the range of 400-4000 wavenumbers (cm-1).

3.4.7 Global river sediment OC dataset

To compare the sediment TOC values of the Amargosa to other rivers, we compiled a global dataset of river sediment OC values. For each river where sediment OC was measured, we extracted all OC values measured on suspended, bedload, bank, and bar sediment and the depth below the floodplain or river surface each sample was collected at in the study. The dataset can be found in Table S2. Coordinates and sampling time are also noted as well as grain size where available.

3.5 Results

Figure 3.2 displays the channels of the Amargosa at Bend 1 and 2 before pits were dug. The channel had steep cutbanks and gently sloping point bars (Figure 3.2D), forming asymmetrical channel cross-sections. The surface was covered with cracked salt crusts (Figure 3.2E) and so no bedforms were visible before digging. Wood debris deposited as a strandline marked a recent bankfull flow (Figure 3.2C). Figure 3.3 shows the stratigraphic column of each pit and TOC measurements at corresponding sample depths. The cutbank in Figure 3.3A was composed of wet and compact, silt-sized grains with a generally massive/structureless texture. Midway through the section, there was a distinct, oxidized red lens. Above that, salt lenses were interbedded in a significant section of the deposit and formed a layer on top of the bank. The opposing point bar in Figure 3.3B was visually coarser (silt to vfs) and fined in the top quarter of the section. There were similar oxidized, red lenses and a bed of ripple cross stratification in the middle of the pit. The point bar in Figure 3.3C had multiple sets of climbing ripple cross-stratification, demonstrating aggradation of sediment due to river meandering. The cutbank in Figure 3.3D had an abundance of red mud lenses and reached coarser grain sizes than the cutbank in Figure 3.3A. Red indicates higher iron content in the mud and red mud layers are present in four of the seven stratigraphic columns we measured as well as different heights in those sections, indicating that sediments from the surface down to ~1 m depth have all been

subject to iron oxidation. The thalweg pits shown in 3.3F and G consisted of largely silt; Thalweg 1 (TW1) coarsened upwards in the section.

3.5.1 Trends in organic matter abundance, distribution, and source

Organic matter abundance is low but persistent across the 28 samples (Table S1) with an average of 0.15±0.09%. Figure 3.4 displays the variation of grain size and TOC content. In general, there is no trend between sediment grain size in the silt range and TOC content ($p>0.05$ for a linear regression) but sand sized samples contained lower TOC.

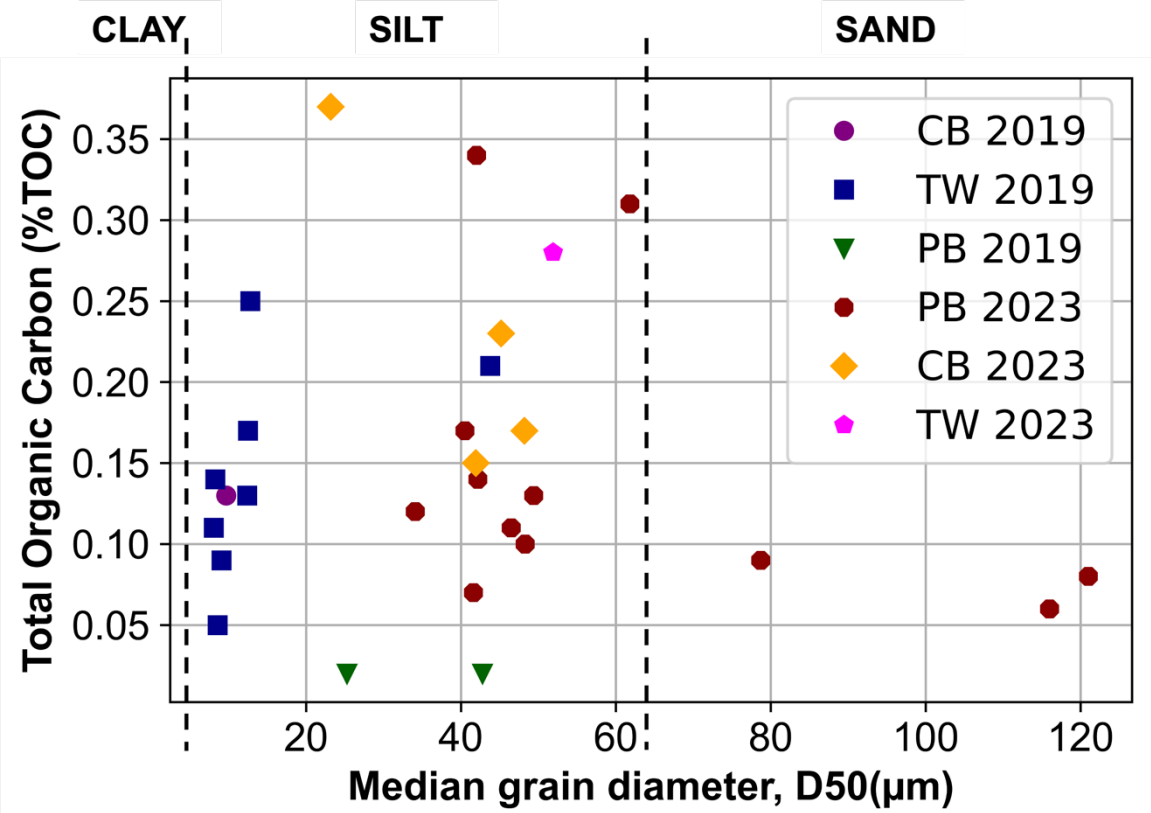

Figure 3.4. Total organic carbon (%TOC) vs Median grain diameter D_{50} (μm), color coded by landform type and year. PB=point bar, CB=cutbank, TW=thalweg. Green triangles show samples with organic carbon below detection limit of 0.02%.

3.5.1.1 2019 dataset (Table S1)

We collected samples from a pointbar-thalweg-cutbank cross section of the channel (PB, CB in Figure 3.1C) and two thalweg pits (TW1, TW2 in Figure 3.1C) from Bend 1 in 2019. The 2019 dataset (subset of samples from Bend 1) has grain sizes on the order of ~10 μm and TOC of ~0.1%. The TOC content of the thalweg at a depth of 5 cm is the highest amongst all samples (0.25%). Cutbank sample TOC is close to the median value of all samples. The point bar was notably coarser than thalweg and cutbank and both samples from the point bar did not contain a detectable amount of organic carbon. Thalweg 1, in terms of grain size, was largely a silt-clay mixture and the TOC wass highest at the deepest point. In general, thalweg 2 samples are more homogeneous silt and contain lower TOC

than thalweg 1, but the highest amount of TOC was also at the deepest point. The $\delta^{13}C$ isotope values for all samples ranged from -21.96 to -25.59 ‰ and the average was 23.80±0.98 ‰ (n=9, Table S1).

3.5.1.2 2023 dataset (Table S1)

We collected samples from a pointbar (2023-PB in Figure 3.1C) at Bend 1 and a pointbar-thalweg-cutbank cross section of the channel (2023-PB-02 and 2023-CB-02 in Figure 3.1D) at Bend 2. The 2023 dataset had grain sizes on the order of ~40 µm and TOC content between 0.05-0.37%. Major floods transported coarse sediment between our sampling campaigns, which resulted in all of our thalweg samples being ~4 times coarser than the previous samples. The point bar and cutbank grain size were not affected by flooding. While coarse deposits of the Amargosa River still contained trace organic carbon, coarser samples typically had lower TOC than fine-grained samples (Figure 3.4). The water fraction loss of the samples after 48 hours at 50 C ranged from 4.72 to 19.82%; the river sediment was highly saturated.

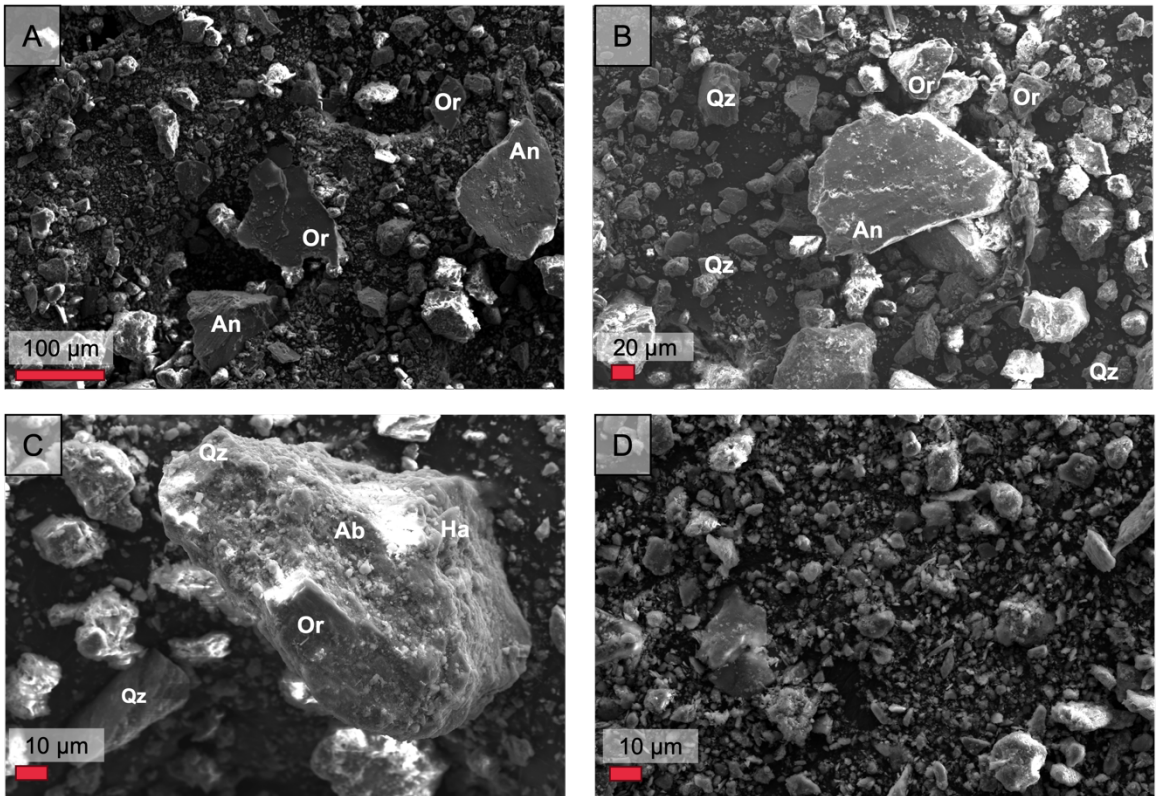

Figure 3.5. SEM images at various scales of samples. A) Sample TW1 at depth 70 cm B) Sample PB at depth 8 cm C) Sample TW at depth 0 cm D) Sample TW1 at depth 60 cm. Or = orthoclase, An = Anorthite, Qz = Quartz, Ab = Albite, Ha = Halite

3.5.2 Mineralogy Trends

Figure 3.5 shows the samples prior to decarbonation at various scales under the scanning electron microscope (SEM). The grains were subangular and in most cases, a few large grains dominated the field of view while the silt formed the majority of the

background. When scanned with the energy dispersive spectrometer (EDS), all visible clasts were mineral mixtures. There was no visible cement, although the samples had not been decarbonated at this stage. The SEM scans revealed that the majority of the sample was made up of detrital grains and that larger grains may have been subject to authigenic mineral precipitation on their surfaces to become even larger in size, the biggest example of a clast being ~150 μm. As Figure 3.2C shows, there was rare wood and plant debris in significant fractions at the strandline of some channels that likely originated from vegetation growing upstream in the catchment.

Section	Height in stratigraphic column (cm)	Feldspar	Salts	Carbonate	Oxides	Clays
CB	20	Albite, Orthoclase	Halite	Calcite	Heavy metal hydroxide	Muscovite
TW	0	Albite	Halite, Brushite	Calcite	Alunogen	Nimite
	−5	Labradorite	X	Calcite, Dolomite	Iron oxide, manganese oxide	Phlogopite
PB	30	Labradorite, Albite	Ardealite	Calcite	X	Phlogopite
	27	Anorthite, Microcline	Halite		Heavy metal hydroxide	X
TW2	80	Labradorite	X	Calcite	Iron oxide, manganese oxide	X
	50	Albite, Sanidine	X	Calcite	Magnetite	X
	10	Anorthite	Brushite, Beryllonite	Calcite	X	Montmorillonite
TW1	50	Anorthite	Brushite	Calcite	X	X
	10	Anorthite	Halite	Calcite, Dolomite	X	Nontronite, Hydrotalcite
	0	Anorthite, Orthoclase	X	Calcite	X	X

Note. All samples are from 2019 and located in Figure 1c. Red columns are oxidized minerals. X signifies a lack of detection. All samples contained significant quartz. CB = cut bank, PB = point bar, TW = thalweg.

Table 3.1. Minerals identified via X-ray Diffraction on Each Sampling Location and Associated Height.

The mineral assemblages showed a river with oxygenated pore fluids all the way to channel depth. Table 3.1 lists the sampling location, depth, and minerals detected via XRD. All samples contained substantial amounts of quartz, feldspar, and carbonate. Potassium and plagioclase feldspar were often co-located. Samples from TW1 contained Ca-rich plagioclase. Samples near the surface of TW2 had higher Na-rich plagioclase while TW2 at 70 cm depth contained very Ca-rich plagioclase. TW and PB became similarly sodium-depleted with depth. The main salts present are halite (NaCl) and brushite ($CaHPO_4 \cdot 2H_2O$) and they were found interchangeably at all depths. There was one occurrence of ardealite (Ca2(HPO4)(SO4)• 4H2O): at the surface of PB and a sodium phosphate salt (Beryllonite, NaBePO4) at TW2-70. Almost all carbonate occurred as calcite except for TW2-70 and TW1-30, where dolomite co-occurred. Several clay minerals were present such as muscovite, nimite, phlogopite, montmorillonite, and nontronite. The ATR data of all samples (the amorphous fraction) were best matched with amorphous forms of bentorite and montmorillonite. The oxide minerals were classes of iron oxides, aluminum oxide, manganese oxide, and heavy metal hydroxides. Most notably, all locations contained oxidized minerals except TW1.

Figure 3.6 compares the Amargosa bank sediment TOC values to the global dataset of bank sediment TOC values (compiled for this study, data in Table S2) and the global suspended sediment TOC compiled by Ke et al. (2022). For suspended TOC, only 85 points were more than 20%. Global bank sediment TOC was skewed to lower %TOC than the

suspended TOC abundance. The median of global suspended sediment TOC was 1.24% and the median of global bank sediment TOC was 1.0%. This is consistent with larger grain sizes (found in bar sediments as opposed to suspended particles and overbank deposits) having lower amounts of OC (Ke et al., 2022; Stecko and Young, 2000; Bianchi et al., 2007). The Amargosa River bank contained on average 0.15±0.09% (n=28) organic carbon.

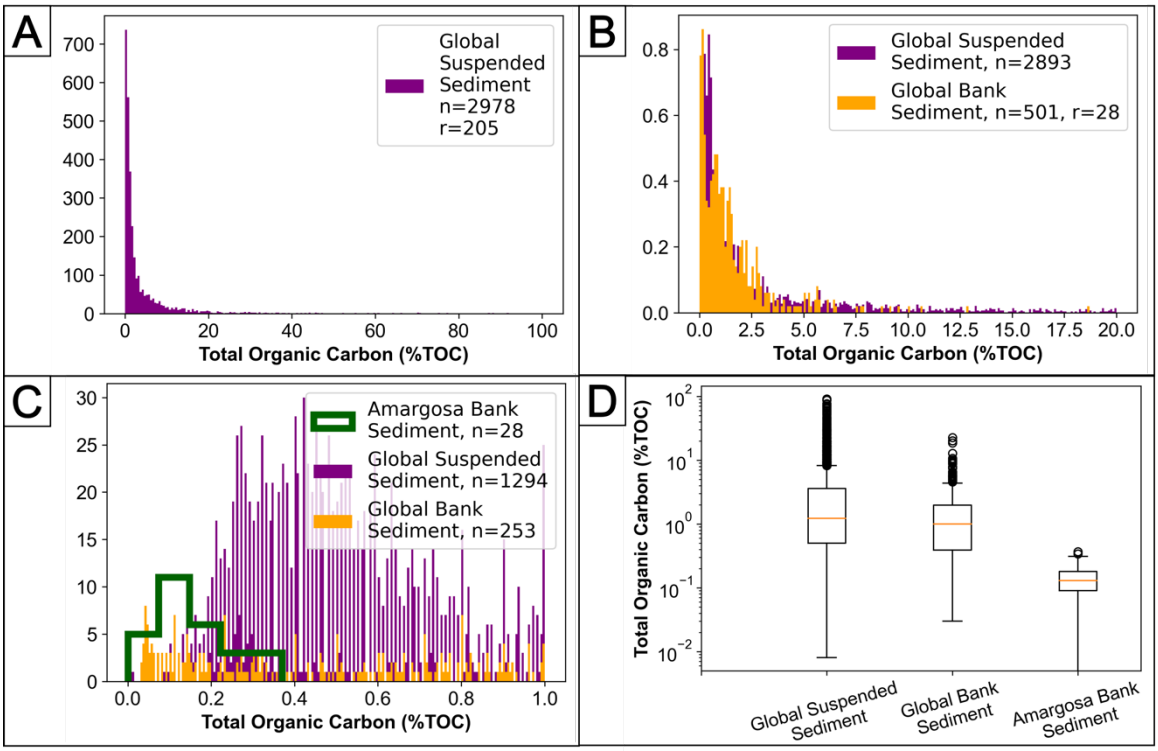

Figure 3.6. Histograms. n = number of data points, r = rivers. A) Histogram with global suspended sediment TOC dataset from MOREPOC (Ke et al., 2022). B) Histogram overlaid of bank sediment TOC measurements compiled in a global dataset for this study (both are normalized as probability distribution functions). C) Histogram of Amargosa bank sediment TOC overlaid. D) Box and whisker plots of all three datasets on a log scale of % TOC.

3.6 Discussion

The organic carbon content is heterogeneously preserved amongst silt-sized grains and an order of magnitude lower in the sand- samples (Figure 3.4). There is no functional relationship between TOC and depth below the floodplain surface in our sample set (Figure 3.3). Areas with vegetation on Earth commonly generate an organic-rich topsoil and TOC is highest in the top ~1 m of river sediment (Ouyang et al., 2006; Cao et al., 2017; Sutherland, 1998; Skorbilowicz and Skorbilowicz, 2008; Zhang et al., 2020). This is not present in Death Valley and our measurements do not show TOC enhanced at the top of the floodplain. Although the 0.15% average OC found in the Amargosa River is significantly lower than the median OC from measurements of ~200 rivers on Earth (Figure

3.6), it is still comparable to some measurements of rivers with high catchment NPP, such as the Brahmaputra River (Pradhan et al., 2020) and the Pearl River (Lin et al., 2019).

As the Amargosa River drains a combination of volcanic units (no petrogenic OC), lower Cambrian and older sedimentary units (old petrogenic OC), and alluvium (eroded, old petrogenic OC), it is difficult to ascertain the fraction of petrogenic carbon in our samples without additional analysis. Global values of petrogenic OC in carbonate (median: 0.13%), siliciclastic (median: 0.1%), and igneous rock (median: 0.02%) have large variation (Zondervan et al., 2023). Relative fraction of petrogenic OC fractions in sediment increases with physical erosion rate in the catchment (Galy et al., 2015). Petrogenic OC oxidation increases in response to increased temperature (Soulet et al., 2021) and in warm and wet climate (Galy et al., 2015; Hemingway et al., 2019). These factors also make it difficult to ascertain the fraction of petrogenic OC loss in the downstream section of the Amargosa river where we sampled.

Biospheric OC in our samples likely originates from upstream plants and wood and microorganisms (young, biospheric OC) present throughout the Amargosa's catchment of the Amargosa as well as older, biospheric OC from Pleistocene lacustrine deposits. We observed wood deposited in flood strandlines, on the floodplain of the Amargosa (Figure 3.2C). In addition, The average δ13C value of the 2019 samples (all silt sized) is -23.80±0.98 ‰ (n=9, Table S1) and aligns with the δ13C values of Death Valley vegetation such as Desert Trumpet (-28 to -23‰), Brittlebush (average of -26.54‰, range of -29.5 to -24‰) (Craft et al., 1998; Driscoll et al., 2020; Smith and Osmond, 1987). Degraded organic carbon and sediments with lower POC content tend to be enriched in δ13C, which may be contributing to our measurements (Figure 2 from Ke et al., 2022). The catchment hydrology is conducive to mobilizing biospheric OC, since biospheric OC tends to be concentrated in sediment entrained by overland flows as opposed to bedrock erosion (Galy et al., 2015), which we expect to be the case since the Amargosa is fed by brief, flashy floods that sustain the Amargosa often accompany debris flows (Douglas, 2023). Low precipitation encourages organic preservation, and physical factors such as high sedimentation rates are able to protect biospheric OC even in warm climates that can promote oxidation (Galy et al., 2007).

In addition to OC produced by a hypothetical early biosphere, Mars also likely accumulated meteoritic carbon delivered to fluvial catchments as calculated above, which will complicate interpreting any TOC measured on martian samples one day. Despite the differences in sources of OC between terrestrial and martian catchments, their similar deposit style and mineralogy provides insight into OC preservation potential.

On Earth, OC loss via oxidation can occur during fluvial transport events when erosion exposes sediment to oxygenated conditions. However, Death Valley is an ephemeral, net-depositional environment similar to Jezero and Gale Craters, such that sediment is not frequently remobilized in the cutbank and point bar deposits (Douglas, 2023). Floodplain storage has been found to enhance oxidation in some environments, with 80% POC oxidation within millennia (Scheingross et al. 2022), and enhance preservation in others

(Douglas et al., 2022). In terms of oxidation of organic matter, once it is deposited in sediment, Mars weathers at a rate 2-3 orders of magnitude more slowly than Earth: meteorites would last 109 years on Mars compared to their lifetime of 106 years in Antarctica (Bland et al. 2000). Thus, organic carbon has a greater chance of surviving into the present. The TOC range of the 165 Mya Atacama Desert alluvial fan, another net-depositional environment, is 0.02-0.11% (Azua-Bustos et al., 2023). This similarly dry and unvegetated system has overlapping TOC with Amargosa River sample TOC abundance, demonstrating the ability of organic carbon to persist in Mars-like environments. Recent modeling estimates propose power-law decay of organic carbon such that TOC is only completely degraded at infinity time, further supporting organic carbon persistence on Mars (Rothman et al., 2024).

The minerals detected in our samples, including neutral pH minerals (clays, carbonates), match very well to a combination of minerals from Pleistocene Lake Tecopa (Starkey and Blackmon, 1849) and bedrock in the catchment area (Belcher et al., 2019), though the samples are enriched in phosphate salts. Amargosa River water is enriched in phosphate compared to other terrestrial rivers, which could explain this difference (Belcher et al. 2019). Mineral assemblages are similar and TOC variance is too small to definitively identify one mineral being responsible for the TOC preservation. However, amorphous and/or crystalline clays are present in every sample and are likely the main contributor of TOC preservation (Kleber et al., 2021; Salmon et al., 2000; Sarkar et al., 2018; Kaiser et al., 2000). In addition, samples taken from red lenses tend to have higher TOC than the surrounding samples. These red lenses likely contain a higher concentration of iron oxides, which can help fix organic carbon to clay particles through covalent bonding (Lalonde et al., 2012).

Unlike the sediment sources of the Amargosa, our samples contain oxidized minerals such as iron and manganese oxides. More importantly, these oxidized minerals are co-located with the clays, salts, and carbonates, suggesting oxic chemical reactions to partial completion. This type of assemblage is reminiscent of Mars (Farley et al., 2022; Wiens et al., 2022). Curiosity's XRD instrument 'Chemin' found assemblages consisting of mafic igneous minerals, hematite, magnetite, phyllosilicates, feldspar, quartz, and Ca-sulfate in the fluvial sediments at Gale Crater (Rampe et al., 2020). The main difference is the ubiquitous presence of Ca-sulfate phases at Gale, which are not present in the Amargosa River sediments but have been previously detected in Badwater Basin (Baldridge et al., 2003). The fluvio-deltaic sediments in Jezero Crater consist of olivine, Fe and Mg rich carbonate, Ca-phosphate, phyllosilicates, pyroxene, spinels, Mg and Ca sulfate, and feldspar (Hurowitz et al., 2023). Jezero carbonate is more iron- and magnesium-rich compared to the Amargosa as a result of its olivine- and pyroxene-dominated bedrock. This assemblage implies that the Amargosa sediments have been subject to harsh oxidation following deposition — just like fluvial basins on Mars — and do not lose all their organic carbon.

The organic carbon in the Amargosa catchment is produced at low rates, so it is perhaps preserved because the degradation of organics via microbial respiration occurs at an even

lower rate. Low rates of microbial respiration occur in Death Valley likely due to a combination of low organic carbon stimulus, anoxic environment in a saturated subsurface, and mineral protection. The OC abundance might be so low that it cannot support the microbial density needed to be able to degrade it (Schuber et al., 2009; Douglas, 2004). Lower terrestrial organic input into a river significantly lowers the flux of ecosystem respiration that occurs (Battin et al., 2023). Subsurface microbial communities in Death Valley are highly dependent on TOC availability to sustain themselves (Merino et al., 2022). The OC is also likely mineral protected, either inside clay nanolayers or adsorption to clay and Fe/Al oxyhdryoxide reactive sites, such that it is shielded from reaction with pore fluids (Kleber et al., 2021; Salmon et al., 2000; Sarkar et al., 2018; Kaiser et al., 2000). This is similar to South Pacific Gyre, where low abundances of OC (<0.1%) persist for 24 million years in oxic, oligotrophic sediment by mineral protection (Estes et al., 2019). Most importantly, the extremely low elevation of Death Valley ensures that the Amargosa floodplain is nearly always fully saturated. Anoxia of the pore water combined with high evaporation rates creates inhospitable brines that do not support significant rates of microbial respiration. This offers a substantial layer of protection to the organic matter.

This study reveals that organic carbon can be preserved over decadal to millennial timescales in a harsh, oxidizing Mars-like environment. It is difficult to predict how preservation carries over longer timescales, especially the billion year timescales of Mars outcrops. However, the environmental factors that protect organic carbon in the Amargosa River also existed on Mars. There is significant evidence for long-standing groundwater in the fluvio-lacustrine sediments of Gale Crater (Thorpe et al., 2022; Schwenzer et al., 2016; Siebach and Grotzinger, 2014; Thomas et al., 2019) and global crustal hydration (Scheller et al., 2021) such that fluvial sediments on Mars likely experienced pore saturation from groundwater for a sustained period. A lack of evidence of any microbial activity thus far on Mars precludes loss of organic matter through respiration, as seen on a less extreme level in the Amargosa River. Significant mineral protection by clay minerals and iron oxides in the fluvio-deltaic mineral assemblages at Gale and Jezero Crater offers the same protection to organic matter on Mars as in the Amargosa river. Furthermore, Mars has been significantly colder and dryer following ancient fluvial activity, which may have enhanced preservation of organic carbon into the modern.

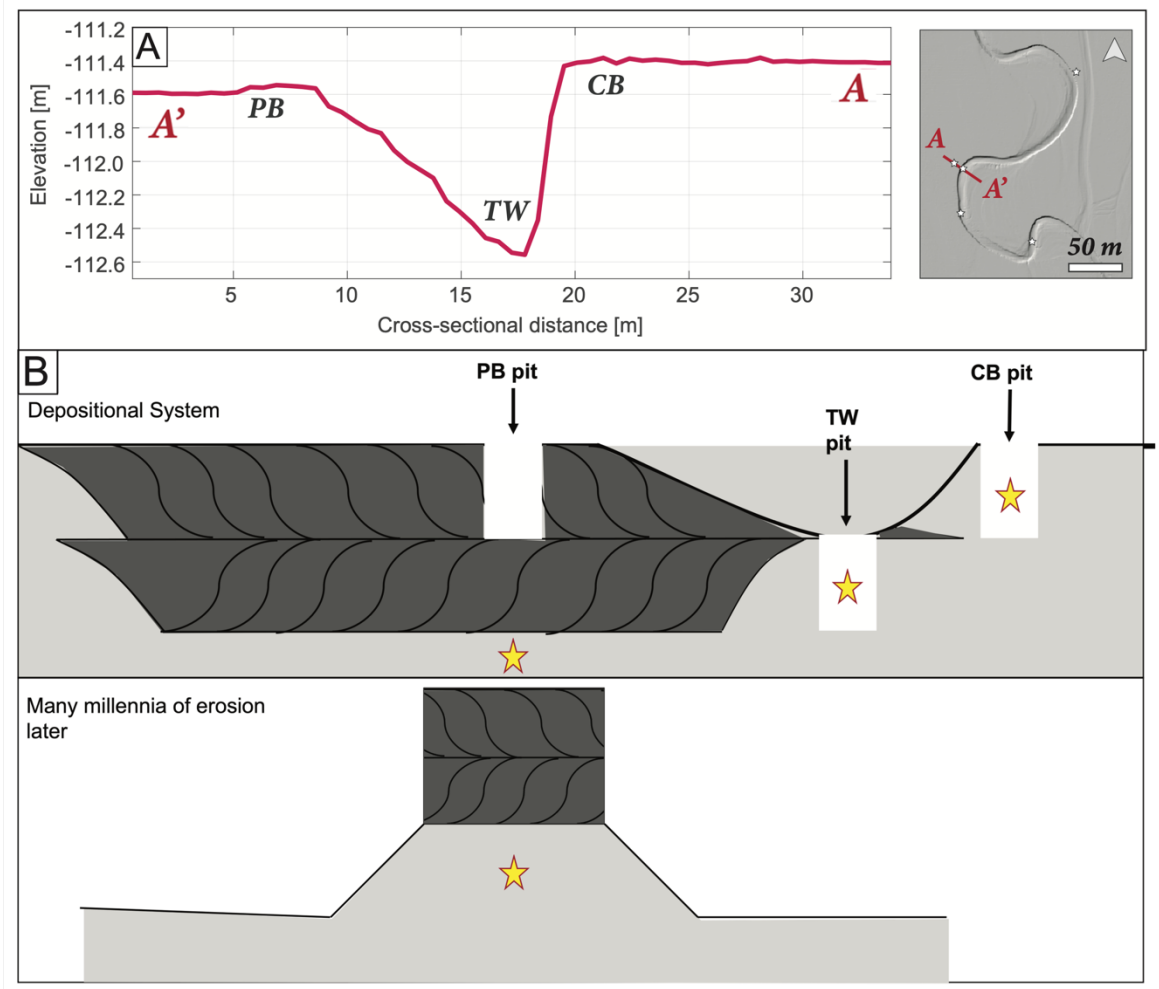

Figure 3.7. Diagram of river deposition and preservation. A) Hillshade LIDAR data of the Amargosa River and elevation profile of cross section, PB, TW, CB highlighted. B) Adapted from Hayden et al, (2019). Cross section of Amargosa River channel shown with PB, TW, and CB pits that we dug highlighted. Equivalent TOC-rich sediment highlighted with yellow stars. Post-erosional ridge caprock shown with equivalent TOC-rich sediment in yellow star.

For comparison to exhumed fluvial deposits on Mars (Dickson et al., 2021), it is useful to put the depositional facies of our study reach into the context of dryland alluvial river architecture (Hasson et al., 2023; Ielpi et al., 2020). The Amargosa River channel banks contain mostly fine-grained sediment. The channel meanders by eroding its cutbank and depositing sandier material on the point bar (Fig. 3.7A). As meanders grow and translate across the floodplain, they leave in their wake a buildup of deposits on the point-bar side in the form of channel-scale cross-bedding (called lateral accretion sets) (Fig. 3.7B; Hayden et al., 2019; Hayden and Lamb, 2020). Thus, former point bar deposits become amalgamated to form part of the floodplain. The floodplain can also be built by overbank flows during flooding which bring finer silt and clay to drape the floodplain surface.

Overtime, these overbank flows can build up the muddy portion of the floodplain. Death Valley is a net-depositional environment, such that sediment aggradation outpaces channel migration and generates isolated sand bodies in a matrix of silt and mud (Douglas, 2023; Jerolmack and Mohrig, 2007), matching the stratigraphic architecture shown in Figure 3.7. Badwater Basin cores also consist of ~1 m thick sandy deposits suspended in mud (Hooke, 1972), further supporting the architecture in Figure 3.7.

Point bars deposits are typically made up of coarser sediment than the rest of the deposits and are therefore the most likely to be preserved as fluvial ridges due to millennia of differential erosion with finer grained floodplain beneath them (Fig. 3.7C; Hayden et al., 2019). Although the Amargosa river is an active channel, not a fluvial ridge, we investigated and sampled each of the same depositional facies that might be expected within fluvial ridges on Mars (Hayden et al., 2019; Hayden and Lamb, 2020). The highest %TOC regions, which are equivalent stratigraphically, though dug in different areas for ease of access, have been marked with yellow stars (Fig. 3.7). The formation left behind will have vertical stacking and crosscutting of ridge-capping sandstone bodies. The ridges are the remnants of carbon-depleted point bars and have a unique identifiable structure: channel-scale, amalgamated lateral accretion sets of sandstone or possibly pebble conglomerate caprock. The ridge caprocks in turn are potentially overlying carbon rich, floodplain sourced, material. These could contain decimeter scale mudstone beds (the remnants of the thalweg pits we dug into), with possibly coarser grained thin beds during major floods. It is important to note that the underlying mudstone is only preserved when the caprock of sandstone is thick enough and well cemented enough to survive erosion and protect the underlying mudstone (Hayden et al., 2019). Access to the preserved organic carbon in the sandstone protected mudstone (yellow star locations) is what all Mars rover missions, future and present, should attempt to sample.

3.7 Conclusions

Prior rubrics that have shaped our search for potential ancient organic on Mars emphasized searching for fine-grained material in deltas and lakes. However, terrestrial river deposits are critical hosts of carbon and should be included in the search for organic carbon on Mars. To help address the gap in understanding of where martian riverine organic carbon would be preserved in highest abundance, we sampled a breadth of fluvial landforms in the Amargosa River as a process analog to martian rivers. The river sediments are made up of iron and manganese oxides mixed with detrital and authigenic silicates and carbonate and sulfate salts. The oxidized mineral assemblages of the river samples were able to retain up to 0.37% TOC in silt-sized grains, which is low but comparable to river sediments globally. Our results suggest that ancient fluvial deposits on Mars may retain traces of organics present during deposition—particularly in finer-grained regions of the floodplain—offering concrete suggestions for future sampling targets by the Perseverance rover. Future rovers on Mars might attempt to sample fluvial floodplain deposits elsewhere on Mars that may be preferentially preserved at the bases of fluvial ridges.

Data Availability

All data collected in this study and Table S1 and S2 are available in the supporting information and on the Zenodo repository at https:// doi.org/10.5281/zenodo.10841213 (Kalucha et al., 2024).

References

Anderson D. E.,Wells S.G., (2003), Latest Pleistocene lake highstands in Death Valley, California. *Paleoenvironments and paleohydrology of the Mojave and southern Great Basin deserts.*

Anderson, D. E. (2005). Holocene fluvial geomorphology of the Amargosa River through Amargosa Canyon, California. *Earth-Science Reviews*, *73*(1-4), 291-307.

Arvidson, R. E., & Catalano, J. G. (2018). Martian habitability as inferred from landed mission observations. In From habitability to life on mars (pp. 77-126). Elsevier.

Azua-Bustos, A., Fairén, A.G., González-Silva, C. *et al.* Dark microbiome and extremely low organics in Atacama fossil delta unveil Mars life detection limits. *Nature Communication* 14, 808 (2023). https://doi.org/10.1038/s41467-023-36172-1

Battin, T.J., Lauerwald, R., Bernhardt, E.S. et al. River ecosystem metabolism and carbon biogeochemistry in a changing world. *Nature* 613, 449–459 (2023). https://doi.org/10.1038/s41586-022-05500-8

Belcher, W.R., Sweetkind, D.S., Hopkins, C.B., and Poff, M.E., 2019, Hydrogeology of Lower Amargosa Valley and groundwater discharge to the Amargosa Wild and Scenic River, Inyo and San Bernardino Counties, California, and adjacent areas in Nye and Clark Counties, Nevada: U.S. Geological Survey Scientific Investigations Report 2018–5151, 131 p., 1 pl., https://doi.org/10.3133/sir20185151.

Bigham, J.M., Fitzpatrick, R.W. and Schulze, D.G. (2002). Iron Oxides. In Soil Mineralogy with Environmental Applications (eds J.B. Dixon and D.G. Schulze). https://doi.org/10.2136/sssabookser7.c10

Baldridge, A. M. (2004). Mars remote-sensing analog studies in the Badwater Basin, Death Valley, California. *Journal of Geophysical Research*, *109*(E12), E12006. https://doi.org/10.1029/2004JE002315

Bianchi, T. S., Mitra, S., & McKee, B. A. (2002). Sources of terrestrially-derived organic carbon in lower Mississippi River and Louisiana shelf sediments: implications for differential sedimentation and transport at the coastal margin. *Marine Chemistry*, *77*(2–3), 211–223. https://doi.org/10.1016/S0304-4203(01)00088-3

Bianchi, T. S., Galler, J. J., & Allison, M. A. (2007). Hydrodynamic sorting and transport of terrestrially derived organic carbon in sediments of the Mississippi and Atchafalaya Rivers. *Estuarine, Coastal and Shelf Science*, *73*(1–2), 211–222. https://doi.org/10.1016/j.ecss.2007.01.004

Bland, P. (2000). Meteorite Accumulations on Mars. *Icarus*, *144*(1), 21–26. https://doi.org/10.1006/icar.1999.6253

Burdige, D. J. (2007). Preservation of organic matter in marine sediments: controls, mechanisms, and an imbalance in sediment organic carbon budgets?. *Chemical Reviews*, *107*(2), 467-485.

Cao, Q., Wang, H., Zhang, Y., Lal, R., Wang, R., Ge, X., & Liu, J. (2017). Factors affecting distribution patterns of organic carbon in sediments at regional and national scales in China. *Scientific Reports*, *7*(1), 5497. https://doi.org/10.1038/s41598-017-06035-z

Court, R. W., & Sephton, M. A. (2014). New estimates of the production of volatile gases from ablating carbonaceous micrometeoroids at Earth and Mars during an E-belt-type Late Heavy Bombardment. *Geochimica et Cosmochimica Acta*, *145*, 175-205.

Craft, C. B., Broome, S. W., Seneca, E. D., & Showers, W. J. (1988). Estimating sources of soil organic matter in natural and transplanted estuarine marshes using stable isotopes of carbon and nitrogen. *Estuarine, Coastal and Shelf Science*, *26*(6), 633–641. https://doi.org/10.1016/0272-7714(88)90039-X

Dan, S. F., Liu, S.-M., Yang, B., Udoh, E. C., Umoh, U., & Ewa-Oboho, I. (2019). Geochemical discrimination of bulk organic matter in surface sediments of the Cross River estuary system and adjacent shelf, South East Nigeria (West Africa). *Science of The Total Environment*, *678*, 351–368. https://doi.org/10.1016/j.scitotenv.2019.04.422

Dickson, J. L., Lamb, M. P., Williams, R. M. E., Hayden, A. T., & Fischer, W. W. (2021). The global distribution of depositional rivers on early Mars. *Geology*, *49*(5), 504–509. https://doi.org/10.1130/G48457.1

Douglas, M. M., Lingappa, U. F., Lamb, M. P., Rowland, J. C., West, A. J., Li, G., et al. (2021). Impact of River Channel Lateral Migration on Microbial Communities across a Discontinuous Permafrost Floodplain. *Applied and Environmental Microbiology*, *87*(20), e01339-21. https://doi.org/10.1128/AEM.01339-21

Douglas, M. M., Li, G. K., Fischer, W. W., Rowland, J. C., Kemeny, P. C., West, A. J., et al. (2022). Organic carbon burial by river meandering partially offsets bank erosion carbon fluxes in a discontinuous permafrost floodplain. *Earth Surface Dynamics*, *10*(3), 421–435. https://doi.org/10.5194/esurf-10-421-2022

Douglas, Madison M. (2023) Mechanics of River Erosion and its Effects on Floodplain Biogeochemistry. Dissertation (Ph.D.), California Institute of Technology. doi:10.7907/rwmn-hq80.

Douglas, S. (2004). Microbial biosignatures in evaporite deposits: evidence from Death Valley, California. *Planetary and Space Science,* 52(1-3), 223-227.

Driscoll, A. W., Bitter, N. Q., Sandquist, D. R., & Ehleringer, J. R. (2020). Multidecadal records of intrinsic water-use efficiency in the desert shrub *Encelia farinosa* reveal strong responses to climate change. *Proceedings of the National Academy of Sciences*, *117*(31), 18161–18168. https://doi.org/10.1073/pnas.2008345117

Eglinton, T. I., Galy, V. V., Hemingway, J. D., Feng, X., Bao, H., Blattmann, T. M., ... & Zhao, M. (2021). *Proceedings of the National Academy of Sciences*, *118*(8), e2011585118.

Eigenbrode, J. L. et al., Organic matter preserved in 3-billion-year-old mudstones at Gale crater, Mars. *Science* **360**, 1096-1101(2018). DOI:10.1126/science.aas9185

Estes, E.R., Pockalny, R., D'Hondt, S. *et al.* Persistent organic matter in oxic subseafloor sediment. *Nature Geoscience* 12, 126–131 (2019). https://doi.org/10.1038/s41561-018-0291-5

Farley, K. A., Stack, K. M., Shuster, D. L., Horgan, B. H. N., Hurowitz, J. A., Tarnas, J. D., et al. (2022). Aqueously altered igneous rocks sampled on the floor of Jezero crater, Mars. *Science*, *377*(6614), eabo2196. https://doi.org/10.1126/science.abo2196

Fernandes, D., Wu, Y., Shirodkar, P. V., Pradhan, U. K., Zhang, J., & Limbu, S. M. (2020). Sources and preservation dynamics of organic matter in surface sediments of Narmada

River, India – Illustrated by amino acids. *Journal of Marine Systems*, *201*, 103239. https://doi.org/10.1016/j.jmarsys.2019.103239

Frantseva, K., Mueller, M., ten Kate, I. L., van der Tak, F. F. S., & Greenstreet, S. (2018). Delivery of organics to Mars through asteroid and comet impacts. *Icarus*, *309*, 125–133. https://doi.org/10.1016/j.icarus.2018.03.006

Freissinet, C., Glavin, D. P., Mahaffy, P. R., Miller, K. E., Eigenbrode, J. L., Summons, R. E., ... & MSL Science Team. (2015). Organic molecules in the sheepbed mudstone, gale crater, mars. *Journal of Geophysical Research: Planets*, *120*(3), 495-514.

Galy, V., Bouchez, J., & France-Lanord, C. (2007). Determination of total organic carbon content and δ13C in carbonate-rich detrital sediments. *Geostandards and Geoanalytical Research,* 31(3), 199-207.

Galy, V., France-Lanord, C., Beyssac, O., Faure, P., Kudrass, H., & Palhol, F. (2007). Efficient organic carbon burial in the Bengal fan sustained by the Himalayan erosional system. *Nature*, *450*(7168), 407–410. https://doi.org/10.1038/nature06273

Galy, V., Beyssac, O., France-Lanord, C., & Eglinton, T. (2008). Recycling of graphite during Himalayan erosion: A geological stabilization of carbon in the crust. *Science*, *322*(5903), 943-945.

Galy, V., Peucker-Ehrenbrink, B., & Eglinton, T. (2015). Global carbon export from the terrestrial biosphere controlled by erosion. *Nature*, *521*(7551), 204–207. https://doi.org/10.1038/nature14400

Gislason, S. R., Oelkers, E. H., & Snorrason, Á. (2006). Role of river-suspended material in the global carbon cycle. *Geology*, *34*(1), 49. https://doi.org/10.1130/G22045.1

Golombek, M. P., Phillips, R. J., Watters, T. R., & Schultz, R. A. (2010). Mars tectonics. *Planetary Tectonics*, *11*, 183-232.

Grant, K., Hilton, R. G., & Galy, V. (2023). Global patterns of radiocarbon depletion in subsoil linked to rock-derived organic carbon. *Geochemical Perspectives Letters*, 25.

Grotzinger, J. P., Gupta, S., Malin, M. C., Rubin, D. M., Schieber, J., Siebach, K., ... & Wilson, S. A. (2015). Deposition, exhumation, and paleoclimate of an ancient lake deposit, Gale crater, Mars. *Science*, *350*(6257), aac7575.

Hartnett, H., Keil, R., Hedges, J. *et al.* Influence of oxygen exposure time on organic carbon preservation in continental margin sediments. *Nature* 391, 572–575 (1998). https://doi.org/10.1038/35351

Hasson, M., Marvin, M. C., Gunn, A., Ielpi, A., & Lapôtre, M. G. (2023). A depositional model for meandering rivers without land plants. *Sedimentology*, 70(7), 2272-2301.

Hayden, A. T., Lamb, M. P., Fischer, W. W., Ewing, R. C., McElroy, B. J., & Williams, R. M. E. (2019). Formation of sinuous ridges by inversion of river-channel belts in Utah, USA, with implications for Mars. *Icarus*, *332*, 92–110. https://doi.org/10.1016/j.icarus.2019.04.019

Hayden, A.T. and Lamb, M.P., 2020, Fluvial Sinuous Ridges of the Morrison Formation, USA: Meandering, Scarp Retreat, and Implications for Mars. Journal of Geophysical Research: Planets, 125, e2020JE006470. doi: 10.1029/2020JE006470.Hemingway, J.D., Rothman, D.H., Grant, K.E. *et al.* Mineral protection regulates long-term global preservation of natural organic carbon. *Nature* 570, 228–231 (2019). https://doi.org/10.1038/s41586-019-1280-6

Hilton, R. G., Galy, V., Gaillardet, J., Dellinger, M., Bryant, C., O'Regan, M., et al. (2015). Erosion of organic carbon in the Arctic as a geological carbon dioxide sink. *Nature*, *524*(7563), 84–87. https://doi.org/10.1038/nature14653

Horgan, B. H. N., Johnson, J. R., Fraeman, A. A., Rice, M. S., Seeger, C., Bell, J. F., et al. (2020). Diagenesis of Vera Rubin Ridge, Gale Crater, Mars, From Mastcam Multispectral Images. *Journal of Geophysical Research: Planets*, *125*(11). https://doi.org/10.1029/2019JE006322

House, C. H., Wong, G. M., Webster, C. R., Flesch, G. J., Franz, H. B., Stern, J. C., ... & Mahaffy, P. R. (2022). Depleted carbon isotope compositions observed at Gale crater, Mars. *Proceedings of the National Academy of Sciences*, *119*(4), e2115651119.

Ielpi, A. (2019a). Morphodynamics of meandering streams devoid of plant life: Amargosa River, Death Valley, California. *GSA Bulletin*, *131*(5–6), 782–802. https://doi.org/10.1130/B31960.1

Hurowitz, J. A., Tice, M. M., Allwood, A. C., Cable, M. L., Bosak, T., Broz, A., ... & Yanchilina, A. (2023, March). The Petrogenetic History of the Jezero Crater Delta Front From Microscale Observations By the Mars 2020 PIXL Instrument. In *54th Lunar and Planetary Science Conference* (Vol. 54).

Ielpi, A. (2019). Morphodynamics of meandering streams devoid of plant life: Amargosa River, Death Valley, California. *GSA Bulletin*, *131*(5–6), 782–802. https://doi.org/10.1130/B31960.1

Ielpi, A., & Lapôtre, M. G. A. (2020). A tenfold slowdown in river meander migration driven by plant life. *Nature Geoscience*, *13*(1), 82–86. https://doi.org/10.1038/s41561-019-0491-7

Ielpi, A., Lapôtre, M. G. A., Finotello, A., Ghinassi, M., & D'Alpaos, A. (2020). Channel mobility drives a diverse stratigraphic architecture in the dryland Mojave River (California, USA). *Earth Surface Processes and Landforms*, *45*(8), 1717–1731. https://doi.org/10.1002/esp.4841

Kaiser, K., & Guggenberger, G. (2000). The role of DOM sorption to mineral surfaces in the preservation of organic matter in soils. *Organic Geochemistry*, *31*(7–8), 711–725. https://doi.org/10.1016/S0146-6380(00)00046-2

Kalucha, H., Douglas, M., Lamb, M., Ke, Y., & Fischer, W. (2024). Organic carbon in Amargosa River bank sediment [Data set]. Zenodo. https://doi.org/10.5281/zenodo.10841213

Kaufman, A. J., Corsetti, F. A., & Varni, M. A. (2007). The effect of rising atmospheric oxygen on carbon and sulfur isotope anomalies in the Neoproterozoic Johnnie Formation, Death Valley, USA. *Chemical Geology*, 237(1-2), 47-63.

Ke, Y., Calmels, D., Bouchez, J., & Quantin, C. (2022). MOdern River archivEs of Particulate Organic Carbon: MOREPOC. *Earth System Science Data*, *14*(10), 4743–4755. https://doi.org/10.5194/essd-14-4743-2022

Kirkels, F. M. S. A., Zwart, H. M., Usman, M. O., Hou, S., Ponton, C., Giosan, L., et al. (2022). From soil to sea: sources and transport of organic carbon traced by tetraether lipids in the monsoonal Godavari River, India. *Biogeosciences*, *19*(17), 3979–4010. https://doi.org/10.5194/bg-19-3979-2022

Kleber, M., Bourg, I. C., Coward, E. K., Hansel, C. M., Myneni, S. C. B., & Nunan, N. (2021). Dynamic interactions at the mineral–organic matter interface. *Nature Reviews Earth & Environment*, *2*(6), 402–421. https://doi.org/10.1038/s43017-021-00162-y

Ku, T.-L., Luo, S., Lowenstein, T. K., Li, J., & Spencer, R. J. (1998). U-Series Chronology of Lacustrine Deposits in Death Valley, California. *Quaternary Research*, *50*(3), 261–275. https://doi.org/10.1006/qres.1998.1995

Lalonde, K., Mucci, A., Ouellet, A., & Gélinas, Y. (2012). Preservation of organic matter in sediments promoted by iron. *Nature*, *483*(7388), 198-200.

Li, J., Lowenstein, T. K., Brown, C. B., Ku, T.-L., & Luo, S. (1996). A 100 ka record of water tables and paleoclimates from salt cores, Death Valley, California. *Palaeogeography, Palaeoclimatology, Palaeoecology*, *123*(1–4), 179–203. https://doi.org/10.1016/0031-0182(95)00123-9

Li, Z., Peterse, F., Wu, Y., Bao, H., Eglinton, T. I., & Zhang, J. (2015). Sources of organic matter in Changjiang (Yangtze River) bed sediments: Preliminary insights from organic geochemical proxies. *Organic Geochemistry*, *85*, 11–21. https://doi.org/10.1016/j.orggeochem.2015.04.006

Lin, B., Liu, Z., Eglinton, T. I., Kandasamy, S., Blattmann, T. M., Haghipour, N., & de Lange, G. J. (2019). Perspectives on provenance and alteration of suspended and sedimentary organic matter in the subtropical Pearl River system, South China. *Geochimica et Cosmochimica Acta*, *259*, 270–287. https://doi.org/10.1016/j.gca.2019.06.018

Lin, B., Liu, Z., Eglinton, T. I., Blattmann, T. M., Kandasamy, S., Haghipour, N., & Siringan, F. P. (2021). Organic Matter Compositions and Loadings in River Sediments From Humid Tropical Volcanic Luzon Island of the Philippines. *Journal of Geophysical Research: Biogeosciences*, *126*(7). https://doi.org/10.1029/2020JG006192

Lininger, K. B., Wohl, E., & Rose, J. R. (2018). Geomorphic Controls on Floodplain Soil Organic Carbon in the Yukon Flats, Interior Alaska, From Reach to River Basin Scales. *Water Resources Research*, *54*(3), 1934–1951. https://doi.org/10.1002/2017WR022042

Liu, S., Kuhn, C., Amatulli, G., Aho, K., Butman, D. E., Allen, G. H., et al. (2022). The importance of hydrology in routing terrestrial carbon to the atmosphere via global streams and rivers. *Proceedings of the National Academy of Sciences*, *119*(11), e2106322119. https://doi.org/10.1073/pnas.2106322119

Loh, P. S., Chen, C.-T. A., Lou, J.-Y., Anshari, G. Z., Chen, H.-Y., & Wang, J.-T. (2012). Comparing Lignin-Derived Phenols, $\delta^{13}C$ Values, OC/N Ratio and 14C Age Between Sediments in the Kaoping (Taiwan) and the Kapuas (Kalimantan, Indonesia) Rivers. *Aquatic Geochemistry*, *18*(2), 141–158. https://doi.org/10.1007/s10498-011-9153-0

Lowenstein, T. K., Li, J., Brown, C., Roberts, S. M., Ku, T.-L., Luo, S., & Yang, W. (1999). 200 k.y. paleoclimate record from Death Valley salt core. *Geology*, *27*(1), 3. https://doi.org/10.1130/0091-7613(1999)027<0003:KYPRFD>2.3.CO;2

Mbaye, M. L., Gaye, A. T., Spitzy, A., Dähnke, K., Afouda, A., & Gaye, B. (2016). Seasonal and spatial variation in suspended matter, organic carbon, nitrogen, and nutrient concentrations of the Senegal River in West Africa. *Limnologica*, *57*, 1–13. https://doi.org/10.1016/j.limno.2015.12.003

McCollom, T. M. (2013). Miller-Urey and beyond: what have we learned about prebiotic organic synthesis reactions in the past 60 years?. *Annual Review of Earth and Planetary Sciences*, *41*, 207-229.

Merino, N., Jackson, T. R., Campbell, J. H., Kersting, A. B., Sackett, J., Fisher, J. C., ... & Moser, D. P. (2022). Subsurface microbial communities as a tool for characterizing regional-scale groundwater flow. *Science of The Total Environment*, *842*, 156768.

Millan, M., Williams, A. J., McAdam, A. C., Eigenbrode, J. L., Steele, A., Freissinet, C., et al. (2022). Sedimentary organics in Glen Torridon, Gale Crater, Mars: Results from the SAM instrument suite and supporting laboratory analyses. *Journal of Geophysical Research: Planets*, 127, e2021JE007107. https://doi.org/10.1029/2021JE007107

Minor, S. A., Sawyer, D. A., Wahl, R. R., Frizzell Jr, V. A., Schilling, S. P., Warren, R. G., ... & Cole, J. C. (1993). *Preliminary Geologic Map of the Pahute Mesa 30'x 60'Quadrangle, Nevada*. US Geological Survey.

Ouyang, Y., Zhang, J. E., & Ou, L.-T. (2006). Temporal and Spatial Distributions of Sediment Total Organic Carbon in an Estuary River. *Journal of Environmental Quality*, *35*(1), 93–100. https://doi.org/10.2134/jeq2005.0221

Pradhan, U. K., Wu, Y., Shirodkar, P. V., Kumar, H. S., & Zhang, J. (2020). Connecting land use−land cover and precipitation with organic matter biogeochemistry in a tropical river–estuary system of western peninsular India. *Journal of Environmental Management*, *271*, 110993. https://doi.org/10.1016/j.jenvman.2020.110993

Rampe, E. B., Blake, D. F., Bristow, T. F., Ming, D. W., Vaniman, D. T., Morris, R. V., et al. (2020). Mineralogy and geochemistry of sedimentary rocks and eolian sediments in Gale crater, Mars: A review after six Earth years of exploration with Curiosity. *Geochemistry*, *80*(2), 125605. https://doi.org/10.1016/j.chemer.2020.125605

Reheis, M. C., Caskey, J., Bright, J., Paces, J. B., Mahan, S., & Wan, E. (2020). Pleistocene lakes and paleohydrologic environments of the Tecopa basin, California: Constraints on the drainage integration of the Amargosa River. *Bulletin*, *132*(7-8), 1537-1565.

Repasch, M., Scheingross, J. S., Hovius, N., Lupker, M., Wittmann, H., Haghipour, N., ... & Sachse, D. (2021). Fluvial organic carbon cycling regulated by sediment transit time and mineral protection. *Nature Geoscience*, *14*(11), 842-848.

Repasch, M., Scheingross, J. S., Hovius, N., Vieth-Hillebrand, A., Mueller, C. W., Höschen, C., et al. (2022). River Organic Carbon Fluxes Modulated by Hydrodynamic Sorting of Particulate Organic Matter. *Geophysical Research Letters*, *49*(3). https://doi.org/10.1029/2021GL096343

Resplandy, L., Keeling, R. F., Rödenbeck, C., Stephens, B. B., Khatiwala, S., Rodgers, K. B., et al. (2018). Revision of global carbon fluxes based on a reassessment of oceanic and riverine carbon transport. *Nature Geoscience*, *11*(7), 504–509. https://doi.org/10.1038/s41561-018-0151-3

Rothman, D. H. (2024). Slow closure of Earth's carbon cycle. *Proceedings of the National Academy of Sciences*, 121(4), e2310998121.

Running, S., Mu, Q., Zhao, M. (2015). *MOD17A3H MODIS/Terra Net Primary Production Yearly L4 Global 500m SIN Grid V006* [Data set]. NASA EOSDIS Land Processes Distributed Active Archive Center. Accessed 2023-10-25 from https://doi.org/10.5067/MODIS/MOD17A3H.006

Salmon, V., Derenne, S., Lallier-Vergès, E., Largeau, C., & Beaudoin, B. (2000). Protection of organic matter by mineral matrix in a Cenomanian black shale. *Organic Geochemistry*, *31*(5), 463–474. https://doi.org/10.1016/S0146-6380(00)00013-9

Sarkar, B. (n.d.). Chapter 3 - Clay Minerals—Organic Matter Interactions in Relation to Carbon Stabilization in Soils, 16.

Sasselov D. D., et al.,The origin of life as a planetary phenomenon. *Science Advances.* **6**, eaax3419 (2020). DOI:10.1126/sciadv.aax3419

Scheingross, J. S., Repasch, M. N., Hovius, N., Sachse, D., Lupker, M., Fuchs, M., et al. (2021). The fate of fluvially-deposited organic carbon during transient floodplain storage. *Earth and Planetary Science Letters*, *561*, 116822. https://doi.org/10.1016/j.epsl.2021.116822

Scherf, M., & Lammer, H. (2021). Did Mars Possess a Dense Atmosphere During the First ~400 Million Years? *Space Science Reviews*, *217*(1), 2. https://doi.org/10.1007/s11214-020-00779-3

Scientific Investigations Report. (2019). (Scientific Investigations Report).

Schubert, B. A., Lowenstein, T. K., & Timofeeff, M. N. (2009). Microscopic identification of prokaryotes in modern and ancient halite, Saline Valley and Death Valley, California. *Astrobiology,* 9(5), 467-482.

Schwenzer, S. P., Bridges, J. C., Wiens, R. C., Conrad, P. G., Kelley, S. P., Leveille, R., ... & Meslin, P. Y. (2016). Fluids during diagenesis and sulfate vein formation in sediments at Gale crater, Mars. *Meteoritics & Planetary Science*, *51*(11), 2175-2202.

Siebach, K. L., & Grotzinger, J. P. (2014). Volumetric estimates of ancient water on Mount Sharp based on boxwork deposits, Gale Crater, Mars. *Journal of Geophysical Research: Planets*, *119*(1), 189-198.

Shi, Z., Allison, S. D., He, Y., Levine, P. A., Hoyt, A. M., Beem-Miller, J., ... & Randerson, J. T. (2020). The age distribution of global soil carbon inferred from radiocarbon measurements. *Nature Geoscience*, *13*(8), 555-559.

Skorbilowicz, M., & Skorbilowicz, E. (2008). Quality of well waters in context of the content of nitrogen and phosphorus compounds in the upper Narew river valley. *Journal of Elementology*, *13*(4), 625-635.

Smith, S. D., & Osmond, C. B. (n.d.). Stem photosynthesis in a desert ephemeral, *Eriogonum inflatum*, 9.

Soulet, G., Hilton, R. G., Garnett, M. H., Roylands, T., Klotz, S., Croissant, T., ... & Le Bouteiller, C. (2021). Temperature control on CO2 emissions from the weathering of sedimentary rocks. *Nature Geoscience*, 14(9), 665-671.

Starkey, H. C., & Blackmon, P. D. (1979). *Clay mineralogy of Pleistocene Lake Tecopa, Inyo County, California* (No. 1061). US Govt. Print.

Stecko, J. R. P., & Bendell-Young, L. I. (2000). Contrasting the geochemistry of suspended particulate matter and deposited sediments within an estuary. *Applied Geochemistry*, *15*(6), 753–775. https://doi.org/10.1016/S0883-2927(99)00090-6

Steele A., et al., Organic synthesis associated with serpentinization and carbonation on early Mars. *Science* 375, 172-177(2022). DOI:10.1126/science.abg7905

Stern, J. C., Malespin, C. A., Eigenbrode, J. L., Webster, C. R., Flesch, G., Franz, H. B., ... & Mahaffy, P. R. (2022). Organic carbon concentrations in 3.5-billion-year-old

lacustrine mudstones of Mars. *Proceedings of the National Academy of Sciences*, *119*(27), e2201139119.

Sutherland, R. A. (n.d.). Loss-on-ignition estimates of organic matter and relationships to organic carbon in fluvial bed sediments, 15.

Sutter, B., Mcadam, A. C., Mahaffy, P. R., Ming, D. W., Edgett, K. S., Rampe, E. B., ... & Yen, A. S. (2017). Evolved gas analyses of sedimentary rocks and eolian sediment in Gale Crater, Mars: Results of the Curiosity rover's sample analysis at Mars instrument from Yellowknife Bay to the Namib Dune. *Journal of Geophysical Research: Planets*, *122*(12), 2574-2609.

Szopa, C., Freissinet, C., Glavin, D. P., Millan, M., Buch, A., Franz, H. B., ... & Cabane, M. (2020). First detections of dichlorobenzene isomers and trichloromethylpropane from organic matter indigenous to Mars mudstone in Gale Crater, Mars: results from the Sample Analysis at Mars instrument onboard the Curiosity rover. *Astrobiology*, *20*(2), 292-306.

Thomas, N. H., Ehlmann, B. L., Meslin, P. Y., Rapin, W., Anderson, D. E., Rivera-Hernández, F., ... & Wiens, R. C. (2019). Mars Science Laboratory observations of chloride salts in Gale crater, Mars. *Geophysical Research Letters*, *46*(19), 10754-10763.

Thorpe, M. T., Bristow, T. F., Rampe, E. B., Tosca, N. J., Grotzinger, J. P., Bennett, K. A., ... & Fedo, C. M. (2022). Mars Science Laboratory CheMin data from the Glen Torridon region and the significance of lake-groundwater interactions in interpreting mineralogy and sedimentary history. *Journal of Geophysical Research: Planets*, *127*(11), e2021JE007099.

Topping, D. J. (1993). Paleogeographic reconstruction of the Death Valley extended region: Evidence from Miocene large rock-avalanche deposits in the Amargosa Chaos Basin, California. Geological Society of America Bulletin, 105(9), 1190-1213.

Torres, M. A., Kemeny, P. C., Lamb, M. P., Cole, T. L., & Fischer, W. W. (2020). Long-Term Storage and Age-Biased Export of Fluvial Organic Carbon: Field Evidence From West Iceland. *Geochemistry, Geophysics, Geosystems*, *21*(4). https://doi.org/10.1029/2019GC008632

Unger, D., Gaye-Haake, B., Neumann, K., Catalina Gebhardt, A., & Ittekkot, V. (2005). Biogeochemistry of suspended and sedimentary material in the Ob and Yenisei rivers and Kara Sea: amino acids and amino sugars. *Continental Shelf Research*, *25*(4), 437–460. https://doi.org/10.1016/j.csr.2004.09.014

Wiens, R. C., Udry, A., Beyssac, O., Quantin-Nataf, C., Mangold, N., Cousin, A., et al. (2022). Compositionally and density stratified igneous terrain in Jezero crater, Mars. *Science Advances*, *8*(34), eabo3399. https://doi.org/10.1126/sciadv.abo3399

Williford, K. H., Farley, K. A., Stack, K. M., Allwood, A. C., Beaty, D., Beegle, L. W., ... & Wiens, R. C. (2018). The NASA Mars 2020 rover mission and the search for extraterrestrial life. In *From habitability to life on Mars* (pp. 275-308). Elsevier.

Wordsworth, R. D., Kerber, L., Pierrehumbert, R. T., Forget, F., & Head, J. W. (2015). Comparison of "warm and wet" and "cold and icy" scenarios for early Mars in a 3-D climate model: WARM AND WET VS. COLD AND ICY EARLY MARS. *Journal of Geophysical Research: Planets*, *120*(6), 1201–1219. https://doi.org/10.1002/2015JE004787

Wu, Y., Zhu, K., Zhang, J., Müller, M., Jiang, S., Mujahid, A., et al. (2019). Distribution and degradation of terrestrial organic matter in the sediments of peat-draining rivers, Sarawak, Malaysian Borneo. *Biogeosciences*, *16*(22), 4517–4533. https://doi.org/10.5194/bg-16-4517-2019

Zhang, S., Liang, C., & Xian, W. (2020). Spatial and temporal distributions of terrestrial and marine organic matter in the surface sediments of the Yangtze River estuary. *Continental Shelf Research*, *203*, 104158. https://doi.org/10.1016/j.csr.2020.104158

Zhu, C., Wang, Z.-H., Xue, B., Yu, P.-S., Pan, J.-M., Wagner, T., & Pancost, R. D. (2011). Characterizing the depositional settings for sedimentary organic matter distributions in the Lower Yangtze River-East China Sea Shelf System. *Estuarine, Coastal and Shelf Science*, *93*(3), 182–191. https://doi.org/10.1016/j.ecss.2010.08.001

Zondervan, J. R., Hilton, R. G., Dellinger, M., Clubb, F. J., Roylands, T., & Ogrič, M. (2023). Rock organic carbon oxidation CO2 release offsets silicate weathering sink. *Nature*, 623(7986), 329-333.

Chapter 4

PROBABLE CONCRETIONS OBSERVED IN THE SHENANDOAH FORMATION OF JEZERO CRATER, MARS AND COMPARISON WITH TERRESTRIAL ANALOGS

H. Kalucha[1], A. Broz[2], N. Randazzo[3], J. Aramendia[4], J.M. Madariaga[4], B. Garczynski[5], N. Lanza[6], L. Mandon[1], T. Fouchet[7], D. C. Catling[8], A.G. Fairén[9], L. Kivrak[10], P. J. Gasda[6], J. I. Núñez[11], E. Cloutis[12], K.P. Hand[13], J.W. Rice, Jr.[14], W. W. Fischer[1], S. Maurice[15], R.C. Wiens[16]

[1]California Institute of Technology

[2]University of Oregon

[3]University of Alberta

[4]University of Basque Country (UPV/EHU)

[5]Western Washington University

[6]Los Alamos National Laboratory

[7]Observatoire de Paris

[8]University of Washingston

[9] Centro de Astrobiologia, CSIC-INTA and Cornell University

[10]University of Florida

[11]Johns Hopkins University Applied Physics Laboratory

[12]University of Winnipeg

[13]Jet Propulsion Laboratory

[14]Arizona State University

[15]IRAP (CNRS, Univ. Toulouse, CNES)

[16]Purdue University

4.1 Abstract

The Mars 2020 *Perseverance* Rover imaged diagenetic textural features in four separate sedimentary units in its exploration of the 25-meter-thick Shenandoah formation at Jezero Crater, Mars, that we interpreted as probable concretions. These concretions were most abundant in the Hogwallow Flats member of the Shenandoah formation and were restricted to the light-toned, platy, sulfur-cemented bedrock at outcrop surfaces, whereas the finely laminated, darker toned, mottled and deformed strata lack concretions. The concretions also had a wide range of morphologies including concentric, oblate, urn, and spheroidal shaped forms that were not clustered, and ranged in size from ~1-16 mm with a median of 2.65 mm. The elemental composition of the concretions compared to the bedrock had greater abundance of magnesium and calcium salts, silicates, and possibly hematite. We compared these Jezero Crater concretions to the geochemistry of concretions from previously published studies and from two new terrestrial analog sites (Gallup Formation, New Mexico and Torrey Pines, California). In addition, we measured organic carbon content of three terrestrial sedimentary analogs of increasing age that contain concretions (Torrey Pines (Pleistocene), Gallup Formation (~89 Ma), and Moodies Group (~3.2 Ga)). All measured concretions contained significant concentrations of organic carbon with the maximum organic carbon content (~2 wt. % TOC) found in the Moodies Group concretions. Organic carbon abundances in terrestrial concretions was controlled more by the formation mechanism and relative timing of concretion development rather than deposit age. These findings suggested that concretions at Jezero Crater reflect local sites of enhanced biosignature preservation potential.

4.2 Plain Language Summary

The Perseverance Rover discovered concretions in its exploration of the rock packages at Jezero Crater, Mars and one of the sample return cores was collected from concretion-rich bedrock. Concretions are resistant cements in the rock that are found in many shapes (usually spherical or oblate) and range from millimeter to meter size scales on Earth; they can be formed through inorganic water-rock reactions or facilitated by microbial metabolisms. We documented the abundance, size, composition, and shape of the concretions to understand how these features were formed. We found that the concretions are mixtures of salts, clay minerals, and iron oxides. We compared these results to terrestrial concretions with similar mineral composition and measured the organic carbon in four terrestrial analogs. Comparisons with terrestrial concretions in this paper and the literature suggested that the concretion composition in Jezero Crater could have high organic preservation potential. Thus, the concretions in Jezero Crater may retain organic carbon and other biosignatures and might therefore be considered high priority samples of astrobiological interest out of the current sample suite for return to Earth.

4.3 Introduction

The Mars 2020 *Perseverance* Rover mission (detailed in Farley et al., 2020) landed in Jezero Crater to explore if ancient life ever existed on Mars. It builds on the work of previous missions that have so far established that ancient Mars was warmer and wetter than today, and once hosted significant bodies and flows of surface water at circumneutral pH with redox couples that would have been able to provide chemical energy of the kind that could be used for life (Williford et al., 2018; Grotzinger et al., 2015). The next step is to ascertain the presence of any potential biosignatures. Concretions are one commonly found sedimentary structure on Earth that often preserves biosignatures better than the surrounding rock (Selles-Martínez,1996; Fisher and Raiswell, 2000; Chan et al., 2022).

Perseverance rover discovered concretions in four separate stratigraphic units in its exploration of the 25-meter-thick Shenandoah formation at Jezero Crater, Mars. Justification of the term 'concretion' in this case is explained in detail below. The Shenandoah formation is part of a sedimentary fan on the western edge of Jezero Crater (Figure 4.1), deposited by an ancient fluvial system as estimated to be 3.5 + 0.1/-0.3 Gy old (Mangold et al., 2020). Near where the concretions occur, the deposits are heterolithic facies containing sandstone and siltstone that indicate deposition in a fluvio-deltaic setting (Stack et al., 2024). The concretions were located in the finer grained units (siltstone to fine sandstone) of the Shenandoah formation (Stack et al., 2024). Hogwallow Flats, Yori Pass, and White rocks (shown in Figure 4.1) are light-toned, platy, fractured rocks with rare planar lamination and have been interpreted as units of deposition in a distal fluvial floodplain (subaerial) or prodeltaic/lacustrine environment (subaqueous). The Devil's Tanyard member (shown in Figure 4.1) is slightly coarser with low angle cross-lamination and has been interpreted as fluvial sandstone (Stack et al., 2024). Notably, these units also share a common lithology consisting of sediment derived from basalt with variable admixtures of authigenic iron oxide, sulfate, and phyllosilicate phases (Benison et al. 2024; Mars 2020 Initial Reports Volume 2 (Samples 11-21)).

The focus of this work was to document the composition, abundance, and morphology of Jezero Crater concretions and compare and contrast them with observations of other concretion occurrences on Earth and Mars. An additional goal was to evaluate the biosignature preservation potential of sedimentary concretions at Jezero Crater by comparison with terrestrial examples. Three potential process analog sites (Torrey Pines, Gallup Sandstone, Moodies Group) were chosen because they host concretions of widely varying age and formed in environments that could have been present at Jezero Crater, including deltaic and/or fluvio-deltaic environments and rock packages that have experienced post-depositional acid-sulfate alteration (Stack et al., 2024; Benison et al., 2024). Analysis of their internal structure, mineralogy, organic carbon abundances, and timing of formation relative to the diagenetic history of the host rock generated insight on possible Jezero Crater concretion characteristics that were not accessible by rover instruments.

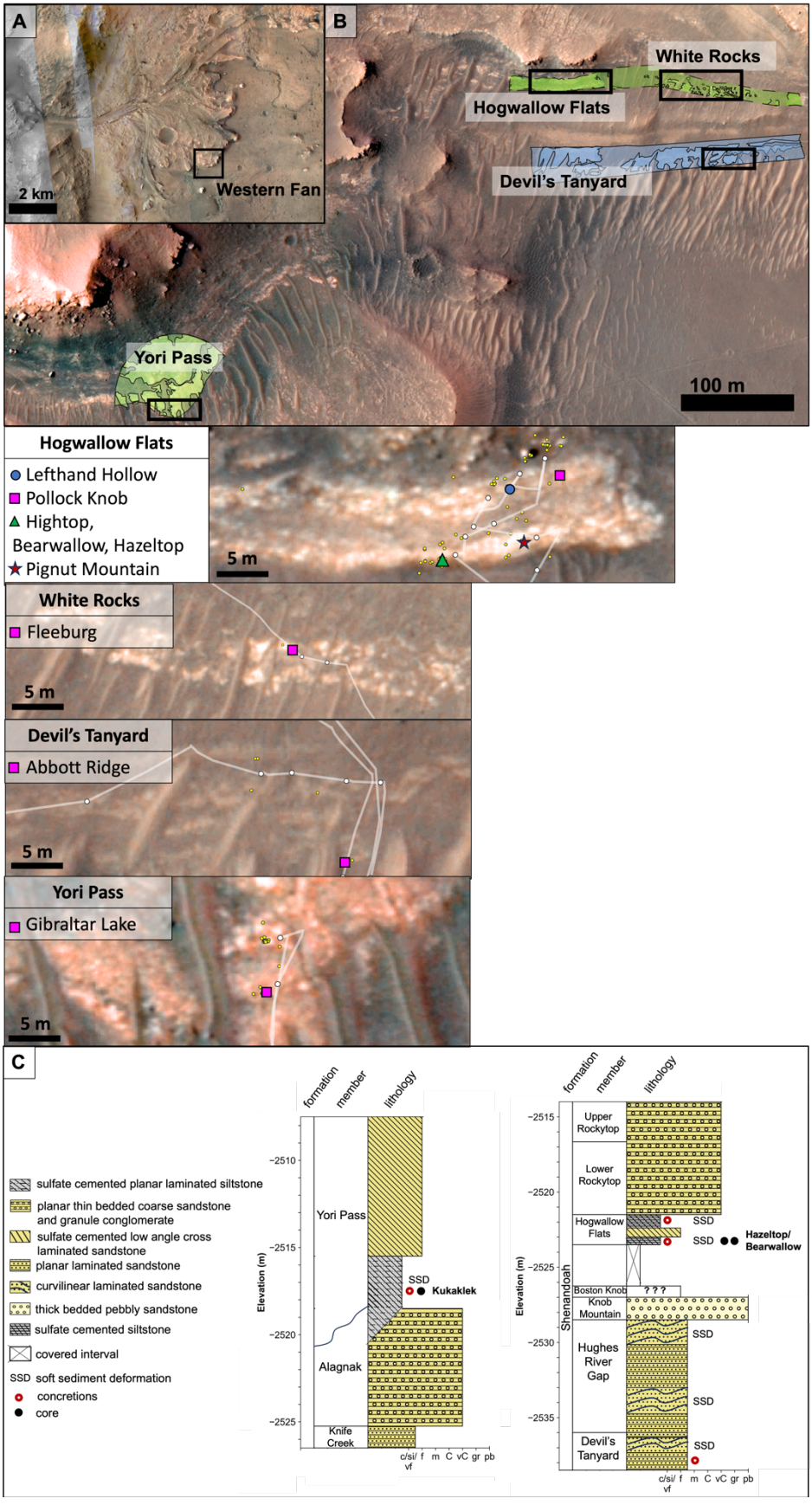
A
2 km
Western Fan
B
White Rocks
Hogwallow Flats
Devil's Tanyard
Yori Pass
100 m
Hogwallow Flats
Lefthand Hollow
Pollock Knob
Hightop,
Bearwallow, Hazeltop
Pignut Mountain
5 m
White Rocks
Fleeburg
5 m
Devil's Tanyard
Abbott Ridge
5 m
Yori Pass
Gibraltar Lake
5 m
C
sulfate cemented planar laminated siltstone
planar thin bedded coarse sandstone and granule conglomerate
sulfate cemented low angle cross laminated sandstone
planar laminated sandstone
curvilinear laminated sandstone
thick bedded pebbly sandstone
sulfate cemented siltstone
covered interval
SSD soft sediment deformation
concretions
core
formation
member
lithology
Elevation (m)
−2510
−2515
−2520
−2525
Yori Pass
Alagnak
Knife Creek
SSD
Kukaklek
c/si/ vf f m C vC gr pb
formation
member
lithology
Elevation (m)
−2515
−2520
−2525
−2530
−2535
Shenandoah
Upper Rockytop
Lower Rockytop
Hogwallow Flats
Boston Knob
Knob Mountain
Hughes River Gap
Devil's Tanyard
SSD
Hazeltop/ Bearwallow
???
c/si/ vf f m C vC gr pb

Figure 4.1. Context Map. A) Western portion of Jezero Crater, Mars, with the western sedimentary fan highlighted. B) Close up of units where concretions were identified along the Western fan. Green = Hogwallow Flats, White Rocks, Yori Pass members. Blue = Devil's Tanyard Member. Modified from a HiRISE image. Mapping credit: Larry Crumpler. Black rectangular inset of each stratigraphic unit shows target names and localities via symbols on map. White trace shows rover traverse. Hogwallow Flats inset: blue circle – Lefthand Hollow, pink square – Pollock Knob, green triangle – Hightop, Bearwallow, Hazeltop, red star – Pignut Mountain. White Rocks inset: pink square – Fleeburg. Devil's Tanyard inset: pink square – Abbott Ridge. Yori Pass inset: pink square – Gibraltar Lake. C) Stratigraphic columns of the Shenanodah formation including units with concretions. Modified from Stack et al. (2024).

4.4 Background

4.4.1 Terrestrial concretions

Concretions are cemented mineral masses formed during diagenesis (Potter-McIntyre et al., 2014). The terms "concretion" and "nodule" are used interchangeably in the literature. From terrestrial examples, both concretions and nodules can lack internal structure and have a composition very similar to the host rock composition (Raiswell and Fischer, 2000; Potter et al., 2011). As such, we have uniformly referred to both concretion and nodule features as concretions.

On Earth, along with some stromatolites and other microbially induced sedimentary structures, certain concretions are considered among the most ancient biomarkers, appearing as far back as 3.22 Ga in the rock record (Nabhan et al., 2016; Chan et al., 2019). They are often preferentially preserved because the mineral precipitation that generates them occludes porosity, and thus they have lower permeability and porosity than the surrounding bedrock, making them less reactive to post-depositional fluids and allowing them to be more resistant to compaction, erosion, and weathering (Seilacher, 2001). There is evidence that their formation is frequently related to subsurface microbial activity but can equally result from abiotic factors. On Earth, a few of the most prominent formation mechanisms are related to anaerobic microbial metabolisms, including microbial sulfate reduction, methanogenesis, or dissolution of existing minerals and reprecipitation (Smith et al., 2023 and references therein). Given that we have observed concretions on Mars in multiple locations, it then becomes useful to ascertain if Martian concretions developed from abiotic or biotic processes and evaluate prospects of them as valuable taphonomic windows that preserve potential biosigantures.

Concretions formed biotically occur from anaerobic microbial processes associated with organic diagenesis in sediments that promote mineral authigenesis (particularly carbonate salts) such as Mn and Fe oxide reduction, sulfate reduction, and methanogenesis (Raiswell, 1987; Berner, 1968). These concretions also tend to form diagenetically early in the top 10 meters of the subsurface prior to and during burial compaction. Abiotic reactions that form concretions tend to occur more slowly and thus much deeper in the subsurface–commonly after burial compaction and lithification (Marshall and Pirrie, 2013). Determining time of formation of a concretion with respect to compaction of the surrounding sediment is therefore valuable as it reveals if microbial processes or abiotic reactions were more likely to be dominant at the time of formation —though this timing is sometimes challenging to establish and there are several other factors to consider. Another potential means of assessing biogenicity leverages differences in the isotopic signatures of authigenic minerals that comprise the concretions. For example, concretions tied to fluxes of carbon and alkalinity during

anaerobic microbial processes that operate on sedimentary organic matter carry light and variable carbon isotopic signatures inherited by minerals in the concretions; and similar logic holds for sulfur-reducing metabolisms that generate light and variable sulfur isotopic signatures (Raiswell and Fischer, 2000; Fischer et al., 2014; Slotznick et al., 2016; Chan et al., 2006). These measurements were not possible with current rover instruments but would be testable with Mars Sample Return, and would help further assess the processes promoting concretion mineralization, including whether or not they included biology.

4.4.2 Concretions Observed Previously on Mars

Sedimentary concretions appear to be somewhat common in exposed strata in sedimentary basins on Mars as described below. They have been previously observed by landed missions on the surface of Mars: at Meridiani Planum, Gale crater and Jezero Crater (i.e., in every rover investigation site except for Gusev crater). Table 4.1 lists the summary of concretion characteristics.

4.4.2.1 Meridiani Planum

Meridiani Planum is a region where pre-rover orbital reconnaissance indicated the conspicuous presence of abundant crystalline hematite (Fe_2O_3), a mineral whose precursors usually form in water (Christensen et al., 2000). The MER-1 Opportunity rover found that the hematite signature seen from orbit was correlated to winnowed clusters of very small hematite-rich spherules, typically 4 to 6 mm in diameter and lacking internal structure, and embedded in Hesperian-aged outcrops, that the team dubbed “blueberries” (Squyres et al., 2004a). As the outcrops are eroded by wind, the hematite spherules, which due to their mineralization are more resistant to erosion, formed a lag deposit atop the regolith (McLennan et al., 2005). Hematite spherules or their broken fragments are prominent and ubiquitous on the lower part of the Burns formation exposed around the Eagle and Endurance craters, and represent leftovers of a large area of rock that has been deflated by wind. Individual spherules were too small to be analyzed by APXS and Mossbauer instruments (Squyres et al., 2004a), however, the miniature thermal emission spectrometer (Mini-TES) did not detect any silicates in the blueberries (Calvin et al., 2008), narrowing the possible hematite weight percentages of the blueberries to high values (Olsen, 2022). The blueberries were interpreted as early burial, diagenetic concretions because their spatial distribution is dispersed in the rock as opposed to concentrated along bedding planes—though they do not disturb the laminations around them—and cross-cutting relationships postdate them compared to earlier vug filling phases (Squyres et al., 2004b). Given these characteristics, the spherules formed in near isotropic permeability and largely static (diffusion dominated transport) fluid conditions; they likely replaced existing sulfate minerals and filled primary porosity (Squyres et al., 2004b). Several textural characteristics listed above and the occurrence of occasional doublets implied concretions in Meridiani rather than other interpretations such as concretionary lapilli or lava spherules (McClennan et al., 2005).

Later in the Opportunity traverse, in some of the rocks on the rim of Endeavour crater, a new type of spherule-shaped sedimentary structure was found dispersed across fine bedding in the Matijevic formation, a late Noachian lithologic unit, colloquially termed “newberries”. The “newberries” are smaller (typically up to 3 mm in diameter) than the blueberries, not iron-enriched, less oxidized, and

showed internal structure with concentric zoning (i.e., hard exteriors) (Arvidson et al., 2014; Farrand et al., 2014). They were interpreted as diagenetic features or accretionary lapilli (impact or volcanic). Both hypotheses invoked groundwater flow within Matijevic rocks. The newberries likely formed earlier than the blueberries, when the environment in Meridiani Planum was less oxidizing and the rocks were not yet dominated by hematite (Arvidson et al., 2014; Farrand et al., 2014)

A third type of concretion was also observed in Meridiani: hollowed blueberries. They are distributed both in regolith atop the Hesperian Burns formation and tightly embedded in bedrock on the highest reaches of the Noachian Matijevic Hill, vastly outnumbering the blueberries (Fairén et al., 2014). They have circular rims with hollow, bowl-like depressions, similar to those reported here below from Jezero Crater. Similar to the newberries, the hollowed blueberries displayed internal structure in the form of an differentially hard outer layer, pointing to a genetic relationship with the newberries characteristic of Matijevic Hill: the hollow center was likely created by the dissolution of a preexisting, more soluble mineral and/or a less well-cemented concretion interior. The mineralogy and formation history of the hollowed blueberries was not constrained.

4.4.2.2 Gale Crater

In Gale crater, solid concretions, hollowed concretions and filled concretions (all mostly spheroidal) were identified by the *Curiosity* rover and were locally abundant with patchy and clustered distributions in the Sheepbed mudstone (Grotzinger et al., 2014). Spheroidal concretions in Sheepbed mudstone were also harder and darker than the surrounding mudstone, and formed during early aqueous alteration of the mudstone by diagenetic pore fluids (Stack et al., 2014). This is because they were cross-cut by veins and fractures and were able to maintain their spherical shape despite compaction of the host rock over time. Compositional data indicated that the concretions and hollowed concretions in Sheepbed mudstone consisted of iron-bearing phases such as magnetite, akageneite, or clay minerals. The mean diameter of concretions in Sheepbed mudstone was 0.8 mm; hollowed concretions had a mean diameter of 1.35 mm, filled concretions had an average of 2.75 mm (Stack et al., 2014). Therefore, concretions in Sheepbed mudstone followed comparable size trends to the blueberries and newberries/hollowed blueberries in Meridiani.

Fe-rich voids and hollow spheroids (~1-23 cm) were also found in the Yellowknife Bay area. Their composition was, at least in one case, in contrast to the felsic host rock and hypothesized to be a result of reduced iron in minerals interacting with oxidizing groundwater and re-precipitating as a cemented rind (Wiens et al., 2017).

Higher up in the section, throughout 300 m of Murray formation stratigraphy and an additional 100 m in the Vera Rubin ridge (Edgar et al., 2020), Curiosity imaged additional spherules. Concretions were prevalent at certain stratigraphic intervals through the traverse between Sols 750–1900, covering all of the Murray formation members, but appeared more prevalent at lower elevations and scarce higher up Mt. Sharp (Sun et al., 2019). Murray formation concretions were comparable in size to those observed in sedimentary rocks in Meridiani and those found in lower in the Sheepbed mudstone, though their size decreased on average with elevation, and there are less than a dozen putative hollow spherules observed throughout Murray stratigraphy.

There were four different concretion assemblages in the Murray formation and three different chemical enrichments (Mg-S-Ni-Cl, Mn-P, Ca-S) at specific stratigraphic intervals, suggesting multiple fluid episodes with different compositions as Gale transitioned to a more acidic, sulfate-rich environment as the water dried out (Sun et al., 2019; Berger et al., 2020). In addition to the spherules, the Murray formation displayed three different types of concretions (Sun et al., 2019): "flat" concretions, characterized by irregular oblate shapes and a limited thickness in the vertical dimension; "dendritic" concretions, consisting of clusters of elongate laths that extend outward from a central point or line; and "irregular" concretions, discrete concretions with defined boundaries that differentiated them from host rock materials but that are not spheroidal, flat, or dendritic. In contrast to the Sheepbed mudstone concretions, concretions in the Murray formation were interpreted as late diagenetic features because they preserve primary host rock laminations without differential compaction. The reduction of concretion size upsection related to decreases in porosity and permeability, further supporting that concretion formation postdates initial cementation and porosity loss (Sun et al., 2019).

Manganese-rich concretions (1-3 mm) were found in the clay-bearing Glen Torridon unit. They are above the saline interval of the stratigraphy, suggesting formation diagenetically after the deposition of the sulfate minerals in oxidizing and circumneutral conditions or enrichment from hydrothermal circulation (Gasda et al., 2022). The bedrock then lithified and fractured; some of these fractures filled with calcium sulfate. In addition, diagenetic concretions consisting of pseudomorphs of vivianite ($Fe_3(PO_4)_2$) occur within the shallow lacustrine/fluvial sediments in Glen Torridon. The concretions were oblate, displayed high relief, did not deflect laminae, and contained twenty times the manganese abundance of the host siltstone. The molar ratio of phosphorus to manganese in these features was approximately two, suggesting that they contain an alteration product of vivianite developed in oxidizing and acidic pore fluids. The distribution of these concretions was limited to the Groken site, which suggests limited local hydrology and access to post-lithification groundwater (Treiman et al., 2023).

Location	Composition	Shape	Size range	Internal structure	Reference
Meridiani Planum	Hematite	Spheroidal	4–6 mm	–	Squyres, Grotzinger, et al. (2004)
	Unconstrained, not iron rich	Spheroidal	Up to 3 mm	Concentric zoning	Arvidson et al. (201)
	Unconstrained	Spheroidal	Up to 3 mm	Hard outer layer, hollow interior depression	Fairén et al. (2014)
Gale Crater (Sheepbed mudstone)	Iron phases (magnetite, akagenite, clays)	Spheroidal	~0.8 mm	Solid	Stack et al. (2014)
		Spheroidal	~1.35 mm	Hollow	
	Unconstrained	Spheroidal	2.75 mm	Filled	
Gale Crater (Yellowknife Bay)	Iron rich	Spheroidal	1–23 cm	Some were voids	Wiens et al. (2017)
Gale Crater (Murray formation)	Mg-S-Ni-Cl/Mn-P/Ca-S	Oblate/Dendritic/Irregular	Up to 7 mm	–	Sun et al. (2019)
Gale Crater (Glen Torridon)	Manganese rich	Spheroidal	1–3 mm	–	Gasda et al. (2022)
	Vivianite pseudomorph, Mn rich	Oblate	1–3 mm	–	Treiman et al. (2023)

Table 4.1. Summary of Concretion Characteristics Observed on Mars

Here, we examined the morphology, size distribution, and geochemical composition of Jezero Crater concretions to constrain the timing of concretion growth, fluid chemistry, formation mechanism(s) and outline the astrobiological implications of each. We used past observations of concretions on Earth and Mars to interpret the nature and biosignature preservation potential of Jezero Crater concretions. As a reference frame for the newly discovered concretions, we also compared Jezero Crater concretion compositions to the geochemistry of concretions in two new terrestrial analog sites (Gallup Formation, New Mexico and Torrey Pines, California) and measured total organic carbon preserved in three terrestrial analogs of increasing age from Pleistocene to Archean: Torrey Pines, Gallup Formation, Moodies Group.

4.5 Materials and Methods

We used Mastcam-Z (landscape and multispectral images) and SuperCam (remote micro-imager [RMI], visible and infrared [VISIR] reflectance spectroscopy, and laser-induced breakdown spectroscopy [LIBS]) to observe concretions in the Shenandoah formation. We analyzed the size, distribution, morphology and geochemical composition of concretions in each of the four stratigraphic units of the Shenandoah formation where putative concretions were observed: Hogwallow Flats, White Rocks, Devil's Tanyard, and Yori Pass. We were able to identify concretions in 196 Mastcam-Z images in the Hogwallow Flats member (Sols 464-508) and only one image in each of the other units. The difference in image quantity at each site resulted from the relatively short time spent at other units (e.g., 1-5 sols) compared to the Hogwallow Flats member (~30 sols). The Mastcam-Z images used in this work had the following parameters: RBG filter, calibrated and processed data product, 110 mm focal length except for three images, and lossless.

Within each stratigraphic unit, the term 'target' refers to the location on an area of float rock or outcrop upon which the instruments conducted science observations. The target area spans the instrument raster area for SuperCam or the field of view for Mastcam-Z images. Target names are universal across instruments and refer to the actual location on the rock, irrespective of the instrument being used.

We selected images with elevation pointing less than -36 degrees such that the view of the concretions was closest to plan view of the flat, ground-level exposures as possible. From this subset, we chose images that contained the most well-defined concretions and measured the long-axis diameter and distance to nearest neighbor in a 6.5 cm square, with an underlying *xyz* coordinate mesh for each image, enabling accurate measurements of features despite varying distance from the camera. Concretions were visible at varying resolutions and distances in each image so each concretion was measured manually based on visual judgment. A feature was classified as a concretion if it displayed positive relief compared to the bedrock and did not appear morphologically consistent with a vein or mottled bedrock. The concretions were also visually sorted into "simple" and "complex" morphologies. Nearest neighbor measurements were manually made between the center of the concretion diameter to the center of the closest concretion's diameter. A total of 104 concretions were measured across 15 images. A total of 69 nearest-neighbor distances were measured. There is a bias in the dataset towards measuring bigger concretions as those were easier

to distinguish from uneven, weathered, or ventifact-marked bedrock. To be conservative, we also refrained from measuring concretions in very small bedrock exposures and along fractures or edges of rocks unless the morphology of the concretion was highly distinct from the bedrock itself. The combination of above factors limited the concretion size measurements to a minimum of ~1 mm and a potential margin of error of +/- 1 mm.

4.5.1 Mastcam-Z Methodology

We used Mastcam-Z enhanced color mosaics and multispectral images of concretions to constrain their morphology, mineralogy and size distribution. The Mastcam-Z instrument is a pair of zoomable charge-coupled device (CDD) cameras with variable focal length and the ability to perform stereoscopic and multispectral observations across variable fields of view (Bell et al., 2021). The visible color (RGB) stereo panoramas are sufficient to resolve features of ~1 mm at a distance of ~2 meters and 3-4 cm at a distance of approximately 100 meters. Mastcam-Z is used to observe the morphology, texture, mineralogy, and structure of rocks and regolith, as well as observations of the atmosphere and sun. The wavelength range (442-1022 nm) spans diagnostic spectral regions that provide insight into primary and alteration mineralogies including the detection and mapping of mafic minerals such as olivine and pyroxene, iron oxides and (oxy)hydroxides, and presence of hydrated phases. A detailed description of calibration and processing of Mastcam-Z image data can be found in Bell et al. (2021) and Merusi et al. (2022)**.** Here, we focused on Mastcam-Z observations of the ferrous and ferric phases and hydrated minerals in concretions and the host rock in which they currently reside. The vertical error bars mark the standard deviation between extracted DN values from pixels in regions of interest marked on the image.

4.5.2 SuperCam Methodology

The SuperCam instrument (Wiens et al., 2020, Maurice et al., 2021) was used to evaluate elemental abundances in the concretions and how they compare to the host rock via LIBS. The spectra were pre-processed by the pipeline described in section 3.1 of Anderson et al. (2022) and then normalized across the whole spectrum. The point-to-point variation plots (Figures 4.8-11) were produced by averaging the major oxide composition (MOC) data for major elements, excluding the first 5 shots (out of 30 at each point) to eliminate dust interference. The depth profiles were produced by fitting the area of the major peak for the four major elements: Ca, Fe, Mg, Si to a Voigt profile for each shot (Pilleri et al., 2023). The peak was chosen due to its prominence in the spectra, such that it did not interfere with other elements. To avoid surface weathering and dust, the first 5 LIBS shots were excluded from the analysis. The visible and infrared (VISIR) spectrometer component (Fouchet et al., 2022) data used in this paper was calibrated and processed as described in Mandon et al. (2023) and Royer et al. (2023).

Using this chemical data to approach a tentative mineral/condensed phase composition, we assumed the presence of more than one mineral at each LIBS spot measurement. Thus, the MOC values set was an average of all the minerals present at the spot size of the LIBS measurements. To ascertain a combination of possible minerals, each % oxide concentration (g/100g) was transformed to mol/kg scale, and the different molar values were fitted to a set of minerals (the candidate minerals selected were based on the visible and infrared observations from these exposures) to obtain the lowest difference between the experimental MOC values and the calculated one, assuming a given percentage of each mineral candidate to be present at each analyzed spot.

4.5.3 Analysis of Terrestrial Analog Samples (Torrey Pines, Gallup Formation, Moodies Group)

We assessed the geochemical composition and the abundance of organic carbon of our analog concretion samples via x-ray fluorescence (*XRF*) and Elemental Analysis (*EA*). Electron microprobe analysis (*EPMA*) was also performed on the Gallup Formation concretions. This enabled us to better understand how environments influence concretion composition and how environment, concretion composition, timing of concretion formation, and size of concretion influences TOC preservation.

4.5.3.1 XRF on Torrey Pines and Gallup Formation

The samples were cut into 1 cm thick, cross-sectional tabular pieces and diamond polished to obtain a flat analytical surface. The concretion elemental mapping was conducted with a Micro-XRF imaging Spectrometer (Bruker M4 TORNADO). The scans had a resolution of 30 micrometers and dwell time of 20 milliseconds. The X-ray was operated at 50 kV and 600 microAmps.

4.5.3.2 EA

Total organic carbon (TOC) of the Torrey Pines concretions (Abbott, 1981) was determined at the University of Oregon with a Thermo-Fisher Flash EA using 60 mg of sample. For preparation, the samples were decarbonated via acid fumigation following the procedure described in Harris et al. (2001). TOC of one Torrey Pines concretion (reanalyzed for comparison) and Gallup Formation and Moodies group concretions was determined on microdrilled powders at the California Institute of Technology with a Costech EA using ~25 mg of each sample. For preparation, the samples were decarbonated with 1M HCl overnight. After neutralization, the samples were dried in the oven at 70 C for 48 hours. The samples were calibrated using an acetanilide standard. The elemental analyzer combusts samples in two consecutive furnaces (at 650 and 980 Celsius, respectively) using flow-through dioxygen. The evolved gas is flowed through a chromatographic column with helium as the carrier gas for separation of gases in the sample. The quantity of non-carrier gas is measured by a thermal conductivity detector.

4.5.3.3 Electron Microprobe Analysis

Quantitative compositional analyses for 8 of the 9 concretions collected from the Gallup Formation (concretion 1-4, 6-9) were acquired on a JEOL 8900 electron microprobe, equipped with 5 tunable wavelength dispersive spectrometers at the University of Alberta. Operating conditions were 40 degrees takeoff angle, and a beam energy of 15 keV. The beam current was 15 nA, and the beam diameter was focused (2-5 microns). Standards for analysis were calcite, siderite, dolomite, anhydrite ($CaSO_4$), tugtupite ($Na_4(AlBeSi_4O_{12})Cl$), hematite (Fe_2O_3), spessartine ($(Mn,Fe)_3Al_2Si_3O_{12}$, Navegadora Mine), sanidine ($KAlSi_3O_8$,Itrongay), garnet ($Mg_3Al_2Si_3O_{12}$, pyrope, Frank Smith Mine), diopside ($CaMgSi_2O_6$, Wakefield), rutile (TiO_2, MTI), and plagioclase ($(Na,Ca)_{1–2}Si_{3–2}\ O_8$, labradorite, NMNH 115900).

4.6 Terrestrial Analogs for Martian Concretions

Decades of work have established a framework for comparing Martian concretions to similar materials on Earth (Chan et al., 2004; Bowen et al., 2008; Loope et al., 2010; Potter et al., 2011; Chan et al., 2012; Wilson et al., 2012; Yoshida et al., 2018; Ray et al., 2021; Chan et al., 2022). Here, we incorporated past observations and integrated these with fresh observations from four terrestrial

analog locations to help better interpret the formation mechanisms and organic preservation potential of concretions in the Shenandoah formation.

4.6.1 Geologic Setting and Sample Collection

4.6.1.1 Torrey Pines, San Diego, California

Late Pleistocene iron-rich concretions grew within siliciclastic strata in acidic pedogenic (soil-forming) environments and created a mantle atop Pleistocene-age coastal terraces in present-day San Diego County. These concretions may be an analog for the "hematite blueberry" class of concretions observed at Jezero Crater (Figure 4.2). At Torrey Pines, California, paleosols formed on sandstone and conglomerate lithologies during glacial and/or interglacial intervals associated with acidic subaerial alteration (Abbott, 1981). In these profiles, ironstone concretions of a narrow size range (0.1 - 2 cm in diameter) form a thick (50-70 cm) horizon, known in US soil taxonomy as a Bir horizon (Soil Survey Staff, 2014), and accumulated as lag on terrace surfaces due to differential weathering of host rock.

We collected a set of samples (32.943°, -117.251°) belonging to a host rock depth profile at approximately 40 cm intervals cm depths according to changes in color and texture (e.g., along soil horizons). We collected a sample where the concretions (~0.5 cm) were embedded in the lithified paleosol as well as two concretion lag samples (1-3 cm). We analyzed new samples of concretions and associated lithified paleosol at Torrey Pines to determine if concretions were enriched in organic carbon relative to the host rock. Because of the relatively young age and lack of burial diagenesis (outcrops were never buried), it is possible to constrain the timing of concretion formation as concomitant with subaerial alteration (e.g., early diagenesis). It is therefore likely that organic matter associated with concretions in Torrey Pines may also represent deposition during soil formation and perhaps led to the precipitation of such concretions, but additions of modern carbon from the present-day biosphere to ancient concretions is possible and perhaps likely (Broz et al., 2023), so caution is appropriate for interpreting the abundances of "preserved" organic carbon.

4.6.1.2 Gallup Formation, New Mexico

The Gallup Formation is a very well sorted sandstone unit that was deposited within the San Juan Basin in New Mexico during the late Turonian to early Coniacian stages of the Cretaceous Period (~89 Ma). This stratigraphic unit is one of the deltaic clastic wedges deposited within the Western Interior Seaway and has been interpreted as an offshore marine transgressive to regressive sequence (Molenaar, 1973; Nummedal and Molenaar, 1995; Molenaar, 1974). There are a number of parasequences associated with the Gallup Formation as identified through lithology, sedimentary structures, as well as ichnology. While the Gallup Formation was previously believed to be entirely deposited in a shallow-marine environment, further analysis has shown that the depositional environments of this stratigraphic unit include a combination of subaerial, subaqueous, and aqueous environments (Lin et al., 2019; Lin et al., 2020). The identified facies are: shelf, offshore transition, pro-deltaic region, delta front, delta plain, distal lower shoreface, proximal lower shoreface upper shoreface, and the foreshore environments (Lin et al., 2019). The depositional environment of the Gallup Formation is hypothesized to have been controlled by multiple processes with storm-wave and fair weather dominance as well as being influenced by river and tidal processes. Shoreline trajectory analysis has also suggested that Gallup was influenced by eustasy (Lin et al., 2020).

The Gallup Formation is a deltaic package like Jezero Crater, albeit marine. The concretions were collected as a process analog to Jezero Crater to assess their internal structure, mineralogy, formation mechanism, and timing of formation relative to host rock. We collected 9 loose concretions of ~2-6 cm in diameter eroded out from a trough cross stratified medium sandstone within a section of the Gallup Formation near Toadlena, New Mexico, USA (36.188601°, -108.872320°) as described in Lin and Bhattacharya (2020). These concretions were found as lag throughout the outcrop and were not confined to a single bed (labeled Concretions 1-9, Figure S17). Two of these samples (concretions 6 and 7) were submitted for x-ray fluorescence and elemental analysis since these two samples appeared to be the most morphologically complex.

4.6.1.3 Moodies Group, Barberton Greenstone Belt, South Africa

The oldest concretions currently known on Earth are found in the 3.2 Ga Moodies Group (Nabhan et al., 2020), located in northeastern South Africa and the uppermost unit of the Barberton Greenstone belt. The Moodies group is a fluvio-deltaic sedimentary package like Jezero Crater and has witnessed low-grade metamorphism (Saitoh et al., 2021). The concretions are made up of calcite and muscovite cemented with sulfate, all of which was silicified by quartz to varying degrees (Nabhan et al., 2016). The surrounding bedrock is quartz-rich sandstone and argillaceous siltstone overlying felsic volcanic rocks. The concretions are interpreted to be early diagenetic features: specifically, the calcite is thought to have precipitated in anoxic, high CO_2 Archean atmosphere (perhaps similar to Mars at the time of Jezero delta activity), the sulfate from brines evaporatively concentrated in the shallow subsurface, and silica from extensive weathering of clay. Multiple sulfur isotope ratio analyses of the pyrite, barite, and anhydrite mineral inclusions in the concretions are consistent with microbial sulfate reduction producing isotopically lighter pyrite overgrowths around the sulfate minerals and minor pyrite oxidation (Nabhan et al., 2020).

4.7 Jezero Crater Results

4.7.1 Distribution and Morphology of Concretion-like Textural Features in Jezero Crater

In Jezero Crater, stratigraphically abundant and concentrated spheroidal, irregular and mushroom-shaped textural elements (Figure 4.2) were observed at the Hogwallow Flats member and were rare in the other units. Within the sulfate-cemented siltstone subunits of the Hogwallow Flats member (Figure 4.1C), the upper portion of each subunit was light-toned, platy, sulfate-cemented bedrock at outcrop surfaces and contained concretions whereas the lower portion of each subunit was finely laminated, darker toned, mottled and deformed strata in outcrop and did not contain concretions (Stack et al., 2024). The concentration of concretions in lighter toned bedrock implies possible bleaching of this host rock leading to mobility of certain elements for concretion formation in both subunits. Light-toned bedrock in the upper siltstone subunit of the Hogwallow Flats member appeared to contain more of these textural elements relative to light-toned bedrock in the lower siltstone subunit of the Hogwallow Flats member, suggesting a further stratigraphic concentration toward the upper part of this stratigraphic subunit. The textural elements of the Devil's Tanyard member were unique in that they contained hollow rimmed features (Figure 4.6D) whereas the other three units displayed a mixture of spheroidal, irregular, mushroom, and complex morphologies (see Figure 4.2). In all cases, it was not possible to uniquely conclude whether these textural elements are consistent with syncompaction or post-compaction because no laminae were traceable into and out

of the features. In the case of the hollow rimmed textural features in the Devil's Tanyard member (Figure 4.6D), they were situated upon laminated bedrock but the plan view exposure of the rock did not reveal the type of cementation of the textural elements within the laminae. The azimuth and elevation of all 196 images with textural elements that we interpreted as concretions found with respect to the Mars coordinate system is shown in Figure S9.

We interpreted these textural elements as concretions because they stood out or have eroded out of bedrock surfaces and so were differentially resistant to erosion, which is consistent with the internal and preferential cementation of concretions. Moreover, as discussed below, some of these textural elements show distinctive internal structure. Indeed, some appeared hollow, which is known to occur with concretions on Earth that have more resistant rims than interiors due to compositional zoning or cement differences that were exploited by differential erosion (Loope et al., 2012).

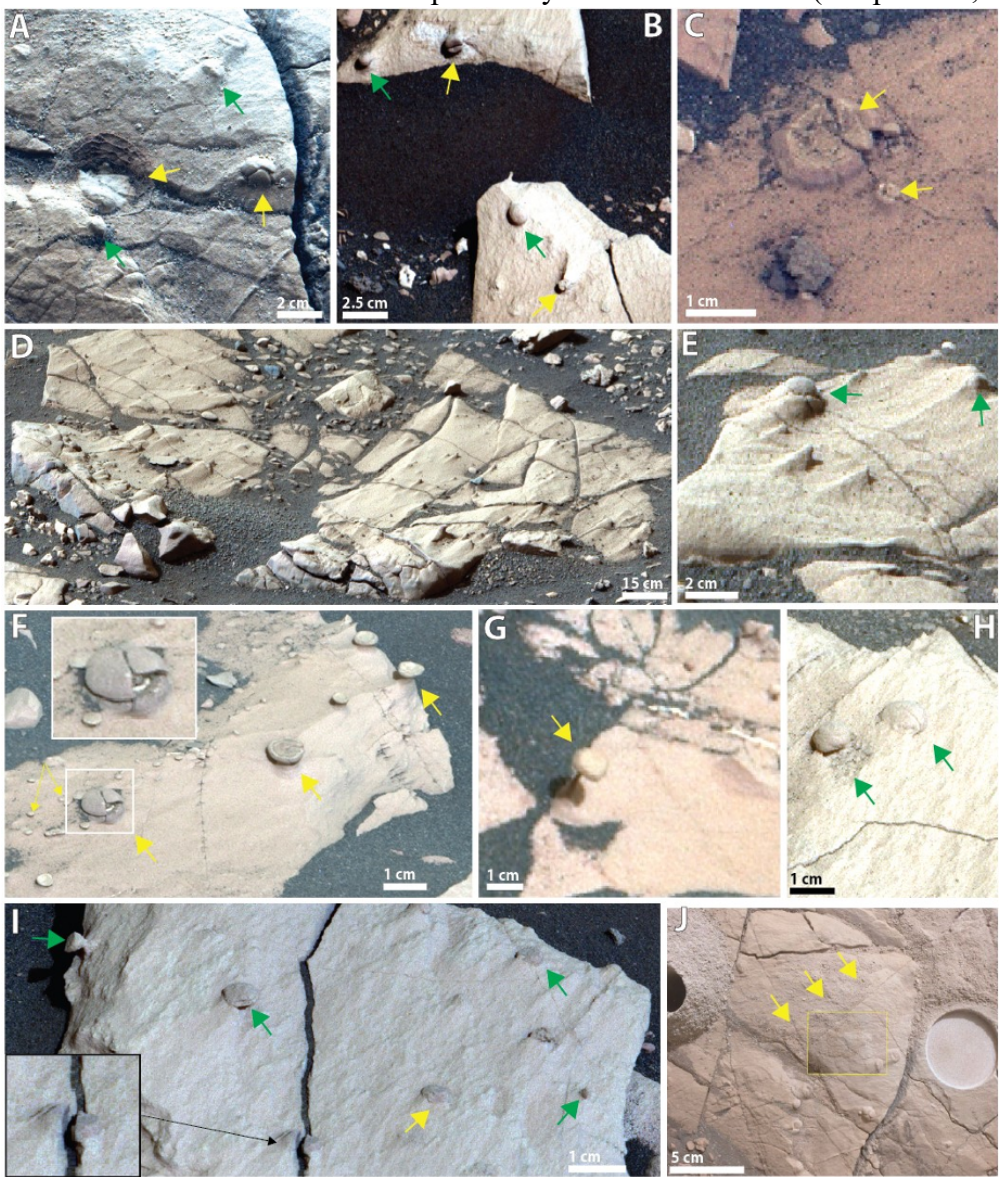

Figure 4.2. Mastcam-Z images showing the distribution, morphology and variation in concretions exposed at the Hogwallow Flats member. Green arrows show spheroidal/irregular concretions and yellow arrows show complex concretion morphologies. A) Wildcat ridge outcrop adjacent to Berry Hollow abrasion patch and coring location (Bearwallow and Hazeltop cores), lower Hogwallow Flats (Sol 504, zcam 08525); B) Lefthand Hollow outcrop, upper Hogwallow Flats (Sol 467, zcam 08488); C) Putative hollow concretions near Lefthand Hollow (Sol 467, zcam 08488); D) Abundant concretions in light-toned bedrock that appear wind-abraded (Sol 464, zcam 08484); E) Dark-toned spheroidal probably concretion eroding out of light-toned bedrock (Sol 464, zcam 08484); F) Diverse concretion morphology at upper Hogwallow Flats showing light-toned material in concretion interior (Sol 467, zcam 08488); G) Relatively uncommon morphology of concretion on stem at upper Hogwallow Flats (Sol 467, zcam 08488); H) Blueberry-like concretions in light-toned bedrock at upper Hogwallow Flats (Sol 467, zcam 08488); I) Bedrock with abundant concretions with diverse morphologies (spheroidal, flat, urn-like); inset box shows fracture through interior of concretion, consistent with concretion emplacement prior to late diagenetic fracturing; J) Image of Bearwallow core (Sol 511 WATSON image 04001). Yellow rectangle shows coring target including raised feature that is a putative concretion.

4.7.2 Morphology

The Jezero Crater concretions exhibited distinct variations in morphology across small spatial scales. For example, even a ~5 cm x 5 cm area of bedrock had a morphologically diverse set of concretions (Figure 4.2A,I). These include large (1-1.5 cm) concretions, oblate concretions, urn-shaped and spherical concretions. The largest concretions tend to have a hard-rimmed, flat-topped concretion morphology (Figure 4.2B,F) and contain differential coloration in the form of a light toned ring (Figure 4.2C,F). Often, a large concretion with a more erosion-resistant rim and a hollower center is surrounded by smaller cases of these hollow concretions (Figure 4.2C). The small, spheroidal concretions in Figure 4.2C are difficult to distinguish from the bedrock. Much of the Hogwallow Flats member bedrock is covered by concretions that are small, difficult to accurately measure, and have asymmetric relief (these have been labelled as 'irregular') (Figure 4.2D,E). These are very common and are underrepresented in the histogram due to measurement confidence limitations. The most unique and rare concretion morphology was found to be mushroom-like (Figure 4.2G). One instance of a concretion that was bisected by a fracture revealed a dark, uniform interior (Figure 4.2I).

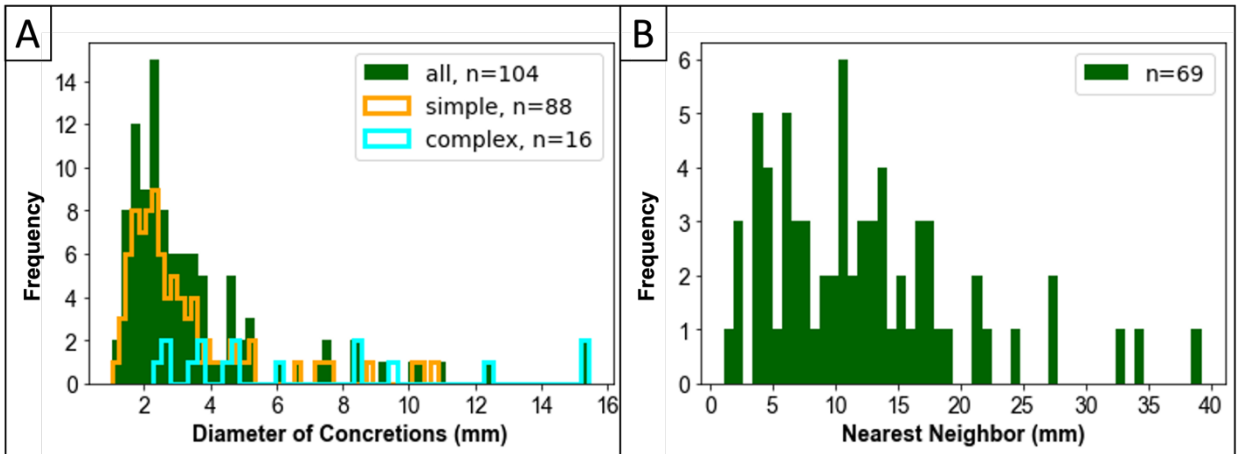

Figure 4.3: Histograms. A) histogram of diameter of all, simple, and complex concretions in the Hogwallow Flats member overlaid. B) histogram of nearest neighbor measurements.

4.7.3 Sizes of the Jezero Crater Concretions

The size and nearest neighbor statistics (Figure 4.3, Table 4.2) revealed that simple concretions (no visible structure) are much more abundant and on average half the size of complex concretions (with visible structure). Complex concretions did not display a size preference, and were able to grow to ~15 mm, as opposed to ~10 mm for simple concretions. The concretions are two to four times as widely spaced on average (from nearest neighbor measurements) relative to their average size , suggesting low levels of overall clustering. Figure S10 shows the in depth breakdown of simple and complex concretions measured in each image.

Unit	Number of concretions counted	Type of concretions	Mean (mm)	Std. Dev	Median (mm)	Min. (mm)	Max. (mm)
Hogwallow Flats	104	Simple + complex	3.71	2.81	2.65	1.04	15.43
	88	Simple	3.17	2.03	2.43	1.04	10.86
	16	Complex	6.74	4.24	4.76	2.26	15.43
	69 (nn)	–	12.11	7.86	10.96	1.17	39.21

Note. (nn) refers to nearest neighbor statistics. "Simple" concretions include both spheroidal and irregular concretions without any visible structure. "Complex" concretions include features with visible structure (e.g., multiple rind layers).

Table 4.2. Size Statistics, Number, and Morphology of Concretions Summarized for the Hogwallow Flats Member.

4.7.4 Geochemical Composition

4.7.4.1 Spectral Reflectance data

A major result from geochemical comparisons was that the spectra of concretions generally resembled the spectra of bedrock in which concretions reside, consistent with the view that the concretions grew from pore fluids that occluded porosity around significant amounts of host sediment and/or rock. Figure 4.4 displays multiple image regions of interest (ROIs) of concretions by the Mastcam-Z multispectral filter on the Gibraltar Lake target of the Yori Pass member (Sol 608). Points A and B are LIBS-cleared bedrock areas, showing almost identical spectra with a well-defined 866 nm feature and a shallower 528 nm feature, likely caused by hematite (e.g., Rice et al., 2022). Points C to H are on different concretions and have very similar spectra to each other and the bedrock with variations only in the band depth of the 866 nm feature and a positive or negative slope towards longer wavelengths.

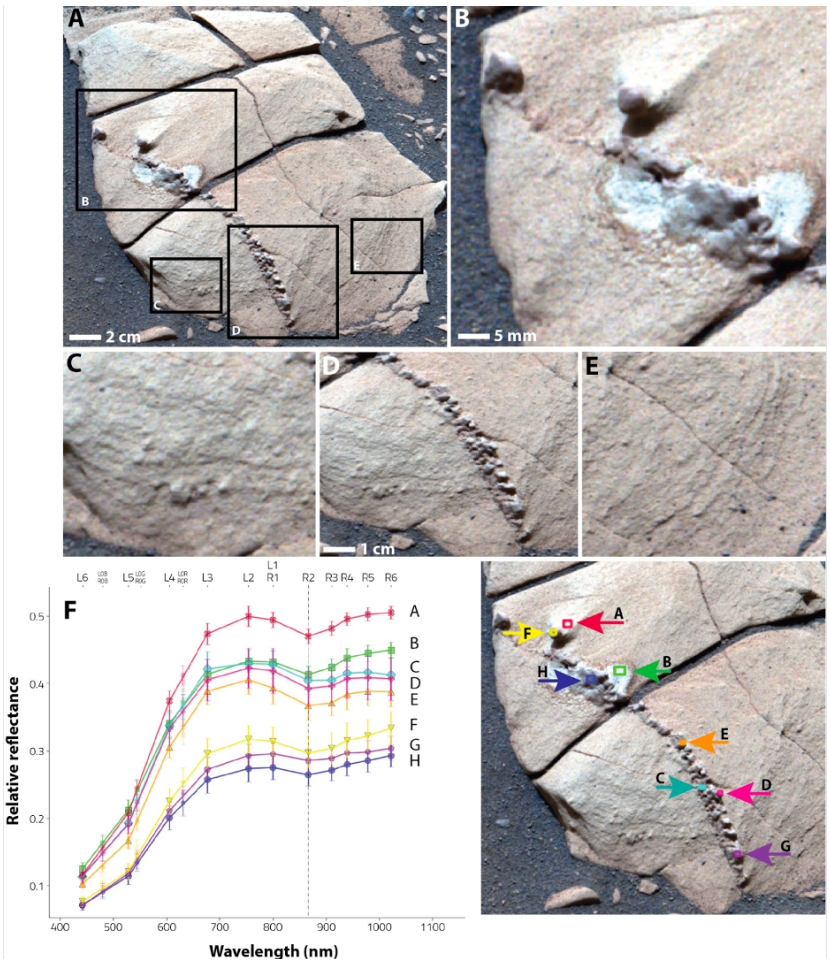

Figure 4.4. Mastcam-Z data. A-E) Mastcam-Z images of concretions at Sol 608 Gibraltar Lake target (Yori Pass member); F) Mastcam-Z spectra of locations (shown at bottom right)

The VISIR (visible-infrared) spectra in Figure 4.5, also of Gibraltar Lake, show collated concretion spectra from the central six points of the raster and bedrock spectra from the 4 endpoints of the raster. These spectra have no significant variation given the variations in relief, illumination, and texture of the target and the effects of these factors on VISIR spectra.

The Mastcam-Z spectra of both bedrock and concretions for different units (Figure 4.6) are similar, possibly suggesting a similar composition. The spectra have a comparable 866 nm band consistent with fine-grained hematite (Haber et al., 2022) though with relatively large uncertainties that preclude direct comparisons between, for example, the 528 or 866 nm band depths of the bedrock-versus-concretion.

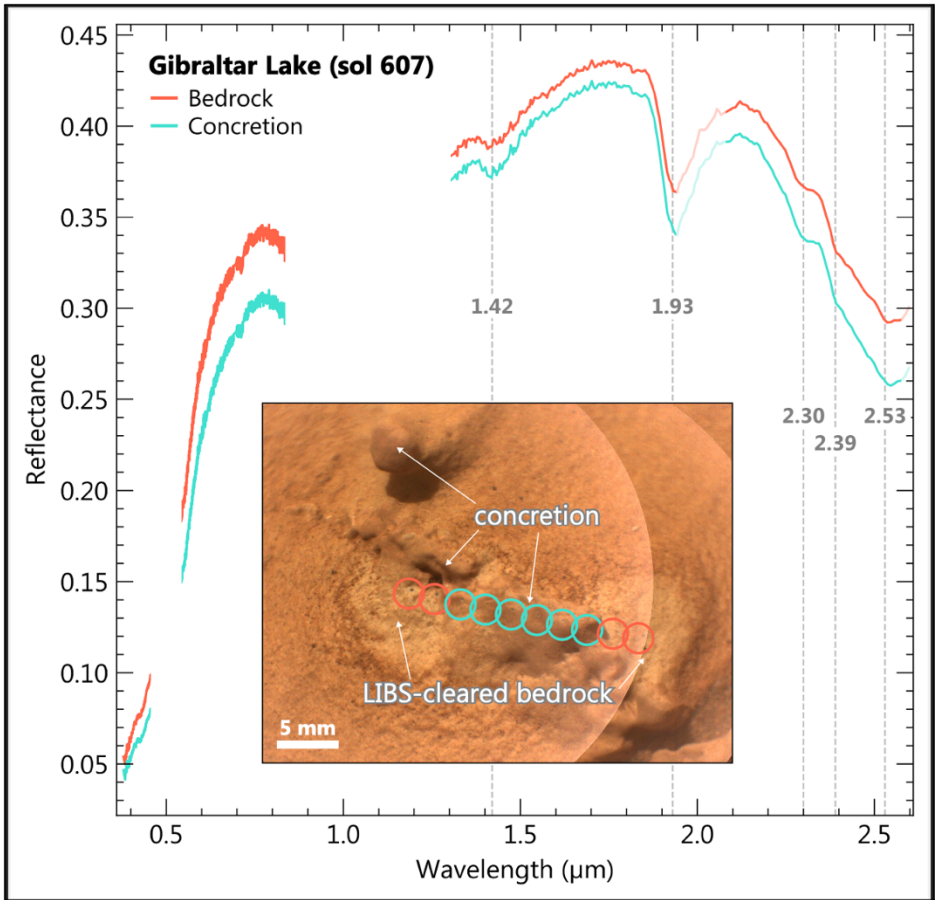

Figure 4.5. Supercam VISIR data of the same concretion in the Yori Pass member as in Figure 4.4 with spectra on the concretion in green and on the bedrock in red. The bands highlighted here are most often used to differentiate rocks at Jezero Crater: 1.42 and 1.93 are hydration bands, 2.3 and 2.53 are carbonate/phyllosilicate bands, 2.39 is a sulfate band.

4.7.4.2 LIBS Data

In the Hogwallow Flats member, the targets Lefthand Hollow, Pollock Knob, and Hightop were analyzed using LIBS to further constrain their geochemistry. The Lefthand Hollow target (Figure 4.7A) is a spheroidal, high relief, cm scale concretion against the bedrock. The elemental abundance of each point reveals a bedrock composition with average to low amounts of magnesium and a concretion composition that is magnesium enriched, with up to ~10% higher magnesium content and up to ~5% lower silica content. One concretion point was also enriched in iron. Points 4-10 have totals < 95%; a total is low either due to the presence of a salt phase or hydration or both (Figure S22A). Bedrock points 6-10 may therefore have a mixture of iron and magnesium salts since those are the two most abundant cations. Concretion points 4 and 5 may have a higher abundance of magnesium salts such as kieserite (Mg sulfate) or magnesite (Mg carbonate). It is unlikely to represent a clay mineral because the LIBS data would presumably show an increase in silica for concretion points, which was not observed. However, it is inherently difficult to assess sulfur content with LIBS due to the weak response of sulfur to this technique (Maurice et al., 2022). For example, the sulfur signal in all 10 points was not above noise, despite detections of ~10-20 wt. % sulfate in

similar light-toned Hogwallow Flats bedrock as determined by PIXL scans on abrasion patches (Mars 2020 Initial Reports Volume 2 (Samples 11-21)). It was also difficult to assess the carbonate content with LIBS due to interference from the Mars atmosphere and the weak response of carbon to this technique (Anderson et al., 2022). It should be noted, however, that putative carbonates were detected by SuperCam's VISIR in the Hogwallow Flats member but such signatures were not seen by PIXL (Mars 2020 Initial Reports Volume 2 (Samples 11-21)).

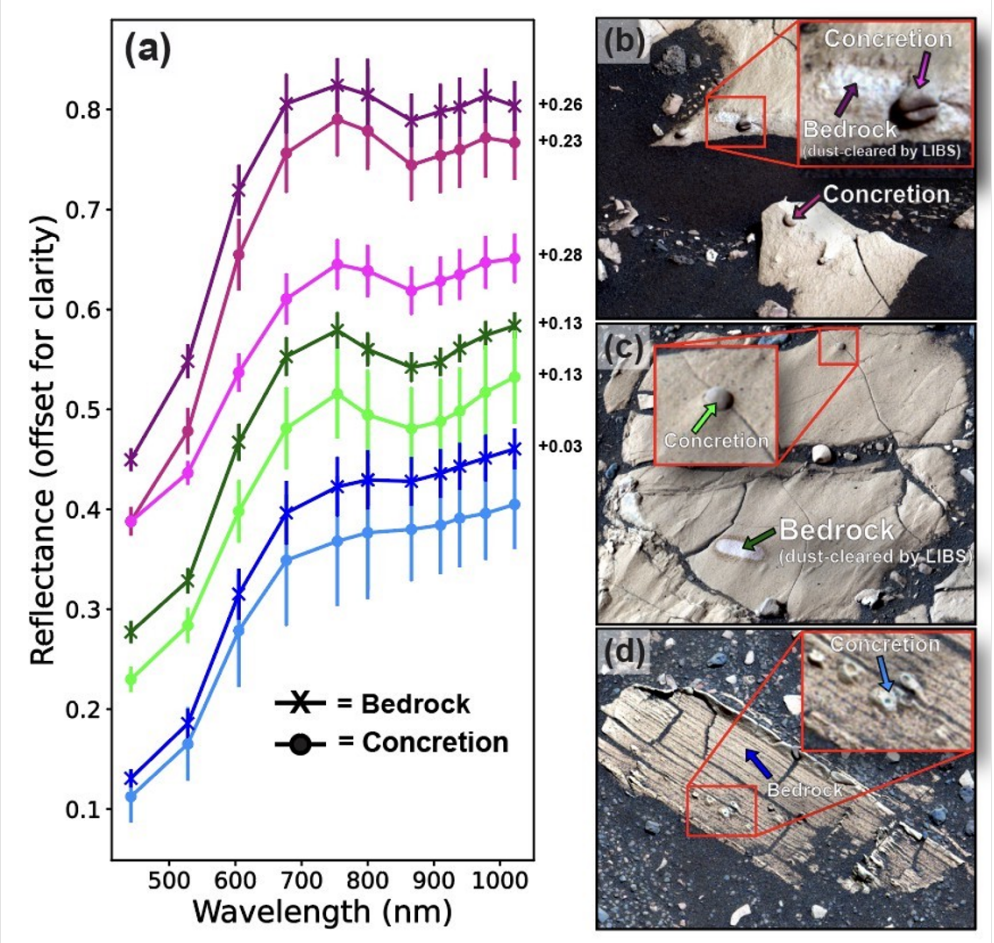

Figure 4.6. Mastcam-Z multispectral observations of concretions and dust-cleared bedrock at the Hogwallow Flats member and the Devil's Tanyard member. A) Mastcam-Z spectra of laser induced breakdown spectroscopy (LIBS)-cleared bedrock and concretions; B) coffee-bean like concretion (scale of concretion = 5 mm) at Lefthand Hollow outcrop at upper Hogwallow Flats (Sol 472, zcam 03386); note 528 and 866 nm bands characteristic of fine-grained hematite in both bedrock and concretion; C) Pignut Mountain outcrop at upper Hogwallow Flats (Sol 464, zcam 03378 with blueberry-like concretions (scale of concretion = 5mm) also showing 528 and 866 nm bands characteristic of fine-grained hematite; D) Hollow rimmed concretions in Abbott Ridge outcrop at the Devil's Tanyard member (Sol 697, zcam 03534) (scale of concretion = 1cm).

Light-toned bedrock at Pollock Knob (Figure 4.8) was targeted twice in different raster shapes to ascertain the compositional variations in concretion and bedrock with increased confidence. The 10 point linear raster detected heterogeneity in magnesium and iron abundance; however, it appears to

be unrelated to the concretion. The 3x3 grid raster (Figure 4.8B) had similar elemental abundances in most all points except for point 1 on the bedrock, which had lower magnesium content. In addition, the total oxide percentages of both these targets was almost always > 95% (Figure S22B,C). From these data, there seems to be only a slight compositional difference between bedrock and concretions.

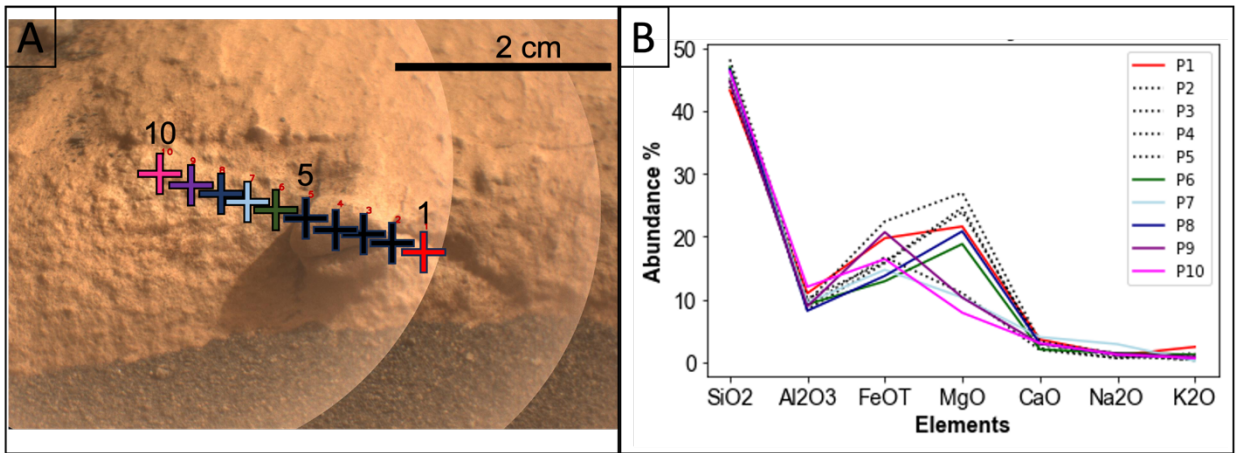

Figure 4.7. Lefthand Hollow. A) Supercam RMI (Remote Micro-Imager) picture of concretion target Lefthand Hollow (Sol 472) in the Hogwallow Flats member with raster locations from 1-10. Color of each raster point correlates to raster element abundance lines in B. B) Major element abundances in each point of the raster with black dotted lines being points on the concretion and colored lines being points on the bedrock. Mean accuracy and precision values for each element are listed in Table S4.

The bedrock of Pollock Knob showed heterogeneity: the linear raster (Figure 4.8A) had a set of points (points 2, 3, 4, 5, 7, 9 and 10) with an average total of 100.2 ± 2.7 wt. % and another set (points 1, 5 and 8) with an average total of 93.2 ± 2.0 wt. %, where both confidence intervals do not coincide. The magnesium abundances can be grouped for the same points averaging 18.8 ± 3.3 MgO wt. % in the first set and 9.1 ± 2.7 MgO wt. % in the second set. After applying the method of mineral deconvolution described in the SuperCam Methods section, the minerals present in the first set of points were found to be: (a) anorthoclase [$(Na,K)AlSi_3O_8$], (b) hematite (Fe_2O_3), and (c) part enstatite ($MgSiO_3$) and part augite [$(Ca,Na)(Mg,Fe,Al,Ti)(Si,Al)_2O_6$]. For the second set, the best combination of minerals was found to be: (a) anorthoclase, (b) hydrated greenalite [$Fe^{3+}{}_2(Si_2O_5)(OH)_4$], (c) augite, and (d) anhydrite [$CaSO_4$]. Table 4.3 summarizes the different abundances of minerals that explain the MOC values of the two sets of points at Pollock Knob. Therefore, the bedrock had heterogeneities in abundances of primary minerals, hematite, clay minerals, and sulfate salts. The concretions would consist of these minerals as well if they grew by occluding porosity (as opposed to displacively), especially anhydrite and hematite (as is common on Earth).

%Mineral	Anorthoclase $(Na,K)AlSi_3O_8$	Enstatite $MgSiO_3$	Augite $(Ca,Na)(Mg,Fe,Al,Ti)(Si,Al)_2O_6$	Hematite Fe_2O_3	Greenalite $Fe^{3+}{}_2(Si_2O_5)(OH)_4$	Anhydrite $CaSO_4$
Points 2, 3, 4, 5, 7, 9, 10	2.9%	35.9%	40.6%	20.6%	0.0%	0.0%
Points 1,5,8	4.6%	0.00%	66.6%	0.00%	22.1%	6.7%

Table 4.3. Relative Abundance of Minerals in the Linear Raster Pollock Knob Target Estimated from Laser-Induced Breakdown Spectroscopy Chemistry.

The target Hightop at Wildcat Ridge (lower Hogwallow Flats member) (Figure 4.1) was analyzed with a four-point LIBS depth profile with 120 shots per point because it measured above the average concretion size observed in the Shenandoah formation (more than 1 cm). The concentric ring structure in the dust (Figure 4.9A) is a result of LIBS shockwaves. The concretion is relatively homogeneous in composition, except for point 1, which is highly depleted in iron. Points 1-3 have totals <95%, consistent with salt (Fe,Mg,Ca) and hydrated phases (Figure S22D). The salt phase is likely carbonates as the points have one of the highest C score values of the analyzed concretions. The MOC values of the four points analyzed with LIBS were translated to the mol/kg scale. The mineral deconvolution (as described in the Supercam Methods) resulted in a combination of anorthoclase, Fe-,Mg-carbonate, hydrated greenalite, and augite. These mineral abundances are consistent with the visible, infrared and LIBS observations.

Each LIBS shot may cut 1-10 micrometers into the rock (depending on rheology); a depth profile of 120 shots penetrates a maximum of 1.2 mm into the target. The LIBS spot size also varies between 150-400 microns depending on the distance (Figure 47 in Maurice et al., 2021). Depth profiles are therefore not always a linear relationship between depth and shot number or focused on the same grain. Despite these limitations, the elemental trends with depth shown in Figures 4.9-11 provide the only insight into material inside the concretion since the rover did not analyze a concretion with an exposed interior. In terms of depth (Figure 4.9B), points 1-3 show an inverse relationship between calcium and magnesium abundance, such that deeper spectra are more calcium rich and magnesium poor. Point 4 shows the opposite trend. In all points, silicon does not increase with depth (Figures S5-8); therefore, the concretion appears to have, along with silicate minerals (Figure 4.9C), a mixture of magnesium and calcium salts in its interior. The *p*-value of all four linear regressions is much less than 0.05, indicating a strong correlation. Two sample cores (Bearwallow and Hazeltop) were collected directly adjacent to the Hightop target; pre-and post-imaging of the Bearwallow coring location shows that the core may have captured a putative concretion or nodular feature as shown in Figure 4.2J.

For Gibraltar Lake, the MOC total values of the bedrock (points 1,2,9 and 10) are higher than those of the concretions (points 3-8) on average (Figure S22E). The mean totals of the cleared bedrock amounts are 95.6±5.5 wt. %; thus the amount of volatiles (hydroxyls, water of crystallization, or carbonates) is rather low because 100% is included in the confidence interval of the average for the bedrock analyzed points. The high 5.5 wt. % of uncertainty shows the diversity of the relative amount of minerals in the bedrock. However, the mean totals of the concretions amount are 90.0±2.8 wt. %, suggesting less diversity of minerals and higher amount of volatiles in comparison to the bedrock. Comparing the elemental concentrations, the bedrock has slightly higher FeO_T% and MgO% averages with regard to the concretions, while also having a slightly lower SiO_2% and Al_2O_3%, suggesting that concretions have a lower amount of hematite and a higher proportion of phyllosilicates. All these assessments are consistent with the visible, infrared and LIBS observations of bedrock and concretions at Gibraltar_Lake.

A single concretion found at the White Rocks member is an irregular, cm-scale, high relief feature. Point 1 (P1) in Figure 4.11C does not fall on the concretion and the spectra may include influences from the lag pebbles seen in the image. If we take point 4 as dust-cleared bedrock composition, the concretion spectra are iron-depleted and slightly magnesium-, sodium-, and aluminum-enriched, suggesting cementation with phyllosilicate phases once more. Since the depth profile of point 1 shows a strong inverse relationship (p-value < 0.05) between Ca and Mg, the salt phase is likely calcium-rich at greater depths. For point 2, the linear regression found no relation between Ca and Mg with depth. This is because Ca decreased and then increased with shot number and Mg decreased steeply after ~20 shots (as illustrated by Figure S2). At depth, point 2 is thus enriched in calcium and depleted in magnesium. Point 3 is also poorly defined by linear regression. Figure S3 reveals that the Ca varies with depth while magnesium decreases. Point 4 shows definite linear enrichment of Ca with depth and magnesium depletion (p-value < 0.05). Overall, the concretion is variably magnesium-depleted with depth and calcium-enriched.

The best set of candidate minerals that could describe the four points of the Fleeburg target (as described in SuperCam Methods) are anorthoclase, pyrophyllite, anhydrite, greenalite or hematite, enstatite or Mg-carbonate, and an excess of anhydrous silica in points 3 and 4. Table 4.4 summarizes the relative abundances of these minerals for the four points of the Fleeburg target.

% Mineral	Anorthoclase $(Na,K)AlSi_3O_8$	Pyrophyllite $Al_2Si_4O_{10}(OH)_2$	Anhydrite $CaSO_4$	Greenalite $Fe^{3+}{}_2(Si_2O_5)(OH)_4$	Hematite Fe_2O_3	Enstatite $MgSiO_3$	Silica SiO_2	Magnesite $MgCO_3$
Point 1	8.3%	10.5%	6.7%	18.1%	0.0%	3.7%	0.0%	52.8%
Point 2	10.4%	9.5%	12.2%	21.2%	0.0%	34.6%	0.0%	12.1%
Point 3	7.5%	8.7%	11.3%	0.0%	19.5%	47.8%	5.3%	0.0%
Point 4	5.2%	7.3%	9.9%	0.0%	18.5%	34.5%	24.5%	0.0%

Table 4.4. Relative Abundances of Minerals in the Four Points of the Fleeburg Target.

As seen, points 1 and 2 (presence of magnesium carbonate and greenalite and absence of hematite and silica) have differences compared to points 3 and 4 (absence of magnesium carbonate and greenalite, and presence of hematite and silica). Since points 2 and 3 fall on the concretion, we note that the concretions consist of multiple salts and share minerals with the host rock.

In summary, these results suggest that the Hogwallow Flats member concretions are enriched in Mg and Ca salts whereas the Yori Pass member concretions appear to contain a greater abundance of phyllosilicates than the host rock. By contrast, the the White Rocks member concretion contains variable primary minerals, clays, salts, hematite, and amorphous silica and shares some of these minerals with the host rock. At depth, it is calcium enriched and magnesium depleted. All concretions have a finely crystalline hematite signature as inferred from Mastcam-Z multispectral observations, and this signature is similar to the bedrock that hosts concretions. Analysis of the MOC totals suggests that the salts in the concretions are likely Mg,Ca carbonates and calcium sulfate, hematite is a ubiquitous component, and that primary minerals and clays have been incorporated into the concretions from the bedrock.

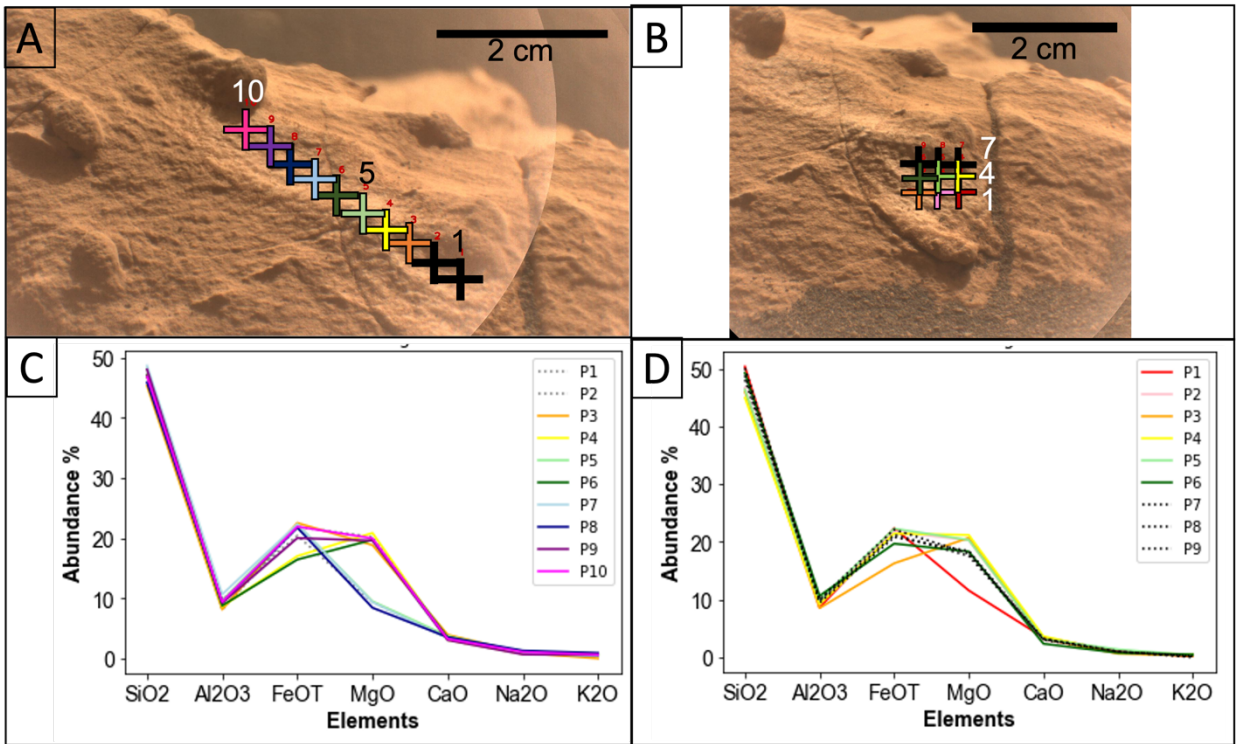

Figure 4.8. Pollock Knob. A and B) RMI images showing LIBS raster points locations targeting concretions from Pollock Knob in the Hogwallow Flats member with raster locations from 1-10 in A and 1-9 in B. Color of each raster point correlates to raster element abundance lines in C and D. C corresponds to panel A. D corresponds to panel B. C and D) Major element abundances in each point of the raster with black dotted lines being points on the concretion and colored lines being points on the bedrock. Mean accuracy and precision values for each element are listed in Table S4.

4.8 Terrestrial Analog Results

The morphology, geochemistry and size distribution of Jezero Crater concretions reported here are similar to those examined in terrestrial settings. Below we discuss the geochemistry of two analogs (Torrey Pines and Gallup Formation) and the TOC of three analogs (Torrey Pines, Gallup Formation, Moodies Group). All analog concretions are pictured in Figure 4.12.

4.8.1 Geochemistry of Concretions of Torrey Pines, California

The concretions collected at Torrey Pines ranged from 0.3 to 3 cm in size and were spheroidal, texturally rough, and reddish to brown in color (Figure 4.12 A-C). Previous studies have concluded that they formed in acidic, sub-aerial fluids (see Geologic Setting of this paper).

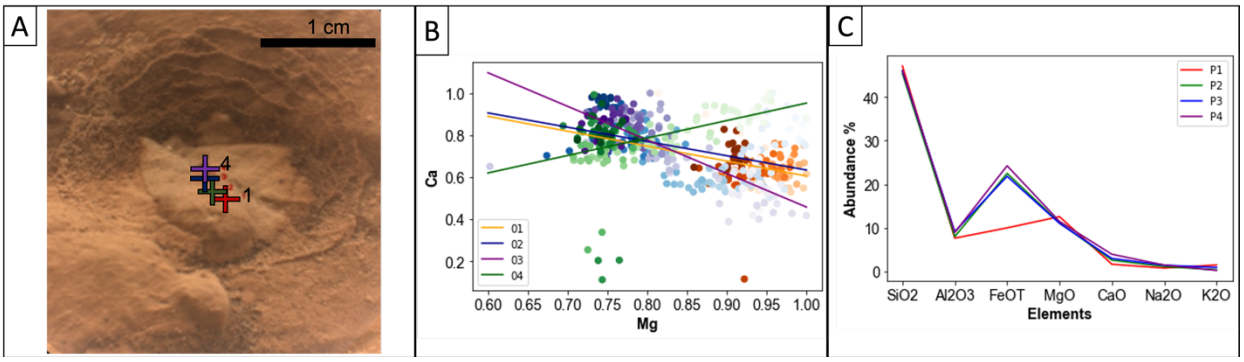

Figure 4.9. Hightop. A) Supercam RMI of concretion target Hightop in the Hogwallow Flats member with raster locations from 1-4. Color of each raster point correlates to raster element abundance lines in C. B) Depth profile showing normalized peak areas of 120 LIBS shots (from light color to dark color) of calcium and magnesium for each point with linear regression fits C) Major element abundances in each point of the raster. Mean accuracy and precision values for each element are listed in Table S4.

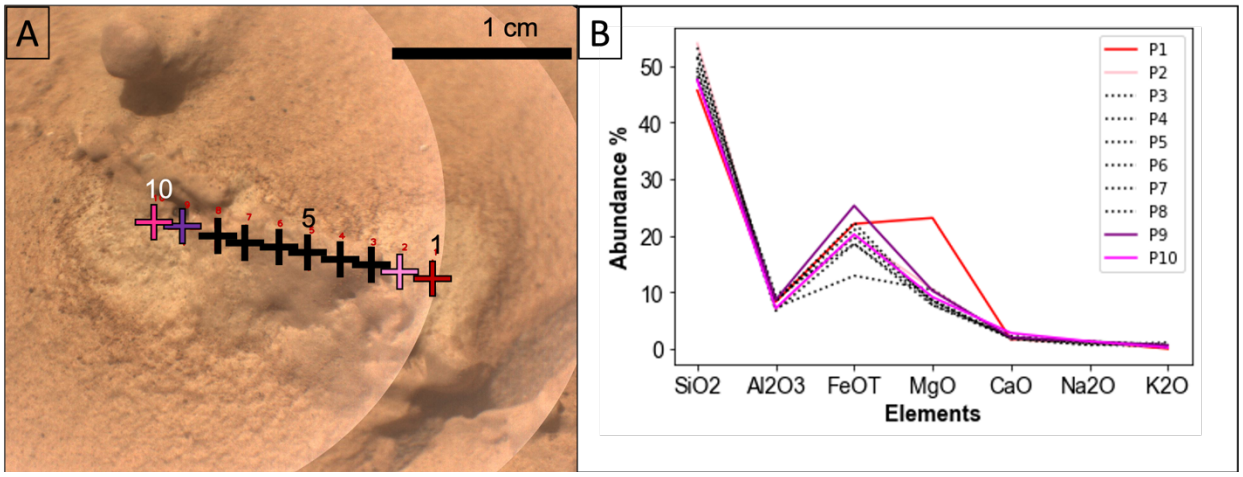

Figure 4.10. Gibraltar Lake. A) Supercam RMI of concretion target Gibraltar Lake in the Yori Pass member with raster locations from 1-10. Color of each raster point correlates to raster element abundance lines in B. B) Major element abundances in each point of the raster with black dotted lines being points on the concretion and colored lines being points on the bedrock. Mean accuracy and precision values for each element are listed in Table S4.

Figure 4.13 shows X-ray fluorescence (XRF) elemental maps of a Torrey Pines concretion (bottom left of Figure 4.12C). The other 3 XRF map sets are in the supplemental materials (Figures S11-13). In plane light, the concretions appear to be non-concentrically zoned with light-toned, coarse-grained regions, dark and fine-grained regions, and a mm-scale outermost coating of dark material. XRF scans reveal that the concretions are variably enriched in iron across the entire surface (Figure 13, Fe map) and that the outer rim is consistently composed of iron oxide. The darkest regions where iron and no other element is concentrated are iron oxides. Coarse quartz grains as well as calcium and potassium feldspars, seen in the Ca, K, and Si maps, exist uniformly in the concretion despite the variation of natural colors of the concretion. Instead, greater cementation with phyllosilicates and

silica, seen in opaque regions of Al and Si maps, correlates to lighter color in plane light. The fact that grains of quartz and feldspar and clays are included in the concretion demonstrates that it grew by occluding porosity. Interestingly, the XRF detects sulfur along zone boundaries and overlaps with iron and no other mineral. However, when quantified by the software, the sulfur has a maximum peak ratio of ~2% of the silicon peak (Figure S19) and is not very abundant. The quantified Si, Al, Fe, and K abundances are shown in Figure S18 and all elemental abundances are in Table S3. Based on similarity of structure to hematite concretions in Potter et al. (2011), Torrey Pines concretions likely grew pervasively after an initial radius of iron oxide rim was set.

Figure S13 presents a complex concretion, where the rim of the initial concretion is iron oxide-rich and the interior is siliciclastic dominated. However, the concretion then appears to have had a second phase of growth which involved preferential siliciclastic addition on one end of the concretion, turning it elongate, with a final iron oxide rim. This kind of episodic growth could also be expected at Jezero Crater if evaporation and groundwater replenishment took place episodically.

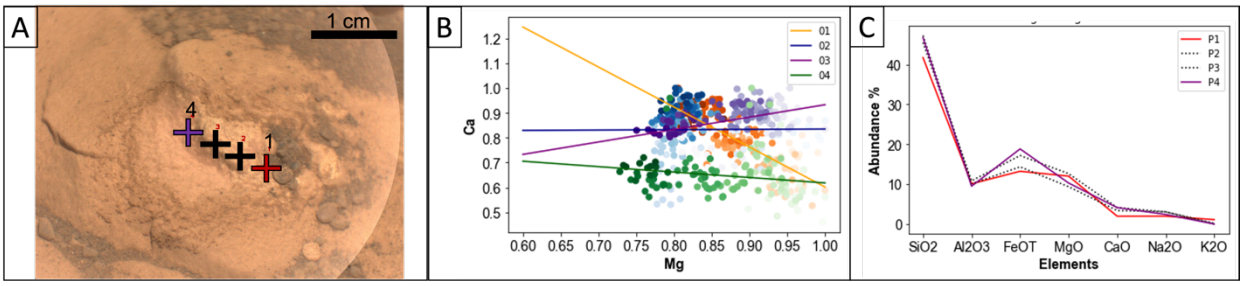

Figure 4.11. Fleeburg. A) Supercam RMI of concretion target Fleeburg in the White Rocks member with raster locations from 1-4. Color of each raster point correlates to raster element abundance lines in C. B) Depth profile showing normalized peak areas of 120 LIBS shots (from light color to dark color) of calcium and magnesium for each point with linear regression fits C) Major element abundances in each point of the raster. Mean accuracy and precision values for each element are listed in Table S4.

4.8.2 Geochemistry of Concretions of Gallup Formation, New Mexico

Concretions collected within a section of Gallup Formation near Toadlena, New Mexico, USA appear to have a variety of internal structures (Figure S20). C1-C4 and C6 are all reddish and have distinctive layering. C5 is anomalous compared to the others and appears dark gray. This sample began to disaggregate when being prepared for thin sections. C7-C9 are all tan/gray and appear to be primarily composed of quartz grains with the exception of C7 which has a white core. C7-C9 are on average larger than their counterparts. Figure 4.12E shows the two representative samples of concretions from the Gallup Formation that were chosen for XRF analysis. The concretion on the left of Figure 4.12E (C6) shows concentric layering from red at the core to dark red to brown at the edge and concretions of this type are on average smaller than the concretion to the right. The concretion on the right of Figure 4.12E (C7) has a much larger gray core and sand filled outer edge. Both concretions have the texture of coarse-grained sandstone on the outside. All concretions collected from the Gallup Formation are spheroidal.

Figure 4.14A reveals a very interesting concentric, internal structure to this type of Gallup Formation sample from innermost to outermost layer: iron oxide and silicate rich, iron oxide rich, siliciclastic rich, siliciclastic and calcium dominated. When quantified by the software, the sulfur in the core has a maximum peak area of 7% (Figure S15) of the silicon peak, and is therefore not very abundant. It has been replaced by iron oxides. This concretion likely grew pervasively but has experienced multiple generations of precipitation infilling porosity, like the spheroidal Navajo Sandstone concretions (Potter et al., 2011). Thus, it is difficult to narrow the timing of formation of this concretion as these episodes of iron oxide cement could have occurred at multiple points throughout diagenesis. Gallup Formation facies in general do not show evidence of oxidizing fluids affecting the depositional mineral assemblage as a whole (Sun and Allen, 1957; Winn et al., 1984; Yoon et al., 2019). Elemental abundances are in Table S1.

Figure 4.14B presents an intriguing concretion composition. It only has two compositional zones, the inner core is barium sulfate mixed with siliciclastics. There is a complete absence of iron, whereas the outer region contains a silicate phase rich in calcium and iron. We can conclude that it is barium sulfate or barite because there is no barium sulfide mineral naturally occurring. Also Figure S16 and Figure S17 show up to 30% sulfur compared to the silicon peak area and even higher amounts of barium. This is enough quantity such that the sulfur is stoichiometrically present as barium sulfate and there is barium included in the siliciclastic components. Elemental abundances are in Table S2. This inner core of this concretion was likely a result of pervasive growth, after which a change in fluid chemistry occurred and the rest of the concretion consisting of siliciclastics and iron oxide cement grew radially from this nucleus of siliciclastic grains with barite cement.

Figure 4.14C-E illustrates the results of the EPMA. All of the eight studied concretions were primarily composed of quartz with occurrences of potassium feldspar and multiple fine-grained iron mineral mixtures. The silica in the XRF mapping (Figure 4.13) is most likely associated with quartz and potassium feldspar while K and Al is probably associated with potassium feldspar and the occasional clay mineral (e.g., kaolinite, illite)). Iron oxyhydroxides (potentially goethite, hematite, lepidocrocite, etc) were identified in concretions 1-4 and 6 but were scarce in concretions 7-9. This iron oxyhydroxide mineral is the main iron-containing mineral responsible for dark coloring of concretions 1-4 and 6. Concretion 6 showed the most mineralogical diversity as it also contained minor amounts of barite, some detrital garnets, and zircons. Kaolinite and other clay minerals may have also been present. Concretion 7 was also found to contain some garnets and zircons as well as albite and, most interestingly of all, a significant amount of barite in its center (giving this sample the white core observed in the image of the concretion in Figures 4.12C and supported by the XRF mapping in Figure 4.14). No other sulfur-containing minerals (e.g.siderite, pyrite, jarosite, or gypsum) were observed in any of the Gallup samples and barite was only observed in concretions 6 and 7, with the latter containing a significantly larger abundance. Therefore, the S observed by the XRF mapping is likely associated with barite only. The lack of sulfur-containing minerals in the Gallup Formation concretions are likely the result of the concretion formation conditions during diagenesis of the host rock being relatively oxic. Concretion 8 was the only sample found to contain detrital magnetite, whereas concretion 9 was the only sample containing a large amount of calcite, although the results of the XRF mapping suggest that some amount of Ca may be incorporated into mineral mixtures in concretion 6. Concretions 1-4 appear to exclusively be composed of quartz potassium feldspar grains with iron oxyhydroxide cement.

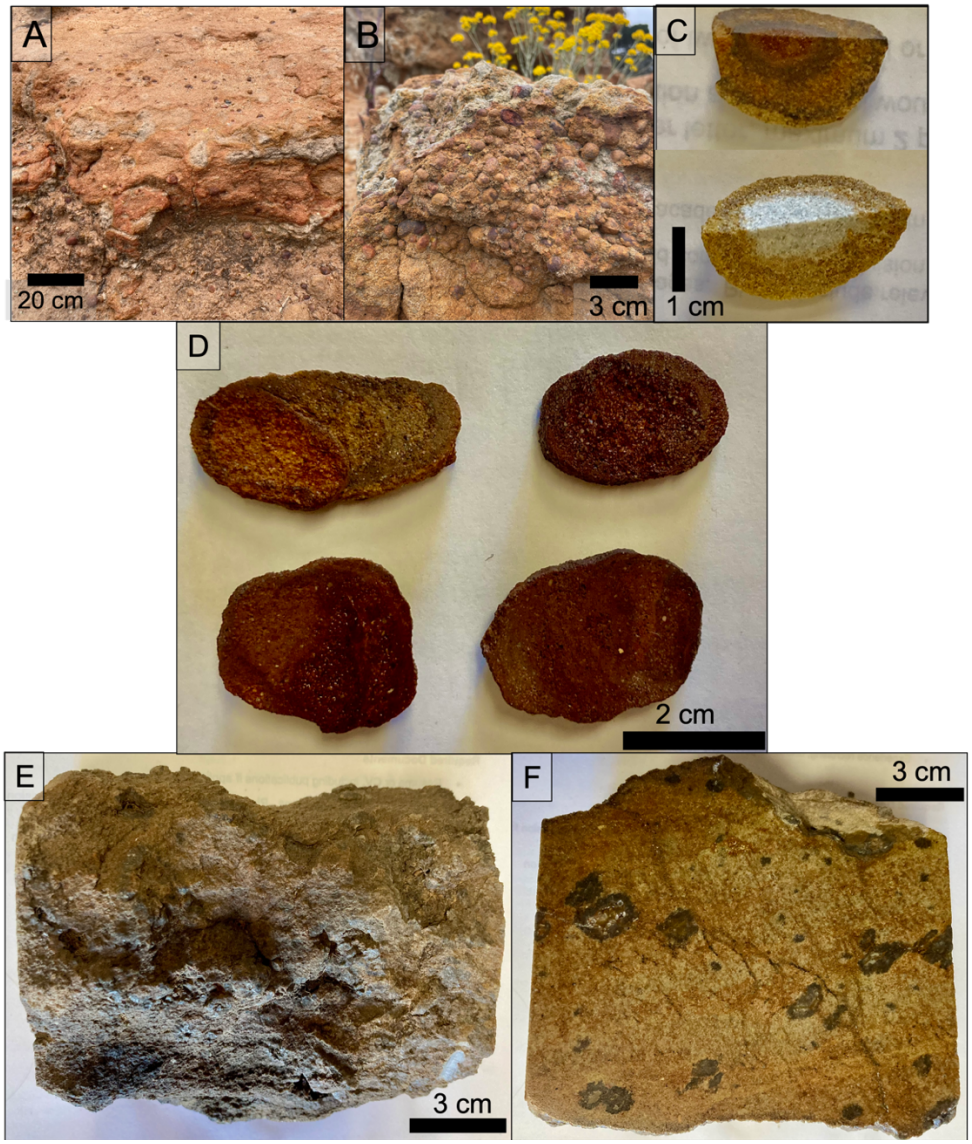

Figure 4.12. Images of all concretion terrestrial analogs collected. A and B) Late Pleistocene pedogenic concretions (up to 1 cm) from Torrey Pines, CA (32.940502, -117.245161) C) Images of representative concretions from Gallup Formation. Concretion 6 is on the top and concretion 7 is on the bottom. D) Cross-sectional cut of four representative concretions from Torrey Pines. E and F) Hand samples of Moodies Group.

4.8.3 Description of the Moodies Group, South Africa Samples

The Moodies group sample (Figure 4.12 E,F) has faint laminae; the uncut face is a highly weathered, brown, medium sandstone. The sample contains ~1 cm concretions with differentiated light brown inner cores and dark brown outer cores and mm to cm sized undifferentiated dark concretions. The concretions are oblate in the direction of the lamination, which is consistent with an early diagenesis formation environment as previously interpreted by Nabhan et al. (2016).

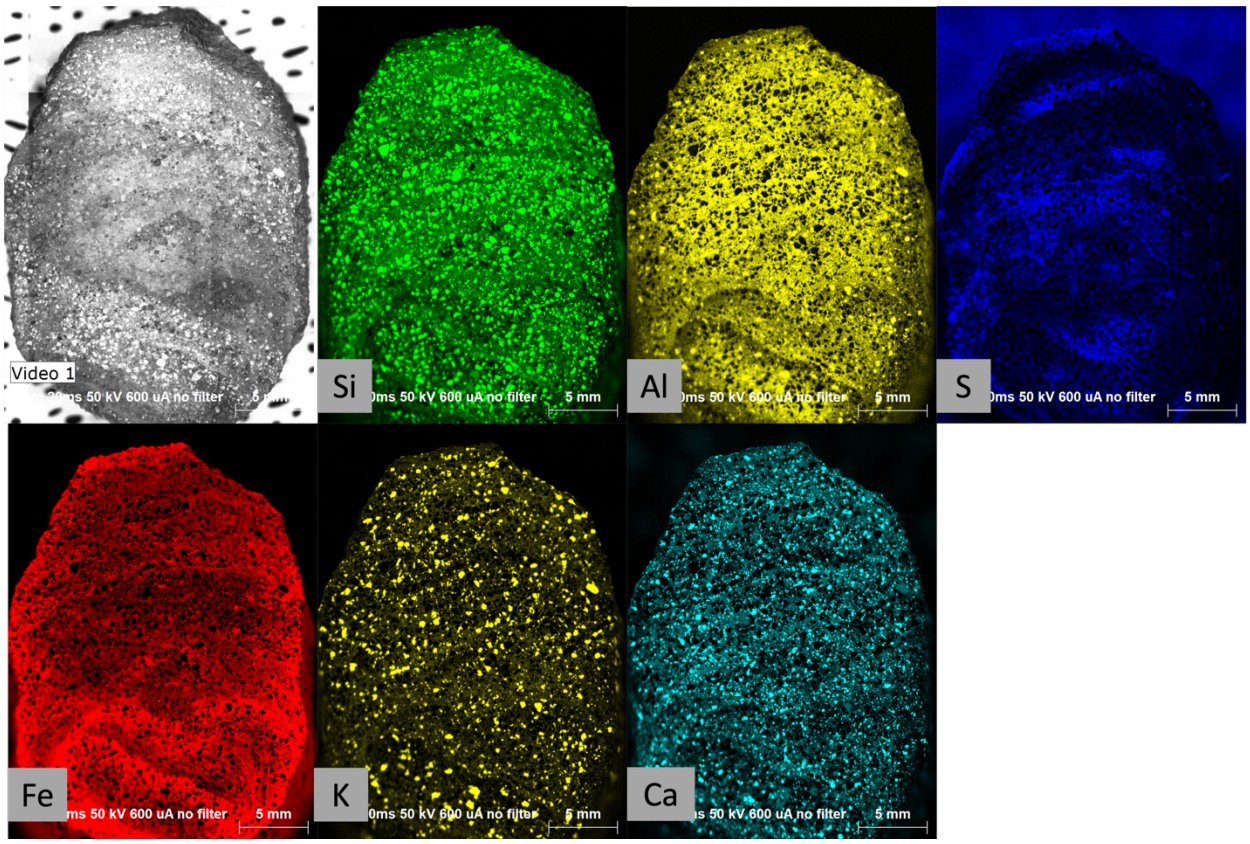

Figure 4.13: Plane light image of concretion (bottom left of Figure 4.12C) and XRF mapping of single elements Si, Al, S, Fe, K, Ca.

4.8.4 TOC of Terrestrial Analogs

The concretions were subsampled in the following way (Figure 4.15). For the Moodies Group, we microdrilled the bedrock, small, fresh, undifferentiated concretion, medium, fresh, differentiated concretion, and large, weathered, differentiated concretion (Figure 4.15 C,D). For the Gallup Formation, the XRF data showed that the inner and outer core of both concretions have different mineral assemblages. We therefore microdrilled the inner and outer core of each (Figure 4.15 A,B). For Torrey Pines, we powdered three concretions whole and the inner core of the concretion in Figure 4.13. The range of error based on the standard deviation of the measurements was 0.003% to 0.1%. However, the standard deviation of measurements of <1% TOC was <0.06%. Only two measurements were higher than 1% TOC.

The host rock in Torrey Pines has an average %TOC of 0.05, the whole concretions have an average TOC of 0.18%, and the inner core of the concretion has an average TOC of 0.74%, which is approximately fifteen times the host rock. This suggests that the Torrey Pines concretions have high organic preservation potential compared to the host rock. Both Gallup Formation concretions have a range of TOC between ~0.3-0.65% and lower amounts of organic carbon in the inner cores compared to the outer cores. C6 has more TOC overall, likely because it is finer grained than C7.

The Moodies group concretions are also enriched in TOC compared to the host rock. The host rock measures ~0.5% TOC, the small, fresh concretion contains ~1% TOC, the medium, fresh concretion contains ~2% TOC, and the highly weathered, large concretion contains ~0.8% TOC. The fact that both the bedrock and concretions show such high TOC values is likely due to the diagenetic silicification of this outcrop. These concretions grew inwards according to previous studies (Nabhan et al., 2020). Therefore, the trend of a larger concretion containing proportionally more organic matter therefore aligns with past observations. This large concretion in the Moodies sample (Figure 4.15C-1) could have experienced reduction of TOC during weathering or diagenesis and now measures less TOC than the small concretion.

Figure 4.15E shows no correlation between age and concretion TOC abundance, suggesting factors other than concretion age are related to the organic content. In the context of comparisons with our other terrestrial analog samples, we therefore propose that depositional age is not the determining factor for TOC preservation in concretions, rather, the formation mechanism and the formation timing compared to surrounding bedrock may be the determining factors of TOC preservation.

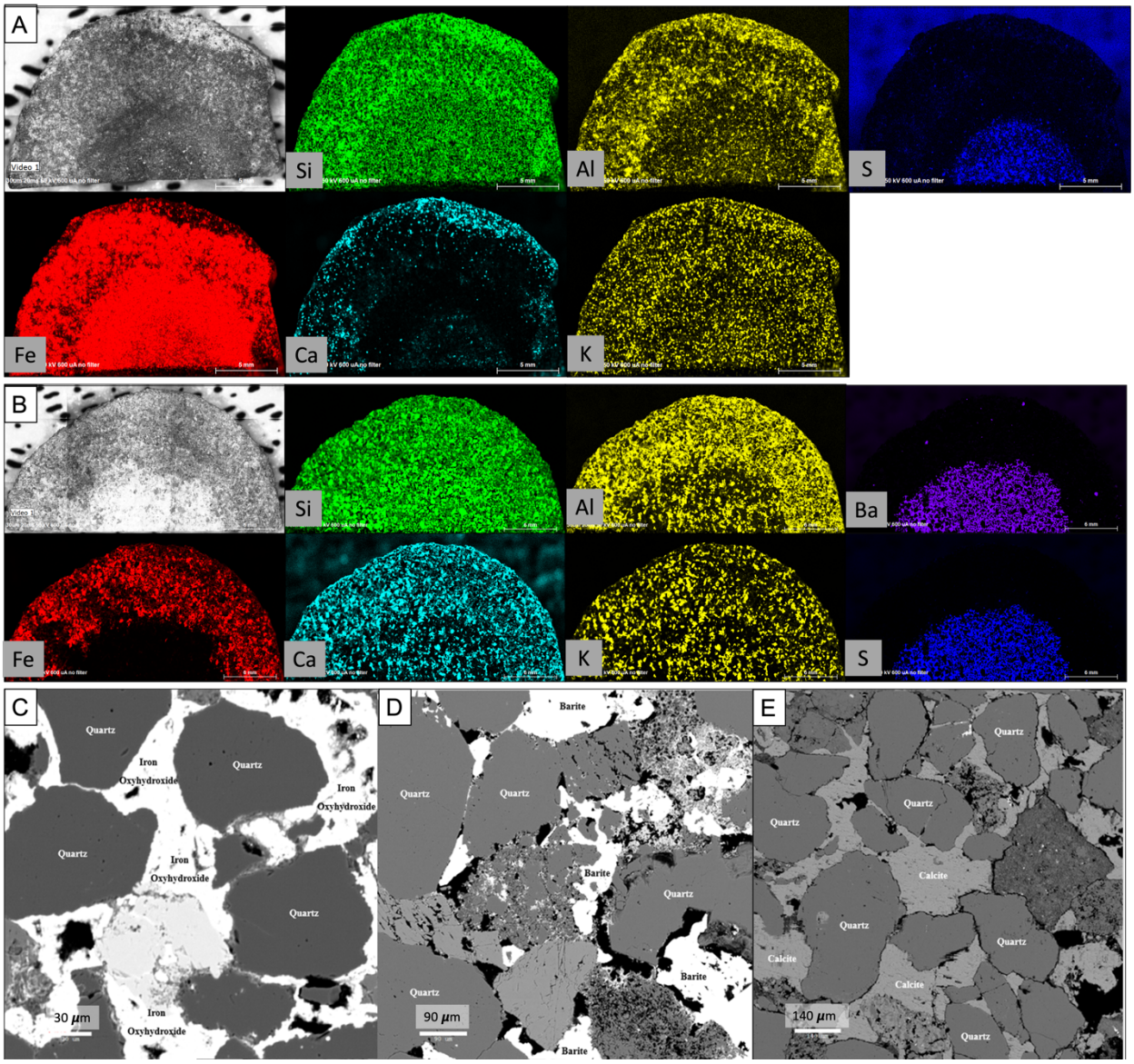

Figure 4.14: XRF and EPMA. A) Plane light image of concretion 6 (left in Figure 4.12E) and XRF mapping of single elements (top row) Si, Al, S (bottom row) Fe, Ca, K. B) Plane light image of concretion 7 (right in Figure 12E) and XRF mapping of single elements (top row) Si, Al, Ba (bottom row) Fe, Ca, K, S. C,D,E) Backscatter electron images illustrating varying cements among quartz grains in the Gallup Formation concretions: (C) iron oxyhydroxide cement in Concretion 6, (D) barite cement in Concretion 7, and (E) calcite cement in Concretion 9.

4.9 Discussion

4.9.1 Comparisons with Analogs

The morphology and size of the concretions in the Hogwallow Flats member is comparable to those of terrestrial analogs in this study and the well known Jurassic Navajo Sandstone concretions (Figure 4.16). The simple, spheroidal concretions are comparable in morphology to those at Torrey Pines. The flattened, spheroidal concretions are of similar size and shape to concretions in the stratigraphic

top of the Jurassic Navajo Sandstone, which precipitated along more porous and permeable, horizontal grain flow laminae (Chan et al., 2022). The hollow and filled concretions of the Moodies Group appear morphologically similar to the concretions in the Hogwallow Flats member bedrock as well as the hollow concretions in the Devil's Tanyard member (Figure 4.6). Figure 4.16 also draws similarities between the potential composition of Jezero Crater concretions and compositions of each of these analogs. Concretions from Torrey Pines and the Moodies Group are formed diagenetically early as established by previous work (Abbot, 1981; Nabhan et al., 2020) but Gallup Formation and Navajo Sandstone concretion timing is less constrained (this study, Potter et al., 2011), which demonstrates the variability and complexity of possibilities in these features. Despite this, in the case of the Gallup Formation concretions, measurements in this study show that organic carbon remains preserved, in lower but comparable quantities to the diagenetically early concretions. This is possibly due to the iron oxide component (Lalonde et al., 2012), pervasive over displacive growth mechanism, early diagenetic growth, or another unidentified factor.

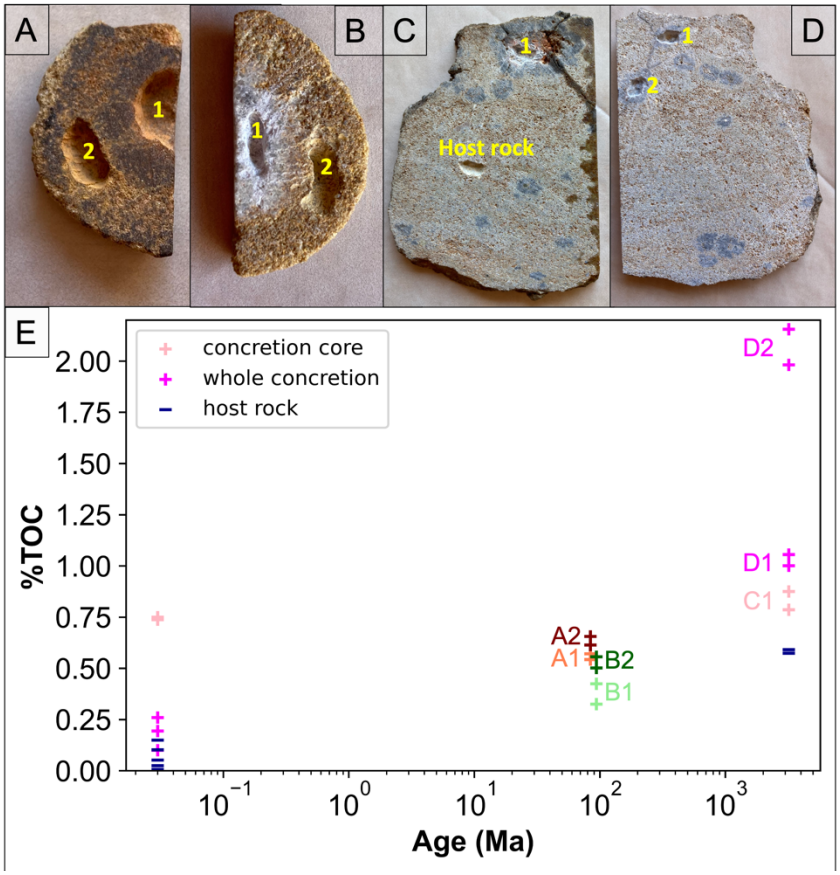

Figure 4.15. Micro-drill hole locations on concretions. A) Gallup Sandstone #6 iron oxide rich concretion 1: inner core, 2: outer core B) Gallup Sandstone #7 quartz rich concretion 1: inner core, 2: outer core C) Moodies Group hand sample 1: differentiated, large, weathered concretion and host rock D) Moodies Group hand sample other side 1: small, fresh, undifferentiated concretion, 2: medium, fresh, differentiated concretion E) TOC vs age in millions of years (Ma) of concretions. All concretion measurements were made in two replicates. Concretion core measurements are in light pink. Whole concretion measurements are in magenta. All concretion measurements have a '+' symbol. All host rock measurements are dark blue and have a '-' symbol. Left most dataset: total

organic carbon of inner core (2 replicates), whole concretions (n=3), and host rock (n=5) in Torrey Pines, San Diego. Coral and maroon measurements correspond to concretion in A. Light green and dark green measurements correspond to concretion in B. Right most dataset measurements belong to the Moodies group in panels C and D.

The concretions from Torrey Pines contain abundant quartz grains, feldspar grains, and fined-grained phyllosilicate phases with iron oxide rims. This is similar to the silica enrichment and predicted composition of the Jezero Crater concretions, which includes aluminum-rich phases like pyrophyllite and potassium feldspar as well as greenalite and the iron oxide phase hematite (Table 4.3 and 4.4). In contrast, the Torrey Pines concretions lack salts compared to the Jezero Crater concretions. This difference may be explained by the environmental conditions during early diagenesis. Pedogenic alteration with acidic fluids, possibly from the leaching of organic acids originating from abundant conifer detritus (Abbott, 1981), may have dissolved any carbonate minerals that would have been incorporated into the concretion. As for sulfate salts, the bedrock of Torrey Pines may have been calcium poor and was too wet (Abbott, 1981) to precipitate any other sulfate minerals as they are extremely soluble (Spencer, 2000). Comparing the mineralogies, it is possible that Jezero Crater concretions thus occurred in more neutral pH and drier conditions and with higher concentrations of calcium and sulfur present. Calcium sulfate veins found in the Hogwallow Flats member further support the probability of a sulfur rich Jezero Crater (Nachon et al., 2024). Futhermore, sulfide-bearing mineral phases are common in Mars' crust. They are present in every Martian meteorite in abundances up to 0.7 wt % (Tarnas et al., 2021); the Gusev Crater Adirondack basalt target contained ~3 wt% S (as SO_3) (Gellert et al., 2004).

The Gallup Formation concretions are composed of iron oxides, siliciclastics, and barite ($BaSO_4$). As above, quartz grains, potassium feldspar grains, aluminum clay phases, and iron oxides are in the predicted mineral mixture of Jezero Crater concretions (Table 4.3 and 4.4). In the case of the Gallup concretions, the poorly soluble sulfate salt phase, barite, is found in the inner core of one concretion. On Earth, concretions containing barite are thought to be formed at a diagenetic front, where barium ions from biogenic barite crystals dissolving in sulfate poor porewater diffuse upwards to combine with sulfate left over in a sulfate reduction zone (Bréhéret and Brumsack, 2000). This occurs at a time of sedimentation quiescence to allow for diffusion timescales and concretion formation during early diagenesis. Although there is no current evidence for barite at Jezero Crater, dissolution of a calcium rich mineral and the subsequent diffusion of calcium through porewater to combine with sulfate ions and precipitate anhydrite enriched concretions is one possible explanation for the sulfate salt phases in the Jezero Crater concretions, albeit at much higher sulfate concentrations. It will only be possible to distinguish if the salt phases in the concretions formed from the process outlined above or from evaporative crystals being incorporated into the concretion through petrographic analysis of the returned samples. Thus, detailed petrographic study of returned samples will reveal how dry the Jezero Crater environment was at the time of concretion formation.

	Torrey Pines	Gallup	Navajo	Moodies	Jezero
Age (Ma)	~0.03	~89	190	3220	~3600-3800
Composition	Fe oxides, phyllosilicates, primary minerals	Fe oxides, primary minerals phyllosilicates, barite	Fe oxides, carbonates	Sulfates (anhydrite), silicified pseudomorphs	Fe oxides, carbonates, phyllosilicates, sulfates
Formation environment	Pedogenic	Deltaic/nearshore	Eolian	Pedogenic	Fluvial/lacustrine/ prodeltaic
Relative time of formation	Early diagenesis	Early diagenesis	Early diagenesis	Early diagenesis	?

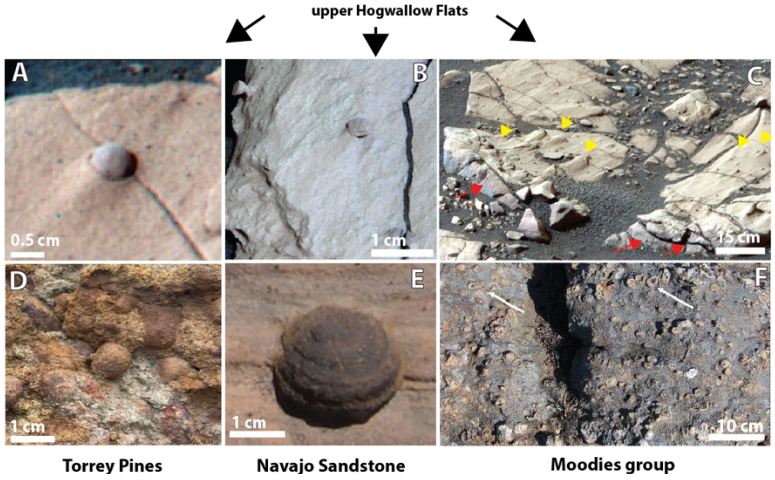

Figure 4.16. Concretions from Hogwallow flats and comparisons with terrestrial analog materials. A) Blueberry-type, Pignut mountain outcrop, upper Hogwallow Flats; B) Flattened, spheroidal concretion, upper Hogwallow Flats, note upper left concretion also with urn-type morphology); C) Abundant putative concretions with positive relief in light-toned outcrop surfaces (yellow arrows) showing transition to darker-toned, mottled material in lower outcrop surface (red arrows), upper Hogwallow Flats; D) Concretion in nodular (Bir) Pleistocene paleosol horizon, Torrey Pines, CA; E), Fe oxide concretion from the Jurassic (~190 Ma) Navajo Sandstone (from Chan et al., 2022); F) Pedogenic sulfate concretions (now silicified pseudomorphs) from gypsic subsurface (By) horizon of Aridisol paleosols in the the Archean (3.2 Ga) Moodies Group, Barberton Greenstone Belt, South Africa (from Nabhan et al., 2016); white arrows indicate hollow concretions with positive relief.

4.9.2 Concretions at Jezero Crater

The concretions found at Jezero Crater most likely precipitated from groundwater present in the Shenandoah formation before lithification and then became exposed post-lithification due to denudation. The nearest neighbor statistics demonstrate that images with concretions that are not highly clustered: the average distance between the concretions is larger than the average size of the concretions, a criterion used in Stack et al. (2014). Widely spaced concretions could be a result of widely spaced favorable nucleation sites, low availability of cementing agent, pH fluctuations, or formation in the presence of more stagnant fluids as noted in some hematite concretions (Abdel-Wahab & McBride, 2001 and references therein; Potter and Chan, 2011). In terms of size and morphology, the only concretions that have maintained spheroidal shape are small (less than ~5 mm). The majority of large and small concretions are flattened, hollow, irregular, or bulbous. The irregularity of shape could have resulted from differential availability of a cementing agent or anisotropies in the host rock that influence the rate of diffusion due to the fine grained matrix (Selles-Martínez, 1996; Stack et al., 2014 and references therein; Potter-Mcintyre et al., 2014; Bowen et al.,

2008). The average concretion is small (2.65 mm), which suggests transport of fluids was limited by the low permeability of the Hogwallow Flats member siltstone host (Chan et al., 2004). The average size is comparable to concretions at Meridiani Planum and in the Sheepbed mudstone at Gale Crater (Table 4.1). However, it is important to note that the largest concretions at Jezero Crater are the largest concretions thus far recorded on Mars (excluding voids and hollow spheroids reported by Wiens et al., (2017)). They are twice as big as the maximum size of concretions reported previously (Sun et al., 2019), implying a longer duration of groundwater presence than ever before to allow greater concretion growth.

The diversity of concretions found suggests a variety of growth mechanisms at play. The homogeneously dark-toned concretion (seen from the fractured concretion, Figure 4.2) is likely a result of pervasive growth (Raiswell and Fischer, 2000). If the light toned rings in the large, complex concretions (Figure 4.2C,F) correspond to compositional differences, it suggests that radial growth may have formed these features from episodes of varying fluid chemistries. Hollow nodules can result from a well-cemented rind and weakly cemented core, dissolution of a secondary soluble mineral phase in the core, or the exsolution of gas bubbles from diagenetic pore fluids but rover data is not available to determine the mechanism (Stack et al., 2014 and references therein). The observation of 'mushroom-like' concretion morphologies is likely a result of wind driven sediment transport abrasion around a concretion producing a form similar to a ventifact or directional subsurface fluid flow and a ventifact like erosion pattern. Another possibility is the bedrock containing fractures parallel to the stem along which cementing waters for the concretion could have preferentially sourced an anisotropic cement phase that appears like a stem.

We cannot conclude the timing of formation of the concretions from the data at hand since we do not have access to a view of the laminations around the concretion, which would inform its compaction history (Schwid et al., 2021). Biosignature preservation potential is highest when early diagenetic precipitation occurs across all mineral precipitates on Earth (Bosak et al. 2021). On the other hand, radiolytic processing can degrade biosignatures significantly (Chan et al. 2019). However, rocks of similar radiation exposure on Earth as Jezero Crater contain biosignatures that persist (Bosak et al., 2024). It will also be critical to differentiate any carbonaceous matter present in these concretions of abiotic origin.

The composition of the concretions reveals the possible composition and geochemical characteristics and processes occurring in the pore fluid(s) that created them (Selles-Martínez, 1996; Chan et al., 2022; Benites et al., 2018; Vuillemin et al., 2013; Wei et al., 2020). At the Hogwallow Flats member, the concretions have variable enrichment of Mg and Ca with no enrichment in silica. In contrast, the concretions at Yori Pass and White Rocks members were more silicic and had different amounts of cations than the bedrock. This could reflect different ratios of clay and salts, or salts and silicification, in the concretions of these units. The concretions therefore potentially contain secondary salt phases (such as carbonate or sulfate) as well as iron oxide rims based on Mastcam-Z data and iron oxide cement based on SuperCam predictions of mineralogy. Another possibility is that these concretions were precipitated in early diagenetic microenvironments where the chemistry is not that much different than the surrounding host rock, and mineralogy is controlled by pore fluid heterogeneities caused by a lack of transmission throughout the host rock because of the fine-grained nature of the

sediments. In other words, the subsurface fluid is not simply one composition throughout because advection is restricted.

If the concretions are partly composed of carbonate minerals with iron oxide rims, they may have precipitated from the pore water in areas of local saturation by circumneutral pH and/or alkaline waters and undergone iron oxidation from the outside in when the fluid composition shifted. Sirono et al. (2021) modeled carbonate concretions in sandstone of 15 mm diameter developing iron oxide rims using a 1-D diffusion reaction simulation and showed a pH of 4.5-6 was required, with formation time ranging between 270-15000 years. Acidic brines would also force silica to precipitate out of solution and could explain the silica enrichments seen in the concretions (Yoshida et al., 2021). The Jezero Crater concretions appear to have heterogeneous placement of salts, which most closely aligns with the structure of concretions in the Moodies Group. Both the Moodies Group and Jezero Crater also contain the same sulfate salt phase, anhydrite, which suggests that Jezero Crater concretions were perhaps made by a similar process as in the Moodies group. The model of concretion formation for the Moodies group described in Nabhan et al. (2016) invokes hysteresis where the initial carbonate precipitating water was later acidified to precipitate sulfate phases and silicify the concretions. This process is independent of the felsic volcanic bedrock; the silica is sourced from the high fraction of mica/clay minerals in the concretion host rock. In all cases, the hardened silica is excellent at preserving any organic matter associated with the concretion; silicified syngenetic concretions from Earth record a total organic carbon content of up to 9.17% (Yoshida et al., 2021). Furthermore, the presence of phyllosilicates is predicted in Jezero Crater concretions (Table 4.3 and 4.4) and abundantly present in the bedrock (Mars 2020 Initial Reports Volume 2 (Samples 11-21)). Clays have long been implicated in the preservation of organic matter on Earth due to their interlayer charged surfaces (Hemingway et al., 2019; Ehlmann et al., 2008; Kennedy et al., 2002; Kennedy et al., 2011; Kaiser and Guggenberger, 2000; Kleber et al., 2015) and would therefore better retain organic matter if present in the concretions.

Hematite concretions can be composed of a wide variety of framework grains (such as silicate minerals, quartz, gypsum, halite, other salts) and usually have multiple generations of iron oxide in between these components. They are found in a diverse range of environments from Torrey Pines acidic soils studied above to acid saline lakes in Western Australia (modern) and Kansas (Nippewalla Group, 270 Ma) and post-depositional fluid alteration of aeolian sandstone in the Jurassic Navajo Sandstone of southern Utah (Bowen et al., 2008; Benison, 2006; Potter et al., 2011). The Jurassic Navajo Sandstone concretions precipitated in three steps: Fe^{3+} sourced from primary minerals formed early diagenetic grain coatings, a reducing fluid mobilized this iron as Fe^{2+}, Fe^{2+} was oxidized in contact with atmospheric oxygen and produced multiple generations of iron oxide cements throughout diagenesis (Potter et al., 2011). Iron oxide concretions in acidic environments precipitate when Fe^{3+}, mobilized in acidic fluids, comes into contact with atmospheric oxygen (Bowen et al., 2008). Acid saline lakes are a highly relevant analog as the deposits in both Western Australia and the Nippewalla Group consist of salt and phyllosilicate rich bedrock lithology similar to the Hogwallow Flats member and form hematite concretions diagenetically early (Benison, 2006; Bowen et al., 2008). The Australian concretions were dated to be younger than 2,913 +/- 48 years old (Bowen et al., 2008). Even though the lakes occur in silicic continental crust, the aqueous chemistry has altered the bedrock to be similar to the Hogwallow Flats member. However, in both cases, the concretions produced can reach sizes of 4-5 cm and are largely spheroidal (Benison, 2006;

Bowen et al., 2008), which distinguishes them from Jezero Crater concretions. Hematite concretions are able to preserve organic carbon, as this study has shown, and have been proven by other studies to retain biosignatures such as aggregations of microbial-derived organic matter (Weber et al., 2012).

Thus, there are many possible scenarios of concretion formation at Jezero Crater and each scenario reconstructs a very different geochemical environment that is key to understanding the geologic history of the crater. Many of these scenarios imply high biosignature preservation potential.

4.10 Conclusions

The concretions found in Jezero Crater have the most varied morphologies (concentric, oblate, urn, and spheroidal) and are the biggest filled concretions (excluding spherical voids) observed on Mars thus far, with the maximum measured size recorded as ~15.5 mm compared to 7 mm at Gale Crater previously. The Hogwallow Flats member concretions are enriched in Mg and Ca salts whereas the Yori Pass member concretions appear to contain a greater abundance of phyllosilicates than the host rock. By contrast, the White Rocks member concretion contains variable primary minerals, clays, salts, hematite, and amorphous silica and shares some of these minerals with the host rock. At depth, it is calcium enriched and magnesium depleted. All concretions have a finely crystalline hematite signature as inferred from Mastcam-Z multispectral observations, and this signature is similar to the bedrock that hosts concretions. SuperCam analysis suggests that the salts in the concretions are likely Mg, Ca carbonates and calcium sulfate, hematite is a ubiquitous component, and primary minerals and clays have been incorporated into the concretions from the bedrock.

Analog concretions from Torrey Pines reveal an assemblage of primary minerals, phyllosilicates, and iron oxide cement. Analog concretions from the Gallup Formation reveal assemblages of primary minerals with highly varied cement phases (barite, iron oxide, calcite) and zonation. In all three sets of concretion TOC measurements, the concretions preserve greater concentrations of organic carbon than the host rock, demonstrating their high biosignature preservation potential. There is a lack of correlation between age and concretion TOC abundance, suggesting factors other than concretion age are related to the organic content. In the context of comparisons with our other terrestrial analog samples, we therefore propose that depositional age is not the determining factor for TOC preservation in concretions, rather, the formation mechanism and the formation timing compared to surrounding bedrock may be the determining factors of TOC preservation.

Comparisons with terrestrial analog concretions suggest that the concretions observed and possibly sampled at Jezero Crater may represent sites of enhanced organic matter preservation, by occlusion of porosity and protection from subsequent oxidation. Thus, the concretions described in this work may be concentrated in organic carbon and other biosignatures. It is possible that one of the drilled rock cores collected by *Perseverance* at the Hogwallow Flats member sampled through a concretion. Therefore, samples from this area of Jezero Crater are considered among the highest priority samples of astrobiological interest out of the current sample suite (as of Sol ~1100)) for possible return to Earth.

Data Availability

All SuperCam and Mastcam-Z raw and processed data used here is available on the PDS (planetary data science) Geosciences node (Bell & Maki, 2021; Wiens & Maurice, 2021). SuperCam: https://pds-geosciences.wustl.edu/ missions/mars2020/supercam.htm Mastcam-Z: https://pds-imaging.jpl.nasa.gov/volumes/mars2020.html. Supplementary information is available at https://doi.org/10.5281/zenodo.13274582 (Kalucha et al., 2024).

References

Abdel-Wahab, A., & McBride, E. F. (2001). Origin of giant calcite-cemented concretions, temple member, Qasr El Sagha formation (Eocene), Faiyum depression, egypt. *Journal of Sedimentary Research*, *71*(1), 70-81.

Anderson, R. B., Forni, O., Cousin, A., Wiens, R. C., Clegg, S. M., Frydenvang, J., ... & Ehlmann, B. (2022). Post-landing major element quantification using SuperCam laser induced breakdown spectroscopy. *Spectrochimica Acta Part B: Atomic Spectroscopy,* 188, 106347.

Arvidson, R.E., Squyres, S.W., Bell III, J.F., Catalano, J.G., Clark, B.C., Crumpler, L.S., de Souza Jr, P.A., Fairén, A.G., Farrand, W.H., Fox, V.K. and Gellert, R. (2014). Ancient aqueous environments at Endeavour crater, Mars. Science, 343(6169), p.1248097.

Bell, J. F., & Maki, J. N. (2021). Mars 2020 mast camera zoom bundle, from Arizona State University Mastcam-Z instrument team, calibrated products. *PDS Imaging Node*, *10*, q3ts-c749.

Bell, J. F., Maki, J. N., Mehall, G. L., Ravine, M. A., Caplinger, M. A., Bailey, Z. J., ... & Wolff, M. J. (2021). The Mars 2020 perseverance rover mast camera zoom (Mastcam-Z) multispectral, stereoscopic imaging investigation. *Space Science Reviews*, *217*, 1-40.

Benites, M., Millo, C., Hein, J., Nath, B. N., Murton, B., Galante, D., & Jovane, L. (2018). Integrated geochemical and morphological data provide insights into the genesis of ferromanganese nodules. *Minerals*, *8*(11), 488.

Benison, K. C. (2006). A martian analog in Kansas: comparing martian strata with Permian acid saline lake deposits. *Geology*, *34*(5), 385-388.

Benison, K. C., Gill, K. K., Sharma, S., Siljeström, S., Zawaski, M., Bosak, T., et al. (2024). Depositional and diagenetic sulfates of Hogwallow Flats and Yori Pass, Jezero Crater: Evaluating preservation potential of environmental indicators and possible biosignatures from past Martian surface waters and groundwaters. *Journal of Geophysical Research: Planets*, *129*, e2023JE008155. https://doi.org/10.1029/2023JE008155

Berger, J.A., Gellert, R., Boyd, N.I., King, P.L., McCraig, M.A., O'Connell-Cooper, C.D., Schmidt, M.E., Spray, J.G., Thompson, L.M., VanBommel, S.J. and Yen, A.S. (2020). Elemental composition and chemical evolution of geologic materials in Gale Crater, Mars: APXS results from Bradbury landing to the Vera Rubin ridge. *Journal of Geophysical Research: Planets*, 125(12), p.e2020JE006536.

Berner, R. A. (1968). Calcium carbonate concretions formed by the decomposition of organic matter. *Science*, *159*(3811), 195-197.

Bosak, T., Moore, K. R., Gong, J., & Grotzinger, J. P. (2021). Searching for biosignatures in sedimentary rocks from early Earth and Mars. *Nature Reviews Earth & Environment*, *2*(7), 490-506.

Bosak, T., Shuster, D. L., Weiss, B., Mayhew, L. E., Scheller, E. L., Siljestroem, S., ... & Williams, A. J. (2024, March). Astrobiological Potential of Rocks Acquired By the Perseverance Rover at the Front of the Western Sediment Fan in Jezero Crater, Mars. In *55th Lunar and Planetary Science Conference*.

Bowen, B. B., Benison, K. C., Oboh-Ikuenobe, F. E., Story, S., & Mormile, M. R. (2008). Active hematite concretion formation in modern acid saline lake sediments, Lake Brown, Western Australia. *Earth and Planetary Science Letters*, 268(1-2), 52-63.

Broz, A., Aguilar, J., Xu, X., & Silva, L. C. (2023). Accumulation of radiocarbon in ancient landscapes: A small but significant input of unknown origin. *Scientific Reports*, *13*(1), 7476.

Calvin, W. M., Shoffner, J. D., Johnson, J. R., Knoll, A. H., Pocock, J. M., Squyres, S. W., ... & Thompson, S. D. (2008). Hematite spherules at Meridiani: Results from MI, Mini-TES, and Pancam. *Journal of Geophysical Research: Planets*, *113*(E12).

Bréhéret, J. G., & Brumsack, H. J. (2000). Barite concretions as evidence of pauses in sedimentation in the Marnes Bleues formation of the Vocontian Basin (SE France). *Sedimentary Geology*, *130*(3-4), 205-228.

Chan, M. A. (2022). A Perspective on Concretions: Deciphering Diagenesis from Earth to Mars. The Journal of the Geological Society of Japan, 128(1), 445-464.

Chan, M. A., Hinman, N. W., Potter-McIntyre, S. L., Schubert, K. E., Gillams, R. J., Awramik, S. M., ... & Cleaves, H. J. (2019). Deciphering biosignatures in planetary contexts. *Astrobiology*, *19*(9), 1075-1102.

Chan, M. A., Johnson, C. M., Beard, B. L., Bowman, J. R., & Parry, W. T. (2006). Iron isotopes constrain the pathways and formation mechanisms of terrestrial oxide concretions: A tool for tracing iron cycling on Mars?. *Geosphere*, *2*(7), 324-332.

Chan, M. A., Beitler, B., Parry, W. T., Ormö, J., & Komatsu, G. (2004). A possible terrestrial analogue for haematite concretions on Mars. *Nature*, *429*(6993), 731-734.

Chan, M. A., Potter, S. L., Bowen, B. B., Parry, W. T., Barge, L. M., Seiler, W., ... & Bowman, J. R. (2012). Characteristics of terrestrial ferric oxide concretions and implications for Mars.

Christensen, P. R., Bandfield, J. L., Clark, R. N., Edgett, K. S., Hamilton, V. E., Hoefen, T., ... & Smith, M. D. (2000). Detection of crystalline hematite mineralization on Mars by the Thermal Emission Spectrometer: Evidence for near-surface water. *Journal of Geophysical Research: Planets*, *105*(E4), 9623-9642.

Decelles, P. G. (1994). Late Cretaceous-Paleocene synorogenic sedimentation and kinematic history of the Sevier thrust belt, Northeast Utah and Southwest Wyoming. *Geological Society of America Bulletin*, *106*(1), 32-56.

Edgar, L. A., Fedo, C. M., Gupta, S., Banham, S. G., Fraeman, A. A., Grotzinger, J. P., ... & Van Beek, J. (2020). A lacustrine paleoenvironment recorded at Vera RubinRidge, Gale crater: Overview of the sedimentology and stratigraphy observed by the Mars ScienceLaboratory Curiosity Rover. *Journal of Geophysical Research: Planets*, *125*(3), e2019JE006307.

Ehlmann, B. L., Mustard, J. F., Fassett, C. I., Schon, S. C., Head III, J. W., Des Marais, D. J., ... & Murchie, S. L. (2008). Clay minerals in delta deposits and organic preservation potential on Mars. *Nature Geoscience*, *1*(6), 355-358.

Fairén, A. G., Squyres, S. W., Grotzinger, J. P., Calvin, W. M., & Ruff, S. W. (2014, March). Hollowed Spherules Identified with the MER Opportunity Near and at Cape York, Western Rim of Endeavour Crater, Mars. In *45th Annual Lunar and Planetary Science Conference* (No. 1777, p. 1566).

Farley, K. A., Williford, K. H., Stack, K. M., Bhartia, R., Chen, A., de la Torre, M., ... & Wiens, R. C. (2020). Mars 2020 mission overview. *Space Science Reviews*, *216*, 1-41.

Farrand, W.H., Bell III, J.F., Johnson, J.R., Rice, M.S., Jolliff, B.L. and Arvidson, R.E., 2014. Observations of rock spectral classes by the Opportunity rover's Pancam on northern Cape York and on Matijevic Hill, Endeavour Crater, Mars. *Journal of Geophysical Research: Planets*, 119(11), pp.2349-2369.

Fischer, W. W., Fike, D. A., Johnson, J. E., Raub, T. D., Guan, Y., Kirschvink, J. L., & Eiler, J. M. (2014). SQUID–SIMS is a useful approach to uncover primary signals in the Archean sulfur cycle. *Proceedings of the National Academy of Sciences*, *111*(15), 5468-5473.

Fouchet, T., Reess, J. M., Montmessin, F., Hassen-Khodja, R., Nguyen-Tuong, N., Humeau, O., ... & Wiens, R. C. (2022). The SuperCam infrared spectrometer for the perseverance rover of the Mars2020 mission. *Icarus*, *373*, 114773.

Gasda, P. J., Comellas, J., Essunfeld, A., Das, D., Bryk, A. B., Dehouck, E., ... & Reyes-Newell, A. (2022). Overview of the morphology and chemistry of diagenetic features in the clay-rich Glen Torridon unit of Gale crater, Mars. *Journal of Geophysical Research: Planets*, *127*(12), e2021JE007097.

Gellert et al. (2004), Chemistry of Rocks and Soils in Gusev Crater from the Alpha Particle X-ray Spectrometer. *Science* 305, 829-832. DOI:10.1126/science.1099913

Giallorenzo, M., Wells, M., Yonkee, W., Stockli, D., & Wernicke, B. (2018). Timing of exhumation, Wheeler pass thrust sheet, southern Nevada and California: Late Jurassic to middle Cretaceous evolution of the southern Sevier fold-and-thrust belt. *GSA Bulletin*, *130*(3-4), 558-579.

Grotzinger, J. P., & Milliken, R. E. (2012). *Sedimentary Geology of Mars*. SEPM Society for Sedimentary Geology.

Grotzinger, J.P., Sumner, D.Y., Kah, L.C., Stack, K., Gupta, S., Edgar, L., Rubin, D., Lewis, K., Schieber, J., Mangold, N. and Milliken, R. (2014). A habitable fluvio-lacustrine environment at Yellowknife Bay, Gale Crater, Mars. *Science,* 343(6169), p.1242777.

Haber, J. T., Horgan, B., Fraeman, A. A., Johnson, J. R., Bell III, J. F., Rice, M. S., ... & Jacob, S. (2022). Mineralogy of a possible ancient lakeshore in the Sutton Island member of Mt. Sharp, Gale crater, Mars, from Mastcam multispectral images. *Journal of Geophysical Research: Planets*, *127*(10), e2022JE007357.

Harris, D., Horwáth, W. R., & Van Kessel, C. (2001). Acid fumigation of soils to remove carbonates prior to total organic carbon or carbon-13 isotopic analysis. *Soil Science Society of America Journal*, 65(6), 1853-1856.

Hemingway, J. D., Rothman, D. H., Grant, K. E., Rosengard, S. Z., Eglinton, T. I., Derry, L. A., & Galy, V. V. (2019). Mineral protection regulates long-term global preservation of natural organic carbon. *Nature*, *570*(7760), 228-231.

Kaiser, K., & Guggenberger, G. (2000). The role of DOM sorption to mineral surfaces in the preservation of organic matter in soils. *Organic Geochemistry*, *31*(7-8), 711-725.

Kennedy, M. J., Pevear, D. R., & Hill, R. J. (2002). Mineral surface control of organic carbon in black shale. *Science*, *295*(5555), 657-660.

Kennedy, M. J., & Wagner, T. (2011). Clay mineral continental amplifier for marine carbon sequestration in a greenhouse ocean. *Proceedings of the National Academy of Sciences*, *108*(24), 9776-9781.

Kleber, M., Eusterhues, K., Keiluweit, M., Mikutta, C., Mikutta, R., & Nico, P. S. (2015). Mineral–organic associations: formation, properties, and relevance in soil environments. *Advances in Agronomy*, *130*, 1-140.

Lalonde, K., Mucci, A., Ouellet, A., & Gélinas, Y. (2012). Preservation of organic matter in sediments promoted by iron. *Nature*, *483*(7388), 198–200. https://doi.org/10.1038/nature10855

Lin, W., Bhattacharya, J. P., & Stockford, A. (2019). High-resolution sequence stratigraphy and implications for Cretaceous Glacioeustasy of the late Cretaceous Gallup system, New Mexico, U.S.A. *Journal of Sedimentary Research*, 89(6), 552-575.

Lin, W., Bhattacharya, J. P., Jicha, B. R., Singer, B. S., & Matthews, W. (2020). Has earth ever been ice-free? Implications for glacio-eustasy in the Cretaceous greenhouse age using high-resolution sequence stratigraphy. *GSA Bulletin*, 133(1-2), 243-252.

Lin, W., & Bhattacharya, J. P. (2020). Storm-flood-dominated delta: A new type of delta in stormy oceans. *Sedimentology,* 68(3), 1109-1136.

Loope, D. B., Kettler, R. M., & Weber, K. A. (2010). Follow the water: Connecting a CO2 reservoir and bleached sandstone to iron-rich concretions in the Navajo Sandstone of south-central Utah, USA. *Geology*, 38(11), 999-1002.

Loope, D. B., Kettler, R. M., Weber, K. A., Hinrichs, N. L., & Burgess, D. T. (2012). Rinded iron-oxide concretions: hallmarks of altered siderite masses of both early and late diagenetic origin. *Sedimentology*, *59*(6), 1769-1781.

Mandon, L., Quantin-Nataf, C., Royer, C., Beck, P., Fouchet, T., Johnson, J.R., Dehouck, E., Le Mouélic, S., Poulet, F., Montmessin, F., Pilorget, C., Gasnault, O., Forni, O., Mayhew, L.E., Beyssac, O., Bertrand, T., Clavé, E., Pinet, P., Brown, A.J., Legett, C., Tarnas, J., Cloutis, E.A., Poggiali, G., Fornaro, T., Maurice, S., Wiens, R.C., Team, T.S., n.d. Reflectance of Jezero crater floor: 2. Mineralogical interpretation. *Journal of Geophysical Research: Planets*, e2022JE007450. https://doi.org/10.1029/2022JE007450

Mangold, N., Dromart, G., Ansan, V., Salese, F., Kleinhans, M. G., Massé, M., ... & Stack, K. M. (2020). Fluvial regimes, morphometry, and age of Jezero crater paleolake inlet valleys and their exobiological significance for the 2020 Rover Mission Landing Site. *Astrobiology*, *20*(8), 994-1013.

Mars 2020 Initial Reports Volume 2 (Samples 11-21), Planetary Data Science Geosciences Node: https://pds-geosciences.wustl.edu/missions/mars2020/returned_sample_science.htm

Marshall, J. D., & Pirrie, D. (2013). Carbonate concretions—explained. *Geology Today*, *29*(2), 53-62.

McLennan, S. M., Bell Iii, J. F., Calvin, W. M., Christensen, P. R., Clark, B. D., De Souza, P. A., ... & Yen, A. (2005). Provenance and diagenesis of the evaporite-bearing Burns formation, Meridiani Planum, Mars. *Earth and Planetary Science Letters*, *240*(1), 95-121.

Merusi, M., Kinch, K. B., Madsen, M. B., Bell III, J. F., Maki, J. N., Hayes, A. G., ... & Gasnault, O. (2022). The Mastcam-Z Radiometric Calibration Targets on NASA's Perseverance Rover: Derived Irradiance Time-Series, Dust Deposition, and Performance Over the First 350 Sols on Mars. *Earth and Space Science*, *9*(12), e2022EA002552.

Molenaar, C. M. (1973). Sedimentary facies and correlation of the Gallup Formation and associated formations, northwestern New Mexico.

Molenaar, C. M. (1974, January). Correlation of the Gallup Formation and associated formations, upper cretaceous, eastern San Juan and Acoma Basins, New Mexico. In *Ghost Ranch, central-*

northern New Mexico: New Mexico Geological Society Guidebook to 25th Field Conference (pp. 251-258).

Nabhan, S., Luber, T., Scheffler, F., & Heubeck, C. (2016). Climatic and geochemical implications of Archean pedogenic gypsum in the Moodies group (~ 3.2 Ga), Barberton Greenstone Belt, South Africa. *Precambrian Research*, 275, 119-134.

Nabhan, S., Marin-Carbonne, J., Mason, P. R., & Heubeck, C. (2020). In situ S-isotope compositions of sulfate and sulfide from the 3.2 Ga Moodies Group, South Africa: A record of oxidative sulfur cycling. *Geobiology*, *18*(4), 426-444.

Nachon, M., López-Reyes, G., Meslin, P. Y., Ollila, A., Mandon, L., Clavé, E., ... & Kanine, O. A. (2024, March). Light-toned veins and material in Jezero crater, Mars, as seen in-situ via Nasa's Perseverance Rover (mars 2020 mission): stratigraphic distribution and compositional results. In *LPSC 2024-55th Lunar and Planetary Science Conference* (p. 2349).

Nummedal, D., & Molenaar, C. M. (1995). Sequence stratigraphy of ramp-setting strand plain successions: the Gallup Formation, New Mexico.

Olsen, R.M. (2022). Searching Mass-Balance Analysis to Find the Composition of Martian Blueberries. *Minerals,* 12(6), p.777.

Pilleri, P., Chen, Z., Cousin, A., Maurice, S., Forni, O., Xin, R., ... & Wiens, R. C. (2023, March). Comparison of ChemCam, SuperCam and MarSCoDe LIBS instruments on Mars. *In 54th Lunar and Planetary Science Conference 2023* (Vol. 54, p. 1351).

Potter-McIntyre, S. L., Chan, M. A., & McPherson, B. J. (2014). Concretion formation in volcaniclastic host rocks: evaluating the role of organics, mineralogy, and geochemistry on early diagenesis. *Journal of Sedimentary Research*, 84(10), 875-892.

Potter, S. L., & Chan, M. A. (2011). Joint controlled fluid flow patterns and iron mass transfer in Jurassic Navajo Sandstone, Southern Utah, USA. *Geofluids*, 11(2), 184-198.

Potter, S. L., Chan, M. A., Petersen, E. U., Dyar, M. D., & Sklute, E. (2011). Characterization of Navajo Sandstone concretions: Mars comparison and criteria for distinguishing diagenetic origins. *Earth and Planetary Science Letters*, 301(3-4), 444-456.

Raiswell, R. (1987). Non-steady state microbiological diagenesis and the origin of concretions and nodular limestones. *Geological Society, London, Special Publications*, *36*(1), 41-54.

Raiswell, R., & Fisher, Q. J. (2000). Mudrock-hosted carbonate concretions: a review of growth mechanisms and their influence on chemical and isotopic composition. *Journal of the Geological Society*, 157(1), 239-251.

Ray, D., Shukla, A. D., Bhattacharya, S., Gupta, S., Jha, P., & Chandra, U. (2021). Hematite concretions from the Late Jurassic Jhuran sandstone, Kutch, western India: Implications for sedimentary diagenesis and origin of "blueberries" on Mars. *Planetary and Space Science*, *197*, 105163.

Rice, M. S., Seeger, C., Bell, J., Calef, F., St. Clair, M., Eng, A., ... & Wellington, D. (2022). Spectral diversity of rocks and soils in Mastcam observations along the Curiosity rover's traverse in Gale crater, Mars. *Journal of Geophysical Research: Planets*, *127*(8), e2021JE007134.

Royer, C., Fouchet, T., Mandon, L., Clavé, E., Montmessin, F., Poulet, F., Forni, O., Johnson, J.R., Gasnault, O., Quantin-Nataf, C., Dehouck, E., Beck, P., Benzerara, K., Mouélic, S.L., Caravaca, G., Brown, A., Pilorget, C., Ollila, A.M., Newell, R., Maurice, S., Wiens, R.C., 2022. Investigation on the Clay-Carbonate Mixture with SuperCam/IRS, Perseverance Rover. *Presented at the AGU Fall Meeting 2022.*

Saitoh, M., Olivier, N., Garçon, M., Boyet, M., Thomazo, C., Alleon, J., ... & Marin-Carbonne, J. (2021). Metamorphic origin of anastomosing and wavy laminas overprinting putative microbial deposits from the 3.22 Ga Moodies Group (Barberton Greenstone Belt). *Precambrian Research*, *362*, 106306.

Schwid, M. F., Xiao, S., Nolan, M. R., & An, Z. (2021). Differential weathering of diagenetic concretions and the formation of Neoproterozoic annulated discoidal structures. *Palaios*, *36*(1), 15-27.

Seilacher, A. (2001). Concretion morphologies reflecting diagenetic and epigenetic pathways. *Sedimentary Geology*, 143(1-2), 41-57.

Sellés-Martínez, J. (1996). Concretion morphology, classification and genesis. *Earth-Science Reviews,* 41(3-4), 177-210.

Sirono, S. I., Shibata, T., Katsuta, N., & Yoshida, H. (2021). Numerical simulation of iron oxide concretions on Earth and Mars through calcite dissolution. *Geochimica et Cosmochimica Acta*, *295*, 194-206.

Slotznick, S. P., & Fischer, W. W. (2016). Examining archean methanotrophy. *Earth and Planetary Science Letters*, *441*, 52-59.

Smith, M. E., McNeill, D. F., Murray, S. T., & Swart, P. K. (2023). Internal isotopic variability of Neogene carbonate concretions: Constraining formational growth mechanisms and isotopic disequilibrium. *Sedimentology.*

Spencer, R. J. (2000). Sulfate minerals in evaporite deposits. *Sulfate Minerals: Crystallography, Geochemistry, and Environmental Significance*, *40*, 173-192.

Squyres, S. W., Grotzinger, J. P., Arvidson, R. E., Bell III, J. F., Calvin, W., Christensen, P. R., ... & Soderblom, L. A. (2004). In situ evidence for an ancient aqueous environment at Meridiani Planum, Mars. *Science*, *306*(5702), 1709-1714.

Squyres, S. W., Arvidson, R. E., Bell Iii, J. F., Bruckner, J., Cabrol, N. A., Calvin, W., ... & Yen, A. (2004). The opportunity rover's Athena science investigation at Meridiani Planum, Mars. *Science*, *306*(5702), 1698-1703.

Stack, K.M., Grotzinger, J.P., Kah, L.C., Schmidt, M.E., Mangold, N., Edgett, K.S., Sumner, D.Y., Siebach, K.L., Nachon, M., Lee, R., Blaney, D.L., L. P. Deflores, L. A. Edgar, A. G. Fairén, L. A. Leshin, S. Maurice, D. Z. Oehler, M. S. Rice, R. C. Wiens (2014). Diagenetic origin of nodules in the Sheepbed member, Yellowknife Bay formation, Gale crater, Mars. *Journal of Geophysical Research: Planets,* 119(7), pp.1637-1664.

Stack, K. M., Ives, L. R., Gupta, S., Lamb, M. P., Tebolt, M., Caravaca, G., ... & Wiens, R. C. (2024). Sedimentology and Stratigraphy of the Shenandoah Formation, Western Fan, Jezero Crater, Mars. *Journal of Geophysical Research: Planets*, *129*(2), e2023JE008187.

Sun, M. S., & Allen, J. E. (1957). Authigenic brookite in Cretaceous Gallup Formation, Gallup, New Mexico. *Journal of Sedimentary Research*, *27*(3), 265-270.

Sun, V.Z., Stack, K.M., Kah, L.C., Thompson, L., Fischer, W., Williams, A.J., Johnson, S.S., Wiens, R.C., Kronyak, R.E., Nachon, M. and House, C.H. (2019). Late-stage diagenetic concretions in the Murray formation, Gale crater, Mars. *Icarus*, 321, pp.866-890.

Tarnas, J. D., Mustard, J. F., Sherwood Lollar, B., Stamenković, V., Cannon, K. M., Lorand, J.-P., et al. (2021), Earth-like Habitable Environments in the Subsurface of Mars. *Astrobiology*, 21(6), 741–756. https://doi.org/10.1089/ast.2020.2386

Treiman, A. H., Lanza, N. L., VanBommel, S., Berger, J., Wiens, R., Bristow, T., ... & Anderson, R. (2023). Manganese-Iron Phosphate Nodules at the Groken Site, Gale Crater, Mars. *Minerals*, *13*(9), 1122.

Vuillemin, A., Ariztegui, D., De Coninck, A. S., Lücke, A., Mayr, C., Schubert, C. J., & PASADO Scientific Team. (2013). Origin and significance of diagenetic concretions in sediments of Laguna Potrok Aike, southern Argentina. *Journal of Paleolimnology*, 50, 275-291.

Weber, K. A., Spanbauer, T. L., Wacey, D., Kilburn, M. R., Loope, D. B., & Kettler, R. M. (2012). Biosignatures link microorganisms to iron mineralization in a paleoaquifer. *Geology*, *40*(8), 747-750.

Wiens, R. C., & Maurice, S. A. (2021). Mars 2020 perseverance rover SuperCam raw, calibrated, and derived data products. *PDS Geosciences Node*, *10*, 1522646.

Williford, K. H., Farley, K. A., Stack, K. M., Allwood, A. C., Beaty, D., Beegle, L. W., ... & Wiens, R. C. (2018). The NASA Mars 2020 rover mission and the search for extraterrestrial life. In *From habitability to life on Mars* (pp. 275-308). Elsevier.

Wilson, J. H., McLennan, S. M., Glotch, T. D., Rasbury, E. T., Gierlowski-Kordesch, E. H., & Tappero, R. V. (2012). Pedogenic hematitic concretions from the Triassic New Haven Arkose, Connecticut: Implications for understanding Martian diagenetic processes. *Chemical Geology*, 312, 195-208.

Winn Jr, R. D., Stonecipher, S. A., & Bishop, M. G. (1984). Sorting and wave abrasion: controls on composition and diagenesis in lower Frontier sandstones, southwestern Wyoming. *AAPG Bulletin*, *68*(3), 268-284.

Yoon, H., Ingraham, M. D., Grigg, J., Rosandick, B., Mozley, P., Rinehart, A., ... & Dewers, T. (2019). Impact of Depositional and Diagenetic Heterogeneity on Multiscale Mechanical Behavior of Mancos Shale, New Mexico and Utah, USA.

Yoshida, H., Hasegawa, H., Katsuta, N., Maruyama, I., Sirono, S., Minami, M., ... & Metcalfe, R. (2018). Fe-oxide concretions formed by interacting carbonate and acidic waters on Earth and Mars. *Science Advances*, *4*(12), eaau0872.

Yoshida, H., Kuma, R., Hasegawa, H., Katsuta, N., Sirono, S. I., Minami, M., ... & Metcalfe, R. (2021). Syngenetic rapid growth of ellipsoidal silica concretions with bitumen cores. *Scientific Reports*, 11(1), 4230.

Chapter 5

BIOTIC AND ABIOTIC SIGNATURES IN SULFATE— AND CARBONATE— RICH HYPERSALINE LAKES AS ANALOGS FOR MARS

Hemani Kalucha[1*], Ben Johnson[2], Miquela Ingalls[3], Hanna C. Leapaldt[3], Ellen Olsen[3], James Mullahoo[1], Woodward Fischer[1]

[1]California Institute of Technology

[2]Iowa State University

[3]Pennsylvania State University

5.1 Abstract

Sulfate and carbonate rich deposits have been detected at Jezero and Gale craters on Mars and are interpreted as lacustrine. The preservation of potential biosignatures in these sites may depend on the nature of precipitated salts and early diagenetic history of *in situ* minerals. Here, we explore a collection of potentially analogous hypersaline depositional environments in British Columbia. Magnesium- and other sulfate and carbonate salts precipitate from the variable water chemistry of Atlin Playa and a suite of lakes on the Cariboo Plateau. We used scanning electron microscopy with energy dispersive spectra (SEM-EDS) to distinguish between authigenic and detrital grains. Authigenic mineral textures tend to be globular or acicular clumps or delicately preserved cement that envelops angular, detrital grains and their composition reveals lake chemistry. However, micro-scale authigenic textures become rare below the surface due to early diagenetic dissolution and reprecipitation cycles occurring in these lakes. They are replaced with ~100 micron salt crystal domains. Such early diagenetic overprinting could pose problems for identifying primary environments in 3-4 billion year old rocks on Mars. We found total organic carbon is correlated with abundance of salt minerals specifically. The samples with the highest organic carbon content have an optimum salt content. This designates hypersaline lakes as key preservers of organic carbon, and salts, as the highest priority mineral target for finding organic carbon on Mars.

5.2 Introduction

The detection of magnesium sulfate at Meridiani Planum, Mars was once used as evidence against the habitability of Mars [Tosca et al., 2008]. The few studies that have measured organic carbon content of sulfate minerals in terrestrial evaporites, gypsum veins, and impactites report a low range from 0.009% to ~0.6% [Aubrey et al., 2006; Schwartz et al., 2003; Dobrea et al., 2016]. However, carbonate endostromatolites in the same impactites preserve up to ~8% organic carbon [Lacelle et al., 2009] and 3.2 Ga gypsum concretions from the Moodies Group in South Africa can host up to ~2% organic carbon [Kalucha et al., 2024]. Organic carbon content in acidic sulfate lakes in Western Australia is also low, never exceeding 1.8% [Ruecker et al., 2016]. Organics in Mars salt-rich deposits were below the detection limits of both Perseverance rover at Hogwallow Flats and Curiosity rover in the Mg-sulfate bearing unit [Broz et al., 2024; Rapin et al., 2023; Clark et al., 2024]. Saline environments have thus been dismissed as good targets for biosignature preservation.

As rovers and orbiters have explored Mars through the decades, evidence for widespread and diverse sulfate salts has emerged. At Curiosity's landing site (Gale crater) [Grotzinger et al., 2012], many sulfate salts (jarosite, gypsum, bassanite, anhydrite, starkeyite, kieserite, and akaganeite) were detected ubiquitously in the stratigraphy as well as in enriched intervals corresponding to the Glen Torridon region, Vera Rubin Ridge, and the Mg-sulfate bearing unit [Vaniman et al., 2024 and references therein]. Textural and sedimentological observations of the sulfate suggest saline groundwater as a source for the calcium sulfates, acidic groundwater for the jarosite, and hypersaline lacustrine deposition for the magnesium sulfate deposits [Vaniman et al., 2024; Rapin et al., 2019; Bristow et al., 2021]. Perseverance's landing site [Farley et al., 2020], Jezero crater, hosts a fan in the sedimentary basin interbedded with lacustrine deposits. The lacustrine unit, Hogwallow Flats, hosts a variety of sulfate salts, such as Fe,Mg sulfates, in the rock matrix (up to 30 wt%), gypsum and anhydrite crystals, and jarosite patches [Broz et al., 2024; Benison et al. 2024; Stack et al. 2024]. Based on textural and chemical analyses, there is evidence of both sulfate deposition in a hypersaline environment and acid weathering. The Mars Sample Return mission will return two samples from

this unit [McCubbin et al., 2025] that have been impacted by both processes. The marginal carbonate unit in Jezero Crater is also possibly an Mg-carbonate rich lacustrine deposit [Horgan et al. 2020; Horgan et al. 2024].

The salts detected in these rock packages on Mars overlap with salts generated by hypersaline lakes on Earth. It then becomes important to determine the biosignature preservation of terrestrial hypersaline lakes. We now know that saline lakes on Earth have rich microbial ecosystems [Tazi et al., 2014; Pontefract et al., 2017; Sorokin et al., 2014] and high organic carbon content in their sediments [Liang et al., 2024 and references therein; Contreras et al. 2018]. To what degree do the deposits of these lakes preserve information about the microbial ecosystem? Does the lake chemistry promote biosignature preservation? We do not have a rich understanding of the biosignature preservation mechanisms of these lakes.

The primary goal of the Perseverance mission is to search for evidence of past life on Mars [Farley et al., 2020]. The rubric for finding evidence of past life has prioritized searching for organic matter in fine grained deposits with ambiguity towards salt deposits [Summons et al., 2011]. Previous findings have included organic matter detections in mudstones at Gale Crater [Eigenbrode et al., 2018] and organic matter detections within authigenic phosphates in fine grained deposits at Jezero Crater [Hurowitz et al., 2025]. The purpose of this study is to investigate if salts can be similarly powerful in preserving organic matter such that they should be added to the mission target strategy.

However, most terrestrial lacustrine environments are not suitable analogs because Mars is an iron and magnesium rich planet [McSween Jr. et al., 2009]. Lacustrine sediments in both Gale and Jezero Crater consist of iron and magnesium sulfates as the dominant lithology [Rapin et al. 2019; Broz et al. 2024]. The marginal carbonate unit in Jezero Crater is made up of magnesium carbonate [Horgan et al. 2020]. Lakes on Earth are dominated by sodium and chloride ions in their waters (Figure 5.1) and calcium carbonate deposits [Gierlowski-Kordesch, 2010]. The Cariboo Plateau is a rare example of chemical weathering of mafic bedrock resulting in lake waters dominated by magnesium and sulfate ions (Figure 5.1). Atlin Playa is one of the few places on Earth where magnesium carbonate is deposited at surface temperatures [Mavromatis et al. 2021]. This is due to chemical weathering of ultramafic bedrock and microbial sulfate reduction [Power et al., 2009], both of which generate large amounts of alkalinity needed for Mg carbonate precipitation [Tosca and Tutolo, 2023]. Basque Lake #1 and Salt Lake ionic concentrations represent the late stage evolution of Martian lakes as they were drying out. Our sampling at Last Chance Lake, which has intermediate concentrations of sulfate (Figure 1, global mean of sulfate concentration in lakes = 44.50 mmol/l), serves as a comparison of how mineral precipitation is affected by lake water concentration and represents an earlier stage of Martian lakes. The concentrations of carbonate ions in the lakes are in the order Salt Lake < Basque Lake #1 < Atlin Playa < Last Chance Lake [Nichols et al. 2023; Power et al. 2014]. This spectrum of dissolved inorganic carbon concentrations allows an evaluation of the relationship between concentration of anions and the dominant salts in the deposits.

Thus, we must use these terrestrial analogs to learn more about how saline environments apply to the search for life on Mars: what do the deposits of these lakes preserve about lake chemistry, how are sediments being made, what biosignatures do these lakes generate, which of those biosignatures are preserved through early diagenesis, and the role of salt precipitates in this preservation. Here, we

investigate these questions by identifying mineral texture and composition of the lake deposits as well as measuring organic carbon content and sulfur isotopes as potential biosignatures. We report sulfur isotopes of the sulfate salts in the lake sediments of the Cariboo Plateau and Atlin Playa for the first time. Isotopes are powerful indicators of process even when textural and molecular information is lost and can be compared to measurements of return samples such as the two cores from the Hogwallow Flats member [McCubbin et al., 2025].

5.3 Geologic setting

Salt Lake, Last Chance Lake, and Basque Lake #1 are located in the Cariboo Plateau (Figure 5.2), which lies between the Coast Mountains and the Rocky Mountains at an altitude of 1050-1250 m. The Plateau is made up of Miocene and Pliocene basalt flows and is covered by up to ~5 m of glaciofluvial sediments [Renaut and Long, 1989]. Deglaciation occurred 10,000 years ago, forming thousands of lakes on the Plateau [Renaut and Long, 1989 and references therein]. The nearby Marble Range is made up of marine limestones, cherts, argillites, greenstones and Permian to Jurassic aged basic lavas of the Cache Creek Terrane [Nesbitt, 1990]. All of these lithologies contribute detrital minerals to the Cariboo lakes and thus determine their water chemistry. Atlin Playa is of similar age (~8,000 years) and situated on ultramafic bedrock of the Middle Jurassic Teslin Plateau (Figure 5.2), consisting of serpentinized harzburgite, dunite, and listvenite [Mavromatis et al., 2021 and references therein; Power et al., 2009 and references therein]. It has an elevation of 674 m [Power et al., 2009].

The Cariboo lakes are closed basin lakes that are fed by groundwater, nearby springs, and snowmelt. They are ephemeral, typically shallow pans in the wet season (April to June) that are reduced to small, individual pools in the dry season (autumn) [Renaut, 1993 and references therein; Nesbitt, 1990; Renaut and Long, 1989 and references therein; Raudsepp et al., 2024 and references therein]. This seasonal drying results in a large range of salinity (<1 to > 350 g/l), depth (<15 m), length (up to 5 km long), and chemical compositions. The saline lakes (> 10 g/l dissolved solids) are small and < 4 m deep [Renaut and Long, 1989 and references therein]. Atlin Playa covers an area of 0.11 km^2 [Power et al., 2009]. All four of the lakes in this study are highly alkaline: Atlin Playa = up to 8,480, Last Chance Lake = 17,600, Salt Lake = 980, Basque Lake = 2,540 mg HCO_3^-/L [Nichols et al., 2023; Power et al., 2014] and rich in microbial life [Foster et al., 2010; Power et al., 2007].

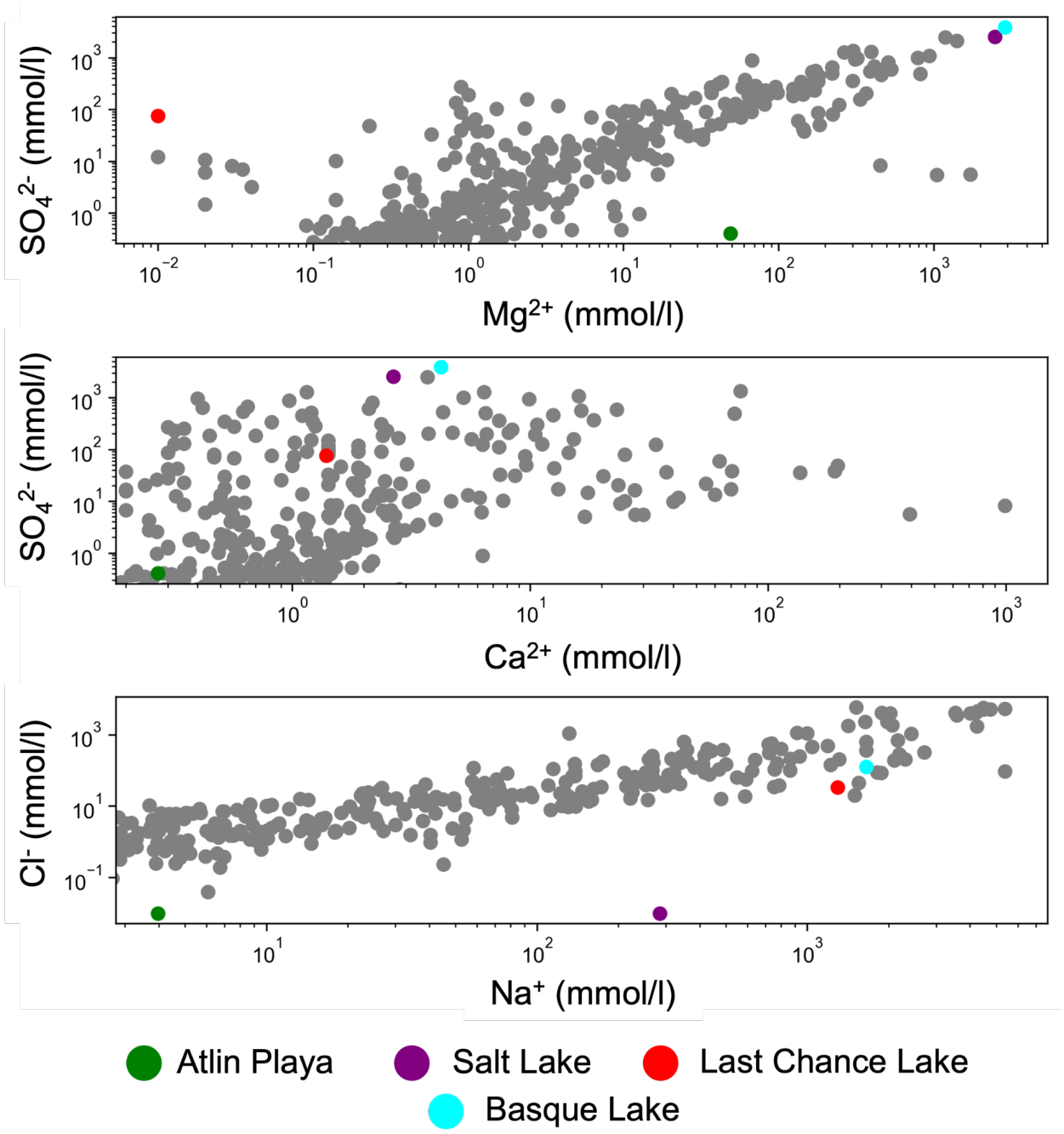

Figure 5.1: Major element chemistry of 663 lakes and 106 reservoirs in grey from Dordoni et al. (2023). Major element chemistry of lakes in this study (Table S1) plotted in green (Atlin Playa), purple (Salt Lake), red (Last Chance Lake), and cyan (Basque Lake). Adapted from Dordoni et al. (2023).

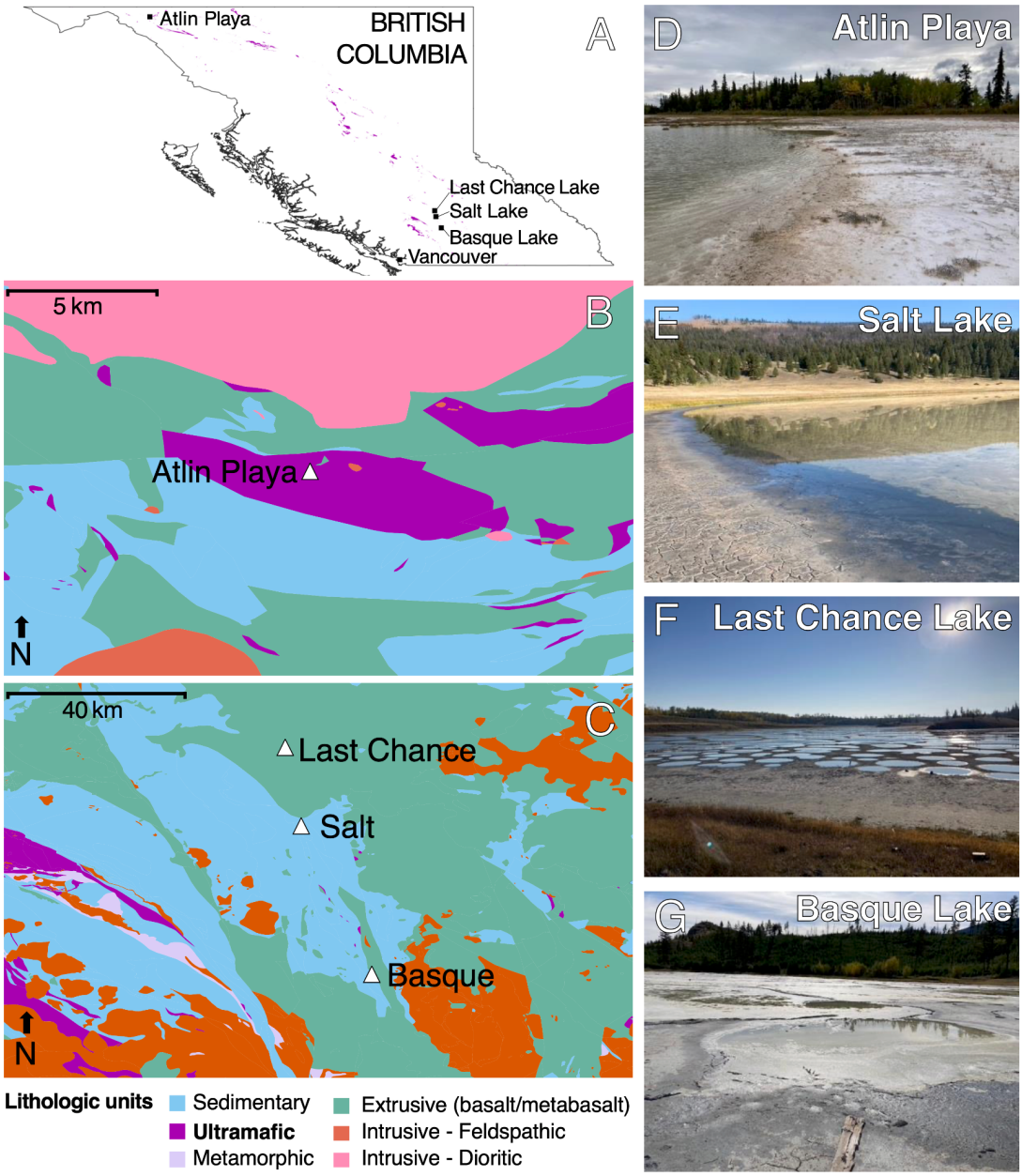

Figure 5.2: Maps and field images. A) Map of British Columbia, Canada with lake and ultramafic bedrock locations B) Bedrock surrounding Atlin Playa (59.573561°, 133.696717°) [Cui et al., 2017] C) Bedrock surrounding Last Chance Lake (LC, 51.32795°, 121.637175°), Salt Lake (S, 51.076028°, 121.585889°), and Basque Lake #1 (BL, 50.600161°, 121.359497°) [Cui et al., 2017] D) Mg-carbonate rich Atlin Playa E) Mg-sulfate rich Salt Lake F) Na-carbonate and sulfate rich Last Chance Lake G) Mg-sulfate rich Basque Lake #1

5.4 Methods

In September 2023, we collected a transect of samples from each lake spanning subaqueous to on shore sites. At each site, we sampled surface sediment and either sediment cores or meter-deep pits at several depth intervals to access the subsurface. Subsurface samples are key in understanding both lake evolution over time and early diagenetic reactions. To acquire information about the spatial patterns of mineral deposition and their textures, we hardened the lake sediments with the method described in the mineralogy section below and turned them into thin sections for imaging.

5.4.1 Field Collection

Lake water from a pond in each lake was collected to measure ion concentration. At Atlin Playa (Figure 5.3, S1), a 15 cm deep core was collected under 5 cm of water and subsampled at 5, 10, and 15 cm depth below the sediment-water interface. A second core (25 cm depth) was collected at the edge of the playa, two meters away from the water edge, and subsampled the core top and at a depth of 2.5, 7.5, 12.5, 17.5, and 22.5 cm. Next to the core, a 20 ml syringe with the ends removed was used to collect a sediment plug for thin section preparation. At Salt Lake (Figure 5.3, S1), three samples were collected from the tan sediment surface one meter apart, one sample was collected from the black sediment surface, and one sample was collected one meter laterally into the water from the crystal sheath surface. Co-located with the furthest sample from the lake water, a 20 ml syringe was used to collect sediment for thin section preparation. At Last Chance Lake (Figure 5.3, S2), the water formed 2-3 meter wide pools (Figure 5.2F), which were 15 cm at their deepest. On the lake margin, a 15 cm core was collected three meters away from the closest pool and subsampled at 5, 10, and 15 cm depth. Two pits were dug at six meters and nine meters from the closest pool and subsampled at 0, 10, 20, and 30 cm depth. Inside the pit that was six meters from the closest pool, 20 ml syringes were used to collect sediment at 15 and 30 cm depth for thin section preparation. At Basque Lake (Figure 5.3, S1, S2), the water formed ~5 meter wide pools of 10 cm maximum depth. Three pits were dug. The first pit was three meters away from the closest pool and sediment was collected at 15 cm depth. The second pit was six meters away from the closest pool and sediment was subsampled at 0,10, and 20 cm depth. A 20 ml syringe was used to collect sediment from the surface of this pit for thin section preparation. The third pit was eleven meters away from the closest pool and sediment was subsampled at 0, 10, 20, 30, and 40 cm depth. 20 ml syringes were used to collect sediment at 20 and 30 cm depth of this pit for thin section preparation.

5.4.2 Geochemistry

Ion Chromatography (IC): Major ions were measured with Dionex Integrion High Pressure Ion Chromatography (HPIC; ThermoFisher, Waltham, MA, USA) systems with anion and cation columns running in parallel (method adapted from Speth et al., [2022]). Lake water was diluted with 18 MΩ water in the following ratios: Atlin Playa 1:10, Salt Lake 1:100, Last Chance Lake 1:50, and Basque Lake 1:100. Standards were not diluted. A Dionex AS-DV autosampler loaded samples to serial anion and cation columns and detectors. Both columns and detectors are maintained at 30 °C. The ion chromatography system was run as described previously [Green-Saxena et al., 2014] with the following modifications. Anions were resolved by a 2x250 mm Dionex IonPac AS19-4µm analytical column protected by a 2x50 mm Dionex IonPac AG19-4µm guard column (ThermoFisher, Waltham, MA, USA). A potassium hydroxide eluent generator cartridge generated a hydroxide gradient that was pumped at 0.25 mL min^{-1}. The gradient was constant at 10 mM for 5 min, increased linearly to 48.5 mM at 27 min, then increased linearly to 50 mM at 40 min. A

Dionex AERS 500 suppressor provided suppressed conductivity detection running on recycle mode with an applied current of 31 mA. Cations were resolved by a 2x250 mm Dionex IonPac CS16-4µm analytical column protected by a 2x50 mm Dionex IonPac CG16-4µm guard column. A methanesulfonic acid eluent generator cartridge generated a methanesulfonic acid gradient that was pumped at 0.16 mL min^{-1}. The gradient was constant at 10 mM for 5 min, nonlinearly increased to 20 mM at 20 min (Chromeleon curve 7, concave up), and nonlinearly increased to 40 mM at 40 min (Chromeleon curve 1, concave down). A Dionex CERS 2 mm suppressor provided suppressed conductivity detection with an applied voltage of 4.2 V. Chromatographic peaks were integrated by Chromeleon 7.2.9 using the Cobra algorithm, and were correlated to concentration by running known standards and generating 4-point calibration curves.

Sediments collected for bulk analysis were dried in the oven at 50°C for 48 hours and subsequently physically disaggregated into uniform powder. Subsets of Salt Lake and Basque Lake samples retained moisture and required subsequent air drying in the fume hood. A further subset required 24-48 hours at 70°C in the oven.

Organic carbon content, total sulfur content, δ13C of organic matter, and δ34S of sulfate salts were determined using elemental Analysis-Isotope ratio mass spectrometry (EA-IRMS). Dried sediment from all lakes was first analyzed for total sulfur and δ34S. Basque Lake sediments, Salt Lake sediments, Last Chance Lake sediments, and carbon-free sand were subject to three rounds of salt dissolution via 1 M HCl in an ultrasonic bath for 30 minutes per round and then analyzed for total organic carbon (TOC) and δ13C. Carbon-free sand served as a contamination control measure for the procedure. Atlin Playa sediments consisted of near 100% carbonate for the mineral fraction and thus required three measurements for each sample. The sample was analyzed for TOC and δ13C with both carbonate and organic carbon included, just organic carbon, and just carbonate. To remove carbonate, the sediments were mixed with carbon-free sand in a 2:1 ratio and subject to 12 M HCl acidification. To remove organic carbon, the sediments were subject to 30% H_2O_2 overnight. Sediments from all lakes were weighed before and after salt dissolution to assess % salt of each sample.

Elemental Analysis-Isotope ratio mass spectrometry (EA-IRMS): Samples were measured at the Earth System Evolution Lab (EaSEL) at Iowa State University using a Thermo IsoLink Elemental analyzer coupled to a Delta Plus Mass spectrometer using a ConFlo IV. Sample powders were weighed into 9x5 mm Sn capsules, with sulfate samples having an excess of V_2O_5 added prior to analyses. Samples were flash combusted at 1020°C with an excess of O_2 gas (300 mL/minute in a 3 second pulse). Combustion products are carried by He stream over oxidizing and reducing agents (electrolytic copper) in a pre-packed reactor (Thermo Scientific 46802015) to convert C species to CO2 and S species to SO2. Concentration and stable isotope ratios of both C and S were determined by comparison to a suite of internal and external standards. For δ13C relative to Vienna Pee Dee Belemnite standard (VPDB), urea (-37.14‰, 18% C), caffeine (-14.79‰, 49.4% C), and peat (-28.17‰, 15.95% C) was used. For δ34S relative to Canyon Diablo meteorite standard (CDT), peat (-17.82‰, 0.43% S), sulfanimide (-1.28‰, 18.62% S), USGS42 (7.84‰, 4.4% S), and NBS127 (20.3‰, 13.74% S) was used.

5.4.3 Mineralogy

Detecting the true assemblage of salt minerals in these lakes is tricky because hydrated phases easily dehydrate and drying may cause additional salts to precipitate. In addition, detecting an assemblage of salt minerals from an instrument perspective is difficult because not all salts diffract well and hydrated phases are hard to measure. This is why we employed a bulk technique on the dried powder as well as a spatially resolved technique on hardened lake sediment. Bulk infrared spectroscopy was informative of stoichiometry and hydration state and electron microscopy imaged spatial distribution, abundance, size, shape, and texture of minerals preserved in thin sections.

Attenuated total reflectance-fourier transform infrared spectroscopy (ATR-FTIR): All bulk sediment powders were analyzed to ~1 μm depth by a Nicolet Magma 860 FTIR with ATR accessory in the sample compartment. The spectra were divided by the background of the sample and 10 spectra were collected per sample in the range of 400-4,000 wavenumbers (cm^{-1}).

Scanning electron microscopy with energy dispersive X-ray spectroscopy (SEM-EDS): Once sediment was collected by plunging the 20 ml syringe vertically or horizontally into the surface and retrieving it, the syringes were subject to a series of ethanol and LR White Resin rinses in the following order. Every 24-48 hours, the syringes were rinsed and plugged with ethanol-water mixtures of increasing concentration: 30%, 50%, 70%, 90%, 95% (three times repeated) and 100% (three times repeated) ethanol. The syringes were then rinsed and plugged with resin-ethanol mixtures of increasing concentration every 24-48 hours: 50%, 70%, 90%, 95%, 100% (three times repeated) resin. The syringes were then dried in an oven at 60 C for 24 hours. The sediment was then dry enough to be turned into thin sections. The thin sections were mounted on to carbon tape, carbon coated, and imaged by a Zeiss 1550VP FESEM (field emission SEM) in both secondary electron and angle-sensitive backscatter modes. The elemental compositions were mapped using an Oxford X-Max SDD EDS. The EHT (accelerating voltage) was set to 10 keV as the thin sections were sensitive to volatilization and the working distance was set to ~5 cm.

5.5 Results

5.5.1 Surface Textures and Materials

As noted above, the depth, chemical composition, and mineral precipitates of these lakes changes seasonally. Here, we describe them at the time of sampling. Atlin Playa had a small pool of water ~10 meters across while the rest of the playa was dry. The water was < 15 cm at the deepest point. The dry parts of the playa were covered with a bright white carbonate mud (Figure 5.3A). Bubbles were seen at the mud surface in certain locations (Figure 5.3B) and were likely produced by a green layered microbial mat, millimeters below the surface. Scooping at the carbonate mud led to black, sulfidic smelling mud within 15 cm (Figure 5.3C). More than 10 meters away from the waters edge, the carbonate mud dried as meter scale mounds with ~10 cm deep mud cracks (Figure 5.3D).

Salt Lake was filled with water and < 15 cm at its deepest point. A layer of crystals had precipitated at the sediment water interface. The lake edge was covered with black, sulfidic smelling sediment. And the sediment around the lake was brown and silty with mud cracks (Figure 5.2, S1).

Last Chance Lake and Basque Lake were both comprised of shallow pools that were 3-5 meters across. The pool edges of Basque Lake had clumps of floating crystals (Figure 5.3E), abundant lenticular white crystals on the dry surface (Figure 5.3F,H), and a higher standing, white, popcorn type texture (Figure 5.3G). Black sulfidic smelling sediment was abundant at the pool edge as well.

Sedimentary structures were not apparent in the dug up pits (Figure 5.3): the pits did not show clear lamination or salt layers. Outsized clasts occasionally were lodged in the sediment. The silt and clay sized sediment had a patchy distribution of lighter brown to black coloring. The only heterogeneity came from occasional lenses of red, oxidized sediment but these were not at consistent depths across pits (Figure 5.3 J, L). Pits were dug to avoid areas with bioturbation by vegetation.

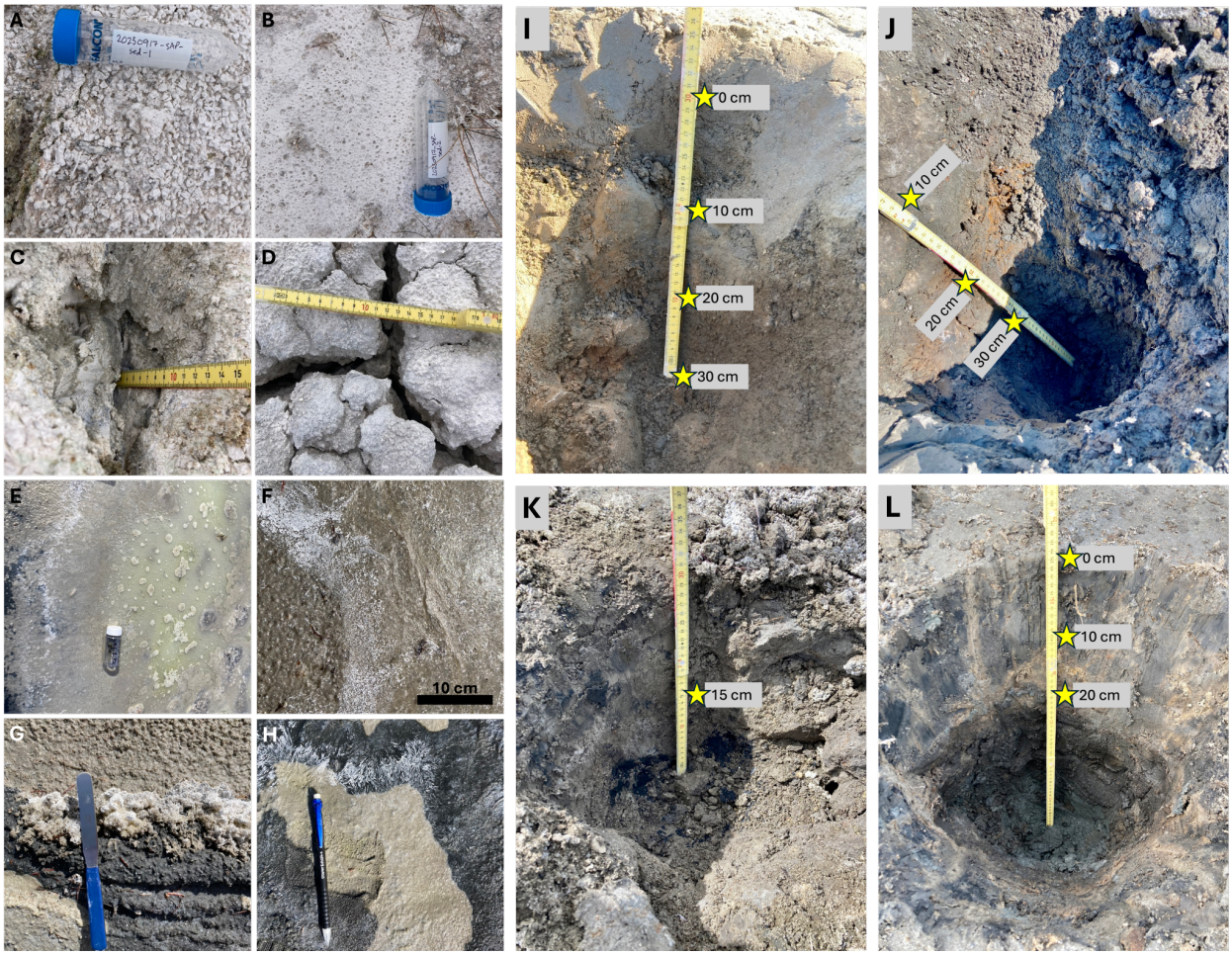

Figure 5.3: Field images of mineral textures observed in shallow sediments of the lakes A) Coarse Mg-carbonate grains in Atlin Playa. B) bubble casts present in Mg-carbonate mud in Atlin Playa. 50 ml falcon tube in A and B is 11.5 cm. C) Mg-carbonate mud with black sediment present. D) deep mud cracks within meter-scale mounds of Mg-carbonate mud. E) small pool of water with sulfate crystal rafts at Basque Lake. Tube in E is 6 cm. F) abundant crystals on lake surface. G) popcorn like texture of crystals at lake edge. Spatula in G is 20 cm. H) black mud with crystal fans on top. Pencil in H is 15 cm. Yellow stars show sampling locations and depths of samples in cm in each pit. I) Pit

dug at Last Chance Lake, six meters from the closest pool J) Pit dug at Last Chance Lake, nine meters from the closest pool K) Pit dug at Basque Lake, three meters from the closest pool L) Pit dug at Basque Lake, six meters from the closest pool.

5.5.2 Bulk Mineralogy (Figure S1,2)

In Atlin Playa, the core from the pond consisted of hydromagnesite and nesquehonite with aragonite only present at 15 cm depth. The second core (sub-aerial), in contrast, was entirely aragonite with minor magnesite. Here we report the presence of Alum-K at Atlin Playa for the first time based on FTIR spectra. Alum-K is a sulfate mineral that precipitates instead of gypsum in alkaline settings with sufficient potassium and sulfate [Merdy et al. 2022; Table S1].

In Salt Lake, a subaqueous sediment sample consisted of multiple sulfate salts and orthoclase. It was the only sample from the lake where epsomite was detected. The rest of the samples had other sulfate salts (romerite, melanterite, thenardite, bloedite), magnesite, aragonite, and sanidine.

The Basque Lake samples taken from the pool edge were all a mixture of epsomite, melanterite, romerite, thenardite, and bloedite. Epsomite was not found in subaerial sediment samples; it is difficult to preserve in deposits. Gypsum was only detected in the sample furthest from the pool water. The Basque Lake pit sediments all had magnesite, orthoclase, albite, gypsum, romerite, and melanterite. The closest pit sample to the water also had bloedite, dolomite, and minor amounts of clay. The top of the middle pit also had bloedite. The FTIR spectra were difficult to deconvolve so any detection of romerite/melanterite could also be interpreted as bloedite/thenardite. Magnesite was detected in all subaerial sediment samples from both Basque Lake and Salt Lake despite the high concentration of sulfate in both these lakes.

The sediments of Last Chance Lake consisted of anatase, calcium sulfate, sanidine, and calcite in all samples.

Sodium and iron sulfate salts were detected via FTIR but not found in thin sections. The same is true for calcium sulfate in Last Chance Lake. It is possible that these salts were not a true part of the lake mineralogy at the time of sampling but simply precipitated when the samples were dried in the lab.

We determined the salt fraction for each sample, which includes all carbonate and sulfate phases detected in the mineralogy. The salt fractions varied between lakes and within lakes (Table S2) but were generally highest near the lake margin and decreased with depth as expected (Figure S5). We recovered a large range of salt fractions, from ~10 to effectively 100% across the four lakes. SEM imaging did not find evidence of reduced sulfur phases in the samples. As such, we could assume that the sulfur wt% measurement from the EA corresponded to sulfate salts. However, sulfur wt% did not follow total salt fraction trends (Table S2).

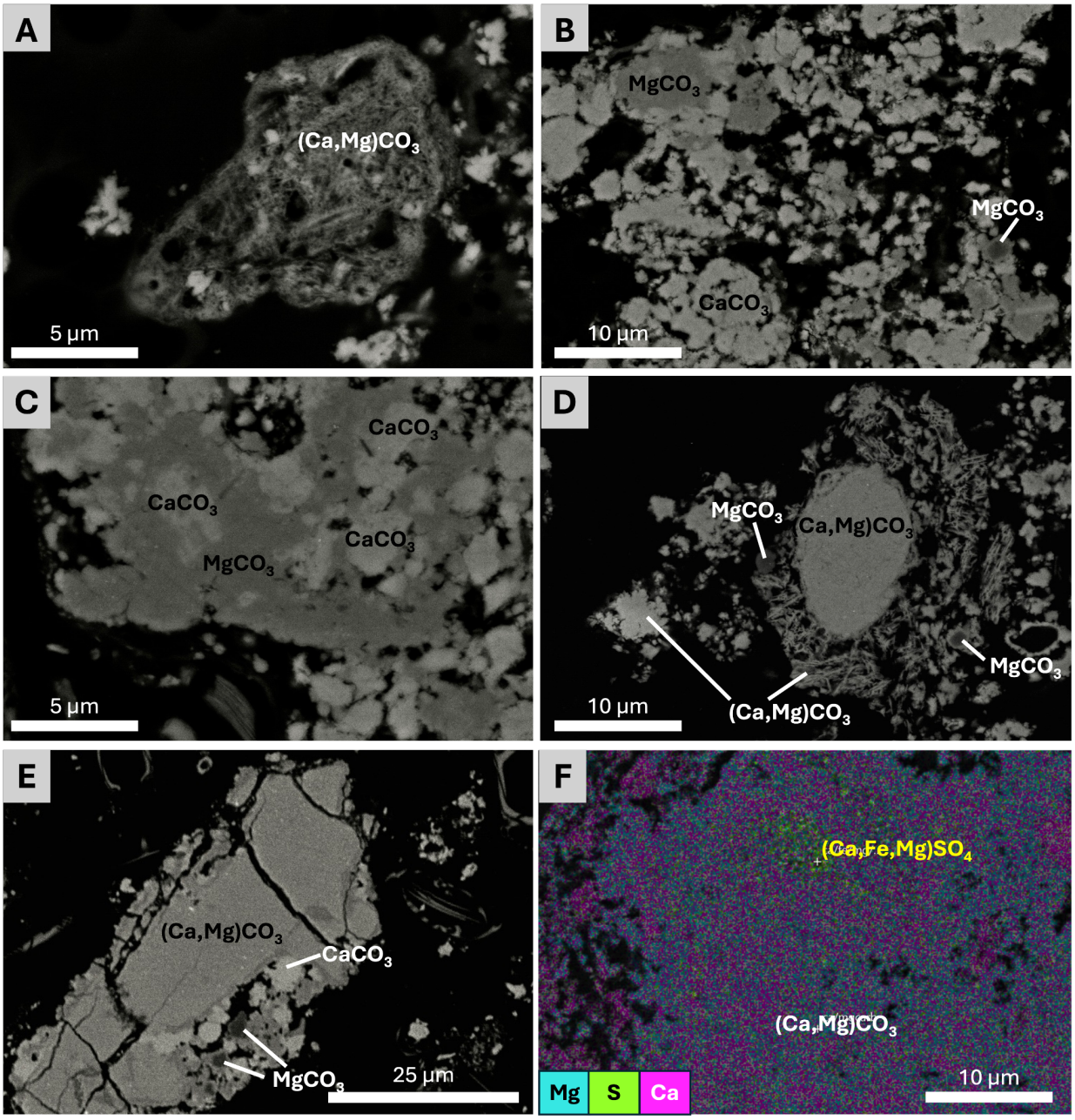

Figure 5.4: Detrital and authigenic textures present in Atlin Playa in SEM images and elemental identifications from EDS. A) authigenic acicular crystal growth of mixed Ca/Mg carbonate. B) authigenic globular crystal growth of Mg and Ca carbonate crystals where Ca carbonate crystals envelop Mg carbonate crystals. C) authigenic globular crystal growth of Mg and Ca carbonate crystals where Mg carbonate crystals envelop Ca carbonate crystals. D) detrital mixed Mg/Ca carbonate grain acting as nucleation point for authigenic acicular growth of Mg and Ca carbonate crystals. E) detrital mixed Ca/Mg carbonate grain acting as nucleation point for authigenic globular growth of Ca carbonate crystals and authigenic Mg/Ca carbonate growth enveloping smaller, detrital

Mg grains. F) in-situ precipitation of mixed cation Mg/Fe/Ca sulfate crystals intergrown with carbonate.

5.5.3 Micro-Scale Textures

SEM analyses allowed us to see how mineral phases, textures, and abundances changed with depth as early diagenesis took place. Authigenic phases carry information about lake chemistry and identify unique characteristics of these deposits. Rich authigenic mineral textures and detrital mineral textures were present and interactions between the two were significant (Figures 5.4-7). Atlin Playa authigenic carbonate precipitation had a delicate, fibrous or a globular appearance (Figure 5.4). In some cases, a detrital grain, which was smooth on the top or angular or both, served as a nucleating point for globular clumps and acicular crystals to precipitate (Figure 5.4D,E). Often, this resulted in a dissolution of the angular grain edges to produce rounded grains (Figure 5.4D). The order of precipitation was equally Mg carbonate precipitating first and being enveloped by Ca carbonate or vice versa. Clumped aggregates could be as large as a few hundred microns. In some cases, mixed cation (Ca, Mg, Fe) sulfate precipitated on top of carbonate crystals (Figure 5.4F), perhaps making use of residual cations after Mg and Ca carbonate formation. Detrital feldspar, Mg-silicate, quartz, iron oxides were present.

In Salt Lake (Figure 5.5), the detrital grains were always smooth and angular, and contained a high abundance of detrital calcite. Dissolution of these grains was evident by etch marks on detrital calcite (Figure 5.5A,B). Mg-carbonate was found as a cement and as a grain with etch marks (Figure 5.5D). Ca-carbonate was found as an aggregate of bladed crystals (Figure 5.5C). Mg-sulfate was present as individual prismatic crystals or a network of fibrous cement branches (Figure 5.5D, H). In rare cases, it also formed globular clumps on top of other salts (Figure 5.5F). Ca sulfate was either a delicate radiating crystal or a cement that engulfed many detrital grains and other authigenic salts (Figure 5.5F,G). The paragenetic order determined was detrital silicate grains < $CaCO_3$ (detrital or in place) < $CaSO_4$ crystal or cement < $MgSO_4$ crystalline or cement. Igneous minerals identified were clinopyroxene, plagioclase, and quartz.

The mineralogy of Last Chance Lake looked notably different from these two lakes. It had much larger detrital grains, up to ~1 mm and rare salts preserved at depth. There were a lot more detrital iron and titanium oxides and apatite compared to other lakes in addition to the usual augite, other pyroxenes, plagioclase, and K feldspar (Figure 5.6A,C). The few instances of authigenic salt were aggregates of bladed calcium carbonate or calcium carbonate precipitating within surficial cracks in grains (6B,D). No sodium or magnesium carbonates or sulfates were identified in the SEM.

In Basque Lake, there was an omnipresence of large, smooth, and sub-rounded gypsum crystals ~50 to 100s of micrometers wide (Figure 5.7C, D). On the other hand, the Mg-carbonate was always much smaller and often grew in globular clumps on the surfaces of other grains (Figure 5.7A,B). Mg-sulfate was present as pseudocubic crystals and bladed aggregates (Figure 5.7C) in addition to prismatic crystals on top of Ca sulfate crystals. There was one instance of an Mg-sulfate cement (Figure 5.7E,F). These thin sections from deeper sediment did not preserve any cement.

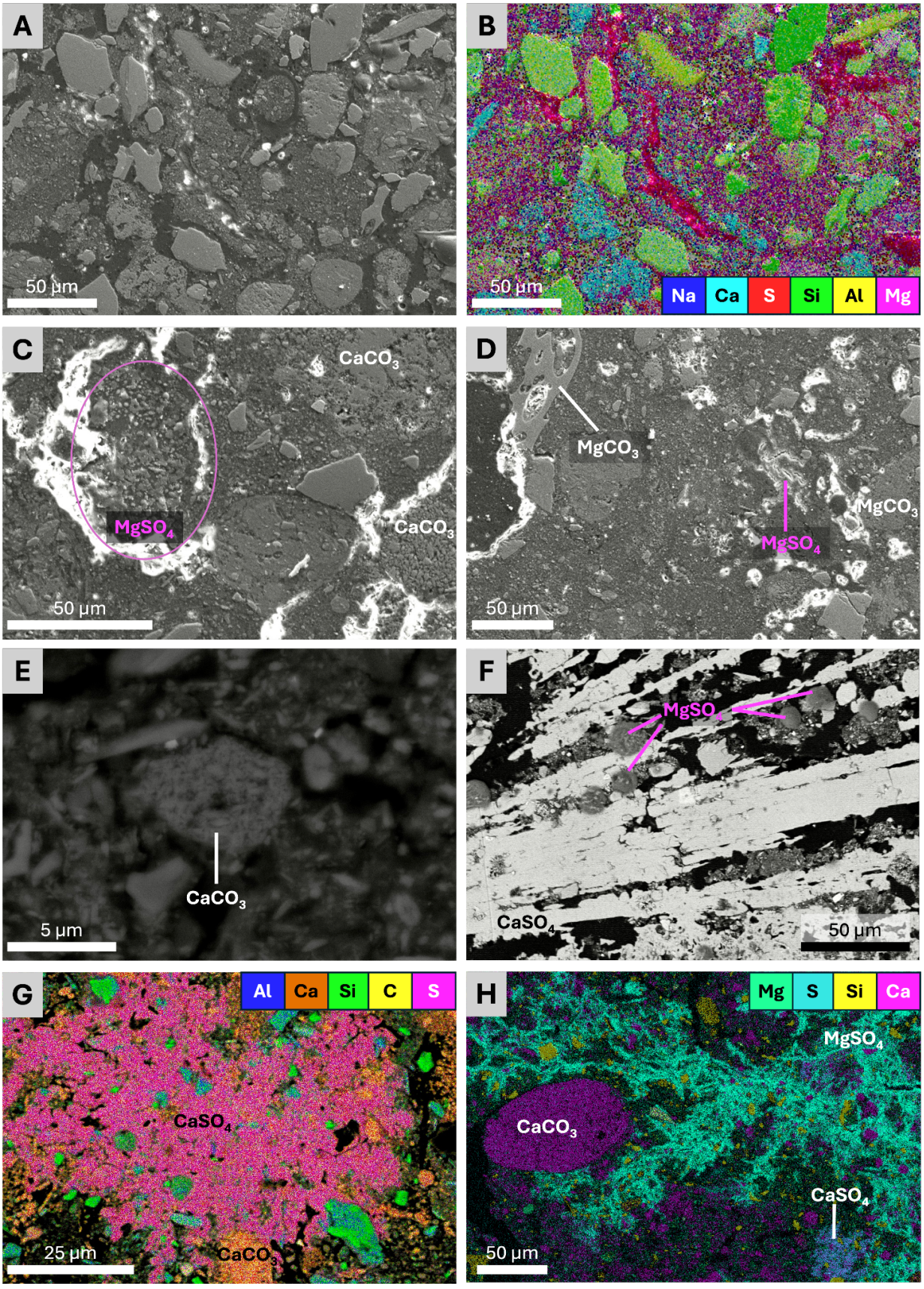
A
50 µm
B
50 µm
Na
Ca
S
Si
Al
Mg
C
CaCO3
MgSO4
CaCO3
50 µm
D
MgCO3
MgCO3
MgSO4
50 µm
E
CaCO3
5 µm
F
MgSO4
CaSO4
50 µm
G
Al
Ca
Si
C
S
CaSO4
25 µm
CaCO3
H
Mg
S
Si
Ca
MgSO4
CaCO3
CaSO4
50 µm

Figure 5.5: Detrital and authigenic textures in Salt Lake in SEM images and elemental identifications from EDS. A) Electron image. B) corresponding EDS image: Mg sulfate cement highlighted as saline fluid traveled through pore spaces between detrital silicate grains with smaller detrital carbonate pieces within them. C) Authigenic globular Mg sulfate and Ca carbonate. D) Individual prismatic crystals of Mg sulfate and mixed Mg/Ca carbonate present in cement form and etched grain form. E) authigenic Ca carbonate acicular aggregate. F) authigenic radiating Ca sulfate crystal with authigenic globular precipitation of Mg sulfate on top. G) authigenic Ca sulfate crystal engulfing detrital silicate grains and Ca carbonate. H) authigenic Mg sulfate cement web engulfing detrital Ca carbonate and silicate grains as well as authigenic Ca sulfate, which is itself engulfing detrital Ca carbonate grains.

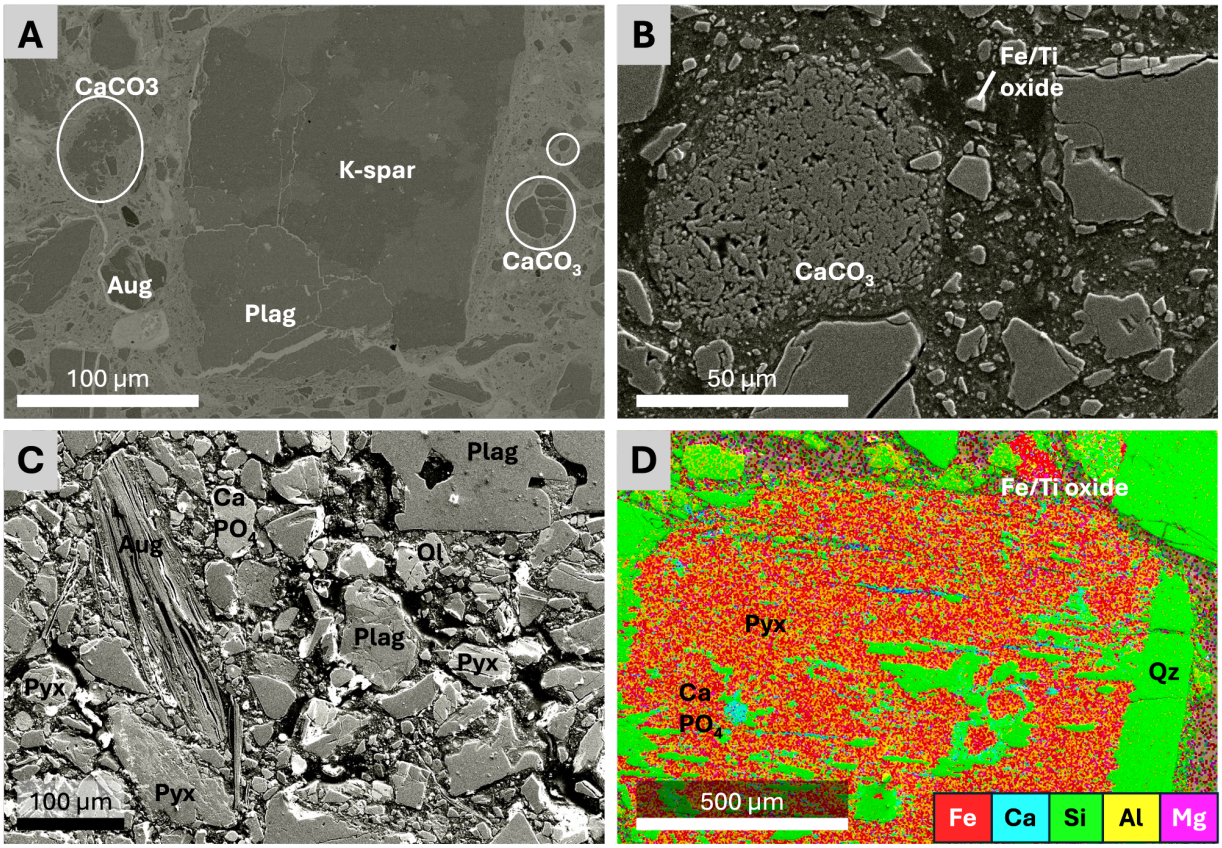

Figure 5.6: Detrital and authigenic textures in Last Chance Lake in SEM images and elemental identifications from EDS. A) Detrital and authigenic Ca carbonate amongst detrital grains at the surface of the lake. B) Authigenic crystal aggregates of Ca carbonate amongst detrital grains at the surface of the lake. C) variety of angular detrital grains with no salt phases detected at 15 cm depth. D) large detrital grain with Ca carbonate and mixed Ca/Mg carbonate precipitated in surficial etches at 15 cm depth. K-spar = potassium feldspar. Plag = plagioclase. Aug = augite. Pyx = pyroxene. Ol = olivine. Qz = quartz.

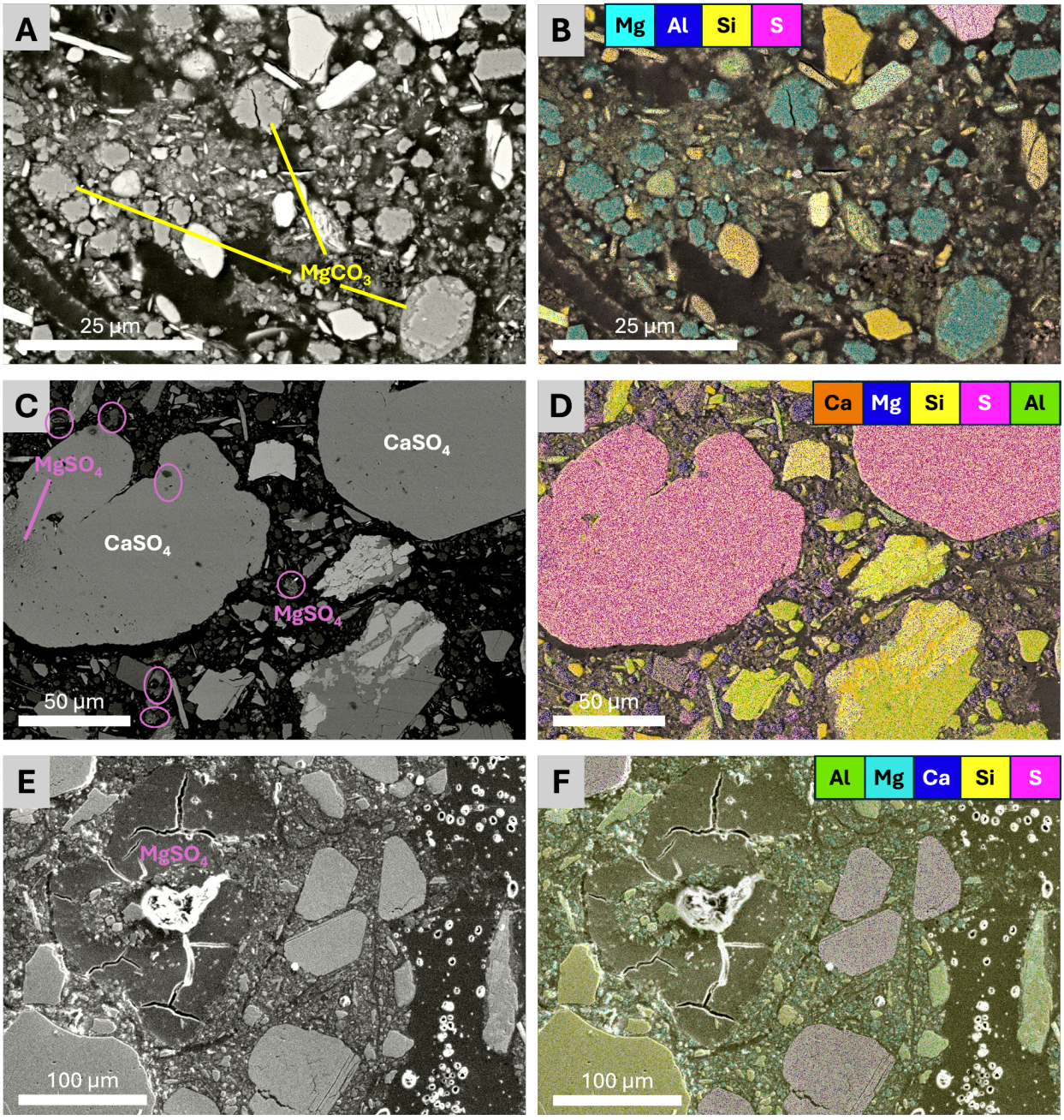

Figure 5.7: Detrital and authigenic textures in Basque Lake in SEM images and elemental identifications from EDS. A) Abundant Mg carbonate aggregates precipitated on top of grains, uneven dissolution of carbonate visible around edges. B) EDS of the corresponding image. C) Ca sulfate precipitated in place with massive smooth texture and twinned Mg sulfate crystals visible, engulfing Mg sulfate, precipitated angular crystals of Mg sulfate identifiable in some cases D) EDS of the corresponding image. E) only case of Mg sulfate cement found preserved in situ around Mg carbonate and detrital silicate grains, surrounded by larger Ca sulfate crystals. F) EDS of the corresponding image.

5.5.4 Organic carbon and isotope trends

Last Chance Lake was the lowest in TOC (average = 0.31%, stddev = 0.19%). The second lowest was Atlin Playa (average = 1.04%, stddev = 0.6%). Salt Lake had a large range of TOC (1.4-13.48%), which was highest in the middle sample of the five samples in the transect (Figure S1) and decreased in both directions. Pure salt samples from Basque Lake were TOC poor (max = 0.27%). Basque Lake sediment samples hovered between ~1.5 to 4 % TOC except for one sample that was 23.54% but was not visually distinct from the rest of the samples. The ratio of carbonate and sulfate salt in the samples did not systematically impact their TOC preservation.

The average $\delta^{13}C$ of Last Chance Lake was -23.9±0.7‰, Salt Lake was -22.1±0.5‰, Atlin Playa was -30.4±1.4‰, and Basque Lake was -20.3±1.5‰ relative to the Vienna Pee Dee Belemnite standard (VPDB) (Figure S3).

TOC generally decreased with depth as expected (Figure S4). However, TOC did not correlate to distance from the lake, or $\delta^{13}C$ of the organic carbon (Figure S3). $\delta^{13}C$ did not show correlation with sample depth or distance from the lake relative to the Canyon Diablo meteorite standard (CDT).

The average $\delta^{34}S$ of Last Chance Lake was 11.35±8.3‰, Salt Lake was -6.59±1.5‰, Atlin Playa was -3.57±0.9‰, and Basque Lake was -5.80±1.1‰. This excluded one measurement from Basque Lake at the pool's edge, which had a $\delta^{34}S$ of -54.61‰ and sampled a microbial mat floating on the surface (Figure 5.8).

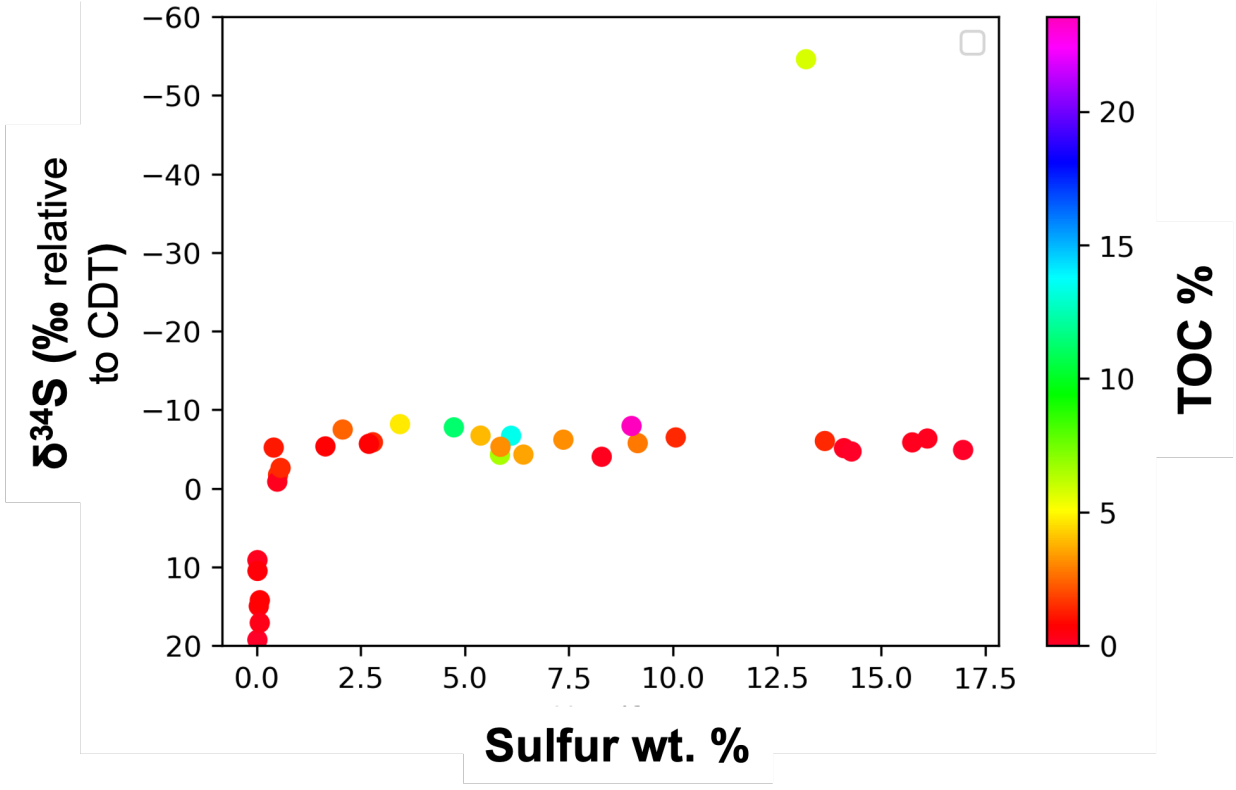

Figure 5.8: $\delta^{34}S$ of lake sediments versus amount of sulfur present in all lake samples. Color bar represents the amount of TOC in the sample. Isotope values have uncertainty smaller than the points plotted (±0.2‰).

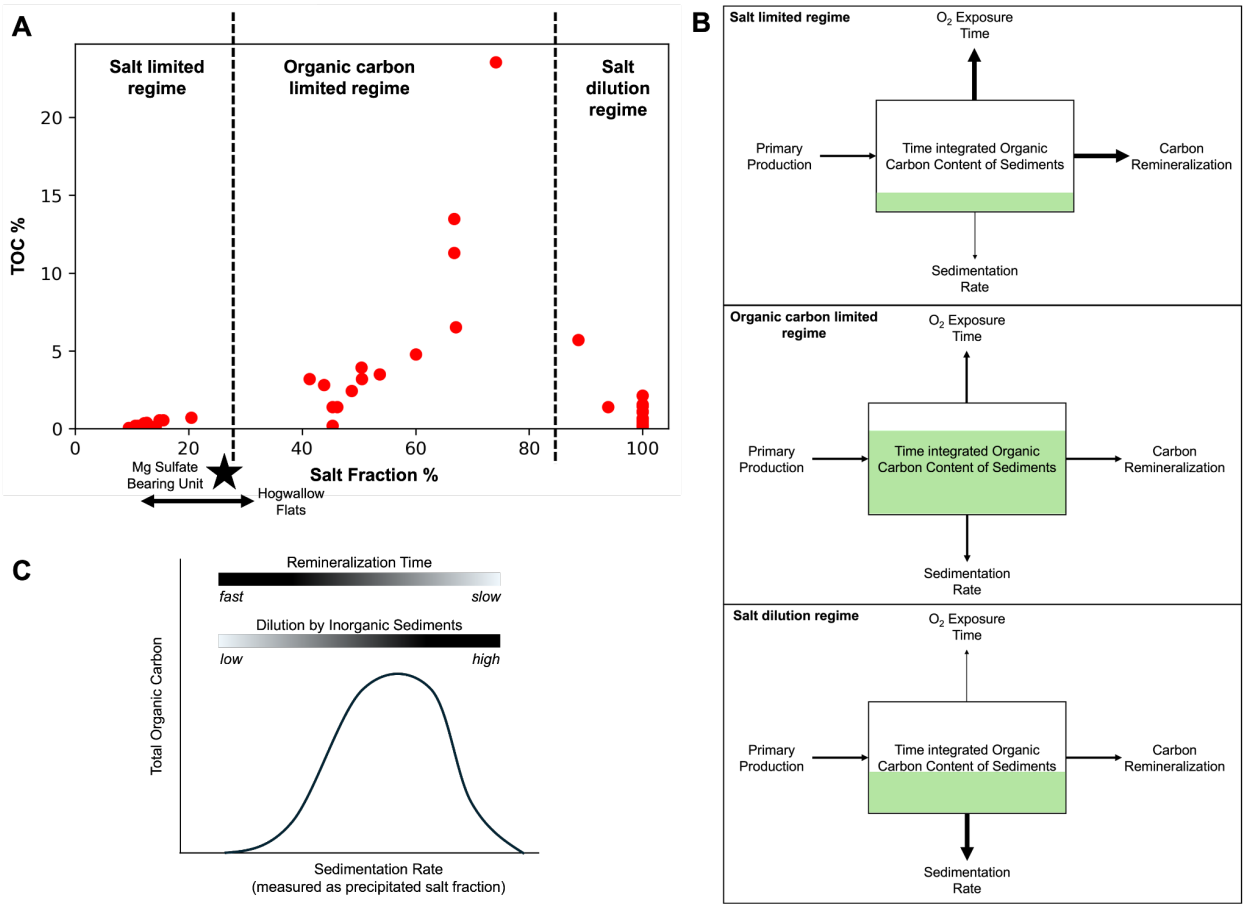

Figure 5.9: TOC Schematic. A) Total organic carbon content versus combined mass of sulfate and carbonate salts as a fraction of sample mass. 10-30% salt fraction reported in Hogwallow Flats, Jezero Crater from Broz et al. (2024) and 26.7% salt fraction reported in Mg sulfate bearing unit, Gale Crater from Chipera et al. (2023). B) Output processes that dominate at each stage of sedimentation or salt production from A. Green box fill represents net TOC preserved. C) Schematic of net TOC preserved with sedimentation rate, measured as precipitated salt fraction in this study, based on Lotem et al. (2025).

5.6 Discussion

The goal of this study was to understand how Mg carbonate and sulfate rich hypersaline lakes are preserved in sediments such that micro and macro scale textures could be compared to returned samples from Mars one day. Furthermore, the purpose of the TOC and isotope measurements was to determine if the biology present in the lakes was recorded in the chemical measurements.

5.6.1 Minerals, Lake Chemistry, and Deposit Construction

There are notable absent and present mineralogies that suggest source lithology and abiotic mineral precipitation dominate over microbially mediated minerals in the deposits. The presence of igneous minerals such as olivine, pyroxene, plagioclase, K-spar, Fe/Ti oxides, and apatite is to be expected given the basaltic and felsic lithologies in the surrounding area (Figure 5.2). The presence of detrital carbonate of varying amounts of calcium and magnesium as seen above is expected. The Cache Creek Terrane of the eastern Marble range has 12.1% total inorganic carbon with Mg/(Ca+Mg) ratios ranging from 0.02 to 0.46 [Stebbins et al., 2019]. An absence of mineralized reduced sulfur (e.g. framboidal pyrite as in Xu et al., 2023) is noted despite evidence of sulfate reducing bacteria existing in the lakes [Foster et al., 2010]. There is also a surprising lack of clay minerals compared to most other lacustrine systems [Jones, 1986], even saline lakes [Calvo et al., 1995]. Iron sulfates such as romerite were detected via FTIR in samples but are not mentioned in previous studies [Raudsepp et al., 2024; Haas et al., 2024] except in Foster et al. (2010).

Lake chemistry is recorded in the authigenic mineral phases of the deposits and requires high resolution imaging to uncover. The authigenic textures of these lakes are primarily acicular aggregates, globular clumps, and an abundance of cement in the form of fibrous networks and encapsulation of detrital grains. There are some minerals like dolomite that are present in detrital and authigenic forms and differentiation is only possible on the basis of texture. Thus, bulk techniques would not reveal a true understanding of the lake chemistry.

In addition, lake chemistry is revealed by spatial imaging of the order of precipitation of mineral phases. The carbonate dominated lakes (Last Chance and Atlin Playa) precipitate sulfate salts < 1 wt% of the sediment. However, sulfate dominated lakes (Basque Lake and Salt Lake) precipitate significant amounts of carbonate minerals and leave behind a diagnostic mineral assemblage that could be used to identify this type of lake in returned samples. The order of salt precipitation in the sulfate dominated lakes as determined by SEM data above is $CaCO_3$ (detrital or authigenic) = $MgCO_3$ (authigenic) < $CaSO_4$ crystalline or cement < $MgSO_4$ crystalline or cement. This is theoretically predicted by salt solubilities and brine evolution [Warren, 2016; Tosca and Tutolo, 2023] but was actually found in lake sediment thin sections in this study that preserve spatial correlations between salts (best examples Figure 5.7G,H). It follows that if a primary sulfate precipitation texture is found on Mars, it implies the brine has already precipitated all carbonate in the system. If a primary Mg sulfate is found, the brine has also lost all of its calcium to mineralization and the brine is at its driest stage of aqueous evolution.

The thin sections in this study show mineral morphologies in 2D projections similar to 3D SEM work traditionally done in other lacustrine studies. As such, there are many comparisons of microbially mediated or authigenic textures from previous studies that apply here (as shown in Figure S6-8). The globular, clumped texture of the carbonates in Atlin Playa and the Mg-sulfate in Salt Lake in this study is likely a projection of spherical morphologies (Figure S6), which are certainly authigenic and likely microbially mediated [Trichet et al. 2001; Barbieri and Stivaletta, 2011]. The carbonate acicular aggregates in this study look similar to authigenic precipitation of mixed cation sulfate minerals in Spotted Lake and organomineralization of iron oxide minerals (Figure S7) [Posth et al., 2014; Cannon, 2012]. The prismatic crystals of Mg-sulfate in our study are

perhaps 2-D projections of authigenic plate shaped aggregates of hydromagnesite in Atlin Playa or more acicular aggregates of sulfate in Spotted Lake (Figure S8) [Power et al., 2009; Cannon, 2012].

5.6.2 Effects of Diagenesis on Deposits

Rich, authigenic textures became significantly rarer below the surface. Instead, the salts fused into large, sub-rounded or angular crystals (Figure 5.7), which poses a real problem for recognizing these environments and the existence of primary salts on Mars. These lake systems are already challenging to identify from physical features at the scale of rover instruments investigating the Martian rock record. We do not see classical lake sedimentology at Hogwallow Flats on Mars for example [Stack et al., 2024; Broz et al., 2024]. Chemical sedimentation does not leave behind physical bedding features [Last and Vance, 1997]. Any laminae that were initially present are disrupted by salts dissolving and reprecipitating over wet-dry cycles. The detrital grains are angular and large because these are glaciofluvial sediments [Renaut and Long, 1989]. There are no physical erosion processes occurring in the lakes that round the grains and point to a lacustrine setting.

Salt fractions in sediments generally decreased with depth in our samples (Figure S5). Since these lakes are groundwater-fed, salt dissolution with depth as diagenesis occurs is to be expected [Renaut and Long, 1989]. However, significant salt fractions still remained at depth in the lakes despite diagenesis. The lack of recorded salts in Last Chance Lake compared to other lakes could be due to its weaker cation concentrations or more intense redissolution from interaction with groundwater as shown in Tutolo et al. (2024). Gale Crater on Mars has a rich history of groundwater alteration and so deposits of certain highly soluble salts could have been erased if they existed [Schwenzer et al., 2016; Gabriel et al., 2022; Gasda et al., 2022] but Jezero Crater was likely not subject to significant groundwater inflow [Horvath and Andrews-Hanna, 2024]. The preservation of salt is a balance between water ion concentration and diagenetic dissolution and so the individual hydrology of Martian lakes would have a significant impact.

TOC also generally decreased with depth but retained the same order of magnitude with depth (Figure S4). TOC is generally high in hypersaline lakes due to shallow burial depth, transition to anoxic and reducing conditions below the highly productive layer, and higher productivity than freshwater lakes [Liang et al., 2024 and references therein; Contreras et al. 2018]. This continues to be true in the Cariboo Plateau, even in lakes as shallow as 15 cm at times of the year and a maximum depth of 4 m [Renaut and Long, 1989]. However, the data here also demonstrates that TOC is not hosted in clay minerals as they are not abundant in Basque Lake, Salt Lake, and Atlin Playa (Figure S1,2). The TOC is hosted by salt minerals as opposed to clay minerals and in significant abundances, not just at the scale of fluid inclusions as previously reported in other saline lakes [Gibson and Benison, 2023].

5.6.3 Implications of Sulfur Isotopes

$\delta^{34}S$ can either be inherited from an inorganic source or can retain an imprint of biological activity. The sulfur isotopes of the lake sediments (Figure 5.8) match closely to source rocks from the Rocky Mountains and Cache Creek Terrane. Sulfate measured from water samples from the Fraser, Skeena, and Nass river basins, which map the entire hydrology of the Plateau, have $\delta^{34}S$ values -8.9 to 14.1‰. 81% of riverine sulfate in these basins originates from magmatic sulfide oxidation [Spence and

Telmer, 2005]. Higher values in Last Chance Lake can be explained by metamorphosed carbonate hosted sulfide deposits in the Western Rocky Mountains, which have $\delta^{34}S$ values ranging from 7.4 to 28.5‰ depending on the degree of alteration [Paradis et al. 2023]. Similarly, the pyrite from microbial sulfate reduction and carbonate associated sulfate from the Cache Creek Terrain in the Marble range has heavy $\delta^{34}S$ values (3-20‰ and 20-40‰, respectively) [Stebbins et al. 2019]. Furthermore, the amount of TOC does not impact the $\delta^{34}S$ value of the sediments in our study (Figure 5.8). Therefore, lake sediment $\delta^{34}S$ isotopes in this study are dominated by source rock chemistry over biologically mediated processes and not applicable to identifying biosignatures in these lakes; this is further supported by other lake studies below.

A review of $\delta^{34}S$ in non-marine evaporites and saline lakes from around the world shows a common range of +3 to +25‰ [Seal et al. 2000]. Sulfate in these environments is derived from atmospheric deposition of marine aerosols, dissolution of pre-existing salts, and weathering of sulfide minerals in basement rocks. Marine aerosols have $\delta^{34}S$ = 21.0 ‰, atmospheric dimethyl sulfide has $\delta^{34}S$ = 15.6±3.1 ‰, and bulk stratospheric sulfur has $\delta^{34}S$ = 2.6±0.3 ‰ [Seal et al. 2000]. Acidic lakes in Western Australia have $\delta^{34}S$ values between ~17-21‰ [Benison and Bowen, 2013], which is consistent with their source groundwater. Qaidam Basin, a sulfate rich basin in Western China, precipitates salts with $\delta^{34}S$ values of ~+6-12‰ [Li et al., 2020]. In all these cases, microbial metabolisms such as microbial sulfate reduction could not be elucidated from the bulk sulfur isotopes. Even when the $\delta^{34}S$ values are much lighter (-10 to -45‰), the isotopes in alkaline and sulfate-rich Pétrola lake in Spain are source driven [Valiente et al., 2017]. The pyrite that oxidizes to sulfate is sourced from organic-rich sediments and, thus, is already ^{34}S-depleted.

Despite the smell of sulfide at lake margins and in all pit samples, our results suggest reduced sulfur makes up a very small fraction of the sediment. There are cyanobacteria, sulfate reducing bacteria, and halophilic archaea in the Cariboo Plateau lakes [Foster et al. 2010]. The $\delta^{34}S$ value of the microbial mat sampled in this study was highly depleted (-54.61‰), indicative of microbial sulfate reduction taking place [Seal et al., 2000]. However, no sulfide minerals were identified in any of the thin sections so the microbial sulfate reduction occurring is not leading to deposition. Secondly, as found in saline lakes in Saskatchewan, sulfate presence does not equate to abundant sulfate reduction. The bioavailable carbon may be used up by oxic zone aerobic bacteria and the rest buried [Lyons et al. 1994]. Thirdly, Valiente et al. (2017) show that the H_2S from microbial sulfate reduction causing the odor in these alkaline, sulfate- rich lakes is quickly reoxidized to sulfate. Thus, reduced sulfur is transient and thus not recorded in the sediments. 50-80% of sulfide produced by sulfate reduction is reused in oxidation [Pellerin et al. 2015]. Lastly, volatile degassing of H_2S can explain the heavy sulfur isotopes as mass balance in closed basin lakes [Crémière et al. 2024].

5.6.4 Controls on TOC in sediment

We propose that TOC preservation is determined by three salt fraction regimes (Figure 5.9). In the low salt fraction regime, TOC uptake increased as salt fraction increased (r^2 = 0.66). In the middle regime, there was enough salt to encapsulate as much TOC as was available. Instead, TOC varied heterogeneously depending on the patchy microbial activity that takes place in these lakes [Foster et al. 2010; Nichols et al. 2023]. In the third or salt dilution regime, data points were from subaqueous locations of highest salinity where salts were actively precipitating in visible crystals out of lake water. TOC preservation was diluted by fast precipitation of salts and potentially decreased microbial

activity due to high salinity. This pattern can be explained by the major controls on TOC at play in these lakes, based on Lotem et al. (2025). High O_2 exposure time due to a lack of protection from the salt leads to high rates of carbon remineralization and lower TOC preservation in the salt limited regime (Figure 5.9B). In these lakes, salts are able to physically enclose or encapsulate the TOC or trap the organics in the matrix because they are forming at the place and time that organic carbon exists. The encapsulation then prevents oxidant diffusion and microbial activity from accessing the organic carbon [Amils et al. 2024; Gibson and Benison, 2023] and allows the salts to retain significant TOC despite microbial activity in the sediments as in the organic limited regime. High sedimentation rate, measured in this study as high salt fractions in the sediment, however, can then become a dilutant in the salt dilution regime, lowering TOC preservation (Figure 5.9B). Thus, without significant changes in TOC production, TOC preservation is altered by these factors as represented in the schematic in Figure 5.9C [Lotem et al., 2025].

Our results suggest that salts of all compositions have the ability to encapsulate extraordinary amounts of TOC when they precipitate in an optimum abundance. These results demonstrate that sediments with up to 75% salt can be very TOC rich (up to 23%). Therefore, if evidence of this abundance of salt precipitation is found, it should be the highest priority organic carbon target for the Mars rovers. We do not, however, see evidence here that carbonate salts and sulfate salts have different TOC preservation potential. For comparison, the salt fractions of salt rich sediments in Gale and Jezero craters are plotted (Figure 5.9). One reason for the lack of organic detections in these units is perhaps that they are both in the salt limited regime compared to these terrestrial analogs.

5.7 Conclusion

The hypersaline and alkaline lakes of British Columbia are hot spots for chemical sedimentation. Source lithology and abiotic mineral precipitation dominate over microbially mediated minerals in the deposits. Lake chemistry is recorded in the order of precipitation of authigenic mineral phases of the deposits. The authigenic textures of these lakes are primarily acicular aggregates, globular clumps, and an abundance of cement in the form of fibrous networks and encapsulation of detrital grains. Our results suggest that salts of all compositions have the ability to encapsulate extraordinary amounts of TOC in the right conditions: salt precipitation should be abundant enough to prevent carbon remineralization but not enough to dilute organic matter preservation. Thus, salt minerals should be prioritized by Mars rovers as targets for organic carbon samples. However, lake sediment $\delta^{34}S$ isotopes in this study are dominated by source rock chemistry over biologically mediated processes and not applicable to identifying biosignatures in these lakes.

Acknowledgements

Thank you to Victoria Cassedy for her method on preparing loose sediment for thin sections, Hannah Dion-Kirschner, Alex Sessions, and Yutian Ke for insights on EA measurements, Paul Asimow for his help with SEM measurements, George Rossman for his help with FTIR measurements, and Noam Lotem for conceptual help with Figure 5.9. We acknowledge funding from NSF EAR 2244707 to MI and the NASA FINESST program award 80NSSC23K1370 to HCL and MI.

References

Amils, R., Escudero, C., Huang, T., & Fernádez-Remolar, D. (2024). Geomicrobiology of Río Tinto (Iberian Pyrite Belt): A Geological and Mineralogical Mars Analogue. In *Geomicrobiology: Natural and Anthropogenic Settings* (pp. 123-150). Cham: Springer Nature Switzerland.

Aubrey, A., Cleaves, H. J., Chalmers, J. H., Skelley, A. M., Mathies, R. A., Grunthaner, F. J., ... & Bada, J. L. (2006). Sulfate minerals and organic compounds on Mars. *Geology*, *34*(5), 357-360.

Barbieri, R., & Stivaletta, N. (2011). Continental evaporites and the search for evidence of life on Mars. *Geological Journal*, *46*(6), 513-524.

Benison, K. C., & Bowen, B. B. (2013). Extreme sulfur-cycling in acid brine lake environments of Western Australia. *Chemical Geology*, *351*, 154-167.

Benison, K. C., Gill, K. K., Sharma, S., Siljeström, S., Zawaski, M., Bosak, T., ... & Yanchilina, A. (2024). Depositional and diagenetic sulfates of Hogwallow Flats and Yori Pass, Jezero Crater: Evaluating preservation potential of environmental indicators and possible biosignatures from past Martian surface waters and groundwaters. *Journal of Geophysical Research: Planets*, *129*(2), e2023JE008155.

Bristow, T. F., Grotzinger, J. P., Rampe, E. B., Cuadros, J., Chipera, S. J., Downs, G. W., ... & Vasavada, A. R. (2021). Brine-driven destruction of clay minerals in Gale crater, Mars. *Science*, *373*(6551), 198-204.

Broz, A. P., Horgan, B., Kalucha, H., Johnson, J. R., Royer, C., Dehouck, E., ... & Wiens, R. C. (2024). Diagenetic History and Biosignature Preservation Potential of Fine-Grained Rocks at Hogwallow Flats, Jezero Crater, Mars. *Journal of Geophysical Research: Planets*, *129*(11), e2024JE008520.

Calvo, J. P., Blanc-Valleron, M. M., Rodriguez-Arandia, J. P., Rouchy, J. M., & Sanz, M. E. (1995). Authigenic clay minerals in continental evaporitic environments. *Palaeoweathering, palaeosurfaces and related continental deposits*, 129-151.

Cannon, K. M. (2012). *Spotted Lake: Analog for Hydrated Sulfate Occurrences in the Last Vestiges of Evaporating Martian Paleolakes* (Doctoral dissertation, PhD Thesis, Queen's University, Ontario).

Chipera, S. J., Vaniman, D. T., Rampe, E. B., Bristow, T. F., Martínez, G., Tu, V. M., ... & Grotzinger, J. P. (2023). Mineralogical investigation of Mg-sulfate at the Canaima drill site, Gale crater, Mars. *Journal of Geophysical Research: Planets*, *128*(11), e2023JE008041.

Clark, J. V., Sutter, B., McAdam, A. C., Lewis, J. M. T., Franz, H., Archer, P. D., ... & Vasavada, A. (2024). Environmental changes recorded in sedimentary rocks in the clay-sulfate transition region in Gale Crater, Mars: Results from the Sample Analysis at Mars-Evolved Gas Analysis instrument onboard the Mars Science Laboratory Curiosity Rover. *Journal of Geophysical Research: Planets*, *129*(12), e2024JE008587.

Contreras, S., Werne, J. P., Araneda, A., Urrutia, R., & Conejero, C. A. (2018). Organic matter geochemical signatures (TOC, TN, C/N ratio, δ13C and δ15N) of surface sediment from lakes distributed along a climatological gradient on the western side of the southern Andes. *Science of the Total Environment*, *630*, 878-888.

Crémière, A., Tino, C. J., Pommer, M. E., Cui, X., Roychowdhury, M., Summons, R. E., ... & Adkins, J. F. (2024). A volatile sulfur sink aids in reconciling the sulfur isotope mass balance of closed basin lakes. *Geochimica et Cosmochimica Acta*, *369*, 196-212.

Cui, Y., Miller, D., Schiarizza, P., and Diakow, L.J., 2017. British Columbia digital geology. British Columbia Ministry of Energy, Mines and Petroleum Resources, British Columbia Geological Survey Open File 2017-8, 9p. Data version 2019-12-19.

Dordoni, M., Zappalà, P., & Barth, J. A. (2023). A preliminary global hydrochemical comparison of lakes and reservoirs. *Frontiers in Water*, *5*, 1084050.

Eigenbrode, J. L., Summons, R. E., Steele, A., Freissinet, C., Millan, M., Navarro-González, R., ... & Coll, P. (2018). Organic matter preserved in 3-billion-year-old mudstones at Gale crater, Mars. *Science*, *360*(6393), 1096-1101.

Farley, K. A., Williford, K. H., Stack, K. M., Bhartia, R., Chen, A., de la Torre, M., ... & Wiens, R. C. (2020). Mars 2020 mission overview. *Space Science Reviews*, *216*, 1-41.

Foster, I. S., King, P. L., Hyde, B. C., & Southam, G. (2010). Characterization of halophiles in natural MgSO4 salts and laboratory enrichment samples: astrobiological implications for Mars. *Planetary and Space Science*, *58*(4), 599-615.

Gabriel, T. S., Hardgrove, C., Achilles, C. N., Rampe, E. B., Rapin, W. N., Nowicki, S., ... & McAdam, A. (2022). On an extensive late hydrologic event in Gale Crater as indicated by water-rich fracture halos. *Journal of Geophysical Research: Planets*, *127*(12), e2020JE006600.

Gasda, P. J., Comellas, J., Essunfeld, A., Das, D., Bryk, A. B., Dehouck, E., ... & Reyes-Newell, A. (2022). Overview of the morphology and chemistry of diagenetic features in the clay-rich Glen Torridon unit of Gale crater, Mars. *Journal of Geophysical Research: Planets*, *127*(12), e2021JE007097.

Gibson, M. E., & Benison, K. C. (2023). It'sa trap!: Modern and ancient halite as Lagerstätten. *Journal of Sedimentary Research*, *93*(9), 642-655.

Gierlowski-Kordesch, E. H. (2010). Lacustrine carbonates. *Developments in Sedimentology*, *61*, 1-101.

Green-Saxena, A., Dekas, A. E., Dalleska, N. F., & Orphan, V. J. (2014). Nitrate-based niche differentiation by distinct sulfate-reducing bacteria involved in the anaerobic oxidation of methane. *The ISME Journal*, *8*(1), 150-163.

Grotzinger, J. P., Crisp, J., Vasavada, A. R., Anderson, R. C., Baker, C. J., Barry, R., ... & Wiens, R. C. (2012). Mars science laboratory mission and science investigation. *Space Science Reviews*, *170*, 5-56.

Haas, S., Sinclair, K. P., & Catling, D. C. (2024). Biogeochemical explanations for the world's most phosphate-rich lake, an origin-of-life analog. *Communications Earth & Environment*, *5*(1), 28.

Horgan, B. H., Anderson, R. B., Dromart, G., Amador, E. S., & Rice, M. S. (2020). The mineral diversity of Jezero crater: Evidence for possible lacustrine carbonates on Mars. *Icarus*, *339*, 113526.

Horgan, B., Garczynski, B., Barnes, R., Bedford, C., Cardarelli, E. L., Clavé, E., ... & Maurice, S. (2024). Exploration of Carbonate-Rich Rocks in the Margin Unit by the Perseverance Rover in Jezero Crater. *LPSC.*

Hurowitz, J. A., Tice, M. M., Allwood, A. C., Cable, M. L., Hand, K. P., Murphy, A. E., ... & Wolf, Z. U. (2025, March). THE DETECTION OF A POTENTIAL BIOSIGNATURE BY THE PERSEVERANCE ROVER ON MARS. In *56th Lunar and Planetary Science Conference* (p. 2581).

Jones, B. F., & Mumpton, F. A. (1986). Clay mineral diagenesis in lacustrine sediments. *United States Geological Survey Bulletin*, *1578*, 291-300.

Kalucha, H., Broz, A., Randazzo, N., Aramendia, J., Madariaga, J. M., Garczynski, B., ... & Wiens, R. C. (2024). Probable concretions observed in the Shenandoah Formation of Jezero Crater, Mars and comparison with terrestrial analogs. *Journal of Geophysical Research: Planets*, *129*(8), e2023JE008138.

Lacelle, D., Pellerin, A., Clark, I. D., Lauriol, B., & Fortin, D. (2009). (Micro) morphological, inorganic–organic isotope geochemisty and microbial populations in endostromatolites (cf. fissure calcretes), Haughton impact structure, Devon Island, Canada: The influence of geochemical pathways on the preservation of isotope biomarkers. *Earth and Planetary Science Letters*, *281*(3-4), 202-214.

Last, W. M., & Vance, R. E. (1997). Bedding characteristics of Holocene sediments from salt lakes of the northern Great Plains, Western Canada. *Journal of Paleolimnology*, *17*, 297-318.

Li, Q., Fan, Q., Wei, H., Qin, Z., Zhang, X., Du, Y., & Shan, F. (2020). Sulfur isotope constraints on the formation of MgSO4-deficient evaporites in the Qarhan salt Lake, western China. *Journal of Asian Earth Sciences*, *189*, 104160.

Liang, C., Yang, B., Cao, Y., Liu, K., Wu, J., Hao, F., ... & Han, W. (2024). Salinization mechanism of lakes and controls on organic matter enrichment: From present to deep-time records. *Earth-Science Reviews*, 104720.

Lotem, N., Rasmussen, B., Zi, J. W., Zeichner, S. S., Present, T. M., Bar-On, Y. M., & W. Fischer, W. (2025). Reconciling Archean organic-rich mudrocks with low primary productivity before the Great Oxygenation Event. *Proceedings of the National Academy of Sciences*, *122*(2), e2417673121.

Lyons, W. B., Hines, M. E., Last, W. M., & Lent, R. M. (1994). Sulfate reduction rates in microbial mat sediments of differing chemistries: implications for organic carbon preservation in saline lakes.

Mavromatis, V., Power, I. M., Harrison, A. L., Beinlich, A., Dipple, G. M., & Bénézeth, P. (2021). Mechanisms controlling the Mg isotope composition of hydromagnesite-magnesite playas near Atlin, British Columbia, Canada. *Chemical Geology*, *579*, 120325.

McCubbin, F. M., Farley, K. A., Harrington, A. D., Hutzler, A., & Smith, C. L. (2025). Mars Sample Return: From collection to curation of samples from a habitable world. *Proceedings of the National Academy of Sciences*, *122*(2), e2404253121.

McSween Jr, H. Y., Hamilton, V. E., & Farley, K. A. (2025). Perspectives on Mars Sample Return: A critical resource for planetary science and exploration. *Proceedings of the National Academy of Sciences*, *122*(2), e2404248121.

McSween Jr, H. Y., Taylor, G. J., & Wyatt, M. B. (2009). Elemental composition of the Martian crust. *Science*, *324*(5928), 736-739.

Merdy, P., Gamrani, M., Montes, C. R., Rezende Filho, A. T., Barbiero, L., Ishida, D. A., ... & Lucas, Y. (2022). Processes and rates of formation defined by modelling in alkaline to acidic soil systems in Brazilian Pantanal wetland. *Catena*, *210*, 105876.

Nesbitt, H. W. (1990). Groundwater evolution, authigenic carbonates and sulfates, of the Basque Lake No. 2 basin, Canada. *Fluid-mineral interactions: A tribute to HP Eugster, special publication*, *2*, 355-371.

Nichols, F., Pontefract, A., Dion-Kirschner, H., Masterson, A. L., & Osburn, M. R. (2023). Lipid biosignatures from SO4-rich hypersaline lakes of the Cariboo Plateau. *Journal of Geophysical Research: Biogeosciences*, *128*(10), e2023JG007480.

Noe Dobrea, E. Z., McAdam, A. C., Freissinet, C., Franz, H., Belmahdi, I., Hamersley, M. R., ... & Aubrey, A. D. (2016). Preservation of organics at the painted desert: Lessons for MSL and beyond. *Biosignature Preservation and Detection in Mars Analog Environments*, *1912*, 2031.

Paradis, S., Petts, D., Simandl, G. J., Sharpe, R., Hamilton, T. S., Fayek, M., & Jackson, S. E. (2023). Impact of deformation and metamorphism on sphalerite chemistry–Element mapping of sphalerite in carbonate-hosted Zn-Pb sulfide deposits of the Kootenay Arc, southern British Columbia, Canada and northeastern Washington, USA. *Ore Geology Reviews*, *158*, 105482.

Pellerin, A., Anderson-Trocmé, L., Whyte, L. G., Zane, G. M., Wall, J. D., & Wing, B. A. (2015). Sulfur isotope fractionation during the evolutionary adaptation of a sulfate-reducing bacterium. *Applied and Environmental Microbiology*, *81*(8), 2676-2689.

Pontefract, A., Zhu, T. F., Walker, V. K., Hepburn, H., Lui, C., Zuber, M. T., ... & Carr, C. E. (2017). Microbial diversity in a hypersaline sulfate lake: a terrestrial analog of ancient Mars. *Frontiers in microbiology*, *8*, 1819.

Posth, N. R., Canfield, D. E., & Kappler, A. (2014). Biogenic Fe (III) minerals: from formation to diagenesis and preservation in the rock record. *Earth-Science Reviews*, *135*, 103-121.

Power, I. M., Wilson, S., Harrison, A. L., Dipple, G. M., McCutcheon, J., Southam, G., & Kenward, P. A. (2014). A depositional model for hydromagnesite–magnesite playas near Atlin, British Columbia, Canada. *Sedimentology*, *61*(6), 1701-1733.

Power, I. M., Wilson, S., Thom, J. M., Dipple, G. M., Gabites, J. E., & Southam, G. (2009). The hydromagnesite playas of Atlin, British Columbia, Canada: A biogeochemical model for CO2 sequestration. *Chemical Geology*, *260*(3-4), 286-300.

Power, I. M., Wilson, S. A., Thom, J. M., Dipple, G. M., & Southam, G. (2007). Biologically induced mineralization of dypingite by cyanobacteria from an alkaline wetland near Atlin, British Columbia, Canada. *Geochemical Transactions*, *8*, 1-16.

Rapin, W., Ehlmann, B. L., Dromart, G., Schieber, J., Thomas, N. H., Fischer, W. W., ... & Vasavada, A. R. (2019). An interval of high salinity in ancient Gale crater lake on Mars. *Nature Geoscience*, *12*(11), 889-895.

Rapin, W., Dromart, G., Clark, B. C., Schieber, J., Kite, E. S., Kah, L. C., ... & Lanza, N. L. (2023). Sustained wet–dry cycling on early Mars. *Nature*, *620*(7973), 299-302.

Raudsepp, M. J., Wilson, S., Zeyen, N., Arizaleta, M. L., & Power, I. M. (2024). Magnesite everywhere: Formation of carbonates in the alkaline lakes and playas of the Cariboo Plateau, British Columbia, Canada. *Chemical Geology*, *648*, 121951.

Renaut, R. W. (1993). Morphology, distribution, and preservation potential of microbial mats in the hydromagnesite-magnesite playas of the Cariboo Plateau, British Columbia, Canada. *Hydrobiologia*, *267*, 75-98.

Renaut, R. W., & Long, P. R. (1989). Sedimentology of the saline lakes of the Cariboo plateau, Interior British Columbia, Canada. *Sedimentary Geology*, *64*(4), 239-264.

Ruecker, A., Schröder, C., Byrne, J., Weigold, P., Behrens, S., & Kappler, A. (2016). Geochemistry and mineralogy of Western Australian salt lake sediments: implications for Meridiani Planum on Mars. *Astrobiology*, *16*(7), 525-538.

Schwartz, H., Sample, J., Weberling, K. D., Minisini, D., & Moore, J. C. (2003). An ancient linked fluid migration system: cold-seep deposits and sandstone intrusions in the Panoche Hills, California, USA. *Geo-Marine Letters*, *23*, 340-350.

Schwenzer, S. P., Bridges, J. C., Wiens, R. C., Conrad, P. G., Kelley, S. P., Leveille, R., ... & Meslin, P. Y. (2016). Fluids during diagenesis and sulfate vein formation in sediments at Gale crater, Mars. *Meteoritics & Planetary Science*, *51*(11), 2175-2202.

Seal, R. R., Alpers, C. N., & Rye, R. O. (2000). Stable isotope systematics of sulfate minerals. *Reviews in Mineralogy and Geochemistry*, *40*(1), 541-602.

Sorokin, D. Y., Berben, T., Melton, E. D., Overmars, L., Vavourakis, C. D., & Muyzer, G. (2014). Microbial diversity and biogeochemical cycling in soda lakes. *Extremophiles*, *18*, 791-809.

Spence, J., & Telmer, K. (2005). The role of sulfur in chemical weathering and atmospheric CO2 fluxes: evidence from major ions, δ13CDIC, and δ34SSO4 in rivers of the Canadian Cordillera. *Geochimica et Cosmochimica Acta*, *69*(23), 5441-5458.

Speth, D. R., Yu, F. B., Connon, S. A., Lim, S., Magyar, J. S., Peña-Salinas, M. E., ... & Orphan, V. J. (2022). Microbial communities of Auka hydrothermal sediments shed light on vent biogeography and the evolutionary history of thermophily. *The ISME Journal*, *16*(7), 1750-1764.

Stack, K. M., Ives, L. R., Gupta, S., Lamb, M. P., Tebolt, M., Caravaca, G., ... & Wiens, R. C. (2024). Sedimentology and stratigraphy of the shenandoah formation, Western Fan, Jezero Crater, Mars. *Journal of Geophysical Research: Planets*, *129*(2), e2023JE008187.

Stebbins, A., Algeo, T. J., Olsen, C., Sano, H., Rowe, H., & Hannigan, R. (2019). Sulfur-isotope evidence for recovery of seawater sulfate concentrations from a PTB minimum by the Smithian-Spathian transition. *Earth-Science Reviews*, *195*, 83-95.

Summons, R. E., Amend, J. P., Bish, D., Buick, R., Cody, G. D., Des Marais, D. J., ... & Sumner, D. Y. (2011). Preservation of martian organic and environmental records: final report of the Mars Biosignature Working Group. *Astrobiology*, *11*(2), 157-181.

Tazi, L., Breakwell, D. P., Harker, A. R., & Crandall, K. A. (2014). Life in extreme environments: microbial diversity in Great Salt Lake, Utah. *Extremophiles*, *18*, 525-535.

Tosca, N. J., Knoll, A. H., & McLennan, S. M. (2008). Water activity and the challenge for life on early Mars. *Science*, *320*(5880), 1204-1207.

Tosca, N. J., & Tutolo, B. M. (2023). How to make an alkaline lake: fifty years of chemical divides. *Elements*, *19*(1), 15-21.

Trichet, J., Défarge, C., Tribble, J., Tribble, G., & Sansone, F. (2001). Christmas Island lagoonal lakes, models for the deposition of carbonate–evaporite–organic laminated sediments. *Sedimentary Geology*, *140*(1-2), 177-189.

Tutolo, B. M., Perrin, R., Lauer, R., Bossaer, S., Tosca, N. J., Hutchings, A., ... & Wilson, T. (2024). Groundwater-driven evolution of prebiotic alkaline lake environments. *Life*, *14*(12), 1624.

Valiente, N., Carrey, R., Otero, N., Gutiérrez-Villanueva, M. A., Soler, A., Sanz, D., ... & Gómez-Alday, J. J. (2017). Tracing sulfate recycling in the hypersaline Pétrola Lake (SE Spain): A combined isotopic and microbiological approach. *Chemical Geology*, *473*, 74-89.

Vaniman, D., Chipera, S., Rampe, E., Bristow, T., Blake, D., Meusburger, J., ... & Fraeman, A. (2024). Gypsum on Mars: A Detailed View at Gale Crater. *Minerals*, *14*(8), 815.

Warren, J. K. (2016). *Evaporites: A geological compendium*. Springer.

Xu, S., Wang, Y., Bai, N., Wu, S., & Liu, B. (2024). Organic matter enrichment mechanism in saline lacustrine basins: A review. *Geological Journal*, *59*(1), 155-168.

Appendix A: Chapter 5 Supplementary Information

BIOTIC AND ABIOTIC SIGNATURES IN SULFATE AND CARBONATE RICH HYPERSALINE LAKES AS ANALOGS FOR MARS

Hemani Kalucha[1*], Ben Johnson[2], Miquela Ingalls[3], Hanna C. Leapaldt[3], Ellen Olsen[3], James Mullahoo[1], Woodward Fischer[1]

[1]California Institute of Technology

[2]Iowa State University

[3]Pennsylvania State University

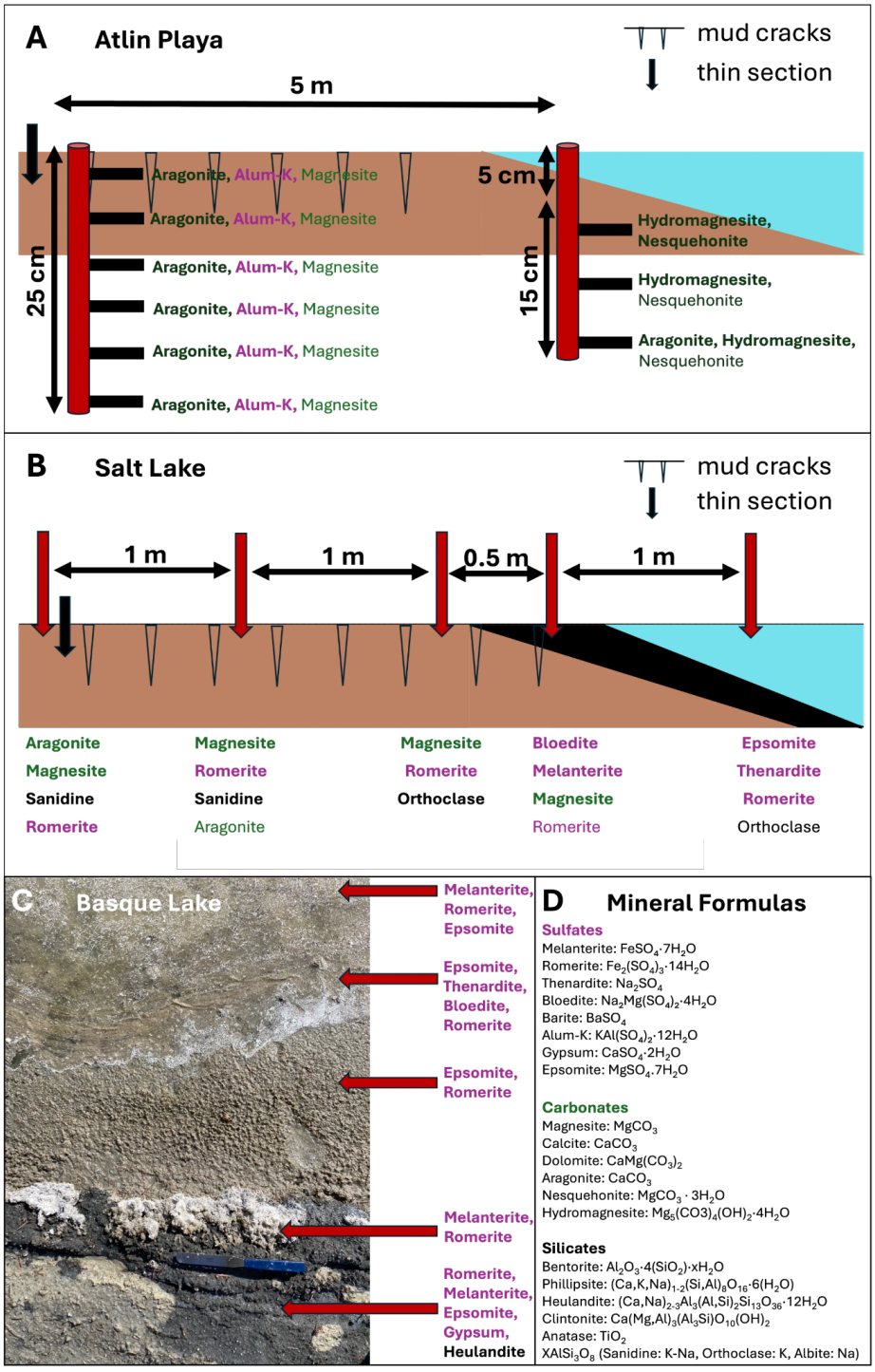

Figure S1: Minerals detected in lake samples via FTIR-ATR. A) Atlin Playa core locations and sample depths with corresponding minerals detected. B) Salt Lake surface sample locations and mineral trends. Thin section core location shown in both with black arrow. C) Textural changes from lake margin to lake water in Basque Lake and corresponding mineral detections. D) Relevant mineral formulas discussed in this study. Carbonate minerals are dark green. Sulfate minerals are magenta.

Silicates are black. Non-bolded font represents minerals that contribute very few peaks to the overall spectrum.

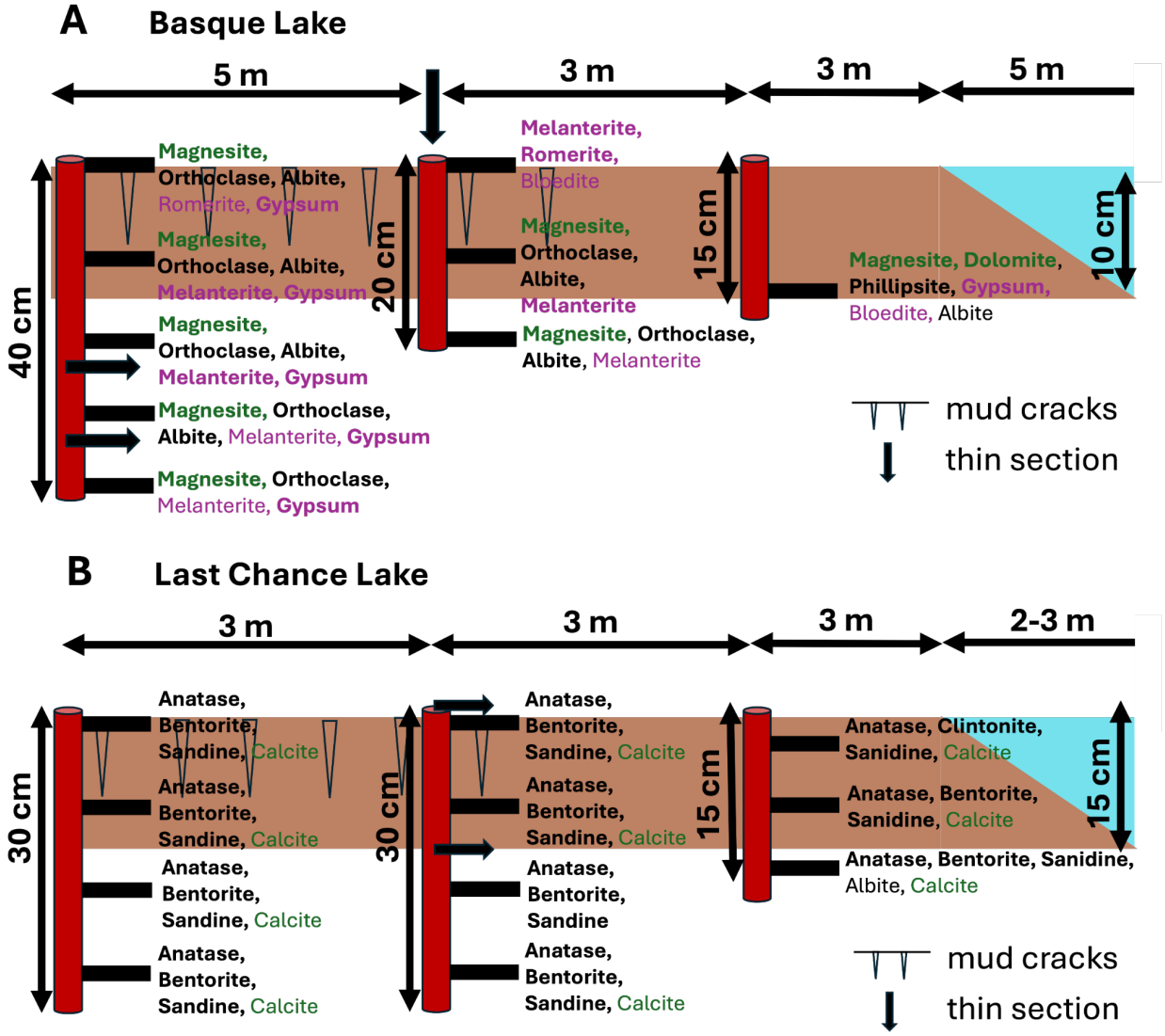

Figure S2: Minerals detected in lake samples via FTIR-ATR. A) Basque Lake core locations and sample depths with corresponding minerals detected. B) Last Chance Lake core locations and sample depths with corresponding minerals detected. Bentorite best matched the spectra but the likely mineral is some form of calcium sulfate. Thin section core location shown in both with black arrow. Carbonate minerals are dark green. Sulfate minerals are magenta. Silicates are black. Non-bolded font represents minerals that contribute very few peaks to the overall spectrum. Mineral formulas are in Figure S1.

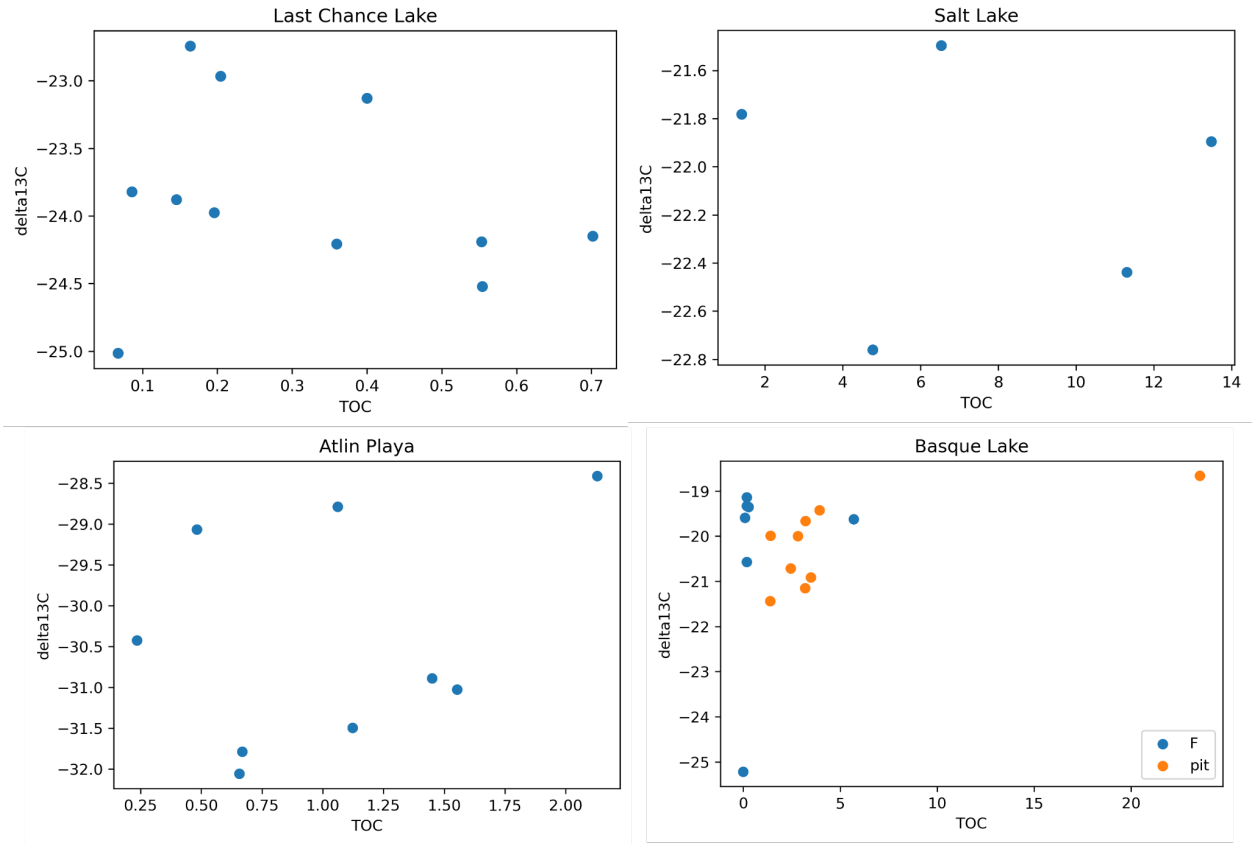

Figure S3: $\delta^{13}C$ of organic carbon in sediments of each of the four lakes. In Basque lakes, points named 'F' refer to pure salt samples at the pool edge and 'pit' refers to sediments taken from pits.

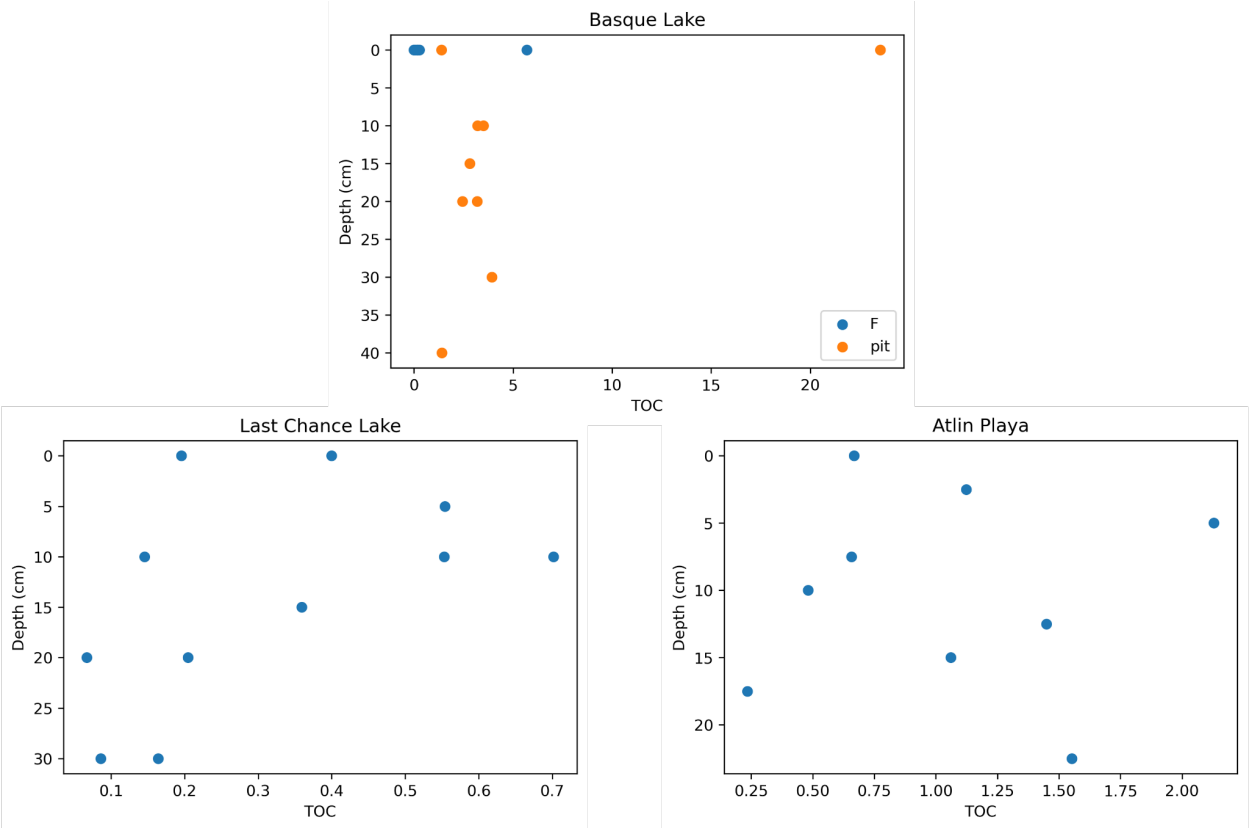

Figure S4: Depth vs % TOC for applicable lakes.

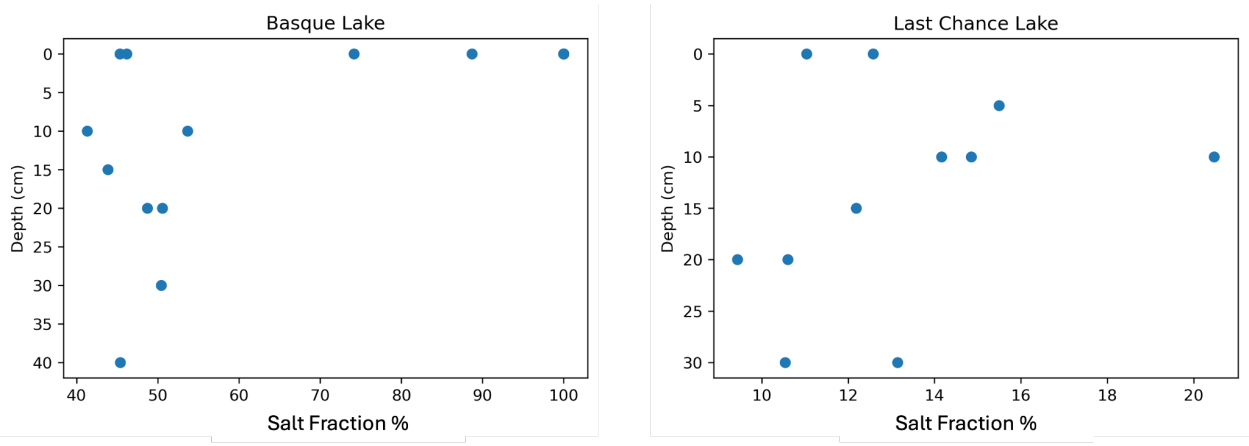

Figure S5: Depth vs salt fraction of sample for applicable lakes.

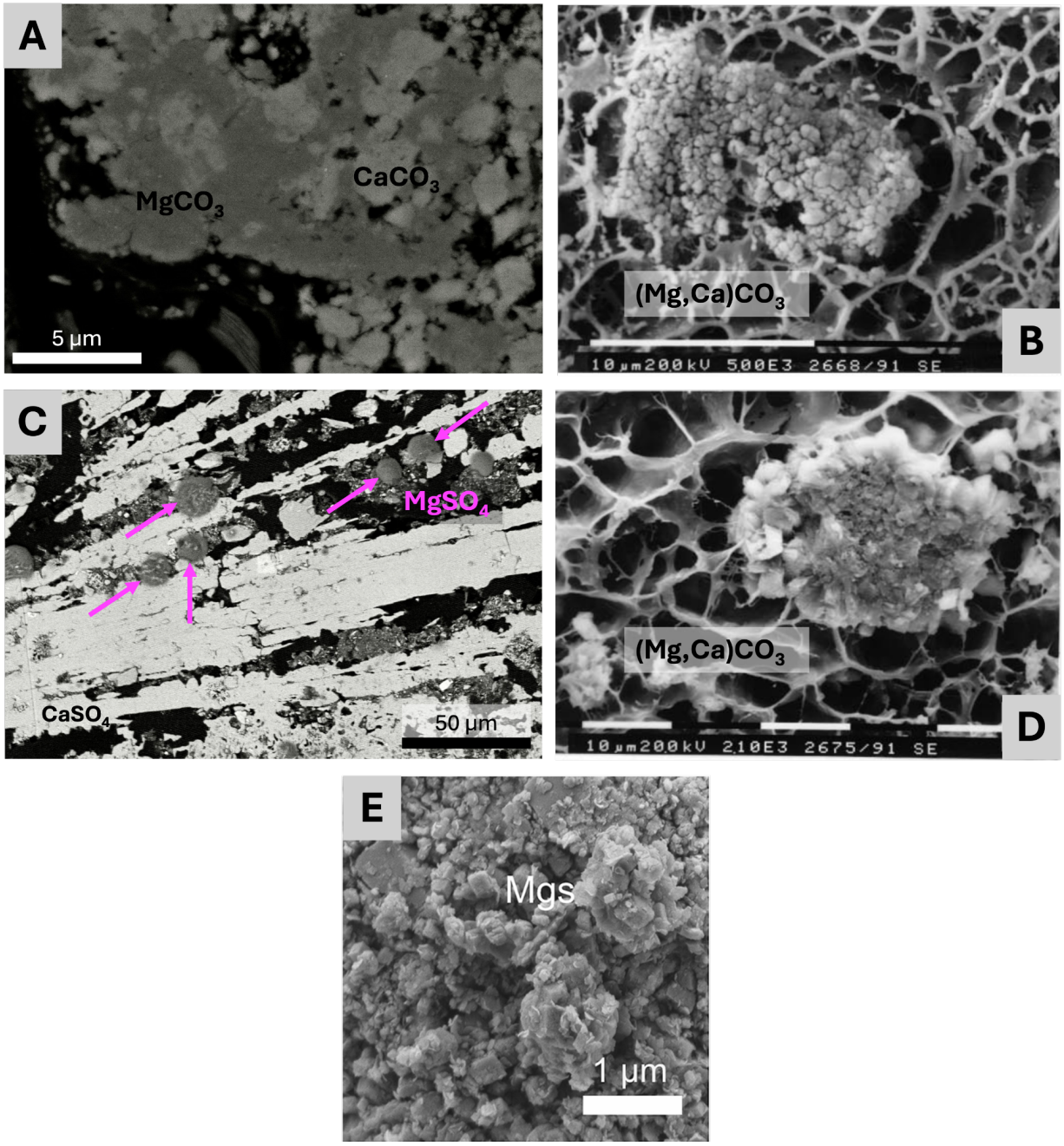

Figure S6: Comparison of globular, clumped textures in our study and previous studies. A) Magnesium and Calcium carbonate from Atlin Playa in our study B,D) (Mg,Ca) carbonate in Christmas Lake in Trichet et al. (2001) C) Mg sulfate clumps in Salt Lake in our study E) Mgs or magnesite clumps in Milk Lake in Raudsepp et al. (2024).

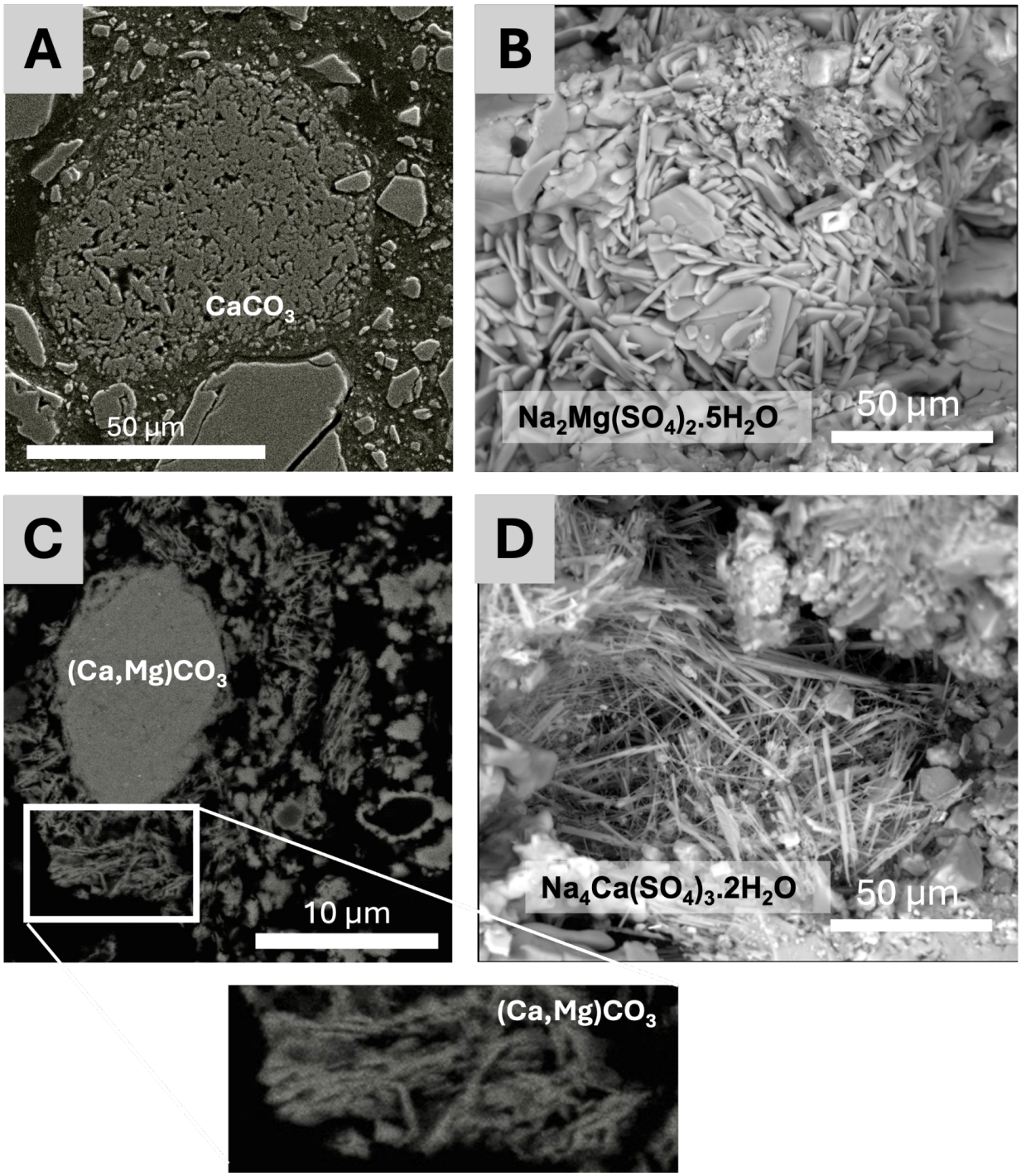

Figure S7: Comparison of acicular textures in our study and previous studies. A) bladed aggregate of Ca-carbonate in Last Chance Lake in our study B) bladed aggregate of Na,Mg-sulfate salt in Spotted Lake from Cannon (2012) C) Acicular aggregate of Ca,Mg-carbonate in Atlin Playa in our study with inset zoom D) Acicular aggregate of Na,Ca-sulfate salt in Spotted Lake from Cannon (2012).

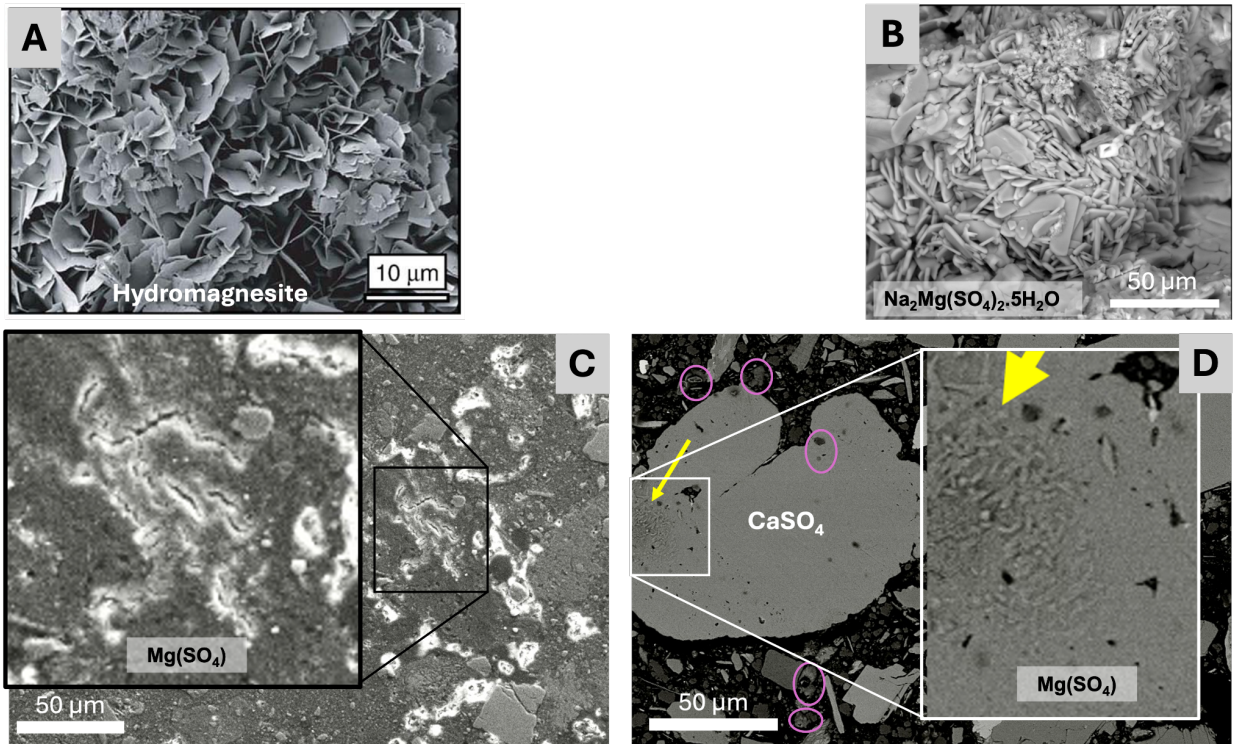

Figure S8: Comparison of prismatic and bladed crystals in our study and previous studies. A) Hydromagnesite in plate like morphologies in Atlin Playa in Power et al. (2009). B) Bladed aggregates of Na,Mg-sulfate salt in Spotted Lake from Cannon (2012). C) Plate like 2D projection of Mg-sulfate crystals in Salt Lake in our study with inset zoom D) Bladed aggregates of Mg-sulfate crystals in Basque Lake in our study

Lake	Chloride	Bromide	Nitrate	Sulfate	Phosphate
Atlin Playa	n.a	n.a	n.a	0.407	n.a
Salt Lake	n.a	n.a	1.3	2537.96	n.a
Last Chance Lake	32.885	0.115	6.45	75.255	1.475
Basque Lake 1	123.52	0.28	n.a	3868.2	n.a
	Lithium	**Sodium**	**Potassium**	**Magnesium**	**Calcium**
Atlin Playa	n.a	3.975	0.395	48.826	0.273
Salt Lake	n.a	284.28	18.5	2478.36	2.66
Last Chance Lake	n.a	1292.615	8.81	n.a	1.39
Basque Lake 1	0.95	1653.09	125.79	2889.34	4.23

Table S1: Cation and anion concentrations measured on the IC for all four lake waters in this study. Concentrations are in mM.

References in figure captions

Cannon, K. M. (2012). *Spotted Lake: Analog for Hydrated Sulfate Occurrences in the Last Vestiges of Evaporating Martian Paleolakes* (Doctoral dissertation, PhD Thesis, Queen's University, Ontario).

Power, I. M., Wilson, S., Thom, J. M., Dipple, G. M., Gabites, J. E., & Southam, G. (2009). The hydromagnesite playas of Atlin, British Columbia, Canada: A biogeochemical model for CO2 sequestration. *Chemical Geology*, *260*(3-4), 286-300.

Raudsepp, M. J., Wilson, S., Zeyen, N., Arizaleta, M. L., & Power, I. M. (2024). Magnesite everywhere: Formation of carbonates in the alkaline lakes and playas of the Cariboo Plateau, British Columbia, Canada. *Chemical Geology*, *648*, 121951.

Trichet, J., Défarge, C., Tribble, J., Tribble, G., & Sansone, F. (2001). Christmas Island lagoonal lakes, models for the deposition of carbonate–evaporite–organic laminated sediments. *Sedimentary Geology*, *140*(1-2), 177-189.